

Stabilization Mechanisms of Non-Polar Metal Colloids with Thin Organic Shells

Dissertation

zu Erlangung des Grades

des Doktors der Naturwissenschaften

der Naturwissenschaftlich-Technischen Fakultät

der Universität des Saarlandes

M. Sc. Tobias Valentin Knapp



Saarbrücken
2025

INM — Leibniz-Institut für Neue Materialien
Naturwissenschaftlich-Technische Fakultät
Universität des Saarlandes

Tag des Kolloquiums:	10.04.2026
Dekan:	Prof. Dr.-Ing. Dirk Bähre
Berichterstatter:	Prod. Dr. Tobias Kraus
	Prof. Dr. Guido Kickelbick
Vorsitz:	Prof. Dr. Andreas Speicher
Akad. Mitarbeiter:	PD Dr. Oliver Janka

Saarbrücken, Dezember 2025

Success is walking from failure to failure with no loss of enthusiasm.
Winston Churchill

Acknowledgements

I had the opportunity to work with many great people during this PhD. I am grateful for the support and the experiences I was able to make during my doctorate.

In particular, I would like to thank my supervisor *Prof. Dr. Tobias Kraus*, who sparked my interest in nanomaterials and colloid chemistry, offered me the opportunity to do a PhD after my Bachelor's and Master's theses. He enabled me to work independently on my project and develop new ideas and skills. Through our supportive and challenging discussions, he has improved my scientific skills. I am grateful to him for his support with my publications and the opportunity to present my research at numerous conferences. He also organized the collaboration with the Australian research group of *Dr. Asaph Widmer-Cooper*.

Dr. Asaph Widmer-Cooper has collaborated with us on several projects investigating the colloidal stability of apolar nanoparticles. I thank him for the molecular dynamics simulations of the ligand shell that he and his group (*Dr. Mohammad Rashedul Hasan, Setare Dodange, Dr. Deborah Monego*) performed.

Special thanks also go to *Dr. Bart-Jan Niebuur*, who was guiding me during my time as a PhD student. He introduced me to the process of performing and analysing small-angle X-ray scattering experiments. I am also grateful for his help with my publications.

I want to thank the Leibniz Institute for New Materials directors, *Prof. Dr. Aránzazu del Campo* and *Prof. Dr. Wilfried Weber*, for the research-friendly working atmosphere.

I would also like to thank my second reviewer *Prof. Dr. Guido Kickelbick* and the members of my examination board.

I would also like to thank my colleagues, other group members of the *structure formation* and *electrofluid group,* and other co-authors. In particular, I would like to thank my office colleagues *Selim Basaran*, *Yannic Curto*, and *Lingyu Liu*. I would also like to thank my laboratory colleagues *Dr. Thomas Kister*, *Muniba Bhatti* and *Michael Klos* for their motivating support. Special thanks also goes to *Dominik Perius* for carrying out scanning electron microscopy measurements and image analyses in various projects. I would also like to thank the specialization, master and exchange students for their curiosity and willingness to learn. I

would especially like to thank *Camila Martinez Briones* for her work on the non-linear ligands project.

I would also like to thank *Anja Colbus* and *Leon Germann* for their support in the laboratory. I thank *Robert Drumm* and *Simon Blum* for carrying out thermogravimetric measurements. For performing transmission electron microscopy measurements, I would like to thank *Dr. Markus Koch*, *Aude Haettich* and *Birgit Nothdurft*. I thank *Sarah Schumacher* for measuring the specific surface area of various samples.

I would also like to thank my *family* and *friends* who supported and motivated me during my doctorate. I would especially like to thank my *parents* for supporting me during my studies and PhD and encouraging me to keep going.

Abstract

Apolar metal nanoparticles are stabilized by ligand shells that enhance colloidal and structural stability, enabling their use as building blocks for functional materials. This dissertation investigates how ligand shell modifications influence two key particle properties: colloidal stability and shape stability.

Colloidal stability—the resistance of dispersed particles to agglomeration—depends on the shell's transition from disordered to ordered states. Three modifications were used. Mixing dispersions with additive molecules partially replaced ligands, moderately improving stability. Non-linear ligands, however, greatly enhanced stability and suppressed shell ordering. Finally, mixed ligand shells showed that stability improvements relied on molecular size differences and the composition and distribution of ligands.

Shape stability refers to the core's resistance to coarsening, mainly governed by the ligand shell's passivating effect. Here, partial ligand exchange with tetrahydrothiophene weakened this protection, enabling controlled coarsening at moderate temperatures. This modification allowed the creation of gold sponges via aggregation and self-assembly.

Keywords: Apolar nanoparticles, shell modification, colloidal stability, shape stability

Zusammenfassung

Apolare Metallnanopartikel werden durch Ligandenschalen stabilisiert, die die kolloidale und strukturelle Stabilität verbessern und somit ihre Verwendung als Bausteine für funktionelle Materialien ermöglichen. Diese Dissertation untersucht, wie Modifikationen der Ligandenschale zwei wichtige Partikeleigenschaften beeinflussen: die kolloidale Stabilität und die Formstabilität.

Die kolloidale Stabilität – die Widerstandsfähigkeit dispergierter Partikel gegen Agglomeration – hängt vom Übergang der Hülle von einem ungeordneten zu einem geordneten Zustand ab. Es wurden drei Modifikationen verwendet. Durch Mischen von Dispersionen mit Additivmolekülen wurden Liganden teilweise ersetzt, was zu einer moderaten Verbesserung der Stabilität führte. Nichtlineare Liganden verbesserten jedoch die Stabilität erheblich und unterdrückten die Hüllenordnung. Schließlich zeigten gemischte Ligandenhüllen, dass Stabilitätsverbesserungen von molekularen Größenunterschieden sowie der Zusammensetzung und Verteilung der Liganden abhingen.

Die Formstabilität bezieht sich auf die Widerstandsfähigkeit des Kerns gegen Vergröberung, die hauptsächlich durch die passivierende Wirkung der Ligandenhülle bestimmt wird. Hier schwächte ein teilweiser Ligandenaustausch mit Tetrahydrothiophen diesen Schutz und ermöglichte eine kontrollierte Vergröberung bei moderaten Temperaturen. Diese Modifikation ermöglichte die Herstellung von Goldschwämmen durch Aggregation und Selbstorganisation.

Keywords: Unpolare Nanopartikel, Hüllenmodifikation, kolloidale Stabilität, Formstabilität

Publications and Contributions

This dissertation contains four manuscripts that have been published in journals or will be published. The contributions of the individual authors are described in the following section within the taxonomy CRediT (Contributors Roles Taxonomy).[1–3]

Publication 1: Knapp, T. V.; Hasan, M. R.; Niebuur, B.-J.; Widmer-Cooper, A.; Kraus, T. Stabilization of Apolar Nanoparticle Dispersions by Molecular Additives. *Langmuir*, vol. 40, no. 26, pp. 13527–13537, 2024.
https://doi.org/10.1021/acs.langmuir.4c00996.
Status: published

- *Tobias Valentin Knapp*: Conceptualization, Data Validation, Formal Analysis, Investigation, Methodology, Writing – Original Draft, Writing – Review and Editing.
- *Mohammad Rashedul Hasan*: Conceptualization, Data Validation, Formal Analysis, Investigation, Methodology, Writing – Original Draft, Writing – Review and Editing.
- *Bart-Jan Niebuur*: Conceptualization, Methodology, Writing – Review and Editing.
- *Asaph Widmer-Cooper*: Conceptualization, Project Administration, Resources, Supervision, Writing – Review and Editing.
- *Tobias Kraus*: Conceptualization, Project Administration, Resources, Supervision, Writing – Review and Editing.

Publication 2: Knapp, T. V.; Dodange, S.; Monego, D.; Briones, C. M.; Hero, D., Niebuur, B.-J.; Gallei, M.; Kraus, T.; Widmer-Cooper, A. Maintaining Shell Disorder with Kinked or Branched Ligands Stabilizes Apolar Nanoparticles. *ACS Nano*, vol. 19, no. 39, pp. 35127–35140, 2025.
https://doi.org/10.1021/acsnano.5c12697
Status: published

- *Tobias Valentin Knapp*: Conceptualization, Data Validation, Formal Analysis, Investigation, Methodology, Writing – Original Draft, Writing – Review and Editing.
- *Setare Dodange*: Conceptualization, Data Validation, Formal Analysis, Investigation, Methodology, Writing – Original Draft, Writing – Review and Editing.
- *Deborah Monego*: Conceptualization, Data Curation, Formal Analysis, Investigation, Methodology, Writing – Review and Editing.

- *Camila Martinez Briones*: Conceptualization, Methodology, Writing – Review and Editing.
- *Devid Hero*: Conceptualization, Methodology, Writing – Review and Editing.
- *Bart-Jan Niebuur*: Conceptualization, Methodology, Writing – Review and Editing.
- *Markus Gallei*: Conceptualization, Methodology, Writing – Review and Editing.
- *Asaph Widmer-Cooper*: Conceptualization, Project Administration, Resources, Supervision, Writing – Review and Editing.
- *Tobias Kraus*: Conceptualization, Project Administration, Resources, Supervision, Writing – Review and Editing.

Publication 3: Knapp, T. V.; Niebuur, B.-J.; Matsarskaia, O.; Kraus, T. Reactive Additive-Induced Joining of Apolar Thiol-Coated Gold Nanoparticle Cores at Low Temperatures.
Status: in preparation

- *Tobias Valentin Knapp*: Conceptualization, Data Validation, Formal Analysis, Investigation, Methodology, Writing – Original Draft, Writing – Review and Editing.
- *Bart-Jan Niebuur*: Conceptualization, Methodology, Writing – Review and Editing.
- *Olga Matsarskaia*: Conceptualization, Methodology, Writing – Review and Editing.
- *Tobias Kraus*: Conceptualization, Project Administration, Resources, Supervision, Writing – Review and Editing.

Publication 4: Knapp, T. V.; Perius, D.; Nothdurft, B.; Niebuur, B.-J.; Kraus, T. Gold Sponge Formation by Temperature-induced Aggregation of a Stable Nanoparticle Dispersion.
Status: in preparation

- *Tobias Valentin Knapp*: Conceptualization, Data Validation, Formal Analysis, Investigation, Methodology, Writing – Original Draft, Writing – Review and Editing.
- *Dominik Perius*: Conceptualization, Data Validation, Formal Analysis, Investigation, Methodology, Writing – Original Draft, Writing – Review and Editing.
- *Birgit Nothdurft*: Conceptualization, Methodology, Writing – Review and Editing.
- *Bart-Jan Niebuur*: Conceptualization, Methodology, Writing – Review and Editing.
- *Tobias Kraus*: Conceptualization, Project Administration, Resources, Supervision, Writing – Review and Editing.

Contributions in other publications that are not relevant to the dissertation:

Publication 5: Beran, L.; Knapp, T. V.; Nexha, A.; Lay, M.; Niebuur, B.; Kraus, T. Combining Structured Data with Domain Knowledge in Battery Materials Research: The Case of Conductive Networks. *Adv. Eng. Mater.*, vol. 27, no. 8, 2025.
https://advanced.onlinelibrary.wiley.com/doi/10.1002/adem.202401813

- *Lisa Beran*: Conceptualization, Data Validation, Formal Analysis, Investigation, Methodology, Writing – Original Draft, Writing – Review and Editing.
- *Tobias Valentin Knapp*: Data Validation, Formal Analysis, Investigation, Methodology, Writing – Review and Editing.
- *Albenc Nexha*: Data Validation, Formal Analysis, Investigation, Methodology, Writing – Review and Editing.
- *Makara Lay*: Data Validation, Formal Analysis, Investigation, Methodology, Writing – Review and Editing.
- *Bart-Jan Niebuur*: Data Validation, Formal Analysis, Investigation, Methodology, Writing – Review and Editing.
- *Tobias Kraus*: Conceptualization, Project Administration, Resources, Supervision, Writing – Review and Editing.

List of Abbreviations

Important abbreviations that have been used in the text and need explanation are briefly presented.

Au	gold
AuNP	gold nanoparticles
AFM	atomic force microscope
CdSe	cadmium selenide
CODEX	center-band only detection of exchange
DLS	dynamic light scattering
DLVO	Derjaguin–Landau–Verwey–Overbeek
DSC	differential scanning calorimetry
e.g.	exempi gratia (“for example”)
et al.	et alia (“and others”)
FIB	focused ion beam
$HAuCl_4 \cdot 3\,H_2O$	chloroauric acid
i.e.	id est (“that is”)
ITC	isothermal titration calorimetry
MALDI-TOF	matrix-assisted laser desorption/ionization time of flight
MD	molecular dynamic
MS	mass spectrometry
NC	nanocrystal
NC_{18}	1-octadecylamine
NMR	nuclear magnetic resonance spectroscopy
NP	nanoparticle
OAm	oleylamine
R5N, THT	pyrrolidine
R9N	azonane, octamethylenimine
R5S	tetrahydrothiophene
R9S	thionane
SAM	self-assembled monolayer
SANS	small-angle neutron scattering
SAXS	small-angle X-ray scattering
SC_6, HT	1-hexanethiol

SC_{12}, DDT	1-dodecanethiol
br-SC_{12}	11-methyldodecanethiol
SC_{16}, HDT	1-hexadecanethiol
dbr-SC_{16}	hexadecyl sulfide
SC_{18}	1-octadecanethiol
SEM	scanning electron microscopy
SFG	sum frequency generation vibrational spectroscopy
STM	scanning tunneling microscopy
T_{agglo}	agglomeration temperature
T_{order}	ordering temperature
TEM	transmission electron microscopy
TGA	thermogravimetric analysis
TiO_2	titanium dioxide
vdW	van der Waals
ZrO_2	zirconium dioxide
χ_{agglo}	agglomeration fraction

Table of Contents

Acknowledgements v

Abstract vii

Zusammenfassung viii

Publications and Contributions ix

List of Abbreviations xii

1 Introduction 1

2 State of the Art 5

2.1 Synthesis and functionalization of gold nanoparticles 6

2.2 Colloidal stability of apolar nanoparticles 8

2.2.1 Effect of the core size 16

2.2.2 Modification of the shell structure 18

2.2.2.1 Non-linear ligands 18

2.2.2.2 Mixed ligand shells 23

2.2.3 Effect of the solvent composition 26

2.3 Shape stability of apolar nanoparticles 29

2.4 Goal of the dissertation 32

3 Results 35

3.1 Publication 1: Stabilization of Apolar Nanoparticle Dispersions by Molecular Additives 36

3.1.1 Abstract 37

3.1.2 Introduction 37

3.1.3 Results and Discussions 39

3.1.4 Conclusion 50

3.1.5 Materials and Methods 51

3.1.6 Acknowledgment 55

3.2 Publication 2: Maintaining Shell Disorder with Kinked or Branched Ligands Stabilizes Apolar Nanoparticles . . . 56
3.2.1 Abstract . . . 57
3.2.2 Introduction . . . 57
3.2.3 Results and Discussion . . . 58
3.2.4 Conclusions . . . 73
3.2.5 Materials and Methods . . . 74
3.2.6 Acknowledgement . . . 81
3.3 Stabilization of Apolar Gold Nanoparticles by Mixed Ligand Shells . . . 82
3.3.1 Introduction . . . 82
3.3.2 Results and Discussions . . . 84
3.3.3 Conclusion . . . 90
3.3.4 Materials and Methods . . . 91
3.4 Publication 3: Reactive Additive-Induced Joining of Apolar Thiol-Coated Gold Nanoparticle Cores at Low Temperatures . . . 94
3.4.1 Abstract . . . 95
3.4.2 Introduction . . . 95
3.4.3 Results and Discussion . . . 97
3.4.4 Conclusion . . . 108
3.4.5 Materials and Methods . . . 109
3.4.6 Acknowledgment . . . 112
3.5 Publication 4: Gold Sponge Formation by Temperature-induced Aggregation of a Stable Nanoparticle Dispersion . . . 113
3.5.1 Abstract . . . 114
3.5.2 Introduction . . . 114
3.5.3 Results and Discussion . . . 116
3.5.4 Conclusion . . . 122
3.5.5 Materials and Methods . . . 124
3.5.6 Acknowledgment . . . 130

4 Discussion **131**
4.1 Stabilization with molecular additives . . . 132
4.2 Stabilization with non-linear ligands . . . 134
4.3 Stabilization with mixed ligand shells . . . 136
4.4 Additive-induced aggregation of apolar thiol-coated gold nanoparticles . . . 138
4.5 Formation of gold sponges . . . 140

5 Conclusion and Outlook **143**

Bibliography **147**

Appendix **175**

7.1 Supporting Information - Stabilization of Apolar Nanoparticle Dispersions by Molecular Additives 176

7.2 Supporting Information - Maintaining Shell Disorder with Kinked or Branched Ligands Stabilizes Apolar Nanoparticles 190

7.3 Supporting Data - Stabilization of Apolar Gold Nanoparticles by Mixed Ligand Shells 209

7.4 Supporting Data - Reactive Additive-Induced Joining of Apolar Thiol-Coated Gold Nanoparticle Cores at Low Temperatures 218

7.5 Supporting Data - Gold Sponge Formation by Temperature-induced Aggregation of a Stable Nanoparticle Dispersion 232

Chapter 1: Introduction

Nanoparticles have become a crucial component of modern science and technology due to their unique physical and chemical properties, which differ significantly from those of bulk materials. With dimensions typically ranging from 1 to 100 nm, nanoparticles have a high surface-to-volume ratio, which leads to their special properties [4]. For this reason, particles can be found in many everyday objects, such as cosmetics [5, 6] (like sunscreen [7]), paints [8, 9], or batteries [10–12]. Nanoparticles, especially made from metals like gold and silver, are playing an increasingly important role in industry (e.g., as catalysts) and medicine (e.g., drug delivery or biosensors) [13–19]. Nanoparticles are becoming an increasingly important role in one specific area: printable technologies [20–22]. Metallic nanoparticles can be used to produce electronics or sensors cost-effectively, for example, via inkjet printing [23, 24]. For conductive inks, gold nanoparticles are used due to their high conductivity and chemical stability [25]. Such gold nanoparticles can be synthesized and modified using different methods, depending on the desired properties of the final ink.

Gold nanoparticles were already being produced in an uncontrolled manner in the manufacture of stained glass in the Roman Empire [26]. The first documented controlled synthesis of gold nanoparticles took place in 1857 by Michael Faraday [27]. Over the next few decades, different nanoparticle syntheses were developed. Most syntheses were carried out with gold salts and a reducing agent in aqueous media, for example, the Turkevich [28] and Frens [29] method. These methods could synthesize particles with diameters between 10 and 150 nm and different dispersities. Synthesis in water has many advantages. Due to the polarity of water, electrostatic stabilization of the particles is possible. In addition, particles can be combined more easily with biological systems. However, the use of water as a solvent also has disadvantages. The final particle concentration is comparably low [30].

Depending on the desired properties, water-insoluble surfactants have to be used [22]. As a result, syntheses were developed in different solvents. The first synthesis of gold nanoparticles in apolar solvents was developed in 1994 by M. Brust [31]. The advantage of synthesis in apolar solvents is better particle size and dispersity control. In addition, smaller particles can be produced (>10 nm). Over the past two decades, the method has been repeatedly adapted. The synthesis used in this work is based on the method of Wu et al. from 2013 [32]. In addition to classic wet-chemical reduction, other methods have been developed, such as sonolysis [33] or laser ablation [34, 35]. The disadvantage of synthesis in apolar solvents is the use of more hazardous chemicals. For this reason, the focus of current research is on the development of so-called greener methods [36].

If apolar particles are produced, they automatically have a shell consisting of so-called ligand molecules [32, 37, 38]. This shell often strongly influences the properties of nanoparticle

systems [39, 40]. In general, ligands can be used to passivate the surface of particles [41, 42], control the distances between particles in coatings [43], alter the electrical properties [44], or enable further functionalization [40]. To adjust the nanoparticle properties, the shell can be adjusted [40]. A frequently used method is ligand exchange, which is based on differences in binding energies. A change of the ligand system can lead to a change in the colloidal stability [45].

The interactions among the individual components influence the properties of dispersions. In particular, the colloidal stability can be controlled by these interactions. Early on, models were developed for aqueous systems to determine dispersion stability. The so-called DLVO theory (Derjaguin-Landau-Verwey-Overbeek) is the best-known [46–48]. This theory summarizes the attractive van der Waals and repulsive electrostatic forces. The attractive forces are based on the size of the particles, the distance between the particles, and the particle material (by the Hamaker constant) [49]. The repulsive forces are due to diffusive electrical double layers formed by ions with charges opposite to those of the particle surface. The structure of these double layers can be described by various models, such as the Helmholtz [50], Gouy-Chapman [51, 52], and Stern models [53]. The repulsion is caused by the equally charged electric fields of the particles. Due to the formation of double layers, the counter-ions weaken this field. The attenuation is defined by the Debye screening length [54]. For this reason, electrostatic repulsion depends on particle size and the concentration of counter-ions. The stronger the attenuation, the more unstable the dispersion becomes, which can lead to agglomeration (reversible) or aggregation (irreversible). Later work has shown that further stabilization or destabilization is possible through non-DLVO interactions [55, 56]. Additional repulsive interactions can be achieved by steric stabilization through the adsorption of a shell consisting of polymer or surfactant molecules [56, 57]. These surface-bound molecules are often called “ligands”. In the case of gold nanoparticles, thiols or amines are often used as ligands for both polar and apolar systems.

As in polar particle systems, in apolar particle systems, colloidal stability is based on the interactions among the individual components: core, ligand, and solvent. The main difference between polar and polar systems is the absence of repulsive electrostatic forces. In apolar systems, the repulsive interactions are based mainly on the ligand shell and the resulting interaction with the solvent [43, 58, 59]. Generally, the shell acts as a barrier, depending on its size and structure, preventing agglomeration and aggregation [60]. The shell structure shows a strong temperature dependence. At high temperatures, ligands are mobile and the shell is disordered. At low temperatures, ligands are less mobile. In the case of linear ligands, a temperature change can cause a disorder-order transition in the shell. In recent years, it has been demonstrated that this tran-

sition in the shell structure results in an inversion of the shell-based interactions from repulsive to attractive [43, 58, 59]. Due to this behavior, these nanoparticle systems can be called shell-dominated. Consequently, modification of the shell structure could prevent or induce the self-assembly of particles.
This work aims to adjust nanoparticle interactions by modifying the shell structure to improve the colloidal stability, specifically by stabilizing the disordered shell state. In addition to the stabilizing effects, destabilizing effects are also discussed, which induce particle self-assembly and aggregation. In this work, the basic system consists of gold particles with a diameter of 4 nm, which are coated with an alkylthiol and redispersed in a apolar solvent (toluene, *n*-hexane, or *n*-decane). This work focuses on modifying the shell structure using molecular additives, non-linear ligands, and mixed-ligand shells. To understand the colloidal stability, nanoparticle systems were investigated experimentally and with molecular dynamics simulations. Experimentally, mainly the agglomeration behavior is investigated. In addition, experiments provide information about the properties of nanoparticle systems, such as core size, shape, and shell density. The simulations can primarily be used to calculate particle interactions or to determine the structure of the ligand shell. The combination of experimental data provides models that can be used to understand the mechanisms of other particle processes.

This thesis is divided into various chapters. Chapter 2 describes the current state of research. The chapter is divided into sections describing the known interactions and processes. Chapter 3 presents the results. A large part of the results is shown as scientific publications. Publication 1 (Chapter 3.1) examines the effect of molecular additives on colloidal stability. Publication 2 (Chapter 3.2) compares the effect of non-linear and linear ligands on colloidal stability. Chapter 3.3 examines the possibility of substituting the stabilizing effects of non-linear ligands with mixed ligand shells. Publication 3 (Chapter 3.4) investigates the additive-induced coarsening of apolar particles. Publication 4 (Chapter 3.5) investigates the use of additive-induced self-assembly and aggregation of nanoparticles into porous gold sponges. Chapter 4 discusses the results of this work and highlights key findings. Chapter 5 summarizes the work and describes possible further research areas in modifying nanoparticle systems.

Chapter 2: State of the Art

2.1 Synthesis and functionalization of gold nanoparticles

This thesis is concerned with nanoparticles prepared using chemical routes that yield dispersions [61, 62]. A range of routes exists that yield particles with different sizes, shapes, dispersities, and core materials [63, 64]. Current research is aimed at improving specific particle properties or making processes more environmentally friendly [36, 65]. Nanoparticles can now be produced from almost any material [66].

Metal nanoparticles [61, 67], and specifically gold, are commonly used due to their chemical and physical properties [68, 69], and only gold nanoparticles are used in this work. Two primary methods exist for producing nanoparticles from precious metals [61, 62]. Top-down syntheses are destructive syntheses [70]; nanostructures are produced from a bulk material by chemical or physical processes [61] by removing material from larger metallic objects via e. g. mechanical milling [71–73], laser ablation [35, 74], or sputtering [75]. Depending on the metal, however, it is difficult to produce certain particle shapes or particles below 10 nm [62]. Bottom-up methods produce nanoparticles by assembling atoms into larger structures, such as clusters or particles [62]. For metals, especially noble metals, these methods are based on the reduction of a precursor using a mechanochemical [76, 77], hydrothermal [78, 79], or wet-chemical process [80, 81].

Spherical gold nanoparticles can be produced by wet chemical reduction of a suitable precursor. The advantage of the wet-chemical method is that monodisperse particles (i.e., particles with a narrow size distribution) can be produced with only four components. Another benefit is that the size of the synthesized nanoparticles can be controlled by changing the concentration of the precursor, ligand, or reducing agent. The original syntheses were in water [27–29]; apolar particles (e.g., gold cores with an apolar shell) were prepared in organic solvents later [31]. A frequently used precursor for the synthesis of apolar gold nanoparticles is gold acid, $HAuCl_4$. As the salt is not soluble in organic solvents, a ligand such as oleylamine is used in the synthesis [32]. This ligand forms complexes with gold and later serves as a shell for the particle. The nucleation of the particles can be induced by the reduction of these complexes (or precursors) using thermal decomposition [37, 38] or by the addition of a reducing agent (like amine-borane complexes or borohydrides) [32, 82].

The exact reaction mechanism of the nanoparticle formation is still under discussion and depends on the method used. The formation of gold nanoparticles in this work is based on the work of Peng et al. [82]. In this method, a solution containing the reducing agent is added to a solution containing a gold precursor (an oleylamine-gold complex). The proposed mechanism is based on nucleation and growth processes that can be described using the models of Burst [31] and LaMer [83]. After nucleation, gold cores can grow by ripening [84] or the absorption of the remaining free gold atoms.

The main difference between the various mechanisms in the literature is the structure of the

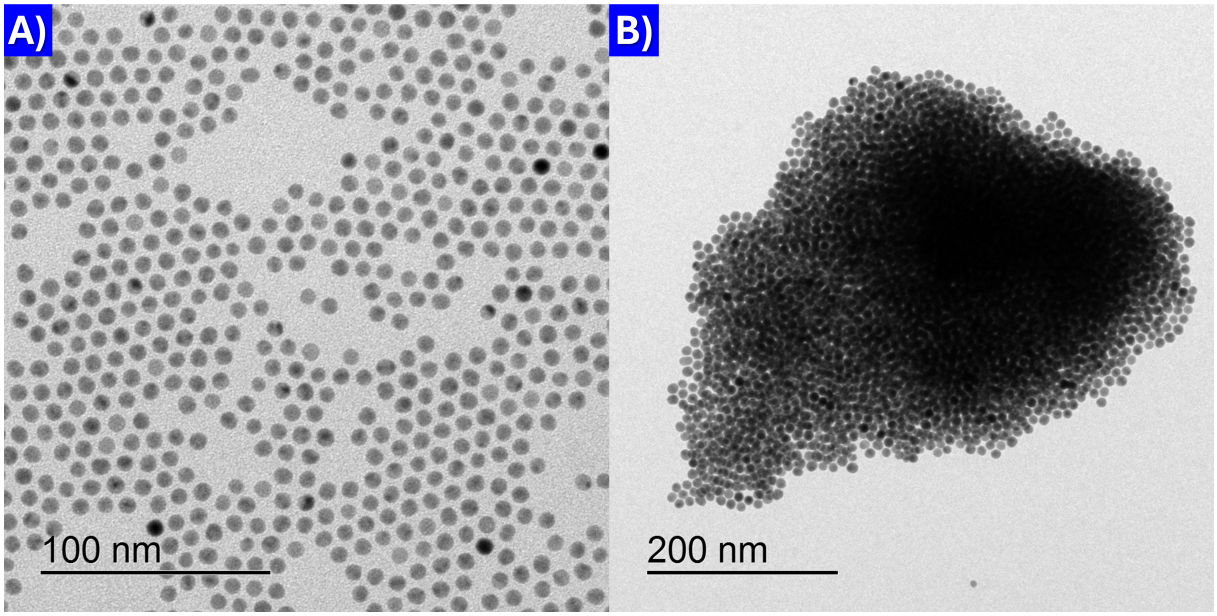


Figure 2.1.1: Transmission electron micrograph of dispersed (A) and agglomerated (B) gold nanoparticles prepared via the method of Kister et al. [58]. Agglomeration of the particles in B) was induced by cooling.

presumed gold-ligand complexes. Kirichkov and co-authors proposed a mechanism based on chain-like complexes [38]. Liu and co-workers proposed a mechanism involving complex formation, complex decomposition into seeds, recombination into particles, and particle growth. These mechanisms strongly depend on the reaction conditions (temperature, ligand, reducing agent, solvent, etc.) [32]. The use of aromatic solvents leads to the formation of larger particles. Even without changing the reaction mixture, the final particle size can be increased by shortening the reaction time when the gold complex is formed [32, 82]. Figure 2.1.1 shows dispersed (A) and agglomerated (B) particles analyzed by transmission electron microscopy.

Apolar gold nanoparticles from wet chemical reduction based on the one-pot reaction of Peng et al. carry organic shells of ligands after the synthesis [82]. The shell structure depends on their molecular structure and functional group. Changing the shell structure by temperature change or ligand exchange affects the self-assembly behavior of particles or their dispersibility [85, 86]. Ligand exchange is used to adjust specific particle properties, like the colloidal stability [58] or the reactivity of the gold surface [42]. The exchange of ligands based on the difference in the binding energy of the old and new ligand, or the use of an excess of the new ligand [87–89]. Gold particles are often modified with amines, phosphines, carbenes, and thiols [88, 89]. This work uses thiols that strongly bind to gold cores, sulfides, and amine additives.

2.2 Colloidal stability of apolar nanoparticles

Apolar nanoparticle dispersions consist of the core, the ligand shell, and the solvent (see Figure 2.2.1, Chapter 2.1) [31]. The interaction between these components determines the colloidal stability [90–92]. Colloidal stability describes their ability to remain dispersed. Agglomeration is the reversible assembly of particles; aggregation denotes an irreversible assembly [93, 94]. Agglomeration can be induced in dispersion by changing the balance between attractive and repulsive interactions [47, 48].

In the past, models such as the DLVO theory have been developed for polar systems to calculate the underlying interactions between particles. The attractive interaction based on van der Waals forces (vdW) between the cores [47, 48]. This attraction is counteracted by repulsion due to electrostatic [47, 48] and steric interactions [45]. Electrostatic interactions result from the cores' surface charge and the resulting double layer of counter-ions. Steric repulsion is the result of surface-bound ligand molecules. These molecules act as "spacer" or "springs" and hinder the attachment of particles [45]. In the case of polar dispersion, both repulsive interactions are essential. Comparable to polar systems, attractive interactions due to vdW forces between the cores are also important in apolar systems. Electrostatic forces can be neglected due to the absence of polar or ionic components. In apolar dispersions, the effect of the ligand shell is decisive for the repulsive interaction between the cores [43, 58].

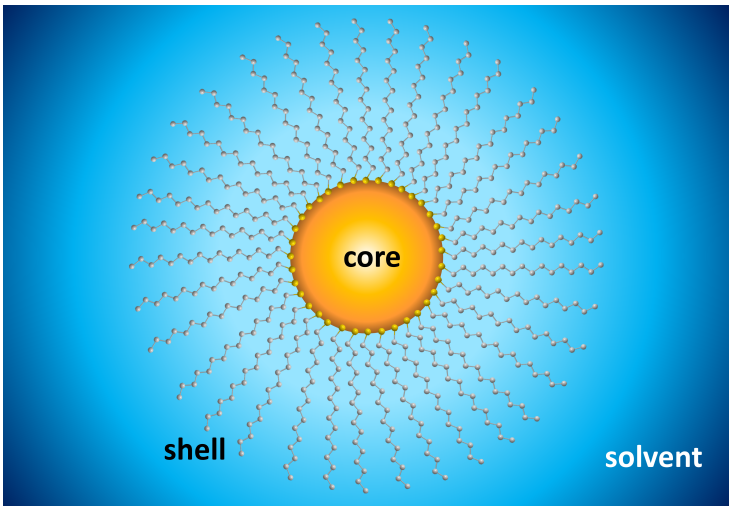


Figure 2.2.1: Schematic representation of a gold nanoparticle system consisting of the metallic core, the ligand shell (here hexadecanethiol, HDT, $C_{16}H_{34}S$), and a solvent.

It is helpful to group the parameters that affect colloidal stability into "dispersion parameters" (solvent, particle concentration, temperature) and "particle parameters" (core size, shell size, shell structure) [90–92]. The effects of different parameters and their connections will be explained in the following chapters and sections.

Generally, the colloidal stability decreases if the number of particles per volume increases [95]. When the particle concentration exceeds a critical value, agglomeration occurs. Napper described this relationship as “critical flocculation point” [96]. Doblas and co-workers could show that this critical particle concentration depends strongly on the used solvent. The mechanisms discussed in the following are based on particle systems, where the particle concentration was below the critical concentration. As mentioned before, the repulsion of apolar particles is based mainly on steric interaction induced by the ligand shell. In literature, the shell is often described as a self-assembled monolayer (SAM) [97, 98] similar to planar surfaces. In these layers, ligand molecules bind to the surface with a head group, and the alkyl chains are oriented away from the particle surface [89, 99]. The structure of this monolayer depends on the size/curvature of the surface and the ligand size [43, 58]. For ligand monolayers on spheres, the “hairy-ball” model can be used to describe the shell structure [100].

Ligand shells are not rigid structures but move dynamically. The alkyl chains have a certain freedom of movement [98]. The mobility increases with temperature [97, 101]. The resulting shell structure is disordered [102, 103]. At low temperatures, the ligand molecules are less mobile. Most alkyl chains adopt all-trans conformations [58] that allow them to align in ligand bundles. The bundle formation increases the anisotropy of the shell [98, 101]. Consequently, reducing the dispersion temperature [104] can induce a ”disorder-order transition” [43, 58] as shown in Figure 2.2.2 for a gold core with a diameter below $8\,\mathrm{nm}$ coated with hexadecanethiol (HDT).

The ordering of the ligand molecules changes the ligand-ligand and ligand-solvent interactions [105]. The short-range interaction between ligand shells becomes more attractive with an increasing degree of order, resulting in the agglomeration of the particles [43, 106]. As a result, nanoparticle systems where the temperature-induced disorder-order transition causes agglomeration are called “shell-dominated”. In contrast, systems in which agglomeration is induced by the van der Waals forces between the cores are called “core-dominated”. The classification is primarily based on the size ratio between the ligand molecule and the core. The special features of core-dominated systems are explained in section 2.2.1. Additionally, agglomeration can be induced by a change of the solvent composition (see section 2.2.3).

In the following paragraphs, the theory of the colloidal stability of shell-dominated particle systems will be explained. The relationship between the degree of order of the shell and the interactions between the particles can be determined using molecular dynamics (MD) simulations. The degree of order of the shell can be estimated using the average dihedral angle φ [107]. This angle is related to the conformation of the alkyl chain of the ligand molecule. A perfect all-trans conformation would lead to an angle of $180°$. During cooling, the conformation of the alkyl chains changes to the all-trans conformation, increasing the dihedral angle. Experimentally, the change in shell structure is challenging to characterize directly. Methods

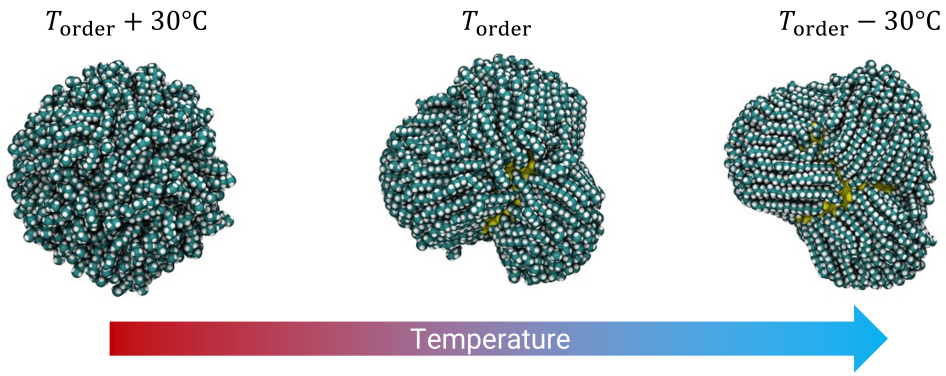


Figure 2.2.2: Snapshots of the temperature-dependent shell structure of simulated 4 nm gold nanocrystal cores coated with hexadecanethiol (HDT, $C_{16}H_{34}S$). The snapshots show the transition of the ligand shell from the disordered state at high temperatures to the ordered state at low temperatures. The middle snapshot shows the shell structure at the ordering temperature T_{order}. Adapted and reprinted with permission from Mohammad Rashedul Hasan.

that can be used to determine the order-disorder transition or phase transition of the shell include differential scanning calorimetry (DSC) [108], small-angle neutron scattering (SANS) [109], variable-temperature Fourier transform infrared spectroscopy (VT-FTIR) [110], or sum frequency generation vibrational spectroscopy (SFG) [110]. The problem with these methods is that they sometimes provide only limited information or can only be used with certain systems. Alternatively, an indirect investigation is carried out by characterizing the agglomeration fraction (χ_{agglo}) using small-angle X-ray scattering (SAXS) [111] or dynamic light scattering (DLS) [112].

To compare different particle systems, the so-called ordering and agglomeration temperatures (T_{order} and T_{agglo}) were introduced. T_{order} is defined as the temperature at which the dihedral angle reaches a value between $135°$ and $155°$, depending on the particle system. In shell-dominated systems the ordering of the shell can be connected to the agglomeration process. T_{agglo} is defined as the temperature at which $20\,\%$ of the particles are agglomerated [43, 58, 59, 109, 113]. The agglomeration temperature is independent of the particle system. As a result, it can be used in shell- and core-dominated systems. Since the agglomeration in shell-dominated systems is induced by the change of the shell structure, T_{agglo} is usually smaller than the ordering temperature T_{order} [43, 58, 59, 109, 113].

The disorder-order transition temperature of the shell depends on the size of the ligand molecules [43]. The melting temperature of pure ligand molecules (without core or solvent), such as alkyl thiols or amines, increases with molecular weight, i.e., the length of the alkyl chain. Various studies have shown that this melting process can be transferred to the bundling of ligand molecules in monolayers on cores [97, 98]. In the work of Monego et al., shell-dominated CdSe nanoparticles with a core diameter of $5.8\,\text{nm}$ were functionalized with alkyl

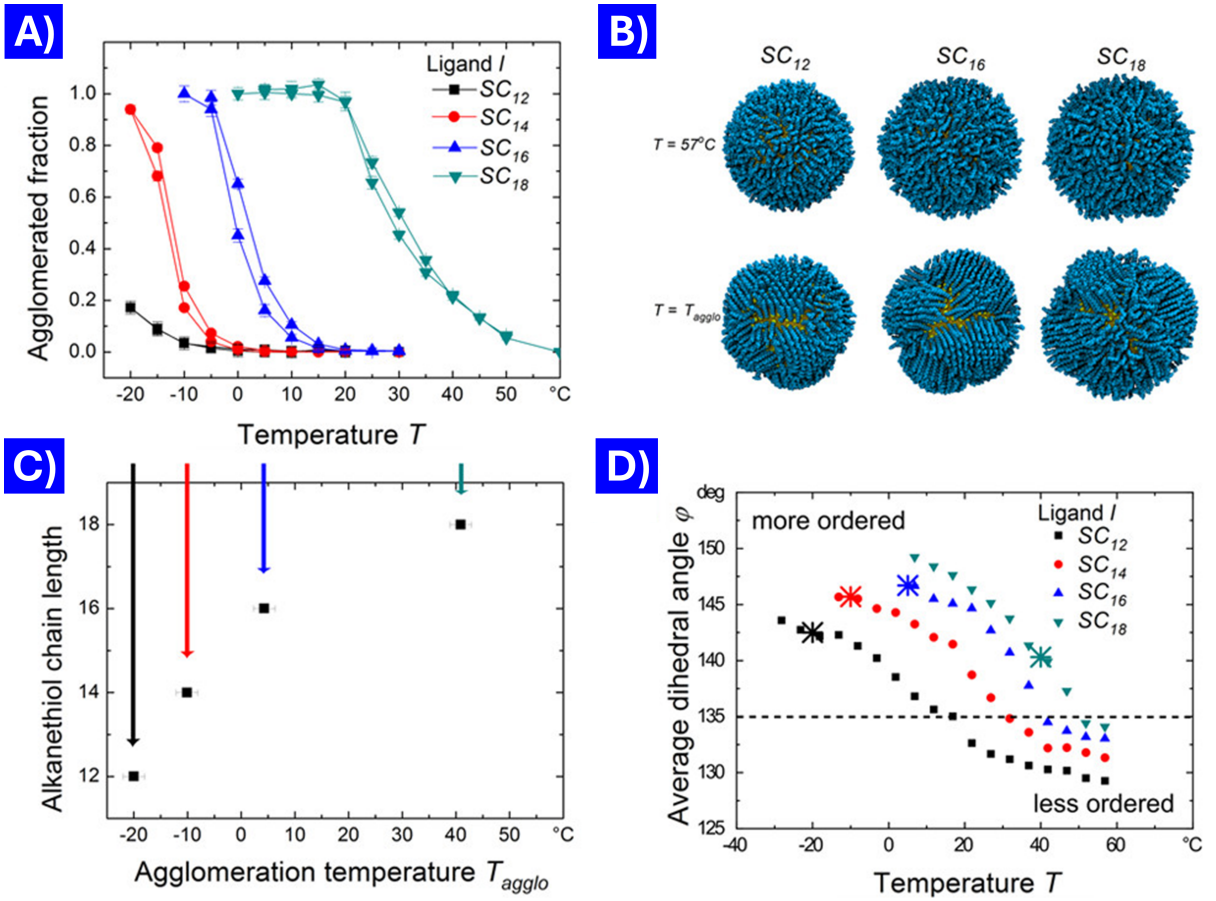


Figure 2.2.3: Effect of the shell structure and ligand size on the colloidal behavior of apolar nanoparticles. (A) shows the temperature-dependent agglomeration fraction of 5.8 nm CdSeNP coated with different linear alkyl thiols (ranging from a C_{12} chain to a C_{18} chain). (B) Chain length-dependent agglomeration temperatures of the different CdSeNP systems. (C) Chain length-dependent core-surface spacing of the different CdSeNP systems. (D) Chain length-dependent simulation snapshots of the different CdSeNP systems at 57 °C and at the agglomeration temperature. Adapted and reprinted with permission from [43]. Copyright © 2025 American Chemical Society.

thiols with chain lengths of 12 to 18 C atoms [43]. The agglomeration temperature T_{agglo} was measured using temperature-dependent SAXS; it increased with increasing alkyl chain length (see Figure 2.2.3A and C). The analysis of the average dihedral angle showed that the increase of the ligand size shifted the ordering process to higher temperatures (see Figure 2.2.3D). Regardless of the size of the ligand molecules, the transition results in an anisotropic shell structure, which influences the interactions between the particles (see Figure 2.2.3B) [43]. Consequently, shorter ligands can improve the colloidal stability for shell-dominated systems. This trend is limited; if the ligands become too short, the shell-dominated system transforms into a core-dominated system.

In the case of shell-dominated systems, the alignment of the ligand molecules changes the

ligand-ligand interaction between ligands of different shells from repulsive to attractive. However, the ligand-ligand interaction is not the only interaction that is influenced by the disorder-order transition of the shell. Additionally, the ligand-solvent interaction must also be considered. A suitable model had to be found to analyze this interaction. In the past, the interaction between ligand and solvent could be approximated by the Flory-Huggins theory [114, 115]. The theory was developed to determine the free energy of mixing a polymer in a solvent. The mixing energy of particles can be determined using equation 2.2.1 [59].

$$\frac{G_{\text{mix}}}{k_{\text{B}}T} = \frac{\pi d^3}{\nu_{\text{S}}}\phi^2\tilde{L}^2\left(\frac{1}{2}-\chi\right)\left(3\ln\frac{\tilde{L}}{\tilde{S}-1}+2\frac{\tilde{S}-1}{\tilde{L}}-\frac{3}{2}\right) \tag{2.2.1}$$

In this equation k_{B} is the Boltzmann constant, T the temperature, d the core diameter of the particle ν_{S} the volume of a single solvent molecule, χ the Flory parameter, $\tilde{L}$ the rescaled ligand length and $\tilde{s}$ the rescaled solvent length. The volume occupied by the ligand shell ϕ can be calculated as follows [59]:

$$\phi = \left(N_{\text{L}} \cdot \frac{\nu_{\text{L}}}{V_{shell}}\right)^2 \tag{2.2.2}$$

Here N_{L} is the number of ligands per shell, ν_{L} the volume of a single ligand molecule and V_{shell} is the shell volume.

The Flory parameter χ can be calculated as follows [59]:

$$\chi = \frac{V_S}{RT}(\delta_{\text{L}}-\delta_{\text{S}})^2 + 0.34 \tag{2.2.3}$$

Here V_{S} is the molar volume of the solvent, R is the universal gas constant, and δ_{L} and δ_{S} are the Hildebrand solubility parameters of the ligand and the solvent.

The Flory-Huggins theory can be used to determine suitable solvents for precipitating the particles. The Flory-Huggins theory for apolar dispersions is based on the idea that there is a connection between the colloidal stability and solubility of the ligand in the used solvent. It could be expected that when the Hildebrand parameters are similar, the interaction between ligand and solvent is best, and consequently, the colloidal stability is best.
For gold particles, hexadecanethiol is a commonly used ligand system [43, 58, 59, 109, 113]. The value of the alkyl chain can approximate the solubility parameter of the thiol [59]. In the case of hexadecanethiol, the value of hexadecane can be used ($\delta = 16.4\,\text{MPa}^{1/2}$). This value can be compared with the solubility parameters of other solvents, such as alkanes. With increasing chain length, the Hildebrand parameter increases for alkanes [116]. Consequently, the

solubility parameters are most similar when the ligand and solvent chain lengths are similar. One would expect the stability to be optimal when the ligand and solvent chain lengths are identical. Lohman et al. could show this relation for decane- and dodecanethiol-coated 5 nm gold nanoparticles. For particles with a hexadecanethiol or octanethiol shell, they found a deviation from this relation. The stability was improved when shorter solvent molecules were used [117].

In the work of Monego et al., similar results were found. If linear alkanes are used as solvents, the stability increases as the chain length of the solvent decreases (n-hexane: $\delta = 14.9\,\mathrm{MPa}^{1/2}$, n-heptane: $\delta = 15.2\,\mathrm{MPa}^{1/2}$, n-nonane: $\delta = 15.6\,\mathrm{MPa}^{1/2}$, n-decane: $\delta = 15.8\,\mathrm{MPa}^{1/2}$ [116]). This behavior could be shown for 4 nm gold nanoparticles coated with a hexadecanethiol shell of different sizes (see Figure 2.2.4A) [59]. Consequently, the colloidal stability increases as the difference between the solubility parameters of the ligand and the solvent increases. However, this trend does not continue as the difference increases. For example, if an alcohol such as ethanol is used ($\delta = 26.5\,\mathrm{MPa}^{1/2}$ [118]), the particles cannot form a stable dispersion. In contrast, very stable dispersions can be formed with cyclic alkanes whose solubility parameters are very similar to the values of the ligand. In the work of Monego et al., gold nanoparticle dispersions with cyclohexane ($\delta = 16.8\,\mathrm{MPa}^{1/2}$ [116]) as solvent were more stable than the dispersions with short-chain alkanes [59]. The experiments showed that the contribution of the solubility of the ligand molecules in a specific solvent has only a minor effect on the colloidal stability. As a result, the use of the Flory-Huggins theory in an apolar particle system is limited. The main limitation of the model is its inability to consider the change in ligand conformation and the shell structure on the ligand-solvent interaction.

As an alternative to the Flory-Huggins theory, Hajiw and coworkers proposed a thermodynamic approach to describe the temperature-dependent ligand-solvent interaction. They analyzed the solvent-dependent self-assembly of gold nanoparticles with a diameter of 2 nm coated with hexadecanethiol and dodecanethiol [119]. The authors hypothesized a correlation between the ligand-solvent interaction and the conformations of both the ligands and the solvent molecules.

In the case of polymer-coated particles, conformational entropy and enthalpic repulsion are often discussed as thermodynamic causes of particle properties [120, 121]. In contrast, Monego et al. propose a stronger connection between the molecular structure of the solvent and the disorder-order transition of the shell. This connection was investigated by performing MD simulations of the disorder-order transition of the shell as a function of the solvent [59]. The results for 4 nm AuNP coated with hexadecanethiol are shown in Figure 2.2.4A and B. The ordering of the shell starts at higher temperatures for larger alkane solvents. Consequently, agglomeration is induced by the transition of the shell structure, such as alkanes, independent of the solvent. To understand the solvent's effect, the temperature-dependent changes in molecular conformations of the ligand-ligand and ligand-solvent interactions must be considered.

Monego and co-workers calculated the vdW interaction energy between the ligand molecules

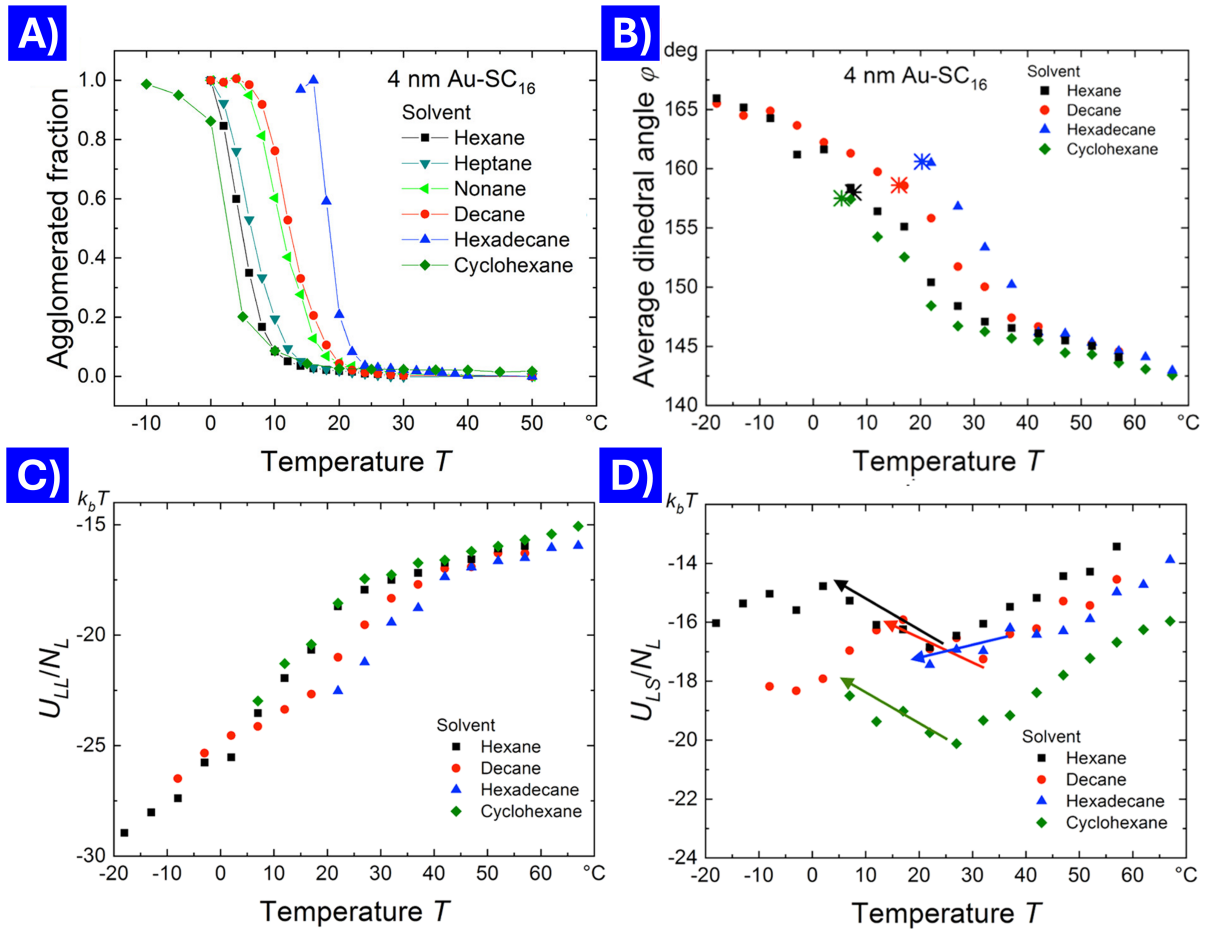


Figure 2.2.4: Effect of the length and structure of different apolar solvents on the colloidal behavior of apolar shell-dominated nanoparticles. (A) Temperature-dependent agglomeration fraction of 4 nm AuNP coated with HDT dispersed in different linear alkanes and cyclohexane. (B) Temperature-dependent average dihedral angle of 4 nm AuNP coated with HDT dispersed in different alkanes and cyclohexane. (C) Temperature-dependent ligand-ligand interaction energy U_{LL} normalized by the number of ligand molecules per shell of 4 nm AuNP coated with HDT dispersed in different alkanes and cyclohexane. (D) Temperature-dependent ligand-solvent interaction energy U_{LS} normalized by the number of ligand molecules per shell of 4 nm AuNP coated with HDT dispersed in different alkanes and cyclohexane. Adapted and reprinted with permission from [59]. Copyright © 2025 American Chemical Society.

within the same shell (U_{LL}) and between the ligand molecules and the solvent molecules (U_{LS}) [59]. The results are shown in Figure 2.2.4C and 2.2.4D. The ligand-ligand interaction U_{LL} increases when the shell structure changes. Depending on the solvent, the onset of the rise in U_{LL} occurs at a lower temperature. However, the profile of the U_{LL} curves is similar for all solvents. The calculation of the ligand-solvent interaction energies U_{LS} shows a stronger influence of the solvent. A continuous increase in the interaction energy can be observed for hexadecane, the solvent most similar to the ligand, independent of the disorder-order transition of the shell. The other solvents exhibit the same trend initially. However, when the temperature is reached at which the ordering of the shell starts, a decrease in U_{LS} occurs. The authors

concluded that a change in the internal energy (which induces the transition of the shell) is lower for smaller solvents. Consequently, smaller solvent molecules cannot arrange themselves with ligand bundles. The larger a solvent molecule becomes, the better the alignment of the solvent molecules with ligand bundles.

In conclusion, the colloidal stability of nanoparticles depends on the size ratio between the ligand molecule and the core. As a result, nanoparticle systems can be categorized into two types: shell-dominated and core-dominated systems. In shell-dominated systems, agglomeration is induced by the transition of the shell from a disordered to an ordered state. The size of the ligand or solvent molecules can influence this transition. For dispersions with only one solvent, the colloidal stability can be influenced by modifying the shell. The theory of the colloidal stability of the core-dominated systems is explained in the next chapter. The above models must be adapted if more than one solvent is used. The effect of binary solvent mixtures is presented in Chapter 2.2.3.

2.2.1 Effect of the core size

Core size affects the core-ligand size ratio, curvature, and the magnitude of van der Waals (vdW) interactions between the cores. Consequently, particle-particle interactions change with core size. In this chapter, the theory of the colloidal stability of "core-dominated" will be discussed. Hamaker's model for van der Waals (vdW) forces can be used to approximate the attractive interaction between two spheres [91, 122]:

$$U_{\text{vdW}} = -\frac{A}{12}\left[\frac{d^2}{r^2-d^2} + \frac{d^2}{r^2} + 2\ln\left(1-\frac{d^2}{r^2}\right)\right] \tag{2.2.4}$$

Here is d, the diameter of the particles, r, the center-center distance between the particles, and A, the effective Hamaker constant. The effective Hamaker constant can be calculated as follows:

$$A = \left(\sqrt{A_{\text{gold}}} - \sqrt{A_{\text{solvent}}}\right)^2 \tag{2.2.5}$$

Here A_{gold} is the Hamaker constant of gold and A_{solvent} the Hamaker constant of the solvent.

The agglomeration temperatures of gold nanoparticles (AuNP) with core diameters between 4 nm and 10 nm and a hexadecanethiol shell in *n*-decane were investigated by Kister et al. using small-angle X-ray scattering (SAXS) [58]. The results are shown in Figure 2.2.5A. Larger cores led to higher agglomeration temperatures; however, the relationship was not linear with core size. Core diameters from 4 nm to 8 nm were shell-dominated, and agglomeration temperature increased by only 20 K for an increase in the core size of 4 nm. Cores with diameters above 8 nmwere core-dominated, and as thier size increase by 2 nm the agglomeration temperature T_{agglo} increased by 40 K [58].

The temperature-dependent shell structure was investigated using simulations [58]. The temperature-dependent average dihedral angles in Figure 2.2.5B show that, regardless of the core size, the disorder-order transition of the shell occurs. A comparison of the simulated and experimental data reveals that core-dominated particles agglomerate before the shells begin to order. The authors concluded that the shells have an exclusively repulsive effect during the agglomeration of core-dominated particles.

The core-surface distances in the agglomerates were measured in the same publication [58] as shown in Figure 2.2.5C. The distance between shell-dominated particles increased with core size as the surface curvature decreased. According to the hairy-ball model, the shell density of small particles decreases strongly with increasing distance to the gold surface. At low temperatures, this effect causes the formation of bundled shell structures with a high anisotropy, enabling the interlocking of ligand bundles. During the interlocking of particles, the bundle of one particle fits in the gap between the bundles of another particle. This effect decreases as the core size

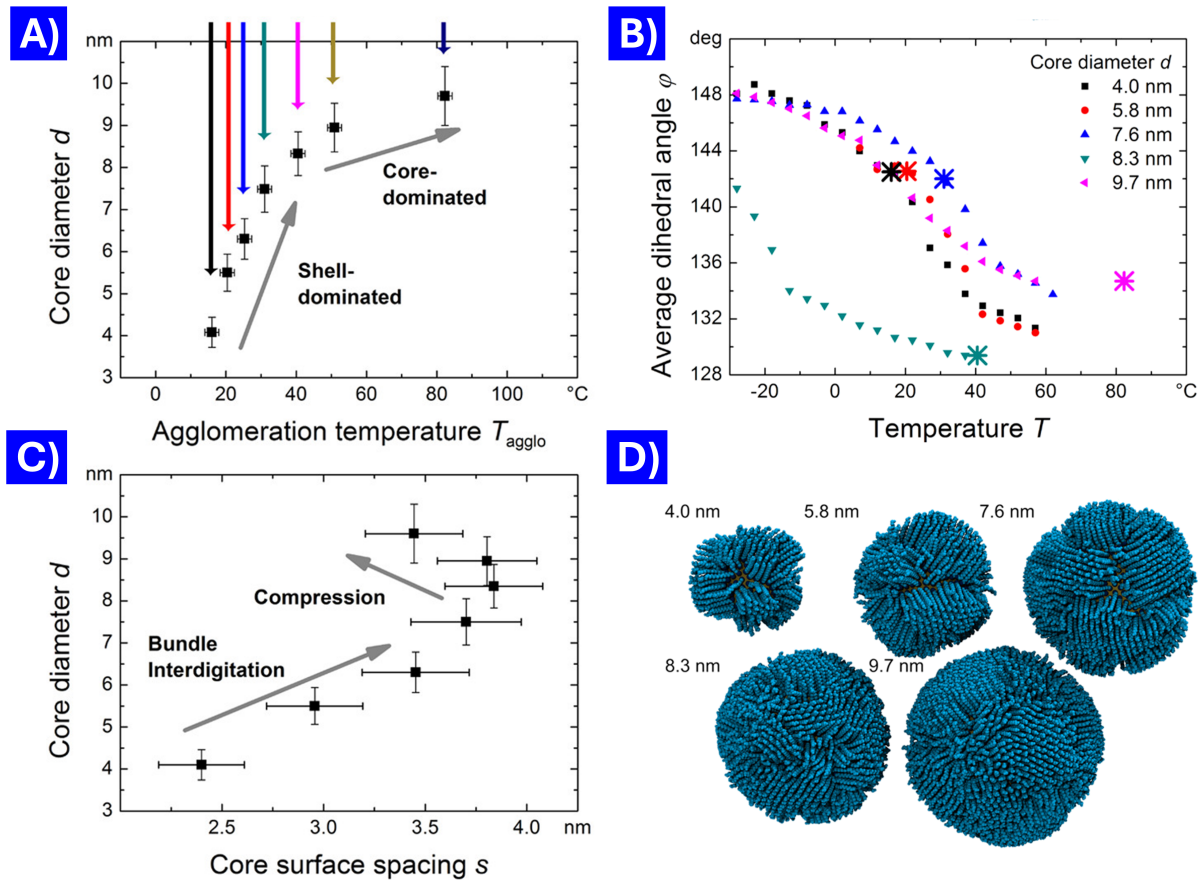


Figure 2.2.5: Effect of the core size on the colloidal behavior of apolar shell-dominated nanoparticles. (A) Core size-dependent agglomeration temperature of AuNP coated with hexadecanethiol (HDT) dispersed in decane. (B) Core-size dependent snapshots of simulated nanoparticles with an ordered shell at low temperatures. (C) Core size-dependent core-surface spacing of AuNP coated with HDT dispersed in decane. (D) Temperature-dependent average dihedral angle φ of AuNP with different diameters coated with HDT. Large cross-shaped symbols represent the experimentally determined agglomeration temperatures. Adapted and reprinted with permission from [58]. Copyright © 2025 American Chemical Society.

increases, due to the isotropic shell structure [58]. A stronger compression of the shell can explain the smaller spacing for large cores due to the strong attractive interaction between cores.

In conclusion, it can be stated that the vdW interaction can no longer be neglected in most cases above a specific core-ligand size ratio. This interaction dominates for large particles. The disorder-order transition of the shell does not influence the agglomeration behavior. In core-dominated systems, the shell has an exclusively repulsive effect. It remains unclear whether it is possible to change the colloidal stability of core-dominated particle systems by modifying the shell, aside from using large ligand molecules. This thesis mainly reports on gold nanoparticles with a diameter of approximately. 4 nm; only in Chapter 3.2 (Publication 2) and Chapter 3.5 (Publication 4) particles with diameters above 8 nm were used.

2.2.2 Modification of the shell structure

Linear alkyl thiols or amines are common ligands for gold nanoparticles [58, 123]. The temperature-dependent conformation of the ligand shells affects the ligand-ligand and ligand-solvent interactions [59]. One way to adjust these interactions and consequently the colloidal stability is to modify the ligand shell. Especially, a change in ordering behavior and the resulting change in ligand-ligand interaction could strongly affect colloidal stability. In the following two chapters, two literature-known modification types are presented that could be used to alter the ligand-ligand interaction. In Chapter 2.2.2.1, the effect of non-linear ligand molecules will be explained. In Chapter 2.2.2.2, the impact of mixed ligand shells is described.

2.2.2.1 Non-linear ligands

In the case of linear ligands, the reduction in temperature results in the ordering of the shell structure, leading to the agglomeration of the particles. The increase in order influences the thermodynamic properties of the shell, particularly its entropic properties. To counteract the ordering process, the entropic properties of the shell can be adjusted by using non-linear ligands.

Non-linear ligands have been used to tune the colloidal stability of different particle systems [86]. Yamashita and colleagues characterized the dispersibility of particles ($4\,$nm ZrO_2 and $5\,$nm TiO_2) coated with linear and non-linear phosphonic acid ligands in various apolar solvents by combining dynamic light scattering and transmittance measurements. They found that the particles exhibited improved dispersibility when coated with branched ligands. They concluded that this improvement is the result of the reduced surface coverage.

Yang and co-authors demonstrated that the solubility of CdSe-NC increases significantly when branched alkanoate ligands (like 4-methyloctanoic acid, 4-ethyloctanoic acid, or 2-hexyldecanoic acid) with side chains were used [124, 125]. In Figure 2.2.6, the reported solubility of different nanoparticle systems is shown as a function of the molecular structure of the ligand molecules.

The solubility of $3.8\,$nm CdSe nanocrystals increased by a factor of 1000-10,000 when branched ligands were used. The authors suspected a correlation between the increase in solubility and the thermodynamics of the ligand-solvent interaction. Using a thermodynamic model [125], they calculated the Gibbs free energy $\Delta_{\text{Mix}}G$:

$$\Delta_{\text{Mix}}G = \Delta_{\text{Mix}}H - T\Delta_{\text{Mix}}S \tag{2.2.6}$$

Here, $\Delta_{\text{Mix}}H$ is the mixing enthalpy and $\Delta_{\text{Mix}}S$ the mixing entropy. $\Delta_{\text{Mix}}H$ is defined as [125]:

$$\Delta_{\text{Mix}}H = n\Delta^{\text{m}}H_{\text{NC}} + n_{\text{s}}\Delta^{\text{m}}H_{\text{s}} \tag{2.2.7}$$

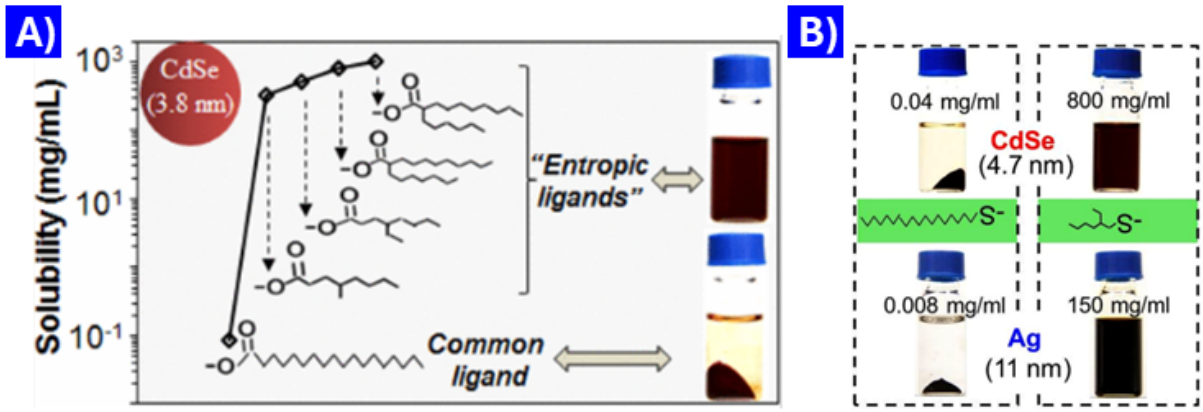


Figure 2.2.6: Solubility thiol-coated CdSe and Ag nanocrystals dispersions. (A) Solubility of CdSe NC with a diameter of 3.8 nm as a function of the size and position of the side chain measured with laser scattering. (B) Images of CdSe and Ag nanoparticle dispersion with a specific particle concentration for a linear octadecanethiol (left column) and branched 2-ethyl-hexadecanethiol (right column) ligand at 303 K. Adapted and reprinted with permission from [124]. Copyright © 2025 American Chemical Society.

with $\Delta^{\mathrm{m}}H_{\mathrm{NC}}$ the partial molar mixing enthalpy of the nanocrystal−ligand complexes , $\Delta^{\mathrm{m}}H_{\mathrm{s}}$ the partial molar mixing enthalpy of the solvent, n the molar amount of ligand and n_{s} the molar amount of the solvent. The mixing entropy $\Delta_{\mathrm{Mix}}S$ is defined as follows [125]:

$$\Delta_{\mathrm{Mix}}S = n\Delta^{\mathrm{m}}S_{\mathrm{NC}} + (-nR\ln(\chi) - n_{\mathrm{S}}R\ln(1-\chi)) + (n\Delta^{\mathrm{m}}S_{\mathrm{NC,ni}} + n_{\mathrm{s}}\Delta^{\mathrm{m}}S_{\mathrm{s,ni}}) \qquad (2.2.8)$$

with $\Delta^{\mathrm{m}}S_{\mathrm{NC}}$ the molar conformational entropy of the NC-ligand complex for dispersed particles, $\Delta^{\mathrm{m}}S_{\mathrm{NC,\,ni}}$ the partial molar non-ideal entropy changes of the nanocrystal−ligand complexes for dispersed particles and $\Delta^{\mathrm{m}}S_{\mathrm{s,\,ni,}}$ the partial molar non-ideal entropy of the solvent. The solubility in molar fraction was defined as $\chi = \frac{n}{n+n_{\mathrm{s}}}$.

Using their model, the authors assumed that the improved solubility is affected by different parameters. They proposed that the presence of a side group in a branched ligand should lead to a gain of conformational (intramolecular) entropy. Additionally, they suggested that branched ligands minimize the enthalpy and, consequently, the temperature for the transition from an ordered to a disordered assembly. The authors also hypothesized that the use of branched ligands hinders the chain-chain interdigitation between different particles. Finally, the authors introduced the term "entropic ligands" for non-linear ligands [124, 125].

Based on this model, Elimelech and co-authors studied the effect of the size and the position of the side chain in branched alkane thiol ligands on 3 nm CdSe NC [126]. Their work focuses on the change in total entropy when using branched ligands compared to linear ligands with the same number of *C*-atoms. The authors used isothermal titration calorimetry (ITC) to determine the enthalpic and entropic changes associated with the ligand exchange reaction of oleic

acid by linear and non-linear thiols [126, 127]. The difference in thermodynamics of the ligand exchange reaction was used to characterize the "entropic nature" of non-linear ligands. The authors assumed that these differences could explain the improved colloidal stability of non-linear ligands. Generally, the exchange of oleic acid with thiols, especially linear ones, is exothermic and leads to a loss in entropy, due to denser shells, stronger interactions between the ligands, and their tendency to form bundles. The authors used branched ligands in which the size and position of the branching group were varied. The results of the comparison between the exchange reaction of linear and non-linear ligands are shown in Figure 2.2.7 [126].

Figure 2.2.7A shows the effect of a single methyl branching group's position. They used branched butanethiol and hexanethiol and compared them with pentanethiol and heptanethiol (linear ligand systems with the same number of C-atoms). The authors showed that the gain in enthalpy and the loss in entropy of the exchange reaction decrease when a side group is present. This effect becomes stronger when the methyl group is in the middle of the backbone chain. Elimelech et al. assumed that the interruption of the ligand packing in the shell is reduced when the branching group shifts toward the end of the backbone chain.

The size of the branching group affected the thermodynamics of the exchange reaction too (see Figure 2.2.7B). If the branching group is located near the head group, the exothermicity and entropy loss decrease with the side chain's increasing size (2-EHT system, 2-ethyl-1-hexanethiol). Elimelech et al. assume that a larger side group close to the surface-bound thiol group leads to a more substantial interruption of the ligand packing. Consequently, the difference in ligand packing on the different sides (facets and edges) is minimized, resulting in a more homogeneously packed shell. If the branching group is located further in the center of the backbone, an inversion in the effect of the size of the branching group can be seen (4-EOT system, 4-ethyl-1-octanethiol). The authors assume that the side chains can form stronger vdW interactions in this position. As a result, the decrease in the gain of enthalpy and the loss of entropy in the case of a larger branching group in the 4-EOT system is smaller than in the 2-EHT.

Finally, the authors investigated the effect of the backbone chain length (see Figure 2.2.7C). Regardless of the presence of a branching group, the enthalpy gain increased with increasing chain length. This effect results from the increasing vdW forces between the ligand molecules. In addition, an increase in entropy loss can be observed, resulting from the reduced degrees of freedom of the larger ligand molecules [127]. The presence of a branching group generally leads to a decrease in exothermicity and loss of entropy. Since the methyl group is always at position 4 in the system studied, one would expect the difference in entropy loss compared to the linear system to increase with increasing backbone length, as the methyl group moves further forward as the chain becomes larger. For the longest system, 4-MNT (4-methyl-1-nonanethiol), however, the opposite is the case. The authors assume that the effect of the branching group is weaker than that of the backbone chain size.

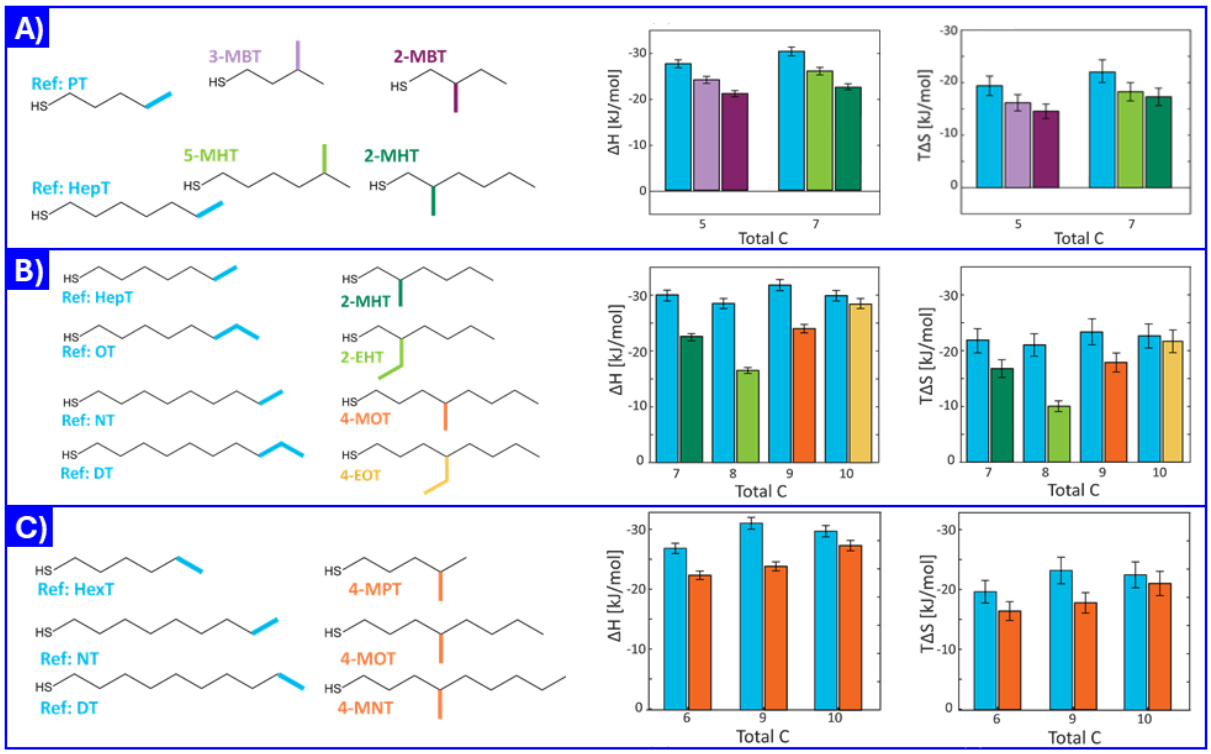


Figure 2.2.7: Effect of the molecular structure of linear and branched ligands on the thermodynamics of the ligand exchange reaction. The diagrams show the change in Gibbs free energy ΔG as a function of the molecular structure. (A) Effect of the position of the methyl side chain. Ligand molecules with the same C-atoms number are located in a row. (B) Effect of the size of the side chain. Ligand molecules with the same C-atoms number are located in a row. (C) Effect of the size of the backbone chain. The branched molecules have a methyl group at position 4. Ligand molecules with the same C-atoms number are located in a row. Adapted and reprinted with permission from [126]. Copyright © 2025 American Chemical Society.

To understand the observed effect, the authors calculated the conformational entropy of the shell structure using a model based on the mean field theory for self-assembled lipid chains [128–130] and a rotational isomeric state model [131]. The results are shown in Figure 2.2.8. The authors first determined the packing conditions of the shell of linear alkyl thiols. For thiol shells, they showed that the ligand molecules are between freely anchored and frozen. Using the model developed in this way, it was possible to show that the entropic loss decreases with increasing chain length. In addition, a clear even-odd effect was observed for the chain length. The authors concluded that the orientation of the CH_3 group strongly influences the ligand packing of linear alkyl thiols.

The shell densities of linear and entropic ligands depended on molecular structure. The position of branching (see Figure 2.2.8A) and the length of the backbone chain (see Figure 2.2.8B) have a significant influence on the conformational entropy. For the branching position, it was shown for x-methyl-1-hexanethiol that the loss of entropy is lowest when the group is located in the middle of the hexyl chain (position 3). If the backbone chain grows, the entropy loss is lowest

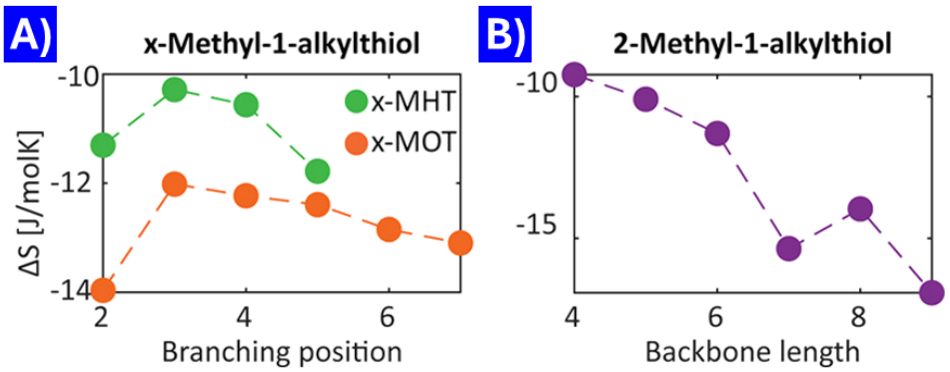


Figure 2.2.8: Conformational entropy of ”entropic” ligands depending on their molecular structure. Effect of the branching group position in x-methyl-1-hexanethiol (x-MHT) and x-methyl-1-octanethiol (x-MOT) on the binding conformational entropy (E). Effect of the backbone length in 2-methyl alkylthiols on the binding conformational entropy (F). Adapted and reprinted with permission from [126]. Copyright © 2025 American Chemical Society.

at position 3. Consequently, the ideal position of the branching shifts toward the head group as the chain length increases. The effect of chain length shows a different trend. The loss of entropy decreases as the backbone chain becomes shorter. The authors concluded that the ideal entropic ligand has a short backbone chain and a short branching in the middle of the chain. The authors also suggest that non-negligible ligand-ligand interactions can occur even with branched ligands.

The existing literature provides detailed information on the thermodynamic properties of shells. The focus is mainly on the thermodynamic properties or the density of the shell. Specific effects are discussed at a single-molecule level. It was found that the conformational entropy is a critical property. For this reason, non-linear ligands were called “entropic” ligands. There remain gaps in the understanding of how the molecular structure of these ligands affects the colloidal stability of a dispersion. Although it is assumed in the literature that a branch group influences the temperature-induced disorder-order transition, this has not been proven. It is unclear to what extent non-linear ligands can form bundles when the temperature is reduced. As a result, the influence of such non-linear ligands on the temperature-induced transition of the shell structure will be investigated in detail in this work.

2.2.2.2 Mixed ligand shells

In the previous Chapter 2.2.2.1, non-linear ligands were used to show that the conformational entropy of the ligand molecules can strongly influence the shells' properties. An alternative strategy to reproduce their unique properties and to overcome the limited commercial availability of these ligands was the use of mixed ligand shells. They are accessible via co-adsorption of ligand mixtures on particles [132]. In this section, the presented literature focuses on the mixing of chemically similar linear ligands with different sizes.

Pang and co-authors have shown that the combination of linear hexanoate (C_6) and myristate (C_{14}) as ligands increases the solubility of CdSe nanoparticles with a diameter of 3 nm in chloroform [133]. Replacing a fraction of myristate (C_{14}) ligand by hexanoate (C_6) increased solubility by a factor of approximately 10,000 (see Figure 2.2.9A). The authors hypothesized that the colloidal properties depend on the ratio of ligands in the shell and the distribution of ligands within the shell. They used ^{13}C-CODEX solid state NMR (center-band only detection of exchange) to analyze the ligand distribution and could show that ligands do not mix randomly but are spatially segregated [133]. The authors didn't describe an exact distribution, but patch-like, stripe-like, or clustered distributions are discussed in other publications [132, 134–138]. Singh et al. connected ligand properties, like tail length and polarity, with shell patterning, ranging from Janus-like to complex stripe-like distributions [132]. Pang et al. characterized the temperature-dependent changes of the chain conformation of the larger myristate ligand during cooling using ^{2}H-NMR quadrupolar measurements to characterize the modes of the different chain segments [133]. They found that cooling of a pure myristate shell led to a reduction in the flexibility of the ligand chain. The authors connected this reduction with the phase transition of the ligand in the shell. In the case of a mixed ligand shell, the flexibility is reduced less. To understand the improved flexibility, Pang and co-workers analyzed the diffusion cone of the myristate ligand. This cone describes the motion mode of each methylene group of the chain. They found that in a mixed ligand shell, the opening angles of the myristate chain (the angle between each methylene group to the central cone axis) were increased. The authors concluded that this increase in angle is the result of an increase in chain dynamics, leading to a reduction in ligand-ligand interactions and, consequently, the improved solubility of particles with a mixed ligand shell [133].

Elimelech and co-authors used isothermal titration calorimetry (ITC) to characterize the ligand exchange reaction of dispersed oleic acid-coated CdSe nanoparticles with a mixture of two thiols with different chain lengths (see Figure 2.2.9B and C) [134]. For binary mixtures of linear alkyl thiols such as hexanethiol and decanethiol on CdSe NP (3 nm), they analyzed the effect of the ligand ratio, the size difference between the ligands, and the distribution of the ligands in the shell. Trichloroethylene was used as a solvent due to its high boiling point and low mixing with the used ligands. The change in Gibbs free energy during the exchange reaction with two ligands hardly depended on ligand ratio because the enthalpy of mixing and entropy compensated for

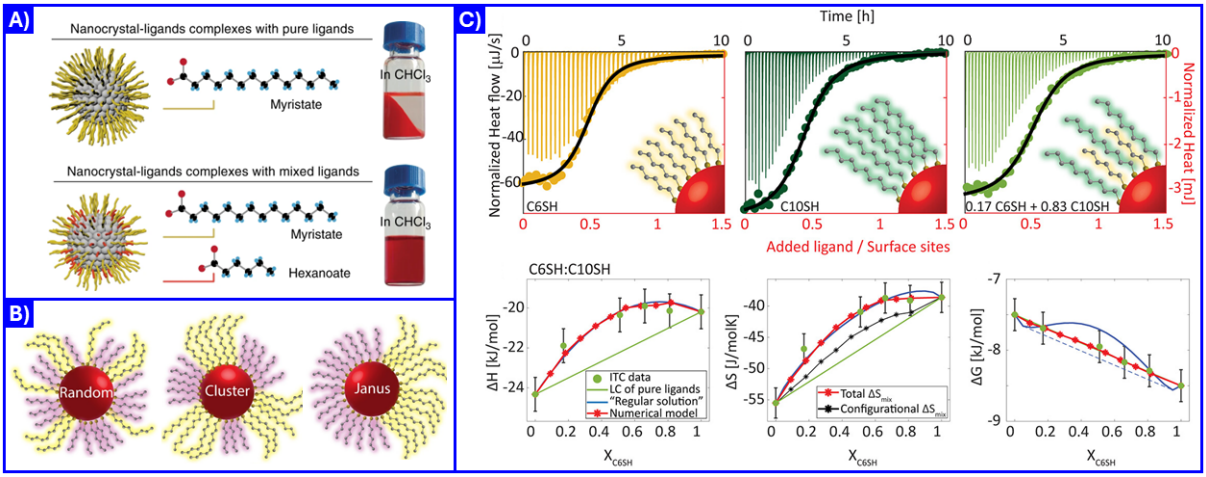


Figure 2.2.9: Overview of different mixed ligand shell systems and their effect on different shell and dispersion properties. (A) Solubility of 3 nm CdSe nanoparticles with a pure myristate shell and a mixed ligand shell of myristate and hexanoate in chloroform. (B) Illustration of different distributions of ligand molecules with varying chain lengths in mixed shells. (C) ITC curves and the extracted thermodynamic parameters for the ligand exchange reaction with pure hexanethiol ($C_6H_{13}SH$) and decanethiol ($C_{10}H_{21}SH$), and a combination of both thiols. (A) Adapted and reprinted with permission from [133]. Copyright © 2025 American Chemical Society. (B), (C) Adapted and reprinted with permission from [134]. Copyright © 2025 American Chemical Society.

each other. A larger fraction of the shorter ligand would lead to a decrease in the entropic loss, but also to a decrease in the mixing exothermicity. As a result, the free energy stays almost unchanged [134].

Additionally, Elimelech and coworkers analyzed the change in the shell structure and ligand-ligand van der Waals (vdW) interaction for different scenarios. A small fraction of longer ligands in a shell consisting of short ligands can lead to a folding-over of the longer ligands. This causes an increase in the ligand-ligand interaction and a denser packing of the short ligand, which again reduces the entropy. On the other hand, the presence of the small ligand in a shell of long ligands reduces the ligand-ligand interaction of the longer ligands. Additionally, the presence of shorter ligands creates free volume, which leads to higher rotational freedom of the longer ligand, increasing the conformational entropy. If the difference in the ligand size increases, the individual entropic and enthalpic contributions increase. Elimelech and co-authors analyzed the distribution of the mixed thiol shell. They found a clustered pattern for the hexanethiol/decanethiol mixture. They concluded that the enthalpic preference for demixing overcomes the entropic preference for mixing. This demixing effect can be enhanced by using chemically distinct ligands, e.g., those with different polarities [132, 134] or molecular structures [110, 139].

Experimentally, the ligand distribution in mixed shells can be characterized using different methods. One approach is matrix-assisted laser desorption ionization time-of-flight mass spectroscopy (MALDI-TOF MS). The particle surface is fragmented, and the ligand distribution

on the fragments is investigated [140, 141]. In the work of Luo et al., the development of the shell composition and the ligand distribution during a ligand exchange reaction was investigated [141]. Additional experimental methods, like NMR, AFM, or STM, have been used to characterize the distribution of the ligands in the shell [135, 136].

In conclusion, mixed ligand shells can be used to create shell structures with enhanced dynamic behaviour, resulting in improved solubility. One advantage of combining linear ligands is the wide commercial availability of linear molecules of various sizes and with different functionalities. However, many questions remain unanswered regarding colloidal stability. It remains unclear whether the temperature-induced disorder-order transition can be effectively suppressed by combining linear thiols, particularly those of longer chain lengths. Additionally, the effect of shell patterning on the bundle formation of the ligands remains unknown.

2.2.3 Effect of the solvent composition

The discussion so far was limited to the stability of apolar nanoparticles in a single, apolar solvent. Mixing solvents opens up new possibilities for applications, such as adjusting the polarity of the dispersions. However, using a co-solvent can influence the solubility and molecular conformations of polymers or ligands [142, 143], or induce the arrangement of particles in crystalline superlattices [144]. Flory-Huggins theory (see equations 2.2.1 and 2.2.3) uses the Hildebrand parameters of the ligand and the solvent to quantify their compatibility. A solvent mixture enables the adjustment of solubility parameters in the dispersion. Hasan et al. used hexadecane as the base solvent ($\delta = 16.4\,\mathrm{MPa}^{1/2}$ [116]) for hexadecanethiol coated $4\,\mathrm{nm}$ gold nanoparticles and added *n*-hexane ($\delta = 14.9\,\mathrm{MPa}^{1/2}$ [116]), cyclohexane ($\delta = 16.8\,\mathrm{MPa}^{1/2}$ [116]) (both stabilizing solvents [59]), and 1-hexanol ($\delta = 14.9\,\mathrm{MPa}^{1/2}$ [145], as destabilizing solvent) as co-solvents. For pure solvents, only a weak influence of the solubility of the ligand and the ligand-solvent interaction was found (see chapter 2.2) [59]. In the case of solvent mixtures, one might expect a stronger influence of the solubility parameters due to the preferred interaction/-solubility of the ligand in only one of the solvents used. Hasan and coworkers are comparing small-angle X-ray scattering results on the colloidal stability and small-angle neutron scattering results on the solvent composition in the shell with simulated data on the shell structure and the solvent composition in the shell [109]. Their work aimed to understand how specific ligand-solvent interactions affect the solvent composition in the shell and the resulting effect on the colloidal stability in binary solvent mixtures.

The composition of binary solvent mixtures affected the agglomeration of hexadecanethiol-coated $4\,\mathrm{nm}$ AuNP (represented by the agglomeration temperature T_{agglo}, see Figure 2.2.10A). In mixtures of an apolar and a polar solvent, increasing the fraction of hexane or cyclohexane led to a decrease in T_{agglo}, while increasing the fraction of 1-hexanol led to an increase in T_{agglo}. The composition-dependent change, $\partial T_{\mathrm{agglo}}/\partial c_i$, strongly depended on the solvent combination. It was linear for the hexadecane/hexane mixture and non-linear for hexadecane/cyclohexane and hexadecane/1-hexanol. The greatest deviation from the linear transition (from the pure cyclohexane to the pure hexadecane system) was achieved in the cyclohexane/hexadecane mixture with approximately $5\,^{\circ}\mathrm{C}$ at a hexadecane bulk solvent amount of $40\,\%$. The greatest deviation from the linear transition (from the pure hexanol to the pure hexadecane system) was achieved in the hexanol/hexadecane mixture with approximately $10\,^{\circ}\mathrm{C}$ at a hexadecane bulk solvent amount of $10\,\%$. The authors concluded that the non-linear correlation between the composition of the solvent mixture and the agglomeration temperatures was due to preferential enrichment in the shell. They expected that cyclohexane tended to enrich in the shell, whereas hexanol enriched in the bulk solvent. The performed molecular dynamics simulation revealed similar composition dependencies for the ordering temperatures.

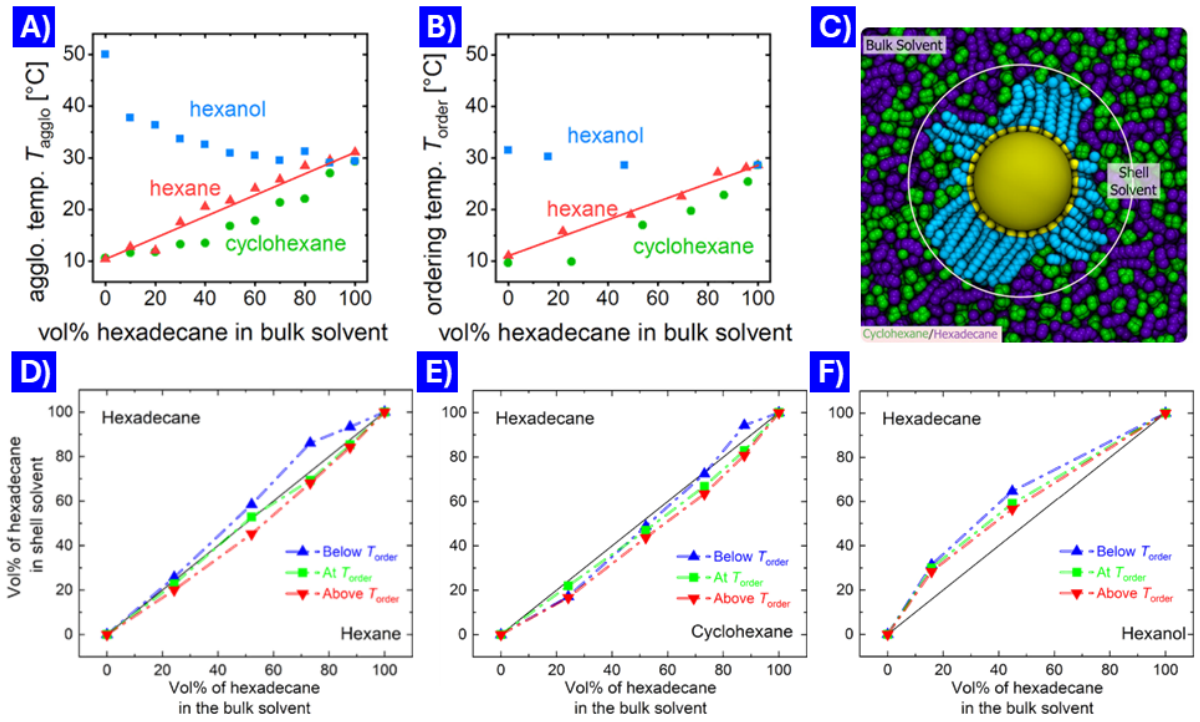


Figure 2.2.10: Effect of the solvent composition on the colloidal stability. (A) Agglomeration temperature T_{agglo} depending on the amount of hexadecane in the hexane/hexadecane (red), cyclohexane/hexadecane (green), and 1-hexanol/hexadecane (blue) mixture. (B) Agglomeration temperature T_{order} depending on the amount of hexadecane in the hexane/hexadecane (red), cyclohexane/hexadecane (green), and 1-hexanol/hexadecane (blue) mixture. (C) Snapshots of a single particle with an ordered hexadecanethiol shell in a solvent mixture of hexadecane (purple) and cyclohexane (green). Composition-dependent vol% of hexadecane in the shell at temperatures greater than T_{order} (red), at T_{order} (green) and less than T_{order} (blue) for: (E) the hexadecane/hexane mixture, the hexadecane/cyclohexane mixture and the hexadecane/1-hexanol mixture. The black line represents a system with a uniform solvent composition in the bulk and shell solvent. Adapted and reprinted with permission from [109]. Copyright © 2025 American Chemical Society.

Temperature-dependent small-angle neutron scattering was used to analyze the solvent composition inside the shell. At temperatures above the shell transition to disorder, *n*-hexane was enriched in the shell for hexane/hexadecane mixtures. At lower temperatures, when the shell was ordered, hexadecane was enriched. Cyclohexane was always enriched in cyclohexane/hexadecane mixtures due to stronger ligand-solvent interactions for this more entropic mixture [59]. In the case of the 1-hexanol/hexadecane mixtures, 1-hexanol forms a hydrogen-bonding network, increasing the solvent-solvent interaction, leading to an enrichment of the alcohol in the bulk solvent. As a result, the ligand molecules interacted with hexadecane, leading to an enrichment of the co-solvent in the shell. This result shows that the destabilizing effect of the polarity of the OH-group is greater than the stabilizing effect that might be expected due to the short alkyl chain.

In conclusion, it can be stated that there are differences between colloidal systems with a pure

solvent and a solvent mixture. In the case of a pure solvent, the solubility of the ligand has only a minor effect on colloidal stability. Instead, ligand-solvent interactions dependent on the shell structure play a decisive role. In the case of solvent mixtures, the ligand's preferential interaction with one of the solvents can lead to significant deviations in colloidal stability from the values expected for the mixing ratio. The results indicate that optimizing the enrichment of such solvent molecules could overcome the limitation to certain apolar solvents. Additionally, it was demonstrated that functional groups have a significant impact on the enrichment of a solvent molecule in the shell. To enhance the stabilizing effect and reduce the amount of co-solvent, less polar molecules with functional groups, such as amines, phosphines, or sulfides, could be used that interact with both the ligand and the core.

2.3 Shape stability of apolar nanoparticles

Ligand molecules can control colloidal stability. A second essential function is to stabilize the particle shape. The particle shape can change over time or with temperature, for example, through processes such as ripening, aggregation, or coalescence. The driving force behind both processes is the reduction in surface area [84]. In classical Ostwald ripening, bigger particles grow at the expense of smaller ones. Figure 2.3.1A-D shows the time-dependent Ostwald ripening of thiol-coated gold nanoparticles at 150 °C.

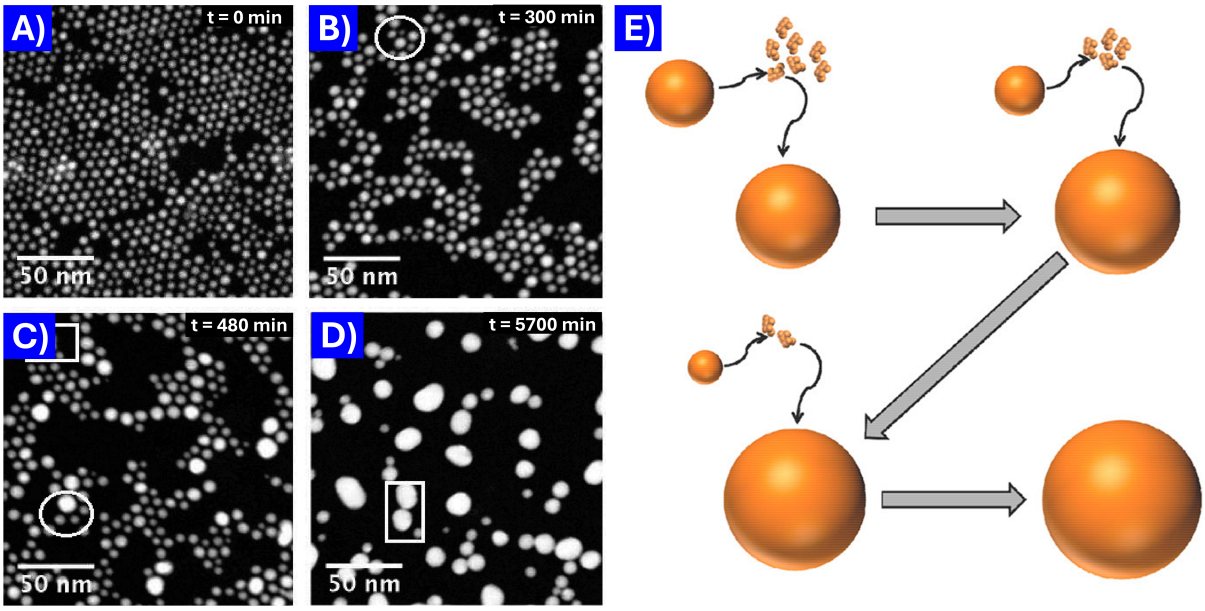


Figure 2.3.1: Time dependent Ostwald ripening of 5 nm gold nanoparticles coated with 1-dodecanethiol at 150 °C after A) 0 min, B) 300 min, C) 480 min and D) 5700 min. Schematic representation of the mechanism of Ostwald ripening, which leads to the formation of larger particles at the expense of smaller particles. A)-D) Adapted and reprinted with permission from [146]. Copyright © 2025 American Chemical Society. E) Adapted and reprinted with permission from [147]. Copyright © 2025 American Chemical Society.

Ripening requires the diffusion of atoms or clusters of the core material between two particles (Figure 2.3.1E). Lifshitz, Slyozov, and Wagner (LSW) developed a model to describe diffusion during ripening in a dispersion [148, 149] that can be applied to many core materials. This "LSW" model and its derivative do not consider the shell, however [147]. Depending on the functional group of the ligand molecule, strong binding occurs [150, 151] that hinders the diffusion of atoms on the core surface [42, 152]. Strongly bound thiols on gold passivate the core against surface diffusion [153, 154] and increase the long-term shape stability. Ostwald ripening of 9 nm gold nanoparticles coated with 1-hexadecanethiol can only be observed at temperatures above 150 °C after heating for 3 h to 5 h [155]. High temperatures weaken the Au-S bond, reducing surface passivation. Depending on the core material, the molecular structure of the ligand,

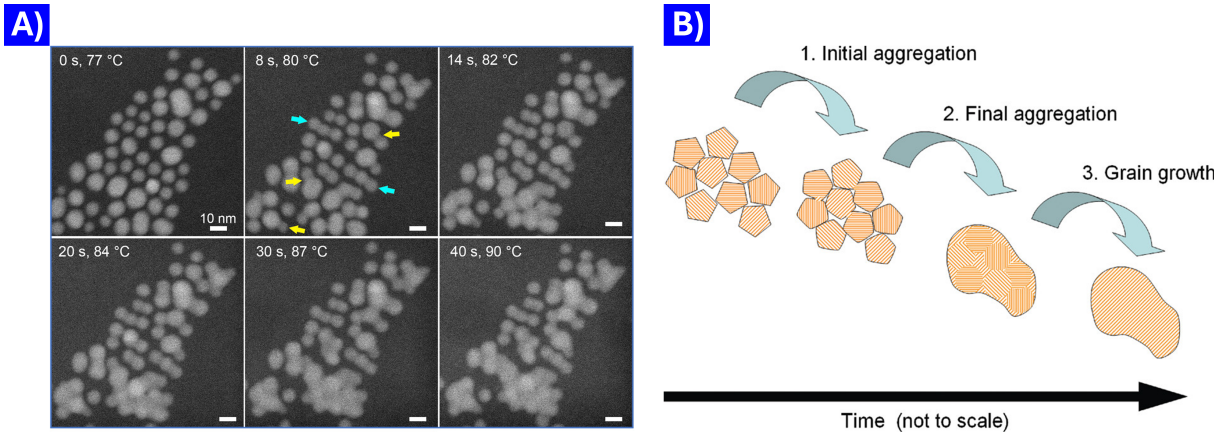


Figure 2.3.2: A) Time-dependent aggregation of 5 nm gold particles coated with oleylamine during heating of the sample from 77 °C to 90 °C. B) Schematic representation of the different aggregation stages of the coalescence process. A) Adapted and reprinted with permission from [158]. Copyright © 2025 American Chemical Society. B) Adapted and reprinted with permission from [159]. Copyright © 2025 American Chemical Society.

and the shell density, temperatures around 150 °C are required to induce Ostwald ripening [146, 155].

The desorption rate of ligands primarily depends on the binding energy of the ligand [156]. The desorption temperature of alkylthiols from gold also increases with increasing alkyl chain length (C_x) [41]. Ito and coworkers have demonstrated that alkylthiol desorption occurs in stages [157]. In the first stage, two neighboring ligands (C_xS-) react to form a dimer (C_xS-SC_x), which then desorbs. Dimerization was suppressed below a certain shell density. The desorption of the remaining monomer then takes place at higher temperatures. This behavior was different when using branched ligands. Depending on the number of branches, the initial shell density was reduced significantly. As shell density decreased, the amount of dimerization of the ligand molecules was reduced. For strongly branched, only the desorption of monomer fragments was observed. Additionally, the authors could show that the desorption temperature of the monomer fragments decreased with increasing number of branching groups. They assumed that this trend was the result of differences in the binding energy [157].

Coalescence refers to the irreversible combination of two or more particles, resulting in a single particle without a remaining interface. The initial stage of coalescence, in which only a connection between particles is formed, is called aggregation. Figure 2.3.2A shows the time-dependent aggregation of gold particles with an oleylamine shell during heating. Figure 2.3.2B shows stages that are defined by the degree of aggregation [159]. In the first stage, initial contacts are formed between the particles. The original particle shape is retained.

The formation of the initial contacts is based on surface-atom diffusion, which depends on the distance between the particles and the ligand coverage [159–162]. In the second stage, the particles aggregate further to close the gaps. The grain boundaries of the original particles exist

within the new structure. In the final stage, grains grow until the boundaries of the individual particles disappear [159, 163]. In their work, Ingham and co-authors discussed the conditions for inducing the first stage. They found that desorption of the ligand allowed neighboring particles to aggregate.

Generally, drying particles into films [164, 165] or assembling particles inside a liquid [158] can be used to reduce the distance between the cores. The ligand shell passivates the particle surface, acting as a barrier between the cores [42, 152, 166]. To induce aggregation of thiol-coated particles, larger parts of the shell must be removed by desorption or decomposition of the ligand molecules at temperatures between $90\,^{\circ}\mathrm{C}$ to $150\,^{\circ}\mathrm{C}$ [41, 157, 167]. The Au-S bond can be split by oxidation using oxygen [60, 168] or nitrogen dioxide [165].

Coarsening processes such as aggregation can be used to produce bulk materials from nanoparticles [169]. Consequently, it is of interest to reduce the temperatures required for such reactions while improving controllability. One promising way to reduce the protective effect of the shell could be non-destructive modifications, like partial ligand exchange with very short molecules.

2.4 Goal of the dissertation

Chapters 2.2 to 2.3 presented various particle properties and identified potential gaps in knowledge. The focus was particularly on adjusting properties such as colloidal stability and shape stability. This work aims to find modifications to the shell that either improve colloidal stability or reduce shape stability.

In Chapter 2.2, it was shown that in the case of shell-dominated systems, the colloidal stability depends strongly on the disorder-order transition of the shell. The modifications performed in this work aim to change the shell structure in such a way that this transition is prevented or delayed.

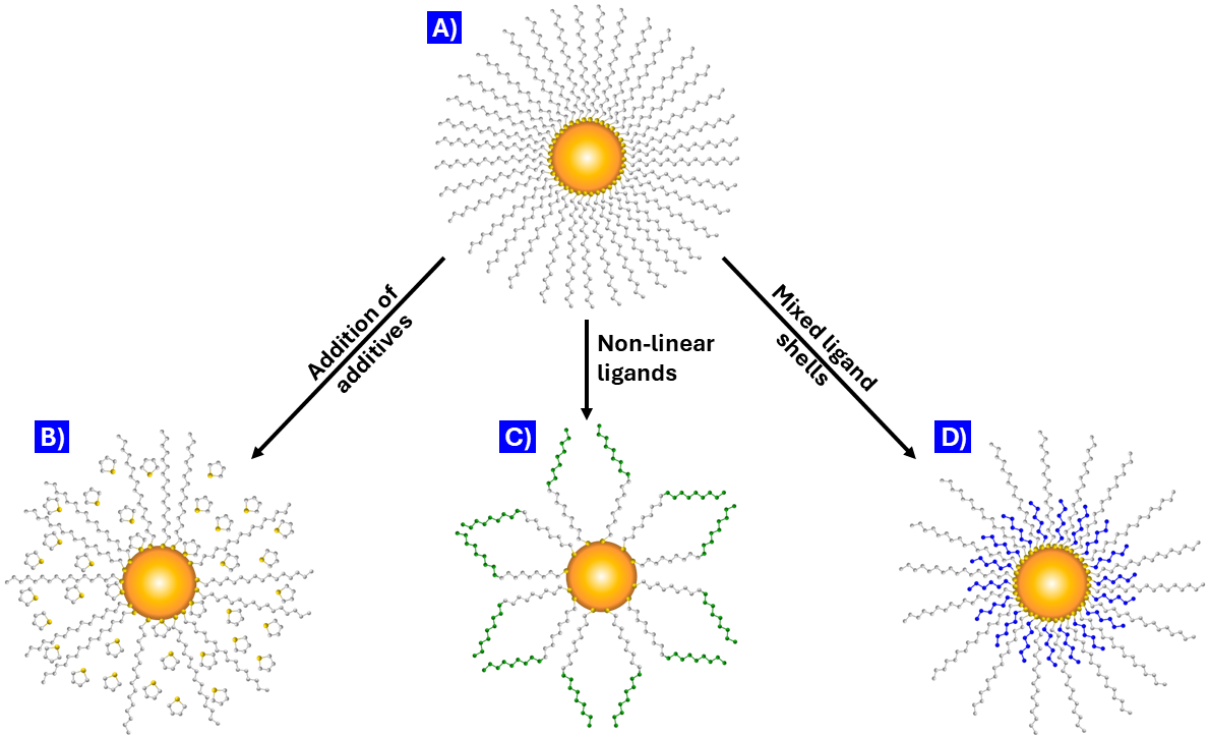


Figure 2.4.1: Schematic representation of the modifications made to the ligand shell in this work to adjust colloidal stability. System A) shows the reference system in which the gold core is coated with hexadecanethiol (HDT). System B) shows a particle after modification with the additive tetrahydrothiophene (R5S). System C) shows a particle coated with a kinked ligand. System D) shows a system with a mixed shell of two thiols with different chain lengths.

In Chapter 2.2.3, it was shown that the targeted enrichment of specific molecules in the shell can improve colloidal stability. In the first part of this work, this approach is used to modify the shell structure by adding small amounts of additives (< 1 vol%). The additives used are small cyclic amines and sulfides, which can interact more strongly with the core (see Figure 2.4.1B). The aim is to achieve a high additive concentration in the shell to stabilize the disordered shell

structure. Chapter 3.1 presents the mechanisms that explain why only certain additives can influence the shell structure.

Chapter 2.2.2.1 presented the modification of the shell structure using non-linear ligands. In the second part of this work, these ligands were used to produce colloidally very stable systems. Branched, kinked, and double-armed ligands were used (see Figure 2.4.1C). The aim was to demonstrate the suppression of the disorder-order transition of the shell. Chapter 3.2 shows the ligand-specific mechanisms and interactions that explain the effects of the molecular structure on the shell structure.

In Chapter 2.2.2.2, another possibility for modifying the shell structure was presented: mixed shells. In the third part of this work, the colloidal stability of such systems is investigated. Similar to the literature, linear thiols with different chain lengths were used (see Figure 2.4.1D). The work aimed to understand the influence of various factors, such as ligand ratios and distributions in the shell, as well as the effect of the size difference of the combined ligands. Chapter 3.3 discusses mechanisms that explain why only certain combinations lead to a significant improvement in colloidal stability.

In addition to the influence of modifications of the ligand shell on the colloidal stability, the effect on the shape stability was also investigated. In Chapter 2.3, it was shown that removing ligand molecules from the shell allows the cores to coarsen. In this work, the shell structure is not altered by desorption, but rather by specific modifications. In particular, modifications that reduce the protective or steric effect of the shell could influence shape stability (see Figure 2.4.2). The fourth part of this work aimed to understand whether specific "non-destructive" changes of the shell can induce coarsening processes under conditions that are as moderate as possible. The focus was on the influence of an advanced replacement of the original passivating long-chain alkylthiols with a smaller sulfide additive on shape stability. Chapter 3.4 shows the additive-induced aggregation and explains the underlying reaction mechanisms.

Chapters 2.2 and 2.3 described the theory behind the colloidal and shape stability of gold nanoparticles. They showed how the self-assembly and aggregation of particles can be induced or prevented. For example, if the shell becomes too small, uncontrolled aggregation or agglomeration of the particles can occur. These self-assemblies are often irreversible, allowing partial aggregation of the cores. The final part of this work examines whether specific modifications can induce controlled self-assembly and aggregation of particles to produce more complex gold materials. The focus here was also on modifying alkylthiol-coated particles using the additive tetrahydrothiophene. Chapter 3.5 shows the additive-induced synthesis of so-called gold

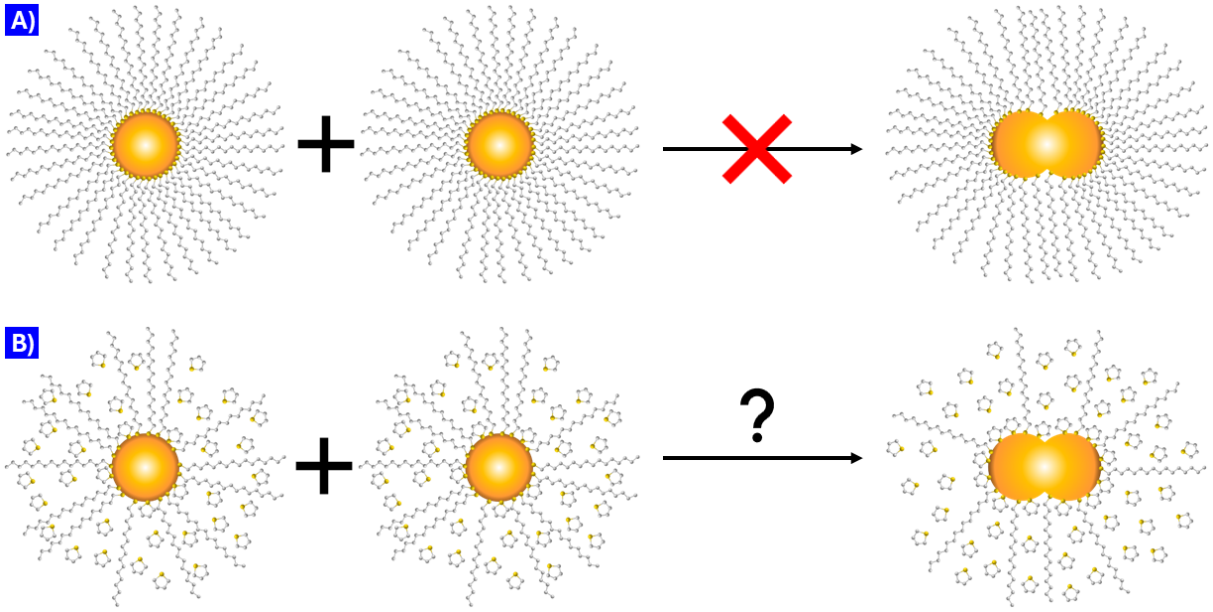


Figure 2.4.2: Schematic representation of the core aggregation of gold nanoparticles. System A) shows the aggregation reaction between alkylthiol-coated gold nanoparticles. This reaction is not possible under normal conditions due to the protective effect of the shell. System B) shows a possible aggregation reaction of particles modified with the additive tetrahydrothiophene.

sponges and discusses the underlying reaction mechanisms.

Chapter 3: Results

3.1 Publication 1: Stabilization of Apolar Nanoparticle Dispersions by Molecular Additives

Knapp, T. V.; Hasan, M. R.; Niebuur, B.-J.; Widmer-Cooper, A.; Kraus, T. Stabilization of Apolar Nanoparticle Dispersions by Molecular Additives. *Langmuir*, vol. 40, no. 26, pp. 13527–13537, 2024.
https://doi.org/10.1021/acs.langmuir.4c00996.

Reprinted with permission from [113]. Copyright © 2025 American Chemical Society.

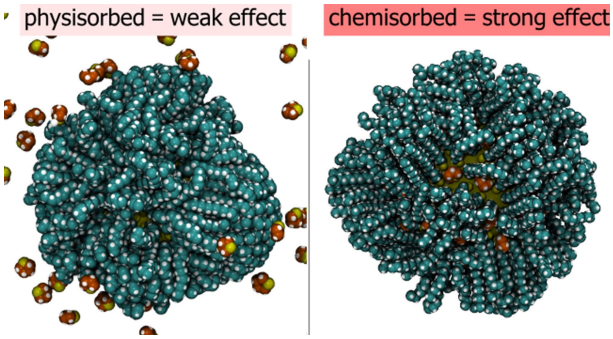


Figure 3.1.1: Table of contents figure of Publication 1. Reprinted with permission from [113]. Copyright © 2025 American Chemical Society.

3.1.1 Abstract

We study the effect of additives on the colloidal stability of alkanethiol-coated gold nanoparticles. Cyclic amines and sulfides of different sizes were added to dispersions in decane at additive concentrations below $128\,\mathrm{mM}$. Small-Angle X-ray Scattering (SAXS) indicated that tetrahydrothiophene reduced the agglomeration temperature, T_{agglo}, by up to $29\,^{\circ}\mathrm{C}$, a considerable increase in colloidal stability. Amines had a much weaker stabilizing effect of up to $2.5\,^{\circ}\mathrm{C}$. We found an unexpected maximum of stabilization for low additive concentrations, where T_{agglo} increased at concentrations above $64\,\mathrm{mM}$. Molecular dynamics simulations were used to correlate these observations with the ligand shell structure. They excluded physisorption of additives as a stabilization mechanism and suggested that sulfides replace hexadecanethiol on the AuNP surfaces by chemisorption. This hinders ligand ordering, thereby reducing T_{agglo}, which explains the stabilizing effect. Clustering of chemisorbed additive molecules at high concentration restabilized the ligand ordered state, explaining the detrimental effect of higher additive concentrations. The predictions of the simulations were confirmed using thermogravimetric analyses and SAXS measurements of washed samples that indicated that the structure of the ligand shell itself, not the presence of physisorbed additives, changes T_{agglo}. Finally, we calculated potentials of mean force, which show that larger sulfide-based additives have a weaker affinity for the gold surface than smaller ones due to stronger steric hindrance. This explains why smaller cyclic sulfides were the most efficient stabilizers.

3.1.2 Introduction

Coating nanoparticles with surface ligands is an effective way of tuning their properties. Besides controlling the nanocrystals' size and shape [170–173], ligands prevent the particles from aggregating in dispersions [43, 58, 59, 105, 125, 174], provide electronic passivation [110, 175–178], and adjust their dispersibility in both polar and apolar solvents [179–182]. Moreover, by strategically arranging different types of ligands on the surface, the self-assembly of nanocrystals can be precisely controlled to form complex superstructures [183, 184].

Apolar nanoparticles and their assemblies are used in applications ranging from sensors, printable electronics [20, 185], and catalysis [186, 187] to photovoltaics [188, 189]. In order to avoid agglomeration or aggregation during synthesis, manufacturing or use of devices, the nanoparticles must be colloidally stable. For example, many printing techniques require inks with a homogeneous particle distribution [20, 21, 25]. The dispersion state of the particles influences optical or thermal properties of devices, too [190, 191].

The colloidal stability of apolar nanoparticles with shells of small, uncharged molecules is governed by an interplay of weak and short-ranged entropic and enthalpic interactions. The stabilizing effect of the shell depends on the conformational entropy of the ligands, which, in turn,

is strongly dependent on the molecular structure of the ligands and the composition of the ligand shell [125]. A disorder-to-order transition of the ligands can thus destabilize dispersions. For example, as temperature decreases, saturated linear alkane tails form ordered bundles which drive particle agglomeration [58, 102]. Mixed ligand shells of different molecules have been used to tune ligand shell structure and colloidal stability [124, 133], with the structure of the ligand shell dependent on both energetic and entropic contributions [132, 133, 192, 193].

Molecular additives that form solutions with the solvent can change the colloidal stability of nanoparticle dispersion. For polar dispersions, salts, polymers, and surfactants have been added to tune particle assembly, for example into 2D materials through interfacial self-assembly [194–197]. Arginine dipeptide additives have also been used to stabilize assemblies of AuNPs in polar media by simultaneous interaction with multiple particles [198]. Literature shows that additives can also strongly affect apolar nanoparticle dispersions. For example, ethanol degrades colloidal stability and is commonly used to precipitate apolar nanoparticles, such as quantum dots, during purification [32]. In contrast, organometallic additives have been used to improve the colloidal stability of $4\,\mathrm{nm}$ to $15\,\mathrm{nm}$ AuNPs in engine lubricants [199]. It is not known, however, whether such stabilization of apolar nanoparticle dispersions is possible at very low additive concentration, which mechanisms are most effective for it, or which molecular features make additives effective.

In this contribution, we combine experimental methods and molecular dynamics (MD) simulations to characterize and explain the concentration-dependent effect of molecular additives on the colloidal stability of small apolar nanoparticles. The stability of AuNPs with $4\,\mathrm{nm}$ diameter cores and hexadecanethiol shells was quantified in the presence of concentrations up to $2\,\mathrm{vol\%}$ of different cyclic amines and sulfides. We found strong stabilizing effects for some additives, with a non-monotonic concentration dependence, and explain the results in terms of the molecular structure of the additives. Our results indicate that the relative affinities of the additives for binding to the nanoparticle surface is key. Suitable additives disrupt the molecular order of the ligand shell, thereby increasing colloidal stability, while the surprising decrease in colloidal stability at higher additive concentration is attributed to a transition from a random to a clustered arrangement of additives on the particle surface.

The following report is structured as follows. We first introduce X-ray scattering results on the stabilizing effect of different additives. Cyclic sulfides had the strongest effect, and we use MD simulations to analyze how the ligand order is affected by their distribution in the solution and on the particle surface. Experimental and simulation results are used to propose explanations for the additives' stabilizing effect as a function of their molecular structure. The final part contains X-ray scattering and thermogravimetry results that illuminate the adsorption mechanisms of the additives and provide additional support for our conclusions.

3.1.3 Results and Discussions

Temperature-dependent stability of additive-containing dispersions

Spherical gold nanoparticles (AuNPs) with narrowly distributed core diameters of $\approx 4\,\mathrm{nm}$ ($\pm$ 11%) were synthesized, purified, functionalized with hexadecanethiol (HDT) ligands, and dispersed at a concentration of $2.5\,\mathrm{mg\,mL^{-1}}$ in decane. Soluble organic molecules (called "additives" in the following) were added to the final dispersions. Previous work has shown that cyclic alkanes are good solvents for apolar nanoparticles [59, 109]. We have taken up these findings and used cyclic molecules with 5 and 9 carbons and a nitrogen or sulfur atom in the ring to evaluate whether their affinity to gold increases the stabilization efficiency. Pyrrolidine (R5N), azonane (R9N), tetrahydrothiophene (R5S) and thionane (R9S) (Figure 3.1.2) were used at different millimolar concentrations.

Temperature-dependent Small-Angle X-ray Scattering (SAXS) was performed to characterize the stability of the dispersions. We have shown previously that SAXS provides accurate data on the attractive interactions between apolar nanoparticles [59, 109]. To determine the temperature at which agglomerates form, samples were cooled from the dispersed state at $36\,^{\circ}\mathrm{C}$ to the agglomerated state at $-20\,^{\circ}\mathrm{C}$ in intervals of $2\,^{\circ}\mathrm{C}$.

All temperature-dependent scattering curves followed the trends illustrated in Figure 3.1.2 a-c. Scattering at $36\,^{\circ}\mathrm{C}$ had an intensity plateau at low q values, a negative slope at $q \approx 0.08\,\mathrm{\AA^{-1}}$, and a small peak at $q \approx 0.3\,\mathrm{\AA^{-1}}$. This reflects the scattering form factor of $4\,\mathrm{nm}$-diameter spheres and indicates that the particles were fully dispersed at $36\,^{\circ}\mathrm{C}$.[200] Upon cooling, strong forward scattering appears for all studied dispersions, indicative of the presence of large-scale agglomerates, as well as a structure factor peak at $q \approx 0.11\,\mathrm{\AA^{-1}}$, which indicates spatial correlation of the AuNPs within agglomerates.

Figure 3.1.2c-f shows temperature-dependent agglomerate fractions, $\chi_{\mathrm{agglo}}(T)$, calculated from the temperature-dependent structure factor peak as in previous publications [43, 58, 59]. Details of the method are described in the Methods section and in the SI. The agglomeration temperature, T_{agglo}, is defined as the temperature at which 20 % of the particles were agglomerated, $T(\chi_{\mathrm{agglo}} = 0.2)$. We calculated it for different additives using sigmoidal fits to χ_{agglo} (see Figure 7.1.4 in the SI) such that the data is consistent with previous publications.

All investigated additives decreased T_{agglo} at $16\,\mathrm{mM}$, i.e., they stabilized the dispersions (Figure 3.1.3). We quantified the stabilizing effect as the change in the agglomeration temperature $\Delta T_{\mathrm{agglo}}(c_{\mathrm{add}}) = T_{\mathrm{agglo}}(c_{\mathrm{add}}) - T_{\mathrm{agglo}}(c_{\mathrm{add}} = 0)$, with c_{add} the concentration of additive in the dispersion. The largest $\Delta T_{\mathrm{agglo}} = -29\,^{\circ}\mathrm{C}$ was observed for R5S at $64\,\mathrm{mM}$, followed by $\Delta T_{\mathrm{agglo}} = -6.5\,^{\circ}\mathrm{C}$ for R9S at $64\,\mathrm{mM}$. Both amine-containing additives stabilized only marginally, with $\Delta T_{\mathrm{agglo}} = -1.1\,^{\circ}\mathrm{C}$ for R5N at $128\,\mathrm{mM}$ and $\Delta T_{\mathrm{agglo}} = -2.5\,^{\circ}\mathrm{C}$ for R9N at $64\,\mathrm{mM}$.

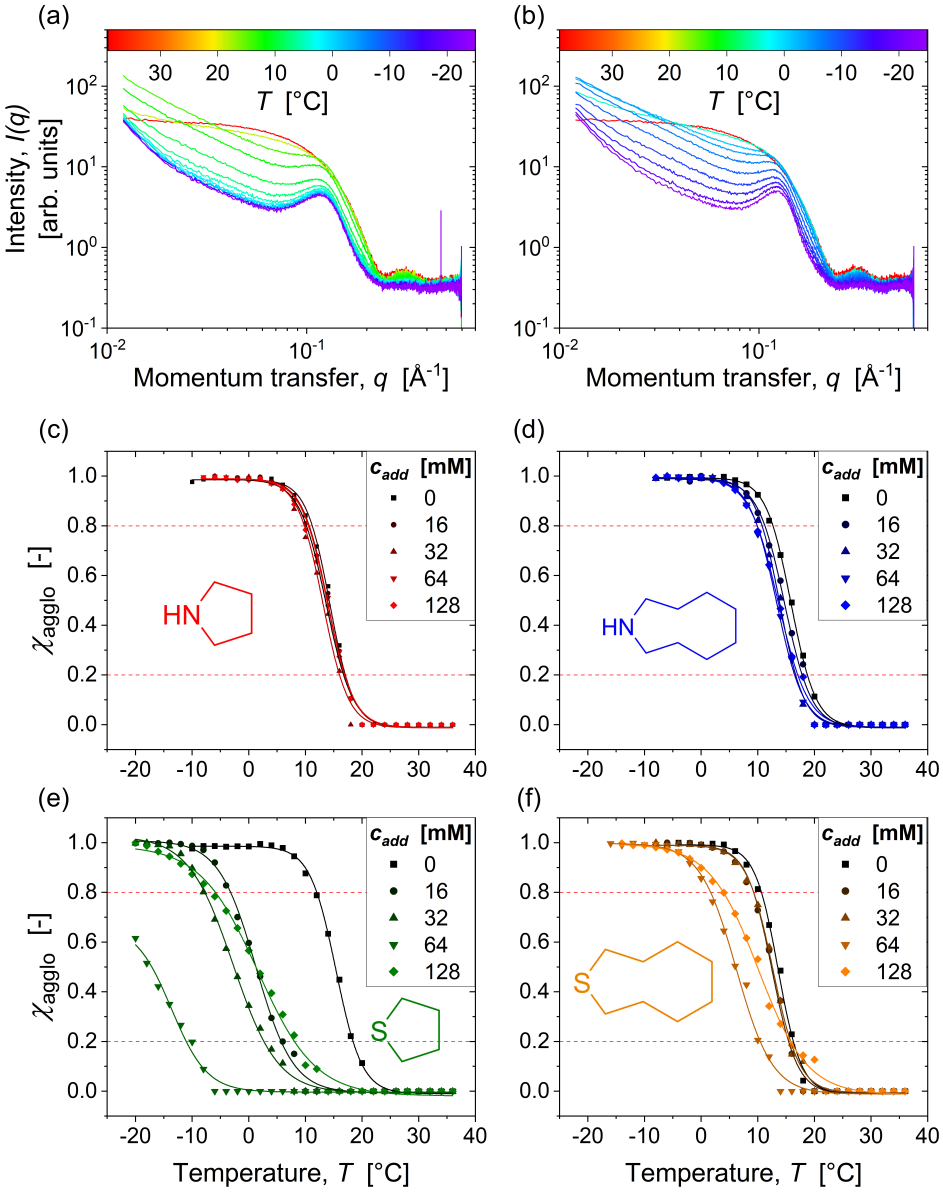


Figure 3.1.2: Temperature-dependent agglomeration stability of apolar AuNP@HDT dispersions from small-angle X-ray scattering. (a) Temperature-dependent scattering of AuNP@HDT in pure n-decane and (b) with tetrahydrothiophene R5S additive at a concentration of 64 mM. (c-f) Temperature-dependent agglomerate fractions calculated from scattering of AuNP@HDT in n-decane containing the additives (c) pyrrolidine R5N, (d) azonane R9N, (e) tetrahydrothiophene R5S, or (f) thionane R9S. The agglomerate fractions at 0.2 (dashed lines) were used to quantify the agglomeration process. Solid lines are fits to the data using a Boltzmann sigmoid function (see Figure 7.1.4 in the SI).

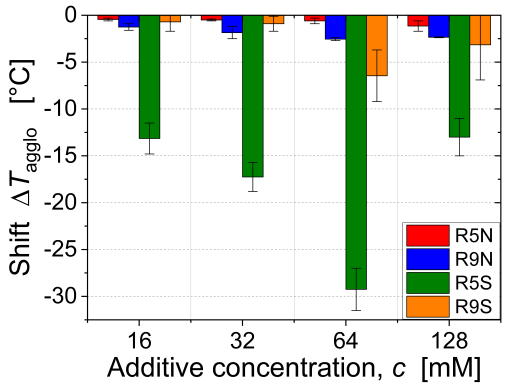


Figure 3.1.3: Stabilizing effects of different cyclic additives. Changes in the agglomeration temperature T_{agglo} are compared to pure n-decane for all amine and sulfide additives. Figure 7.1.5 in the SI shows the effect of the amines.

The agglomeration of AuNP with 4 nm cores and HDT shells is shell-dominated in common alkane solvents [58], but their colloidal stability requires sufficiently favorable ligand-solvent interactions. For example, AuNP@HDTs dispersed in hexanol agglomerate even above the ligand ordering temperature because the hexanol prefers to interact with itself [109]. An additive that adsorbs on the particle surface may physisorb and act like a surfactant or chemisorb, act like a ligand, and change the density or structure of the ligand shell. The magnitude of this change will be connected to the number of adsorbed additives and the position that they assume in the shell.

Two basic stabilization mechanisms are therefore conceivable and may occur concurrently. First, the presence of the additive can change the composition and structure of the ligand shell by chemisorption, which may reduce the temperature at which the ligands order. Second, the presence of the additive can change the solvent polarity and the resulting solvent-shell interaction by physisorption. We discuss both mechanisms and their consistency with our experimental observations in the following.

Primary and secondary amines have weak affinities for gold surfaces, and they are unlikely to replace the alkanethiol ligand that is present on the surface [201]. They can still affect ligand shell structure as a physisorbed intercalant that sits between alkyl chains. Sulfides, on the other hand, strongly bind to gold and can displace alkanethiol ligands [202, 203]. Therefore, it is expected that R5S and R9S can both physisorb and chemisorb. If additives act through ligand shell structure, one would thus expect larger ΔT_{agglo} for sulfides than amines. This is consistent with the experimental observations. The ΔT_{agglo} of R5N and R9N are large enough, however, to suggest that physisorption is sufficient to cause at least some stabilization.

The disproportionally larger stabilization of R5S, a smaller molecule that should cause less distortion of the ligand shell than R9S, suggests that steric hindrance also plays an important role.

In this picture, the smaller R5S can penetrate the shell more easily, adsorb at larger densities, and cause larger disruption of the shell structure. This size effect is consistent with either of the stabilization mechanisms discussed above.

The stabilizing effects of R5S, R9S, and R9N increased with their concentrations up to 64 mM and decreased at higher concentrations. The effect of R5N increased beyond 64 mM, but its absolute effect was always smaller than that of the sulfides. This may indicate that weakly interacting additives causes limited distortion. The change in the polarity of the solvent is too small to influence the agglomeration behavior. We assume that significant effects comparable to those of 1-hexanol in solvent mixtures [109] can only be observed at much higher concentrations of the most polar additive R5N. The detrimental effect of larger concentrations of the other additives is surprising and will be further discussed below.

In summary, the experimental results above are consistent with a combination of both proposed stabilization mechanisms, where chemisorption and distortion of the ligand shell appears to be the most efficient stabilization mechanism. In the following, we use MD simulations to distinguish between the possible effects of physisorption, the change of solvent quality, and chemisorption for the strongly stabilizing R5S additive. We analyze the effect of additive concentration and consider the surprising decrease of stabilization. The results are compared to additional SAXS and thermogravimetric analyses in the final part.

Simulations of physisorbed additives

We start by considering the case where the additives do not chemically bind to the AuNP, which we will refer to as the physisorption scenario. To do this, we placed an isolated AuNP@HDT in either pure n-decane or in an n-decane solution containing R5S additives at concentrations of either 76 mM or 718 mM, with the lower value similar to the experimental concentration at which the largest shift in T_{agglo} was observed (cf. Figure 3.1.3). MD simulations were then used to characterize the equilibrium distribution of R5S around the AuNP and their effect on the ligand ordering transition. As in previous work, we assumed that the HDT ligands were uniformly distributed over the AuNP surface. Figure 3.1.4a shows an equilibrated configuration for a AuNP@HDT particle immersed in decane containing R5S at roughly 76 mM concentration. This shows that R5S is well dispersed throughout the solution within the experimental concentration range.

The effect of physisorbed R5S on the ligand ordering transition was quantified by calculating the dihedral angle, φ, averaged along the hydrocarbon tails of the HDT ligands as a function of temperature. This is shown in Figure 3.1.4b for the cases of pure decane, 76 mM R5S and 718 mM R5S. The temperature at which $\varphi = 150°$ was determined using a sigmoidal fit (see Ref. [109] for details) and is referred to as the ligand ordering temperature (T_{order}) in the follow-

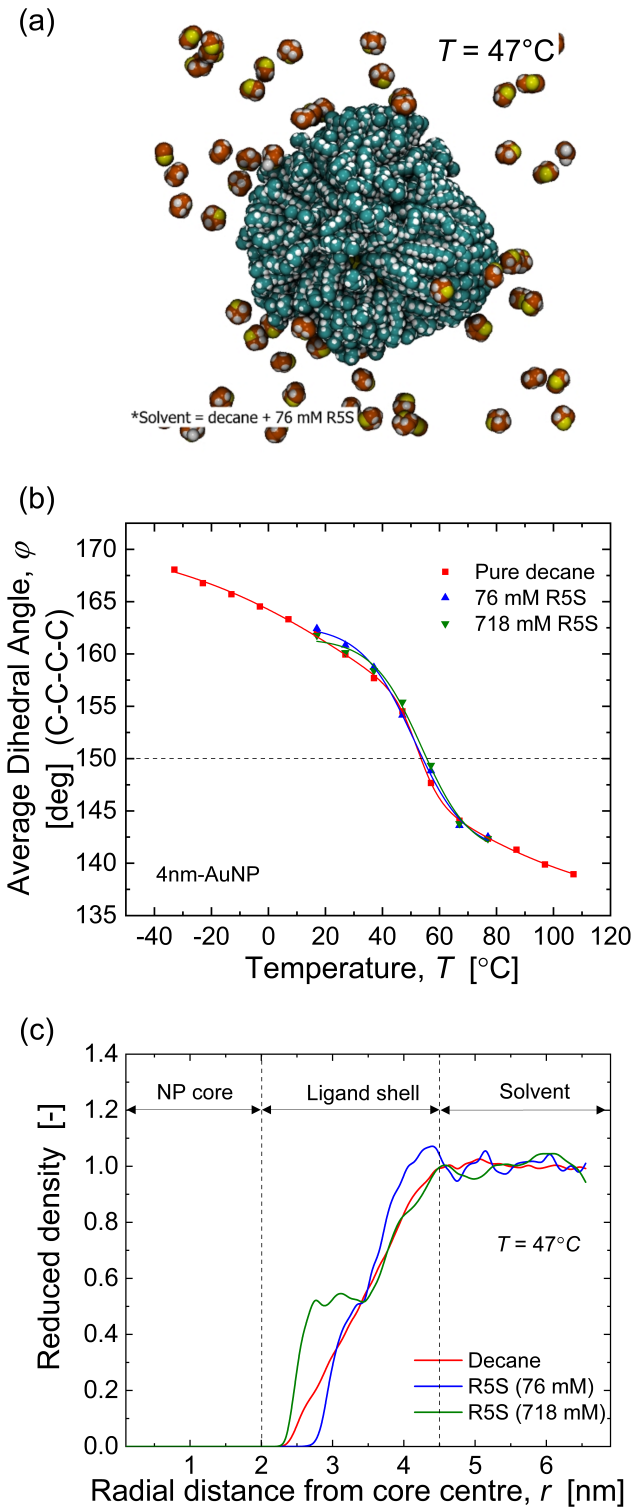


Figure 3.1.4: Effect of physisorbed R5S from MD simulations. (a) Snapshot of an equilibrated 4 nm AuNP@HDT particle (S atoms in yellow, C in cyan, H in white) in n-decane (hidden for clarity) at 76 mM R5S concentration (C-atoms in red). (b) Temperature dependence of the average dihedral angle between the carbon atoms of the HDT ligands in pure decane (red squares and fit), 76 mM R5S (blue triangles and fit), and 718 mM R5S (green upside down triangles and fit). The dashed horizontal line indicates the criterion used to determine the ligand ordering temperature T_{order}. (c) Reduced radial density distributions of n-decane and of R5S at 76 mM and 718 mM concentrations, measured from the centre of the AuNP at T_{order}. The density of each solvent component has been divided by its density in the bulk solution.

ing. As can be seen, the R5S in solution has almost no effect on the ligand ordering transition, even at a concentration well in excess of that used experimentally. We conclude that the effect of physisorbed R5S on the disorder-order transition cannot explain the increase in colloidal stability that is observed experimentally.

To better understand this behavior, and other possible effects of physisorbed R5S, we examined the equilibrium distribution of decane and R5S molecules around the AuNP@HDT. This was done by calculating the radial density distribution for each of the components normalized by their densities in the bulk solvent region. These reduced densities at T_{order} are shown in Figure 3.1.4c. The decane distribution is almost identical in pure decane and in the two R5S mixtures (see Figure 7.1.11 in the SI), so only the pure decane curve is shown here. This shows a roughly linear decrease in density within the ligand shell. In comparison, at 76 mM concentration the R5S is slightly enhanced in the outer part of the ligand shell (relative to the bulk solvent composition), while at 718 mM concentration the R5S is enhanced within the inner part of the ligand shell. As discussed above, these slight variations are insufficient to affect the ligand ordering transition. The R5S distributions also seem to preclude substantial contribution from other mechanisms that could drive agglomeration of the AuNPs. For example, the diffuse interface, the small size of the R5S and the AuNPs, and the low concentration of the R5S in the experiments make it highly unlikely that depletion attraction is important; and the similar relative amounts of R5S and decane within the ligand shell, along with the chemical nature of R5S, make it highly unlikely that solvophobic effects are important.

Simulations of chemisorbed additives

We next consider the case where the additives bind chemically to the Au core of the NPs, which we will refer to as the chemisorption scenario. All of the additives have functional groups that can bind to Au and Figure 3.1.4c shows that R5S is sufficiently small to penetrate deep into the ligand shell at high additive concentration. Ligand exchange by additive molecules, therefore, appears to be a possibility. In the following, we test the hypothesis that R5S and R9S covalently bind to the particle surface by replacing some of the HDT ligands. We quantify how this exchange affects the ordering transition of the HDT ligands, and compare the predicted shifts in T_{order} with the experimental shifts in T_{agglo}.

To do this, we replaced some of the HDT ligands with either R5S or R9S ligands in a one-to-one swap, considering both randomly distributed and clustered arrangements of the additives on the AuNP surface. In line with experimental results discussed in the next section, we considered up to 40 substitutions on the AuNP surface. Representative simulation snapshots for R5S-coated particles at T_{order} are shown in Figure 3.1.5.

Upon cooling, the HDT ligands in pure ligand shells align with each other and form large bundles

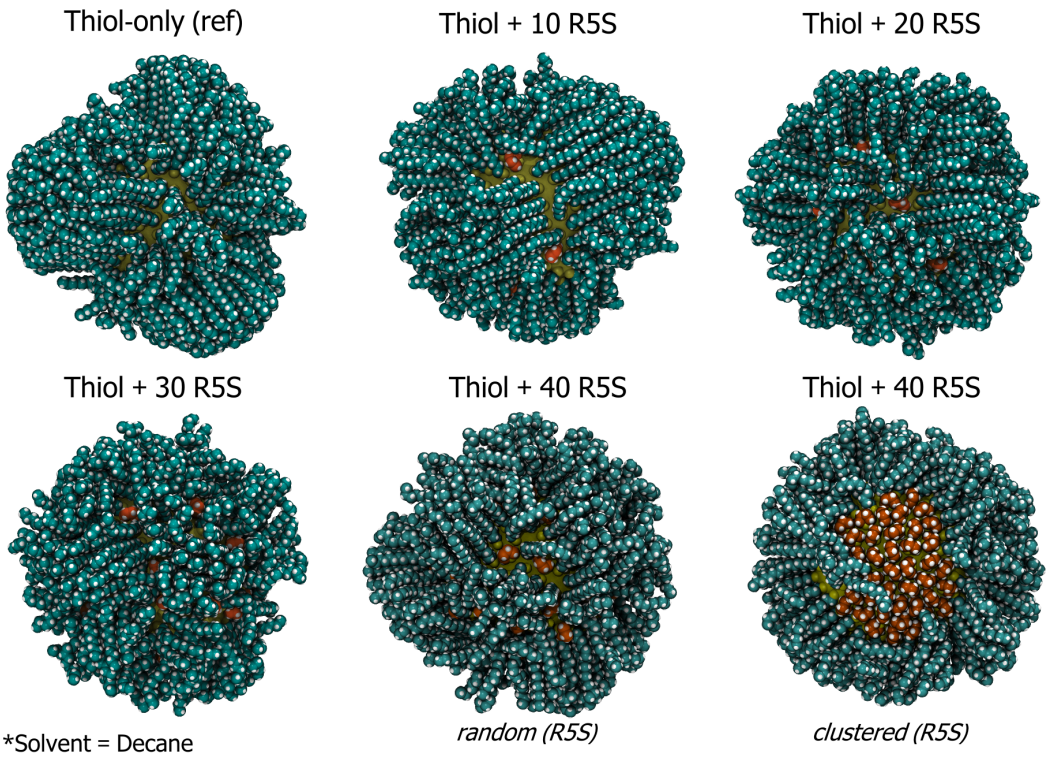


Figure 3.1.5: Simulation snapshots of 4 nm AuNPs in decane at the ligand ordering temperature with different amounts of R5S bound to the particle surface. Both randomly distributed and clustered arrangements of the R5S were considered. The base system without any HDT replaced by R5S is labeled as AuNP@HDT, and solvent molecules have been hidden for clarity.

that are separated by grooves with lower ligand density [43, 59]. We observe similar behavior when the R5S on the surface is clustered, as shown in Figure 7.1.13 in the SI. In contrast, in shells where the R5S is randomly distributed on the surface, smaller bundles form because the long HDTs cannot easily wrap around the smaller R5S while interacting with other HDTs (see Figure 7.1.13 in the SI).

As a consequence of this, the HDT ligand ordering transition is affected by both the quantity and distribution of chemisorbed R5S, as shown in Figure 3.1.6. In all cases, T_{order} is shifted to lower temperatures compared to the AuNP@HDT base system, consistent with the experimental changes in T_{agglo}. The effect is particularly strong when the R5S is randomly distributed on the AuNP surface, with a continual decrease in T_{order} as the number of bound R5S increases. Both the trend and magnitude of the shifts in T_{order} are similar to the experimental results for T_{agglo} up to 64 mM concentration. This strongly suggests that chemisorption of R5S is largely responsible for the increase in colloidal stability observed experimentally. Consistent with this conclusion, much smaller temperature shifts are observed experimentally for the nitrogen-containing additives, which are expected to have lower affinity for gold than the sulfur-containing ones [201]. Chemisorption also appears capable of explaining other aspects of the experimental results, including the surprising inversion of the stabilizing effect at high additive concentrations (see Fig-

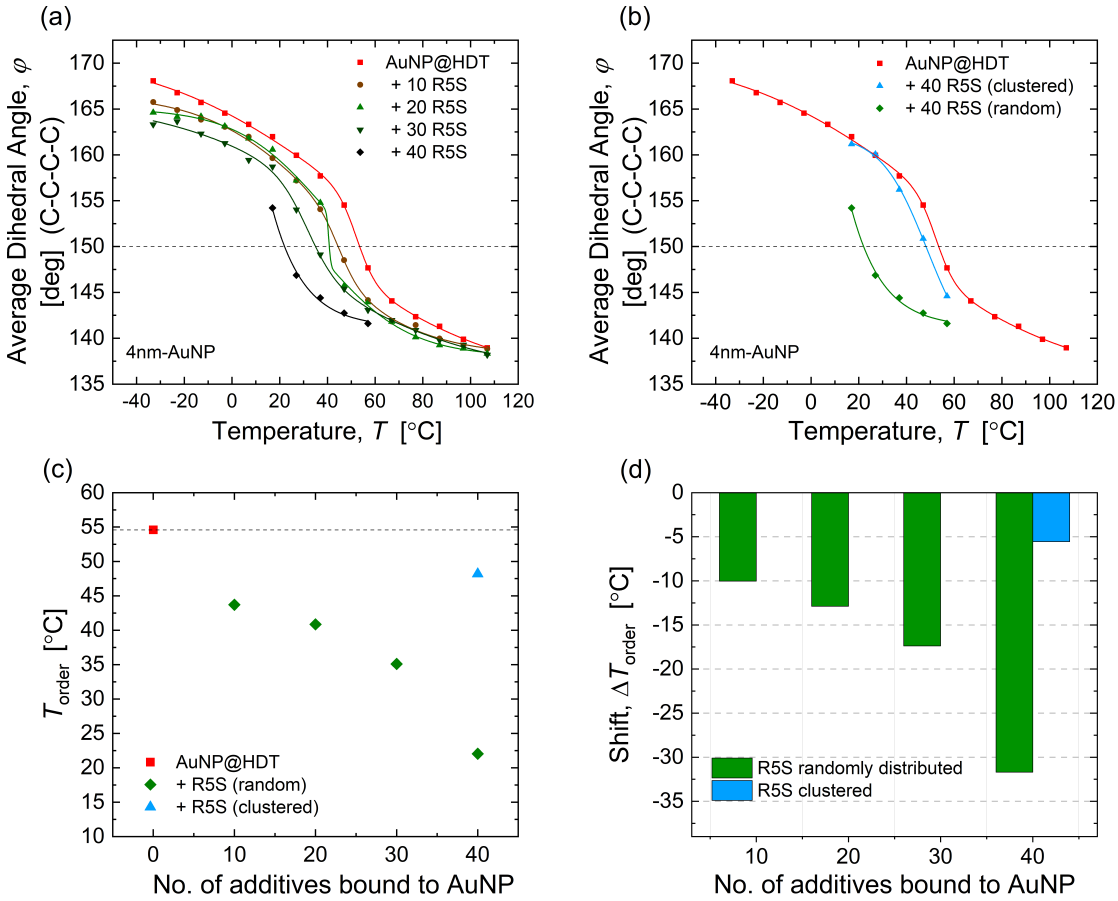


Figure 3.1.6: Effect of chemisorbed R5S from MD simulations. The colors used for lines and symbols in the plots are explained in the corresponding legends. (a,b) Temperature dependence of the average dihedral angle between carbon atoms of the HDT ligands in pure decane. (a) Effect of changing the amount of randomly distributed R5S bound to the AuNP. (b) Comparison of clustered and random R5S distributions at the same density. (c) The ligand ordering temperature T_{order} as a function of the number of R5S bound to the AuNP. (d) The shift in T_{order} relative to that of the AuNP@HDT base system.

ure 3.1.3). While T_{order} continues to decrease when more R5S molecules are bound to the AuNP surface at random positions (see Figure 3.1.6c), we find that the inversion can be explained by a transition in the additive distribution on the particle surface from random at lower concentrations to clustered at higher concentrations, similar to a demixing transition. In particular, when 40 R5S molecules are clustered together on the surface, rather than being randomly distributed, the HDT ligands are able to form larger bundles at low temperatures (see Figure 7.1.13 in the SI). This stabilizes the ligand ordered state compared to when R5S molecules are randomly distributed on the particle surface, and results in a much smaller decrease in T_{order}, with the shift changing from -32°C to -5°C (see Figure 3.1.6b and d). Such a transition in the spatial distribution of additives on the NP surface would therefore be consistent with the inversion of the stabilizing effect that is observed experimentally.

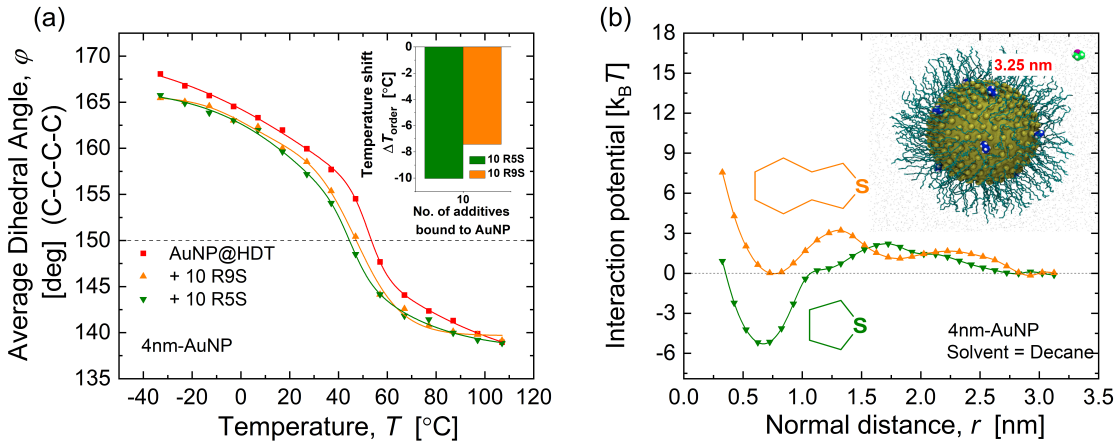


Figure 3.1.7: Effect of changing the additive size. Comparison of simulation results for 10 R5S or R9S bound to the AuNP. The colors used for lines and symbols in the plots are explained in the corresponding legends. (a) Temperature dependence of the average dihedral angle between carbon atoms of the HDT ligands in pure decane. Inset shows the shift in the ligand ordering temperature T_{order} relative to the AuNP@HDT base system. (b) Potential of mean force (PMF) between an unbound R5S or R9S and a vacant site on the AuNP surface, calculated at 67°C, i.e., above T_{order}. Inset shows the pathway used to calculate the PMF. The normal distance is the separation between the surface of the Au core and the sulfur atom of the unbound R5S or R9S.

To explain the large difference in stabilization between R5S and R9S, we investigated the influence of additive size on the ligand order and ability to traverse the ligand shell. SAXS indicated that AuNPs agglomerate at a much lower temperature in the presence of R5S than of R9S, even though both molecules possess a sulfide group that can bind to the AuNP core. First, we compared the ligand ordering transition with the same quantity of additives on the particle surface. We randomly replaced 10 HDT ligands by R9S (or R5S) molecules, and analyzed how this affected T_{order}. Snapshots of the particles at T_{order} can be found in Figure 7.1.14 in the SI, with the temperature-dependence of the ligand order shown in Figure 3.1.7a. As can be seen, both additives shift the disorder-to-order transition to lower temperature by a similar amount compared to the AuNP@HDT base system, and the values of φ nearly overlap at each temperature. Therefore, the difference in additive size alone cannot explain the large observed difference in T_{agglo} if the tendency of the additives to bind to the AuNP surface is the same.

Instead, the reason why the AuNPs have better colloidal stability in the presence of R5S appears due to less steric hindrance for R5S to approach the NP core compared to R9S. To test this hypothesis, we calculated the potential of mean force (PMF) between the additives and a ligand-coated NP. We did this by gradually moving one of the additives from the surface into the surrounding decane solution while allowing the the rest of the system to undergo normal dynamics (see Figure 7.1.15 in the SI for snapshots along this trajectory). In making this calculation, we ignored contributions from covalent bonding between the gold particle and the sulfur atoms of the additives, which should be very similar for R5S and R9S, in order to focus on the

effect of the difference in size.

Figure 3.1.7b shows the PMFs obtained for R5S and R9S at 67°C, i.e., just above the ligand ordering transitions. For R9S, the interaction between the additive molecule and the AuNP is unfavorable throughout the shell relative to the additive being dispersed in the decane. In contrast, there is a favorable interaction between R5S and the AuNP, with a minimum close to the gold surface. This indicates that the larger R9S has a less favorable affinity for binding to the gold core than R5S due to greater steric interaction with the densely packed HDT ligands near the surface. This provides an explanation for why the experimental agglomeration temperature is much lower in the presence of R5S than of R9S.

Experimental evidence for chemisorption

The MD simulations indicate that chemisorption of additives is the most effective stabilization mechanism. Comparison with our experiments suggests that this mechanism is particularly strong for the sulfur-containing R5S. In this section, we combine results from SAXS with thermogravimetric analyses (TGA) to experimentally test if R5S indeed replaces HDT on the AuNP. AuNP dispersions with an R5S concentration of $64\,\mathrm{mM}$ were compared to reference AuNP@HDT in pure n-decane.

We stored R5S-containing dispersions for one day, washed, and analyzed them (cf. SI for detailed procedures). The washed particles were redispersed in n-pentane for TGA or in n-decane for SAXS. Thermogravimetric analysis showed washing removed 99.7% of R5S from the dispersion (see Table 7.1.1 in the SI).

The colloidal stability of the washed dispersion was quantified with temperature-dependent SAXS. Figure 3.1.8a shows that T_{agglo} remained almost unchanged after washing. Removing free R5S from the solution by washing did not change the $\Delta T_{\mathrm{agglo}}$ of a dispersion that had once contained R5S. This is only explainable by a fraction of R5S that is chemisorbed on the particle surface and was not removed by washing.

Linear thiols such as HDT form compact ligand shells with a comparatively high ligand density [87, 88]. It is unlikely that there is free space left on the AuNP surface to additionally bind R5S. More likely is a partial ligand exchange. An R5S concentration of $64\,\mathrm{mM}$ is sufficient to replace all HDT molecules 40 times (see Table 7.1.1 in the SI) relative to an estimated 280 HDT ligands per original AuNP. Reference experiments showed that AuNP with a pure R5S shell are not colloidally stable (see Figure 7.1.9 and Figure 7.1.10 of the SI). We, therefore, conclude that R5S replaced some of the HDT, forming a mixed ligand shell (as illustrated in Figure 3.1.8c).

We used TGA to confirm the partial ligand exchange (Figure 3.1.8b). It is impossible to distinguish overall reduced ligand densities from a partial replacement of HDT with R5S in a single TGA measurement. We thus used reference experiments without R5S to assess the loss of HDT

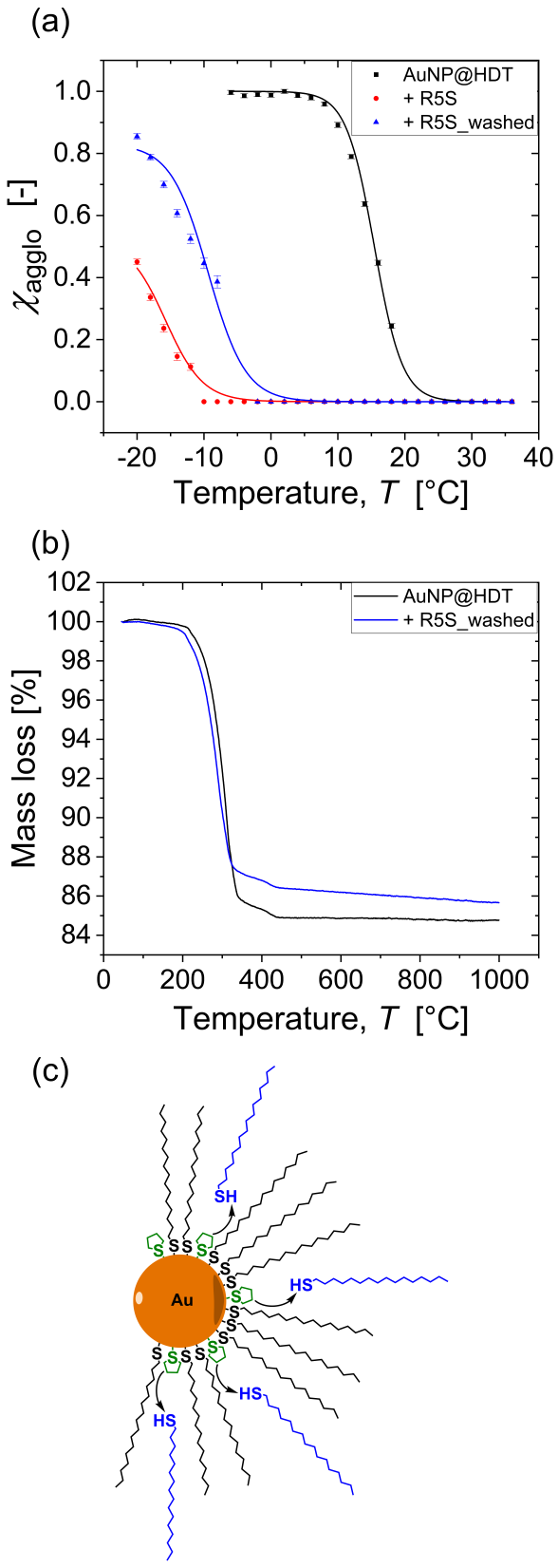


Figure 3.1.8: Role of chemisorption in the stabilization mechanism of R5S. (a) Temperature-dependent agglomerate fractions χ_{agglo} from SAXS for AuNP@HDT dispersions in pure n-decane (black curve), a dispersion with 64 mM of R5S (red curve), and the same dispersion after a washing step that removed the unbound additive (blue curve). Washing the additive-free AuNP@HDT system showed no effect on the agglomeration curve (see Figure 7.1.8 in the SI). (b) Thermogravimetric mass loss during heating of the additive-free AuNP@HDT sample (black) and averaged thermogravimetric mass losses of two samples with an R5S concentration of 64 mM after one additional washing step (blue). (c) Illustration of the ligand exchange by R5S additive molecules.

upon washing and found a mass loss of $0.4\,\%$ that corresponds to a ligand loss of 3 num% (cf. equation 7.1.16 in the SI). This small loss of HDT molecules from the shell correlates with the marginal change in the agglomeration curve ($\Delta T_{\text{agglo}} = -0.25\,°\text{C}$, see Figure 7.1.8 in the SI). The change in ΔT_{agglo} and the higher mass loss in the presence of R5S of $0.7-1.3\,\%$ is consistent with partial ligand exchange. If we assume that the difference in shell mass is caused by partial replacement of HDT molecules by R5S, a mass loss of $1.0\,\%$ indicates the replacement of 12 num% of HDT (See equations 7.1.7-7.1.15 in the SI) and 9 num% if we consider a loss of 3 num% HDT in washing.

An exchange of $9-12$ num% of HDT by R5S for particles with 280 HDT molecules (as used in the MD simulation) corresponds to 25-35 R5S molecules. The MD results in Figure 3.1.6d predict a reduction of T_{order} by $18\,°\text{C}$ for 30 molecules and more than $30\,°\text{C}$ for 40 randomly distributed R5S molecules. This indicates that the largest part of the stabilizing effect of R5S is due to chemisorption. This conclusion is supported by a more detailed analysis of the washed dispersions. Figure 3.1.8a shows that the removed physisorbed and unbound R5S fraction led to a decrease in the change in T_{agglo} of less then $1.5\,°\text{C}$.

3.1.4 Conclusion

We characterized the effects of adding a few vol-% of pyrrolidine (R5N), azonane (R9N), tetrahydrothiophene (R5S) and thionane (R9S) on the colloidal stability of apolar nanoparticle dispersions in n-decane. Experimental small-angle x-ray scattering (SAXS) studies showed strongly stabilizing effects of the sulfides R5S and R9S, which reduced the agglomeration temperature T_{agglo} by up to $28\,°\text{C}$. The amines had weaker stabilizing effects of up to $2\,°\text{C}$ for R9N. Stability increased with concentration for R5S, R9S and R9N until a concentration of $64\,\text{mM}$ ($0.5-1$vol%), then decreased.

The large differences in stabilization are due to the relative affinities of the additives for the gold surface and their effects on ligand shell structure. Molecular Dynamics (MD) simulations show that physisorbed additives, such as R5N and R9N, only weakly affect the ligand disorder-to-order transition that sets the colloidal stability of shell-dominated, hexadecanethiol (HDT)-coated particles. Covalently bound R5S that randomly replaces HDT, on the other hand, strongly decreases the ligand ordering temperature T_{order}, with the predicted changes in T_{order} similar in magnitude to the changes in colloidal stability ΔT_{agglo} detected by SAXS.

We confirmed the replacement of HDT by R5S through TGA analyses. The increased stability remained almost unchanged after removing the free additive from the dispersion. This confirms that additives that strongly interact with the particle surface stabilize the dispersion through changes in the ligand shell structure.

Simulations provided further insight into these changes. The unexpected decrease of stabiliza-

tion at increased additive concentrations was shown to be consistent with a transition from a random to clustered distribution of chemisorbed additives on the Au surface; while the smaller efficiency of the larger additive R9S was explained by repulsion between the HDT shells of AuNPs and R9S, indicated in Potentials of Mean Force that we calculated. This suggests that R5S more readily enters the shell, replaces HDT, and changes the ligand shell structure.

The results of this contribution highlight the link between additives and mixed ligand monolayers, too. We show that mixed ligand shells can be readily created through additives, and that they increase stability. It will be interesting to consider whether the long-term stability of nanoparticle dispersions can profit from additives that cause the slow formation of mixed monolayers.

3.1.5 Materials and Methods

Nanoparticle synthesis

Gold nanoparticle with a core diameter of 4 nm were synthesized following a method described previously [58]: A mixture of 9 mL of n-pentane (Carl Roth, 99 %) and 9 mL oleylamine (Sigma Alrich, technical grade, $80-90$ %) was added to 100 mg of tetrachloroauric(III) acid trihydrate $HAuCl_4 \cdot 3\,H_2O$. The mixture was stirred (with a magnetic stirrer bar, 300 rpm) for 21 min at $22\,^{\circ}C$ under argon atmosphere. Then, a mixture of 1 mL n-pentane, 1 mL of oleylamine and 40 mg tert-butylamine borane complex (FLUKA, 97 %) was added to the gold precursor solution. The mixture was stirred for 90 min. The dispersion was purified by precipitation with 50 mL of a mixture of ethanol and methanol (ratio 3:2) and centrifugation at 2000 rpm (689 rcf) for 5 min. The supernatant was removed, and the nanoparticles were redispersed in 2.5 mL toluene (gold concentration of 10 mg/mL).

Multiple batches of AuNPs were synthesized for this study, and characterized using SAXS (see Figure 7.1.1 in the SI). In all cases, the AuNP had an r_{avg} in the range of $3.8-4.1$ nm and σ in the range of $10-11$ %. Transmission electron microscopy confirmed the spherical shape of the AuNPs (see Figure 7.1.2 in the SI).

Ligand exchange

The ligand exchange, following a previously described procedure [58], was performed at $80\,^{\circ}C$ by adding 0.4 mL of hexadecanethiol (Sigma Aldrich, GC, 95 %) to 1 mL of the 10 mg/mL dispersion and stirring for 15 min at 300 rpm. The dispersion was purified by precipitation with 3 mL of a mixture of ethanol and methanol (ratio 2:1) for 1 mL dispersion and centrifugation at 2000 rpm (689 rcf) for 5 min. The supernatant was removed, and the nanoparticles were redispersed in 1 mL toluene. The washing step was repeated once with a cooled mixture of

Table 3.1.1: Additive volume for the sample preparation for the different additive-AuNP ratio.

Additive volume per 1 mL AuNP dispersion for the used additive concentrations					
Additives	16 mM	32 mM	48 mM	64 mM	128 mM
R5S	1.41 µL	2.83 µL	4.24 µL	5.66 µL	11.32 µL
R9S	2.57 µL	5.15 µL	–	10.29 µL	20.58 µL
R5N	1.33 µL	2.65 µL	–	5.31 µL	10.62 µL
R9N	2.55 µL	5.11 µL	–	10.21 µL	20.42 µL

ethanol and methanol (2:1). After the last washing step, the sample was redispersed in n-decane and diluted to a gold concentration of $2.5\,\mathrm{mg/mL}$.

Synthesis of thionane (R9S)

Thionane was synthesized following the protocol of Sinqh et al. [204] $1.35\,\mathrm{mL}$ of 1,8-dibromoctane (Sigma Aldrich, $98\,\%$) were dissolved in $36\,\mathrm{mL}$ of absolute ethanol. While stirring, $3.53\,\mathrm{mg}$ of sodium sulfide nonahydrate (ABCR, $98\,\%$) were added, and the reaction mixture was stirred over night at room temperature. The remaining solid was removed from the product by filtration, the solvent of the supernatant was removed in the rotary evaporator, and the residue washed with $150-200\,\mathrm{mL}$ of n-hexane. The solution was evaporated, and a waxy solid formed at room temperature. Nuclear magnetic resonance spectroscopy and elemental analysis (CHNS) indicates a purity of more than $95\,\%$ (NMR-spectra and CHNS-data can be found in the SI).

Additives

Pure, liquid additives were mixed into AuNP dispersions in n-decane with a gold concentration of $2.5\,\mathrm{mg/mL}$ at at $30\,^{\circ}\mathrm{C}$ to $40\,^{\circ}\mathrm{C}$, the mixtures where shaken for $1-2\,\mathrm{min}$, and stored for $24\,\mathrm{h}$ before any measurement. We used tetrahydrothiophene R5S (Sigma Aldrich, GC, $99\,\%$), thionane R9S (cf. synthesis above), pyrrolidine R5N (Sigma Aldrich, GC, $99\,\%$), and azonane R9N (TCI, $98\,\%$). The final sample contents are given in Table 3.1.1.

Small-Angle X-ray Scattering

A laboratory-scale Xeuss 2.0 instrument (Xenocs SA, France) was used for all SAXS measurements. The X-ray beam was produced by a copper K_α source (wavelength $1.54\,\text{Å}$) and focused on the sample with a spot size of $0.25\,\mathrm{mm}^2$. The measurements were performed with a sample-detector distance (SDD) of $1020\,\mathrm{mm}$. The measurable momentum transfer q ranges from $0.01\,\text{Å}^{-1}$ to $0.6\,\text{Å}^{-1}$, with q being defined as $q = 4\pi\sin(\theta/2)/\lambda$ and θ the scattering angle. The samples were measured in borosilicate capillaries with a diameter of $1.5\,\mathrm{mm}$. Temperature-dependent measurements were performed on a Peltier-controlled heating stage. All samples

were cooled from 36 °C to −20 °C in steps of 2 °C, with a waiting time 20 min after each step that was followed by the acquisition of a scattering image with an integration time of 10 min. The data were analyzed as described in the SI (equations 7.1.1-7.1.5).

Transmission Electron Microscopy

AuNPs were imaged using a JEOL JEM2100 LaB6 electron microscope (JEOL ltd. Tokyo, Japan) with 200 kV acceleration voltage, 0.14 nm line resolution, and a Gatan Orius SC1000 camera (Gatan Inc. Pleasanton, CA, USA) in brightfield mode was used. Suitable samples were prepared by drop-casting of 10 µg to 20 µg of the particle dispersion in n-decane (2.5 mg/mL) on a TEM copper grid.

Thermogravimetric Analysis

Samples were prepared for thermogravimetric analysis by drop-casting the AuNP dispersion into Al_2O_3 crucibles. We analyzed AuNP@HDT and AuNP@HDT dispersion with a R5S concentration of 64 mM.

The dispersions without additive were transferred to n-pentane after the second washing step after the ligand exchange. The dispersions with additive were washed one day after the addition of the additive and transferred to n-pentane. Washing was necessary to remove the physisorbed and free additive molecules from the dispersion. The samples that were measured contained only chemisorbed R5S. The particles were redispersed in 1.5 −2mL of pentane (gold concentration of 20 mg/mL to 30 mg/mL). The dispersion were transferred to the crucibles. The solvent n-pentane was evaporated at room temperature. After the evaporation at room temperature the samples were dried in a vacuum oven (p = 10 mbar) overnight.

The crucibles were mounted in a NETRSCH STA 449F3 setup and heated to 1000 °C in 90 min in an argon atmosphere. In a second heating interval, the temperature of the sample was kept constant at 1000 °C for 10 min in pure oxygen.

Simulation details

We modeled the nanoparticles as 4 nm Au cores coated with hexadecanthiol ligands (–S($C_{16}H_{34}$)) and surrounded by decane solvent. In addition, we introduced two types of sulfur-containing additives, tetrahydrothiophene (R5S) and thionane (R9S), into the system in two ways: by dispersing them in the solution (see Figure 3.1.4a) or by binding them to the particle's surface, either randomly distributed or clustered (see Figure 7.1.12). As in previous work, the Au core was treated as a virtual sphere, with the ligands bound irreversibly to this at fixed points distributed across the surface [58]. We assumed a ligand shell density of 5.5 ligands nm^{-2}, based on prior measurements for the same core size [58], and employed the RATTLE algorithm to restrict the positions of the sulfur atoms on a spherical shell with a radius 0.25 nm larger than the Au core. The sulfur atoms were allowed to optimize their positions on this shell while experiencing a repulsive Coulombic interaction with other sulfur atoms, before having their positions fixed. As a result, the binding sites were approximately evenly spaced from each other. After this step, the sulfur atoms were treated as part of the particle's rigid core.

Each atom within the ligand, solvent, and additive molecules was modeled explicitly, using parameters from the OPLS all-atom force field [205, 206]. Interactions between atoms were described using Lennard-Jones (LJ) potentials, truncated and shifted at a radius of 1.3 nm. Coulomb interactions between atoms were explicitly computed with a cutoff radius of 1.4 nm, and long-range interactions were determined using the PPPM summation method [207] with a high precision of 10^{-5}. A scaling factor of 0.5 was applied to reduce the short-range 1–4 interactions. We employed the SHAKE algorithm to keep C–H bond lengths within ligand and solvent molecules fixed, making these bonds rigid. To model van der Waals interactions between the virtual gold core and ligand or solvent atoms, we used a 9–3 LJ potential (non-shifted with ϵ/k_B = 88 K and σ = 3.54 Å, truncated at 30 Å).

MD simulations with periodic boundary conditions were conducted for systems containing up to approximately 205,000 atoms using the LAMMPS package [208]. The initial simulation cells were gradually compressed until the solvent density far from the nanoparticles matched the experimental solvent density at the chosen temperature. Following this, we conducted a 100 ps run at constant volume using a time step of 1 fs. Subsequent equilibration runs of at least 10 ns applied the Nose-Hoover thermostat and barostat to control pressure (at 80 atm) and temperature. While the use of a pressure greater than 1 atm is not necessary to obtain reasonable decane densities with the OPLS-AA force field, in practice we found that the solvent densities were close to experimental values at 80 atm and that the elevated pressure had little effect on the ligand ordering transition. Finally, production runs lasting from 1 to 5 ns were executed to collect the necessary data. The average bulk solvent densities in these runs closely matched experimental values for pure solvents, deviating by no more than 2%. Further details can be found in the MD section of the SI.

Potential of mean force calculations

We used biased molecular dynamics to calculate the potential of mean force (PMF) between an isolated AuNP and an unbound additive (R5S or R9S) in decane. The system was first equilibrated at fixed temperature with 10 R5S or R9S randomly bound to the particle surface along with hexadecanethiol ligands. Then, one of the additives was unbound from the surface and harmonic constraints applied to the sulfur atom of the unbound R5S and its previous binding point on the Au surface, using spring constants of 5 kcal $mol^{-1}Å^{-1}$ (for the binding position on the core) and 0.5 kcal $mol^{-1}Å^{-1}$ (for the sulfur of the unbound additive). This caused the unbound additive to be biased toward a particular distance from its previous binding point. The unbound additive was then moved away from the particle surface in 1 Å increments by moving the position of the harmonic constraint (see Figure 7.1.15). At each constraint distance, the system was equilibrated for 100 ps, followed by a 200 ps production run during which the distance between the sulfur of the unbound additive and the original binding point was monitored. The PMF was then determined using the weighted histogram analysis method (WHAM) [209] to remove the bias and derive an unbiased free energy profile.

3.1.6 Acknowledgment

T.V.K. thanks the DFG for financial support (Geschäftszeichen: KR 3729/18-1). R.H. and A.W. were supported by the ARC Centre of Excellence in Exciton Science (CE170100026). This research was supported by the Australian Government's National Collaborative Research Infrastructure Strategy (NCRIS), with access to computational resources provided by NCI and Pawsey through the National Computational Merit Allocation Scheme and the NCI Flagship program. This research was supported in part by grant NSF PHY-1748958 to the Kavli Institute for Theoretical Physics (KITP).

3.2 Publication 2: Maintaining Shell Disorder with Kinked or Branched Ligands Stabilizes Apolar Nanoparticles

Knapp, T. V.; Dodange, S.; Monego, D.; Briones, C. M.; Hero, D., Niebuur, B.-J.; Gallei, M.; Kraus, T.; Widmer-Cooper, A. Maintaining Shell Disorder with Kinked or Branched Ligands Stabilizes Apolar Nanoparticles. *ACS Nano*, vol. 19, no. 39, pp. 35127–35140, 2025. https://doi.org/10.1021/acsnano.5c12697

Reprinted with permission from [210]. Copyright © 2025 American Chemical Society.

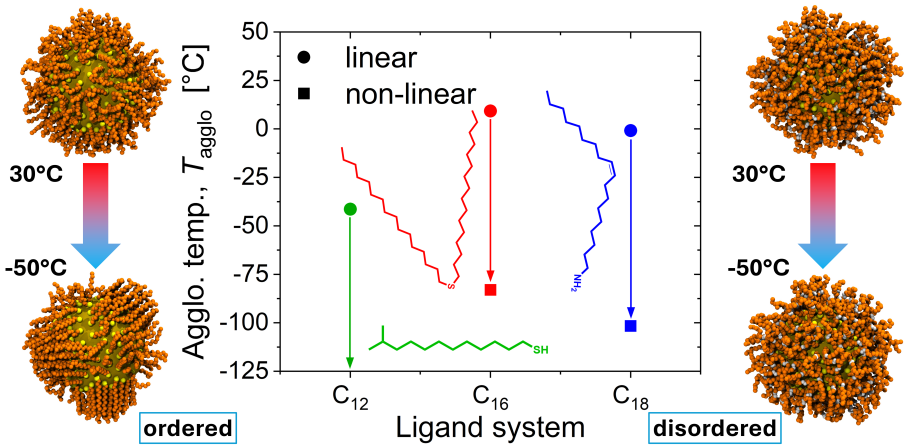


Figure 3.2.1: Table of contents figure of Publication 2. Reprinted with permission from [210]. Copyright © 2025 American Chemical Society.

3.2.1 Abstract

Understanding how nanoparticles form stable colloids is fundamental to their practical applications. Nonlinear ligands are known to increase the stability of nanoparticles in apolar solvents compared to shells of linear alkyl chains. Here, we reveal the molecular origin of this colloidal stability. We observe that even a single methyl side chain can suppress disorder-order transitions in the ligand shell, with double bonds or branches leading to drastic decreases in agglomeration temperature in such dispersions. Through a combination of temperature-dependent X-ray scattering and molecular dynamics simulations, we show that these simple structural modifications prevent ligand molecules from forming ordered bundles, maintaining shell disorder even at temperatures approaching solvent freezing. The absence of ligand order enhances colloidal stability by weakening attraction between the ligand shells via a combination of energetic and entropic factors. This mechanism extends dispersion stability by more than 100 K compared to linear ligands of equivalent length. Our findings provide a molecular-level explanation for the enhanced stability previously observed with branched and unsaturated ligands, offering an effective strategy for engineering nanoparticle dispersions that remain stable across broad temperature ranges.

3.2.2 Introduction

The development of stable colloidal nanoparticle dispersions has traditionally relied on various stabilization mechanisms, with electrostatic or steric repulsion through surface-bound ligands being key approaches [49, 211]. In apolar solvents, where electrostatic stabilization is negligible, steric repulsion has been commonly enhanced by increasing ligand length [125]. However, this approach can have unexpected consequences. Upon cooling, or a change in solvent environment, linear ligands can undergo an ordering transition, where they align and pack together in ways that actually promote rather than prevent agglomeration [102]. This temperature-dependent behavior has been observed across different systems, from CdSe nanoparticles with amine ligands [212] to gold nanoparticles with alkanethiol shells [43, 58], fundamentally challenging our understanding of colloidal stability. The ordered ligand state enhances van der Waals attraction between particles and reduces steric stabilization, leading to aggregation even under conditions where classical theories would predict stability.

Understanding these ligand-mediated interactions is crucial for applications in optoelectronics, catalysis, and biomedicine [213–215], where the unique size-dependent properties derived from quantum confinement must be preserved through precise surface functionalization [171, 172]. Beyond their stabilizing role, ligands guide nanoparticle growth, modify surface energy, and control interparticle interactions in dispersions [37, 170]. The complexity of these ligand-dependent phenomena underscores the need for a deeper understanding of shell organization principles to enable rational design of stable colloidal systems.

Various approaches have demonstrated success in enhancing colloidal stability. This includes modification of the solvent environment [59, 109], the use of molecular additives [113], and changes to ligand composition and structure. For example, branched and mixed ligands have been shown to enhance stability at higher particle concentrations [124, 133], with the argument made that this is related to their effect on the ligand shell structure and thermodynamics. While detailed observations of ligand shell packing have been reported [216], and correlations between shell crystallinity and solvent-ligand interactions have been proposed [57], the mechanistic relationship between shell organization and colloidal stability remains to be fully elucidated.

In particular, we lack a detailed understanding of how the ligand backbone structure, regardless of length, affects shell ordering and subsequent colloidal stability. While some correlations between ligand structure and stability have been established [124], the underlying thermodynamic mechanisms remain elusive, particularly regarding how structural features promote or inhibit shell ordering and how this affects the interaction between the particles [126]. Features such as kinks, branches, and conformational constraints may influence these interactions through related mechanisms, highlighting the need for systematic investigation of structure-stability relationships.

In this study, we address this knowledge gap by examining how ligand backbone structure influences shell ordering and colloidal stability for apolar nanoparticles. By comparing linear, kinked, and branched ligands of similar lengths, we isolate the effects of backbone structure from those of ligand length. Through a combination of temperature-dependent small-angle X-ray scattering (SAXS) and molecular dynamics (MD) simulations, we establish clear relationships between ligand structure, shell ordering, and particle-particle interactions. Our findings reveal how ligand backbone structure can be used to maintain shell disorder and achieve robust colloidal stability across diverse environments.

3.2.3 Results and Discussion

We experimentally compared the colloidal stability of gold nanoparticles (AuNP) with core diameters of $3.9-4.4\,\mathrm{nm}$ and $8.0-8.8\,\mathrm{nm}$ and ligand shells composed of three linear and three nonlinear ligands in *n*-hexane. All dispersions contained particles at concentrations of $2.5\,\mathrm{mg/mL}$. Temperature-dependent small-angle X-ray scattering (SAXS) was used to quantify particle agglomeration upon cooling until either all particles had agglomerated or the solvent froze. Solvent freezing was detected using concurrent wide-angle X-ray scattering (WAXS). Pure *n*-hexane in SAXS capillaries froze between $-105\,^{\circ}\mathrm{C}$ and $-110\,^{\circ}\mathrm{C}$ due to supercooling.

The linear alkylthiols serve as reference systems for the branched and kinked ligands. Linear alkyl shells of 1-hexadecanethiol on AuNP with diameters between $4\,\mathrm{nm}$ and $10\,\mathrm{nm}$ have been studied previously. Such shells undergo a disorder-order transition that drives the

agglomeration of "shell-dominated" particles that have cores with diameters below $8-9$ nm [58]. For example, 4 nm core AuNP with 1-hexadecanethiol shells agglomerates at $8\,^{\circ}$C in hexane [59]. We denote them as "AuNP@SC_n" in the following, where n is the number of carbon atoms in the chain.

Oleylamine as a "kinked" ligand

Oleylamine (OAm, (Z)-octadec-9-en-1-amine) is commonly used as ligand [217] in the synthesis of spherical gold [32] and silver [218] nanoparticles and gold nanowires [219]. We compared the stabilizing effect of this kinked ligand with 18 carbon atoms and a double bond at position C_9 with its saturated analog, octadecylamine.

Figure 3.2.2a shows the temperature-dependent SAXS patterns of AuNPs with 3.9 nm diameter cores coated with octadecylamine (AuNP@NC_{18}). Scattering at $50\,^{\circ}$C was dominated by an intensity plateau at q <$0.05\,$Å^{-1} and decreased in intensities above, followed by an intensity maximum at $q = 0.2\,$Å^{-1} to $0.3\,$Å^{-1} from the form factor of spherical particles [200]. The plateau indicates the lack of particle-particle correlations in a fully dispersed sample.

Cooling the AuNP@NC_{18} dispersion to $-30\,^{\circ}$C led to the emergence of a peak at $q_0 \approx 0.1\,$Å^{-1}. This structure factor peak indicates spatial correlation of AuNPs that is caused by agglomeration. We used it to quantify the temperature-dependent stability of the dispersion following a previously published approach [43, 58]: A model-based analysis of the temperature-dependent scattering (see Supporting Information for details) yielded the fraction of AuNPs within agglomerates, χ_{agglo}.

χ_{agglo} increased non-linearly when cooling below $T < 40\,^{\circ}$C, following a sigmoidal trend (Figure 3.2.2c, black circles). We fitted it using eq. 7.2.10 in the Supporting Information. Following literature [58], we defined the agglomeration temperature, T_{agglo}, as the temperature at which the sigmoidal fit reached $\chi_{\text{agglo}} = 0.2$ and found $T_{\text{agglo}} = -0.85\,^{\circ}$C.

Previous stabilization studies with this method focused on thiol ligands [43]. Here, we find that the binding group has a moderate effect on colloidal stability: The agglomeration temperature of AuNP@NC_{18} was approximately $30\,$K below that of AuNP@SC_{18} (see detailed data below and in Figure 7.2.7 in the Supporting Information) and approximately $20\,$K below that of 6 nm CdSeNP with linear SC_{18} [43]. This moderate increase of stabilization through the more weakly bonded amines is likely an effect of reduced shell density and greater lability, as we discuss in more detail in the section below on Ligand shell densities.

The stabilizing effect of unsaturated "kinked" ligands was considerably larger. Figure 3.2.2b shows the temperature-dependent X-ray scattering of OAm-coated 4.4 nm diameter gold cores ("AuNP@OAm" (Figure 3.2.2b). The scattering at $40\,^{\circ}$C was almost identical to that of AuNP@NC_{18}, but it remained unchanged down to $-90\,^{\circ}$C, in stark contrast to the linear AuNP@NC_{18}. The agglomeration temperature of AuNP@OAm was $-101.6\,^{\circ}$C. A single

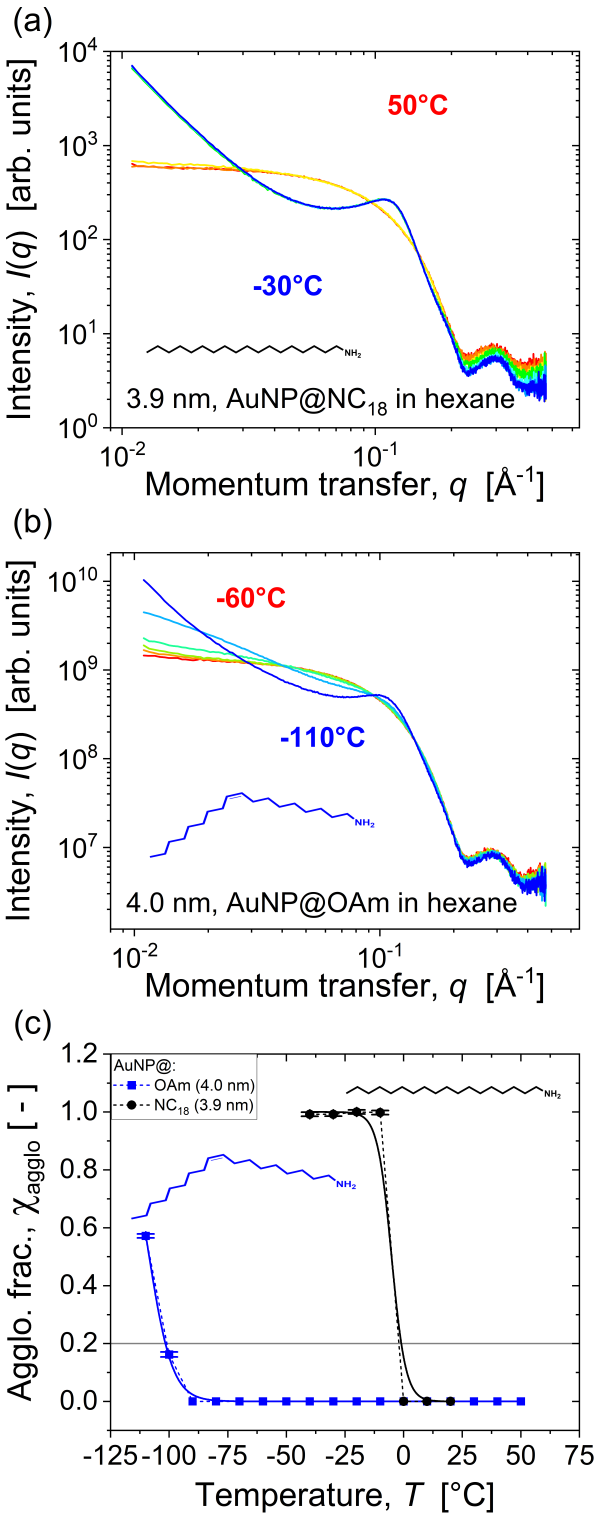


Figure 3.2.2: Temperature-dependent stability of AuNP with $\approx 4\,\mathrm{nm}$ diameter cores with octadecylamine and oleylamine shells as quantified by SAXS. Scattering patterns were recorded while cooling dispersions in n-hexane from $50\,^{\circ}\mathrm{C}$ to $-30\,^{\circ}\mathrm{C}$ in steps of $10\,^{\circ}\mathrm{C}$ for particles coated with (a) linear octadecylamine, and from $50\,^{\circ}\mathrm{C}$ to $-110\,^{\circ}\mathrm{C}$ in steps of $10\,^{\circ}\mathrm{C}$ for particles coated with (b) kinked oleylamine ligands with the same number of carbon atoms per ligand. (c) Fraction of AuNPs within agglomerates, χ_{agglo}, in dependence on temperature as determined using model fits according to equation 7.2.10 in the Supporting Information.

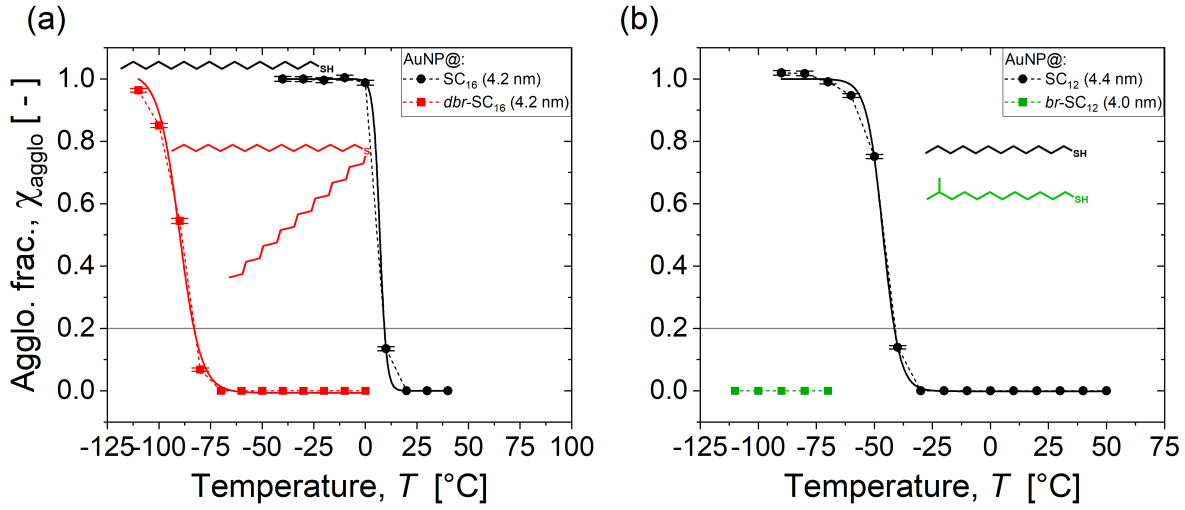


Figure 3.2.3: Temperature-dependent agglomerate fractions of AuNP with ligand shells composed of (b) linear SC_{16} and double-armed *dbr*-SC_{16} ligands with 16 carbon atoms in the chains (core diameter of both systems 4.2 nm), (b) linear SC_{12} (core diameter of 4.4 nm) and branched *br*-SC_{12}(core diameter of 4.0 nm) with 12 carbon atoms in the main chains. Solid lines represent sigmoidal fits to eq. 7.2.10 in the Supporting Information.

double bond thus increased the temperature-dependent stability of the dispersion drastically by more than 100 K.

Branched ligands

We now consider branched ligands of similar length. As a minimal case, we synthesized 11-methyldodecanethiol (cf. Experimental Section) with a methyl side group at the second to last position of the main dodecyl chain. At the other extreme, we considered the "double-armed" dihexadecylsulfide with two hexadecyl chains connected to the sulfur atom.

Figure 3.2.3 shows the temperature-dependent agglomeration fraction of AuNPs with 4.4 nm diameter cores and ligand shells of 11-methyldodecanthiol (AuNP@*br*-SC_{12}) and dihexadecylsulfide (AuNP@*dbr*-SC_{16}). The same data for linear alkylthiols of the same lengths (AuNP@SC_{12} and AuNP@SC_{16}) are shown as references.

Branched ligands consistently reduced T_{agglo} by at least 70 °C. For example, χ_{agglo} remained at zero down to −70 °C for AuNP@*dbr*-SC_{16} and did not exceed 0.96 before the solvent froze (at temperatures below −110 °C), while AuNP@SC_{16} had fully agglomerated already at 0 °C. We found T_{agglo} of −83 °C and 9.2 °C for AuNP@*dbr*-SC_{16} and AuNP@SC_{16}, respectively. Remarkably, the minimally branched AuNP@*br*-SC_{12} did not agglomerate at all before the solvent froze, while its linear counterpart AuNP@SC_{12} had an agglomeration temperature of $T_{agglo} = -41.3$ °C.

Ligand shell densities

Differences in ligand structure lead to ligand shells with different densities. The ligand shell density is known to affect the colloidal stability of nanoparticles. Simulations predicted a reduction of the ordering temperature of octadecanethiol ligands on CdSe nanorods by $50\,\mathrm{K}$ when the ligand density was decreased by $25\,\%$ [105]. If the ligand density becomes too low, the repulsive interactions of the shell can no longer compensate for the attractive interactions of the cores, resulting in agglomeration [85, 86]. Yamashita et al. compared the surface coverages of linear and nonlinear organophosphonic acids on $4\,\mathrm{nm}$ ZrO_2 and $5\,\mathrm{nm}$ TiO_2nanoparticles. Nonlinear 1-octyldecyl phosphonic acid and 1-butyltetradecyl phosphonic acid had only $65-70\,\%$ of the surface density of linear analogs. It was shown that the reduction in coverage in the case of linear ligands leads to a deterioration in colloidal stability. In contrast, a change in surface coverage is significantly better compensated by non-linear ligands.

We performed thermogravimetric analysis (TGA) to determine the ligand shell densities and analyze whether they are responsible for the observed differences in colloidal stability. The results are summarized in Figure 3.2.4a and Table 3.2.2 (cf. Figure 7.2.14 in the Supporting Information). The ligand density of AuNP@OAm was $4.6\,\mathrm{nm^{-2}}$, similar to that of AuNP@NC_{18} ($5.0\,\mathrm{nm^{-2}}$). The density of the corresponding alkylthiol SC_{18} was $30\,\%$ higher ($6.7\,\mathrm{nm^{-2}}$). The branched ligand AuNP@*br*-SC_{12} had a density $5.1\,\mathrm{nm^{-2}}$. This value corresponds to $91\,\%$ of the linear reference AuNP@SC_{12} ($5.6\,\mathrm{nm^{-2}}$). Given the two-armed structure of dihexadecylsulfide, it is more useful to compare the density of its alkyl chains on the surface; this density was $5.2\,\mathrm{nm^{-2}}$, $83\,\%$ of AuNP@SC_{16} ($6.3\,\mathrm{nm^{-2}}$). The difference in shell density can be explained by the molecular structure, but also by the binding energy. The binding energy of thiols is generally higher (by a factor of 1.5 to 2) than that of sulfides [89, 220]. Unfortunately, there are hardly any binding energies in the literature that compare the adsorption of alkyl thiols and alkyl sulfides with the same chain length. However, the difference is significantly smaller than that between a thiol and an amine.

The alkylthiol SC_{18} agglomerated at $T_{\mathrm{agglo}} = 30.6\,^{\circ}\mathrm{C}$, $30\,\mathrm{K}$ above the corresponding amine NC_{18}. This difference is likely due to the higher ligand density of the thiol ($6.7\,\mathrm{nm^{-2}}$ versus $5.0\,\mathrm{nm^{-2}}$ for the amine) that results from the lower binding energy of the amine [201]. Reduced densities change the energy/entropy balance of the ligand shell, thus reducing the transition temperature where the ligands form ordered bundles and increasing colloidal stability [43, 58, 105, 221].

We investigated the shell structure by determining temperature-dependent, average, nearest-neighbor surface-to-surface distances s between particles from SAXS measurements. The structure factor of AuNPs within agglomerates was determined using a model-based fit. The interparticle distance was extracted and the average particle diameter subtracted to obtain s (see the SAXS section in the Supporting Information for details of this analysis). We note that this approach differs from that used in previous work [43, 58], in which s was estimated using a sim-

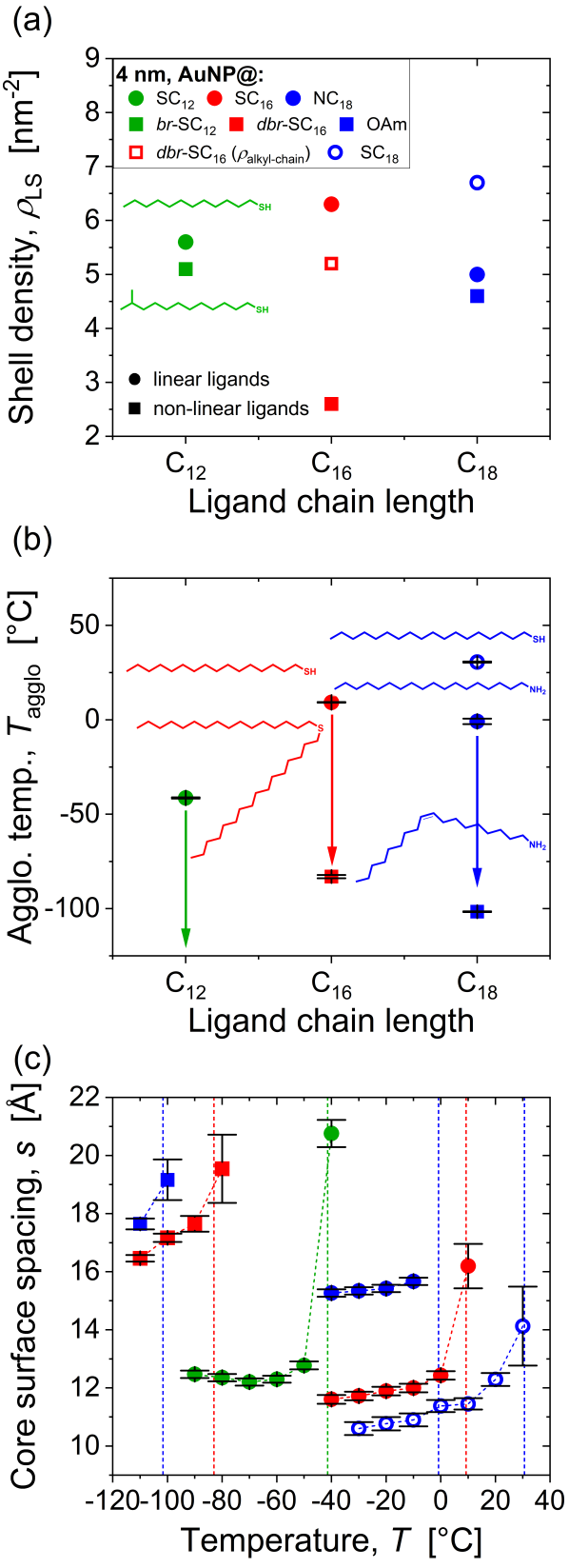


Figure 3.2.4: Structure and stability of AuNPs with core diameters of approximately 4 nm and different ligand shells. (a) Shell densities ρ_{LS} of linear and non-linear ligands. (b) Agglomeration temperatures T_{agglo}, where 20 % of the particles were part of agglomerates. (c) Core-surface spacings s of particles in agglomerates. Spacings were calculated as $s = 2 \cdot (r_{\mathrm{HS}} - r_{\mathrm{core}})$ with r_{HS} from SAXS (cf. SI).

plified analysis and only at a temperature close to T_{agglo}. The structural model used here is more established and believed to be more accurate; cf. the SAXS section in the Supporting Information for a detailed comparison between both methods. The absolute difference in the spacing values determined using the two analysis methods was 0.6 nm to 1 nm, and the new method consistently yielded smaller spacings. The temperature-dependent evaluation of s that we present here also provides a more nuanced picture of the shell structure during AuNP agglomeration.

Figure 3.2.4c shows that the linear ligands consistently resulted in smaller spacing than the respective (or any) nonlinear ligand shell. The determined values of s of all ligand systems were smaller even than the lengths of the respective linear ligand when assuming a stretched all-trans conformation and considering C-C bond length and C-C-C bond angle (17.1 Å for SC_{12}, 22.8 Å for SC_{16} and 25.4 Å for NC_{18}) [222, 223]. It is known that linear ligands can form bundles on small NPs that can interlock and reduce s [43, 221]. Apparently, this mechanism is not active in nonlinear ligand shells, even in cases where their density is lower.

The increased spacing may contribute to the increased stability of such particles, but a difference in density of less than $10\,\%$ cannot explain why the *br*-SC_{12} does not agglomerate before the solvent freezes [105]. The high colloidal stability must therefore be the result of another shell property of the nonlinear ligands. At the same time, it is unclear why the spacings between kinked and branched ligand shells are much larger than for linear ones. In the following, we use Molecular Dynamics (MD) simulations to better understand the structural and thermodynamic origins of the enhanced colloidal stability and larger spacing observed for kinked and branched ligands.

Temperature dependence of ligand shell structure

To separate the effect of ligand structure from shell density, we used a constant ligand density of $4.5\,\text{nm}^{-2}$ in most of our simulations. This is similar to our experimental measurements for both kinked ($4.6\,\text{nm}^{-2}$) and branched ($5.1\,\text{nm}^{-2}$) ligands on 4 nm cores. While Yang et al. reported lower ligand densities ($2\,\text{nm}^{-2}$ to $3\,\text{nm}^{-2}$) for branched thiols on CdSe nanocrystals [124], our chosen density allows a more direct comparison between simulation and experimental results for the systems studied here. To examine density-dependent effects, some additional simulations at lower surface coverage ($3\,\text{nm}^{-2}$) were performed for branched ligands.

We first examined the temperature-dependent behavior of various ligands on a 3.8 nm Au nanoparticle by quantifying their average dihedral angles in hexane (Figure 3.2.5). To separate the effect of ligand structure from ligand length, we limited the length of the longest ligand chain to 11 or 16 carbon atoms, but otherwise considered all structural variations present in the experimental ligands, including a kink in the middle of the chain, as well as branches at the binding group and near the end of the chain (structures at left). We found that the linear ligands (undecane and hexadecanethiol) exhibited a nonlinear transition to higher dihedral angles at reduced

temperatures, consistent with the formation of ordered ligand bundles as described in previous studies of linear alkanethiol-coated nanoparticles [58]. Ligands in such ordered shells are on average more extended with a larger proportion of trans dihedral angles and undergo fewer conformational changes than mobile disordered ligands, which results in a higher average dihedral angle in their tails (diagram at bottom right). In contrast, both kinked (cis-8-hexadecenethiol) and branched (6-pentylundecanethiol, 10-methylundecanethiol, and dihexadecylsulfide) ligands maintained lower dihedral angles throughout the temperature range, suggesting persistent disorder even at low temperatures. These differences in the behavior of shells composed of linear and nonlinear ligands can be clearly seen by comparing snapshots at high and low temperatures (top right of Figure 3.2.5), which show that the structure of the nonlinear shells hardly changes. This insensitivity of the shell structure to cooling aligns with our experimental observations where OAm-coated particles remained stable down to $-101.6\,^{\circ}\mathrm{C}$ and branched ligand systems showed no agglomeration before solvent freezing.

Importantly, this disordered state proved to be a robust feature of nonlinear ligands, persisting across variations in molecular features, including different ligand lengths, branch points, and branch lengths (Figure 7.2.15(b), Supporting Information). To isolate this intrinsic structural effect from solvent-ligand interactions, we performed additional simulations in the absence of solvent (Figure 7.2.15(a), Supporting Information). Even at these conditions and at temperatures as low as $-90\,^{\circ}\mathrm{C}$, almost all branched and kinked ligands remained disordered, in stark contrast with their linear counterparts. This persistence of disorder even when no ligand-solvent interactions are present indicates that there is simply no stable ordered state for most nonlinear ligands on small nanoparticles. Only dihexadecylsulfide was able to partially order in solution, forming small bundles composed of a single chain from each ligand (Figure 7.2.21), while 10-methylundecanethiol was the only additional ligand to order in vacuum (Figure 7.2.16).

Particle stabilization by disordered shells

Calculation of the potential of mean force (PMF) between pairs of nanoparticles in hexane (see Methods) showed that this prevention of ligand ordering has profound effects on interparticle interactions. Particles coated in linear hexadecanethiol ligands are already strongly attractive at $-23\,^{\circ}\mathrm{C}$ (Figure 3.2.6a) due to strong attraction between the ordered ligand bundles (red inverted triangles). Interdigitation of ordered bundles also allows the cores to get close together, consistent with the small core-surface spacings observed experimentally. In sharp contrast, particles coated in both kinked and branched ligands are still strongly repulsive at $-53\,^{\circ}\mathrm{C}$ (Figures 3.2.6b and c), with the disordered ligand shells preventing the cores from moving as close together. Even at $-93\,^{\circ}\mathrm{C}$, the interaction between kinked ligand shells remains repulsive (Figure 3.2.6d), consistent with our experimental findings for OAm-coated particles. The main reason for the repulsive total interaction between nonlinear ligand shells (green circles) is that the ligand-ligand

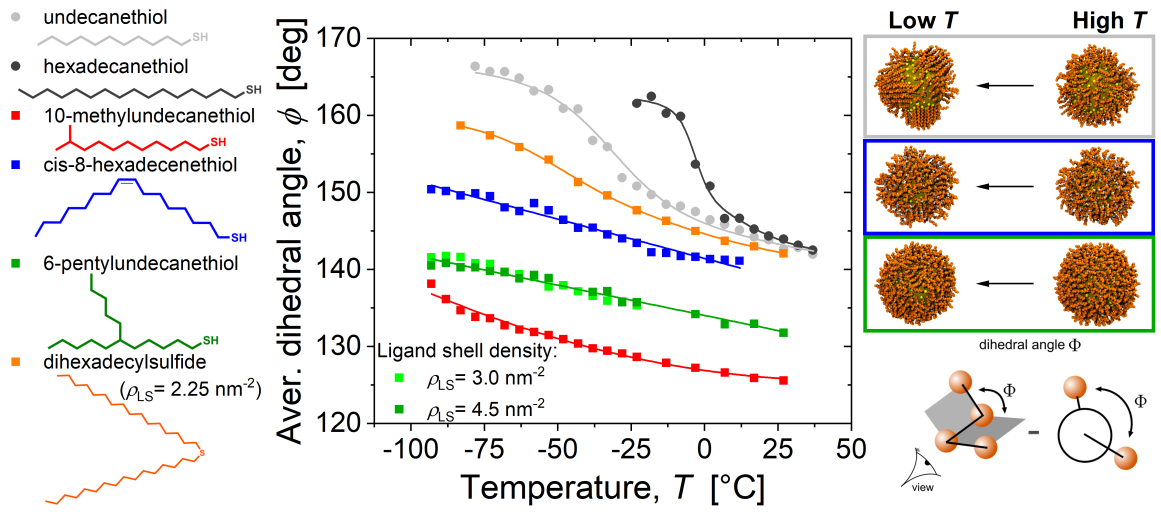


Figure 3.2.5: Average dihedral angle between CH_x groups for various ligands on 3.8 nm Au particles in hexane. This reveals an ordering transition upon cooling for linear ligands and the absence of one for nonlinear ligands. For comparison, simulation snapshots for some of the ligands are shown at temperatures that are high (23 °C for undecanethiol and 6-pentylundecanthiol, 7 °C for cis-8-hexadecenethiol) and low (−53 °C for all three ligands) with respect to the ligand ordering transition for undecanethiol. To clearly illustrate the trends in the values, curves for linear ligands were fit to a two-step sigmoid function, while curves for other ligands were fit to linear and polynomial functions.

component (red inverted triangles) remains only weakly attractive, even at low temperature. And this, in turn, is due to the inability of the nonlinear ligands to access a densely packed ordered state.

We note that this conclusion differs from the argument made in a recent review [57], that the colloidal stability is due to stronger ligand-solvent interactions when ligands pack less efficiently. Calculation of the ligand-solvent interaction energies as a function of temperature for isolated particles (see Figure 7.2.17, Supporting Information), shows that there is indeed a decrease when the linear ligands order in hexane, but the absolute values of the ligand-solvent interaction energies are larger in some cases for linear ligands even when those particles are not colloidally stable. We also note that in hexadecane, the ligand-solvent interaction energy continues to increase in magnitude upon ordering of hexadecanethiol ligands, which has the opposite effect of destabilizing the particles [59]. So the magnitude of the ligand-solvent interaction does not appear to be the most important distinction between the colloidal stability of linear and nonlinear ligands.

The similar repulsive behavior observed in this work for both kinked and branched ligands indicates that preventing ligand ordering enhances colloidal stability regardless of the specific nonlinear ligand structure. These molecular-level findings help explain our experimental observations of remarkable stability of OAm-coated particles and the lack of agglomeration in branched ligand systems before solvent freezing. In the absence of agglomeration driven by

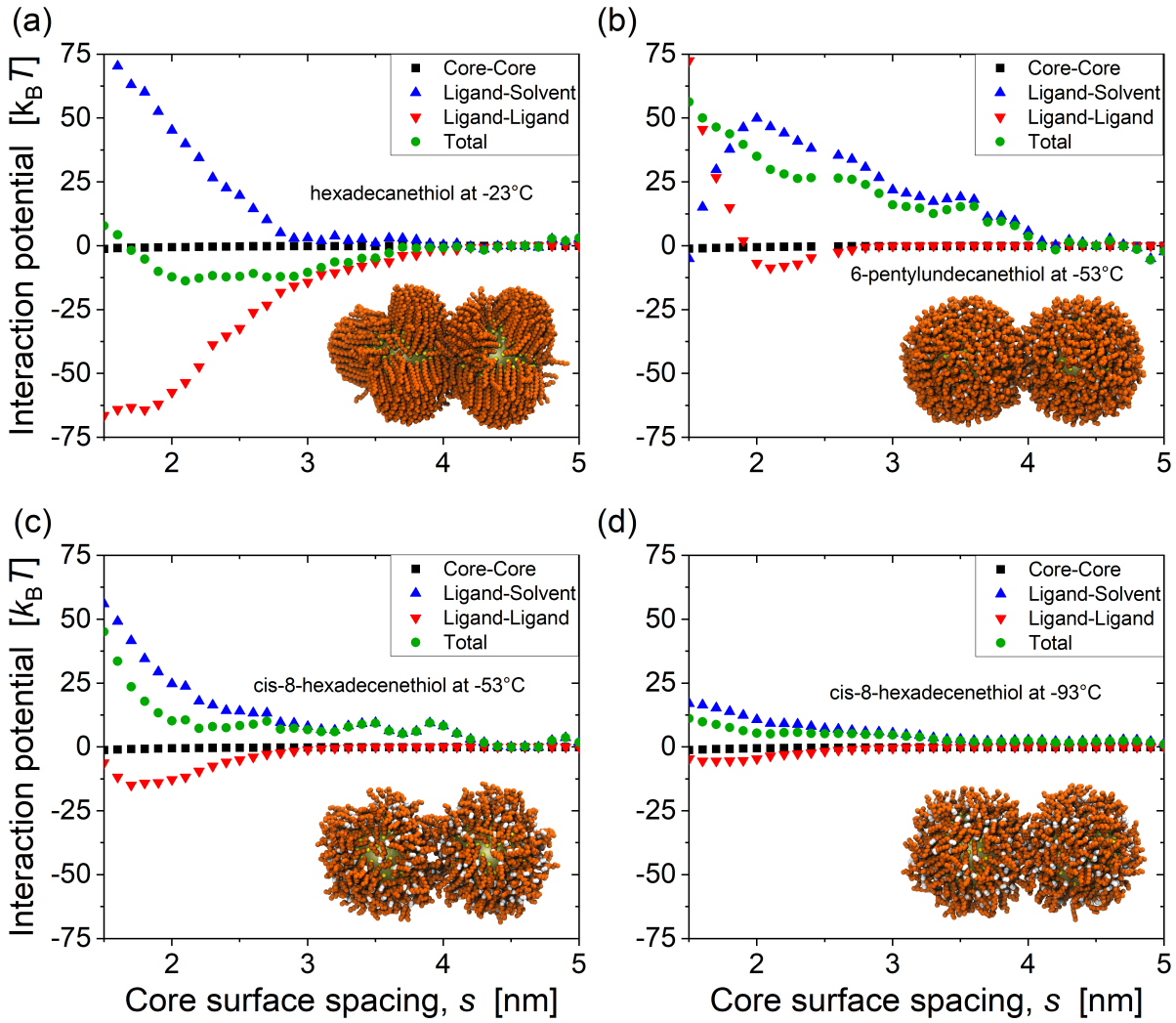


Figure 3.2.6: Potentials of mean force in hexane between 3.8nm Au NPs coated with (a) hexadecanethiol at $-23\,^{\circ}$C, (b) 6-pentylundecanethiol at $-53\,^{\circ}$C, and cis-8-hexadecenethiol at (c) $-53\,^{\circ}$C, and (d) $-93\,^{\circ}$C. Results are shown separately for the total potential (green circles) and its ligand-solvent (blue triangles), ligand-ligand (red inverted triangles) and core-core (black squares) components. The inserts show simulation snapshots at a core surface spacing of 1.9 nm, with the solvent hidden for clarity.

ligand ordering, the particles remain colloidally stable until the remaining sources of attraction between them, i.e., the core-core vdW attraction and the ligand-solvent interfacial energy, become sufficiently large relative to the entropy of mixing to drive the particles together. The start of this change can be seen by comparing Figures 3.2.6c and d where the repulsive contribution due to ligand-solvent forces becomes weaker upon cooling.

Conformational entropy and dynamics of the ligand shell

We further analyzed how ligand structure affects the thermodynamics and dynamics of the ligand shell, as several papers have argued that branched ligands enhance colloidal stability due to

entropic effects. For example, Yang et al. proposed that branched ligands enhance stability by maximizing the intramolecular entropy of the ligand shell while reducing the thermodynamic stability of the crystalline state [124]; while Elimelech et al. argued that conformational entropy differences between linear and branched thiol ligands contribute to the stabilizing effect of branched ligands on gold nanoparticles [126].

To do this, we considered isolated particles in solution and calculated the vdW interaction between the ligands, and their conformational entropies, as a function of temperature. These results are shown in Figure 3.2.7, with conformational entropies quantified using the CENCALC software package [224] (see the Methods section for details). The ligand-ligand interaction energies (shown in panel a) increase only slightly in magnitude upon cooling for most nonlinear ligands, whereas there are dramatic increases for the linear ligands as they order to form tightly packed bundles. The dihexadecylsulfide ligands exhibit intermediate behavior, as they partially order to form small bundles consisting of a single chain from each ligand (Figure 7.2.21). In contrast, the conformational entropies (shown in panel b) exhibit more subtle differences. While the branched ligands have a higher conformational entropy than their linear counterparts, the kinked C16 ligands have an entropy similar to that of linear C16 ligands in their disordered state. This shows that the main distinction between linear and nonlinear ligands lies not in the absolute values of the conformational entropies but rather in their temperature dependence: linear ligands undergo a step-like entropy decrease coinciding with their ordering transition, while most branched and kinked ligands exhibit more gradual linear decreases upon cooling.

Over a sufficiently large temperature range, though, most ligands lose the same amount of conformational entropy relative to the number of dihedral angles. Strikingly, the conformational entropy of the kinked C16 ligand shell at $-93\,^{\circ}\mathrm{C}$ is lower than that of the linear C16 ligand shell at $-23\,^{\circ}\mathrm{C}$, yet the interaction between the former particles is repulsive (Figures 3.2.6d) while the interaction between the latter particles is attractive (Figures 3.2.6a). This shows that shell disorder can maintain colloidal stability (due to weak vdW attraction between poorly packed ligands) even when the conformational entropy of the ligands becomes very small.

Somewhat surprisingly, our results indicate that the molecular structure of the ligands, rather than their surface density, is the dominant factor in determining conformational entropy. For example, 10-methylundecanethiol exhibited notably higher conformational entropy than other ligands at all temperatures. In contrast, 6-pentylundecanethiol showed intermediate entropy values that only increased slightly when the surface coverage was reduced from 4.5 to $3\,\mathrm{ligands/nm^2}$. Reducing the size of the side chain at the 6-position, from a pentyl to a methyl group, had a similarly small effect on the conformational entropy (see Figure 3.2.7b), whereas moving that methyl group from the 6- to the 10-position, i.e. from the middle to the end of the chain, had a much larger effect. The reason for this behavior is that the ligand with a branch at the end of the chain retains more conformational flexibility at low temperature compared to the ligand

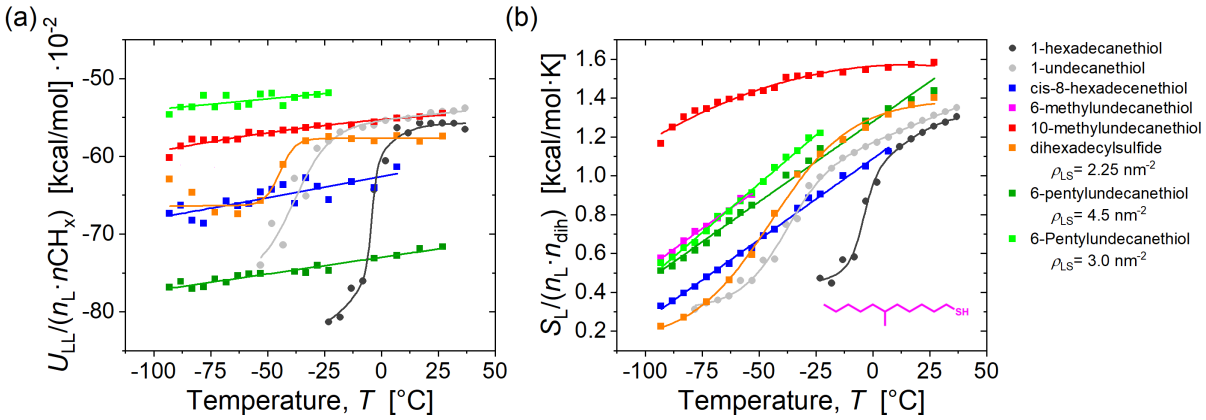


Figure 3.2.7: (a) Ligand-ligand interaction energy, and (b) conformational entropy of ligands on isolated 3.8 nm Au NPs in hexane. The energy values have been normalized by the number of carbon atoms in all ligands $n_L.nCH_x$ while the entropy values have been normalized by both the number of ligands n_L and the number of dihedral angles in each ligand n_{dih}. To clearly distinguish the trends, we fitted the curves for linear ligands to a two-step sigmoid function, whereas the curves for other ligands were fitted to linear or polynomial functions.

with a branch near the middle of the chain, likely due to radial packing effects. This can be seen when comparing probability distributions for the dihedral angles near $-85\,°C$, discretized into trans and gauche states (see Figure 7.2.20). The branch at the end of the chain results in the most uniform distribution and thus the highest conformational entropy, as the conformational entropy is related to the product of the probabilities of the dihedral states along the ligand chains. Geometrically, it would make sense that radial packing effects are responsible, as the high surface curvature of the approximately spherical 4 nm cores will provide more space for ligand motion when the branch is near the end of the chain. Comparison of our results with other recent work [225], however, suggests that the optimal branch position may vary with particle size and shape, or ligand length, although more work is needed to fully understand the effects of ligand structure on colloidal stability.

To further compare the dynamic nature of these ligands, we calculated the mean square displacement of the ligand atoms at several temperatures (Figure 7.2.18). As the ligands are not free to diffuse, this eventually reaches a plateau value characteristic of the conformational freedom of each ligand shell (Figure 3.2.8). These results show that all ligands become less mobile upon cooling, with a slower approach to the plateau, but that differences in ligand structure result in vastly different changes in the plateau value. For linear hexadecanethiol ligands, there is a large decrease in conformational freedom when they bundle together. In contrast, the conformational freedom of 10-methylundecanethiol ligands hardly changes upon cooling from $7\,°C$ to $-93\,°C$, consistent with the very weak temperature dependence of their conformational entropy.

Together, these results explain why even a single methyl group near the end of a linear tail can inhibit the ligand shell from ordering in hexane (as seen in our simulations) and enhance col-

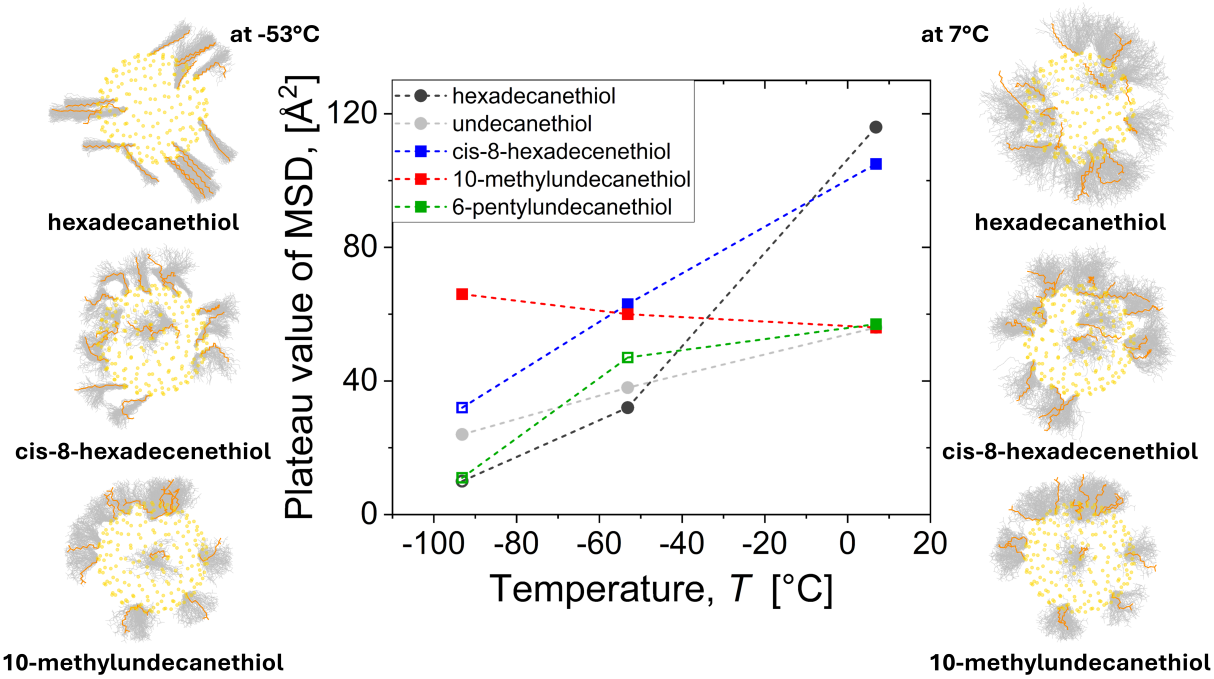


Figure 3.2.8: Conformational freedom of ligands on isolated 3.8 nm Au NPs in hexane as quantified by the plateau value in their mean square displacement versus time. Data points shown as open symbols are lower bounds corresponding to non-plateau values reached after 15 ns. The snapshots show trajectories of ligands with different sensitivities to cooling. Each snapshot is composed of 100 overlaid frames, captured at intervals of 0.025 ns.

loidal stability (as observed experimentally for particles covered with 11-methyldodecanethiol ligands). Interestingly, we find that the 10-methylundecane ligands do order in vacuum at around $-100\,^{\circ}\mathrm{C}$ (see Figure 7.2.16), i.e. they have the ability to pack into a mostly ordered state, but this only becomes thermodynamically favorable at low temperature in the worst possible solvent environment for our particles.

Core size effects

The particles considered so far had gold cores with diameters below $5\,\mathrm{nm}$. The van der Waals attraction between such cores is known to be weak enough that the stability is dominated by ligand ordering for linear octadecanethiol shells [43, 58]. The agglomeration of dodecanethiol-stabilized AuNP with $9.0\,\mathrm{nm}$ cores, on the other hand, is known to be core-dominated and to occur well before the temperature-dependent transition in the ligand shell [43, 58]. Given our hypothesis that the increased stabilization by nonlinear ligands is connected to the inability of such ligands to pack together tightly, it is interesting to compare the shell-dominated cases with $4.4\,\mathrm{nm}$ diameter cores to larger cores, as we do in the following.

Figure 3.2.9 shows agglomeration temperatures and surface spacings of particles with diameters of approximately $8.5\,\mathrm{nm}$. These cores were too large to be stabilized by linear or branched

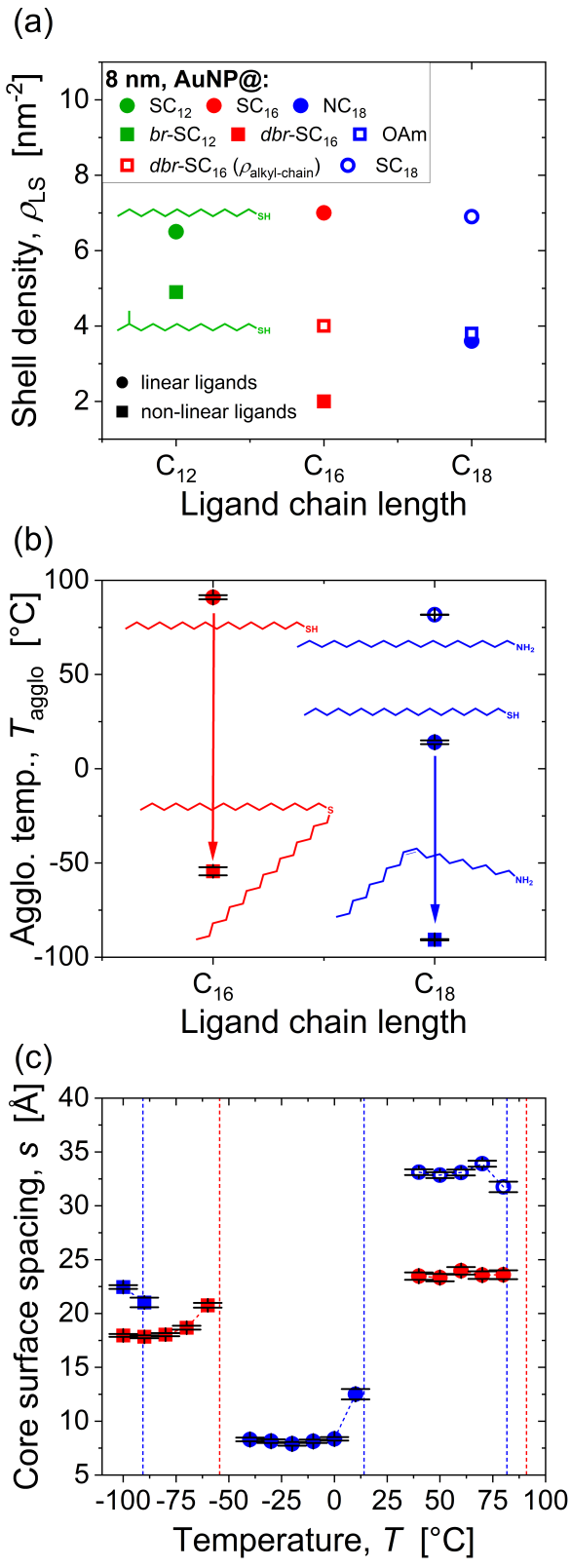


Figure 3.2.9: Structure and stability of AuNPs cores of approx. 8.5 nm diameter coated in different ligand shells. (a) Shell density ρ_{LS} of linear and nonlinear ligands (and chain density of the double-armed *dbr*-SC_{16}). (b) Agglomeration temperatures T_{agglo}, where 20 % of the particles were part of agglomerates. (c) Core-surface spacings s of particles in agglomerates.

ligands with 12 carbon atoms below the solvent boiling temperature, indicating that nonlinear ligands do not substantially enhance colloidal stability in the core-dominated regime, i.e., when the vdW attraction between the cores is sufficiently strong (more than $2k_{\mathrm{B}}T$ at $100\,^{\circ}\mathrm{C}$) to drive agglomeration on its own [43].

However, in the intermediate regime, where the ligands are long enough to limit vdW attraction between the cores to the order of $k_{\mathrm{B}}T$ [43], more complex behavior was observed as shown in Figure 3.2.9. Linear SC_{16} ligands yielded dispersions with $T_{\mathrm{agglo}} = 91\,^{\circ}\mathrm{C}$, 80 K above that of the respective 4.2 nm cores, whereas the longer linear NC_{18} had $T_{\mathrm{agglo}} = 14.0\,^{\circ}\mathrm{C}$, only 15 K above that for 3.9 nm cores. For the nonlinear ligands, similar but weaker effects of core size were observed: the agglomeration temperature of AuNP@*dbr*-SC_{16} increased by 29 K, from $-83\,^{\circ}\mathrm{C}$ for 4.2 nm to $-54.4\,^{\circ}\mathrm{C}$ for 8.5 nm cores, whereas the agglomeration temperature of particles with longer OAm ligands increased by only 10 K, from $-101.7\,^{\circ}\mathrm{C}$ for 4.2 nm to $-90.6\,^{\circ}\mathrm{C}$ for 8.5 nm cores.

The stability enhancement due to nonlinearity was also greater for these larger particles (up to 150 K) than for the smaller ones discussed earlier. This is surprising if one assumes that the destabilizing attraction of the cores is independent of the shell structure. This unexpected behavior appears to be related to changes in surface curvature and ligand coverage. The use of large cores increased the shell density for linear ligands (by up to 16 % for AuNP coated with SC_{12}) but consistently decreased it for nonlinear or amine ligands (by up to 30 % for AuNP coated with *dbr*-SC_{16}), such that the difference in shell density between linear and nonlinear ligands is greater for larger cores. This is likely explained by the "hairy ball effect" [43, 58] that describes the geometrical arrangement of ligands on a highly curved surface. Whereas large gaps will form between linear ligands on highly curved, small cores, nonlinear ligands with a more conical overall shape can fill these gaps, allowing them to pack more densely on small cores than on large ones.

Increasing the core size, therefore, affects the colloidal stability in at least three ways, one largely independent of ligand structure (for a similar ligand length) and two strongly dependent on ligand structure. First, the increased vdW attraction between the larger cores increases T_{agglo} by 10 K to 150 K, depending on the ligand length, with a larger increase for particles coated in shorter ligands. As shown in Figure 3.2.9c, the core spacings are now also more similar for linear and nonlinear ligands of similar length, probably due to the lack of gaps large enough to allow for interlocking of bundles formed by linear ligands. Second, the decreased surface curvature results in more substantial differences in ligand density between shells composed of linear and nonlinear ligands, with the nonlinear shells less dense than on smaller cores. This should enhance the relative stability of particles coated in nonlinear ligands, e.g. due to weaker vdW attraction between less dense ligand shells and greater solvent association with them, as long as the ligand shell is thick enough that the particles are not in the core-dominated regime.

Third, the decrease in curvature increases the temperature at which shells composed of linear ligands order. For spherical cores, the expected increase from 4.2 nm to 8.5 nm is approximately 20 K at constant ligand density [58]. Furthermore, larger gold cores are known to be faceted, with the (100) facets having higher ligand density [226], which should further increase the tendency of ligands to form ordered bundles [105, 227]. Lastly, it has been shown that extended particle contact, which is more likely to occur for the more attractive large cores, can induce ligand ordering at least 10 K above the ordering temperature for an isolated particle [105]. The end result is that nonlinear ligands can enhance the stability of larger cores even more than small ones.

3.2.4 Conclusions

A single double bond or methyl branch in the ligands of apolar nanoparticles drastically increases their temperature-dependent colloidal stability. We used X-ray scattering to show that the resulting difference in agglomeration temperature exceeds 100 K in many cases. The stability of many such colloids is not limited by agglomeration but by freezing of the solvent.

The superior stabilization by nonlinear ligands cannot be explained solely by differences in ligand shell density. Molecular kinks and branches that reduced ligand surface coverage by less than 10% increased stabilization drastically. Instead, their efficacy is due to large changes in the overall shell structure that are caused by small molecular differences.

Ligand shell disorder turns out to be the main prerequisite for stabilization. Molecular Dynamics (MD) simulations show that double bonds and branches stabilize a disordered ligand shell, which keeps the particles stable in solution even at low temperatures. Such nonlinear ligands inhibit the disorder-order transition that leads to the formation of attractive crystalline bundles in shells composed of linear ligands.

Nonlinear ligands also lose mobility upon cooling much more slowly than the corresponding linear ligands, which aids colloidal stability. In terms of conformational entropy, nonlinear ligands exhibit a diverse range of behavior, with some retaining high conformational entropy at low temperature and others not. However, even the less mobile, disordered state that they finally reach stabilizes nanoparticles better than the bundled state of linear ligands. Whereas linear ligands bundle and form areas of high ligand density that exclude solvent and strongly attract each other, nonlinear ligands usually do not form such areas, resulting in much weaker attraction between their ligand shells, even at temperatures where the conformational entropies are similar.

The stabilizing mechanism of nonlinear ligands cannot be understood at the single-molecule level alone. It is an emergent property of the interacting molecules in the ligand shell. The molecular dynamics in this shell deviates from the conventional bulk state as a result of the

ligand-core bond. Stability is affected not only by the molecular ligand structure but also by the core size and geometry. For example, the presence of facets can result in differences in ligand density across the nanoparticle surface, while the relative orientation and size of facets influences the local order and dynamics of the ligand shell [105].

While core-dominated agglomeration that is driven by the attraction between larger cores cannot be prevented by nonlinear ligand shells, their effectiveness extends into the transition region where the core alone cannot induce agglomeration. For example, oleylamine stabilized even cores with $8.5\,\mathrm{nm}$ diameter down to $-90\,^{\circ}\mathrm{C}$.

Ligand shell disorder and mobility can be increased with other strategies, too. Mixed shells of linear ligands, for example, have been shown to dramatically enhance concentration-dependent stability while reducing the enthalpic gain of bundle formation [57]. It will be interesting to assess whether they provide increased temperature-dependent stability as well, without the need for new molecular ligand structures.

3.2.5 Materials and Methods

Nanoparticle synthesis

Gold nanoparticles stabilized by oleylamine and a core diameter of $4\,\mathrm{nm}$ were synthesized following a method described previously [58]. A mixture of $9\,\mathrm{mL}$ of n-pentane (Carl Roth, $99\,\%$) and $9\,\mathrm{mL}$ oleylamine (Sigma Alrich, technical grade, $80-90\,\%$) was added to $100\,\mathrm{mg}$ of tetrachloroauric(III) acid trihydrate $HAuCl_4 \cdot 3\,H_2O$. The stirring time and the temperature used depend on the target particle size. Table 3.2.1 shows the parameter of the synthesis of the gold precursor for the different particle sizes. Then, a mixture of $1\,\mathrm{mL}$ n-pentane, $1\,\mathrm{mL}$ oleylamine and $40\,\mathrm{mg}$ tert-butylamine borane complex (FLUKA, $97\,\%$) was added to the gold precursor solution. The mixture was stirred for $90\,\mathrm{min}$. The dispersion was purified by precipitation with $50\,\mathrm{mL}$ of a mixture of ethanol and methanol (ratio 3:2) and centrifugation at $2000\,\mathrm{rpm}$ ($689\,\mathrm{rcf}$) for $5\,\mathrm{min}$. The supernatant was removed, and the nanoparticles were redispersed in $2.5\,\mathrm{mL}$ toluene (gold concentration of $2.5\,\mathrm{mg/mL}$).

Table 3.2.1: Parameter of the synthesis for the used nanoparticle diameter.

Temperature T	Time t	Particle diameter	Solvent
$21\,^{\circ}\mathrm{C}$	$21\,\mathrm{min}$	$4\,\mathrm{nm}$	n-pentane
$21\,^{\circ}\mathrm{C}$	$2\,\mathrm{min}$	$8.3\,\mathrm{nm}$ ($7\,\mathrm{nm}$)	benzene

The larger particle with a diameter of $8.3\,\mathrm{nm}$ must be synthesized in two steps. First particles with a diameter of $\sim 7\,\mathrm{nm}$ were synthesized. This particles were dispersed in toluene and diluted to a gold concentration of $2.5\,\mathrm{mg/mL}$ (dispersion volume of $20\,\mathrm{mL}$). The dispersion was heated to $60\,^{\circ}\mathrm{C}$. A solution of $60\,\mathrm{mg}$ of tetrachloroauric(III) acid trihydrate $HAuCl_4 \cdot 3\,H_2O$

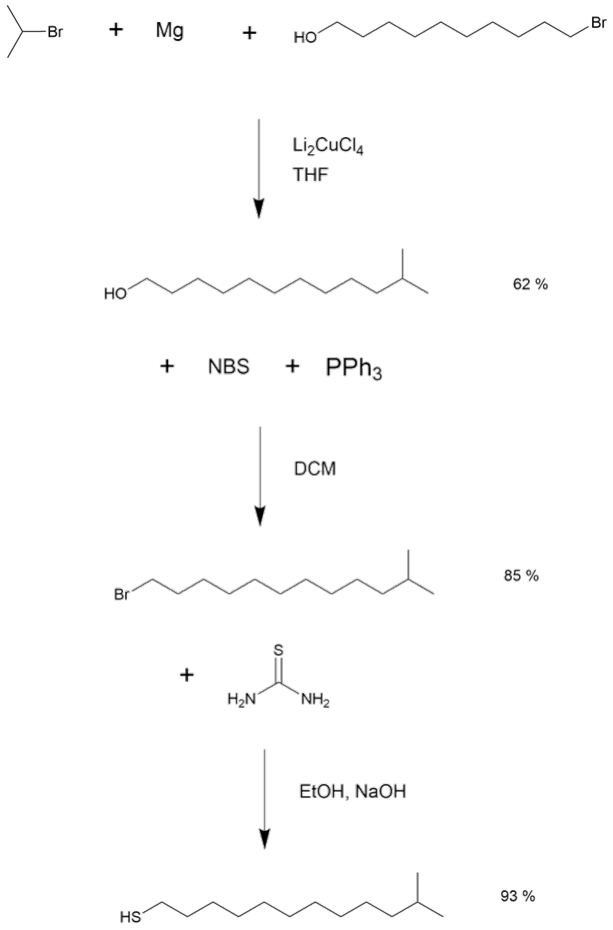


Figure 3.2.10: Synthesis of 11-methyldodecanthiol. In the first step 11-methyldodecanol was synthesized from 10-bromodecanol using *iso*-propyl and magnesium in a tertahyrofuran (THF) solution. In the second step 11-methylbromide was synthesized using *N*-brom succinimide (NBS) and triphenylphosphine (PPh_3) in a dichloromethane (DCM) solution. In the last step 11-methyldodecanethiol was synthesized using thiourea and sodium hydroxide (NaOH) in an ethanol (EtOH) solution.

in 5 mL toluene and 1 mL was added to the warm dispersion. The mixture was stirred for 6 hours at 60 °C. The dispersion was purified by precipitation with 50 mL of a mixture of ethanol and methanol (ratio 3:2) and centrifugation at 2000 rpm (689 rcf) for 5 min. The supernatant was removed, and the nanoparticles were redispersed in 2.5 mL toluene (gold concentration of 10 mg/mL).

Synthesis of 11-methyldodecanthiol

11-Methyldodecanthiol was synthesized by sequential synthesis of 11-methyldodecanol, 11-methyldodecylbromide and 11-methyldodecanthiol following the scheme shown in Figure 3.2.10.

11-Methyldodecanol

To the *iso*-propyl magnesium bromide in THF solution (prepared from 4.25 g magnesium (173 mmol, 2.8 eq) and 21.5 g isopropyl bromide (173 mmol, 2.8 eq) in 100 ml THF), 21.6 mL Li_2CuCl_4 0.1 M in THF (2.16 mmol, 3 M%) was added for 20 min at −25 °C and followed by stirring for 30 min. 14.65 g of 10-bromodecanol (61.77 mmol, 1 eq) in 50 mL THF was added at −25 °C and the reaction mixture was then stirred for 3 h at the same temperature. After that time the mixture was added to 250 mL of 3M HCl solution, stirred for 10 min, and extracted three times with 200 mL of diisopropyl ether. The combined organic layers were washed with 200 mL of brine and concentrated in vacuo. The residue was distilled under reduced pressure. 7.67 g of a colorless oil was obtained. Yield 62 %, bp. 105 °C at 0.02 mbar.

11-Methyldodecylbromide

To a solution of 7.50 g of 11-methyldodecanol (37.4 mmol, 1 eq) and 11.87 g of triphenylphosphine (45.25 mmol, 1.21 eq) in 50 mL of dichloromethane, 7.59 g of N bromosuccinimide (42.6 mmol, 1.14 eq) was added in portions over 30 min maintaining the reaction flask at 4 −8 °C. The reaction mixture was stirred for 30 min and followed by removal of the solvent by evaporation. The residue was diluted with hexane and the solid was removed by filtration and washed with hexane. The solution was concentrated and passed over a silica pad. After removing the solvent by evaporation, 8.37 g of the product was obtained as a colorless oil. Yield 85 %.

11-Methyldodecanthiol

9.25 g 11-methyldodecylbromide (35.1 mmol, 1 eq) was added to a solution of 3.02 g thiourea (39.6 mmol, 1.1 eq) in 60 mL ethanol. The mixture was heated at reflux overnight. 1.59 g sodium hydroxide (39.6 mmol, 1.1 eq) in 30 mL of water was added and the mixture was stirred at reflux for 2 h. The reaction mixture was cooled, poured into 100 mL of water and extracted three times with 250 mL dichloromethane. The organic layer was dried over $MgSO_4$, filtered, and the solvent was removed in vacuo. 7.10 g of 11-methyldodecanthiol was obtained as a colorless liquid in a yield of 93.4 %.

Ligand exchange

The ligand exchange was based on a previously published method [228]. For the ligand exchange, the dispersion (2.5 mL, c = 10 mg/mL) was heated to 80 °C, followed by the addition of 1 mL hexadecanethiol (Sigma Aldrich, GC, 95 %) (0.4 mL per 1 mL of the concentrated dispersion, 1.3 M). The mixture was stirred for 15 min at 300 rpm. The dispersion was purified by precipitation with 3 times the sample volume (3 mL for 1 mL dispersion) of a mixture of ethanol and methanol (ratio 2:1) and centrifugation at 2000 rpm (689 rcf) for 5 min. The supernatant

was removed, and the nanoparticles were redispersed in $2.5\,\mathrm{mL}$ toluene. The washing step was repeated once with a cooled mixture of ethanol and methanol (2:1). After the last washing step, the sample was redispersed in *n*-hexane and diluted to a gold concentration of $2.5\,\mathrm{mg/mL}$.

Ligand exchange with 11-methyldodecanthiol and 1-dodecanethiol was performed in a similar way. A ligand concentration of $1.3\,\mathrm{M}$ used. Due to the higher stability of the particles with the shorter ligands, higher rotation speeds were used during centrifugation ($4000\,\mathrm{rpm}$, $2755\,\mathrm{rcf}$).

Ligand exchange with dihexadecylsulfide differed from classical exchange with thiols. Due to the limited solubility of this ligand, the concentration during the ligand exchange was reduced to $25\,\mathrm{mg}$ (dispersion volume of $2.5\,\mathrm{mL}$) and the reaction time was extended to 20 minutes. For the purification, the nanoparticles must be precipitated without washing agents; an "optima XE-90" ultra-centrifuge (Beckman Coulter, U.S.) was used for the precipitation of the nanoparticles. The dispersion was diluted to a volume of $4\,\mathrm{mL}$ and centrifuged at 60,000 rpm for 60 minutes. The supernatant was removed. The washing process was repeated once. The sample was dried and than redispersed in $2.5\,\mathrm{mL}$ of *n*-hexane.

Ligand exchange with octadecylamine was performed in a similar way. The ligand was added to reach a concentration of $1.3\,\mathrm{M}$ in a dispersion at $60\,^{\circ}\mathrm{C}$ ($0.89\,\mathrm{g}$ for $2.5\,\mathrm{mL}$ of the dispersion). The mixture was stirred for $15\,\mathrm{min}$. The dispersion was purified by precipitation with 3 times the sample volume of ethanol and centrifugation at $2000\,\mathrm{rpm}$ ($689\,\mathrm{rcf}$) for $5\,\mathrm{min}$. The washing step was repeated once. The completed ligand exchange and purification process was repeated twice. After the last addition of octadecylamine, the sample was washed three times. The particles were redispersed in *n*-hexane to a gold concentration of $2.5\,\mathrm{mg/mL}$.

Small- and Wide-Angle X-ray Scattering

SAXS measurements were performed on a Xeuss 2.0 instrument (Xenocs SA, Grenoble, France). The X-ray beam was produced by a copper K_α source (wavelength 1.54 Å) and focused on the sample with a spot size of $0.25\,\mathrm{mm}^2$. The measurements were performed with a sample-detector distance (SDD) of $1200\,\mathrm{mm}$. The measurable momentum transfer q ranges from $0.01\,\mathrm{Å}^{-1}$ to $0.5\,\mathrm{Å}^{-1}$, with q being defined as $q = 4\pi\sin(\theta/2)/\lambda$, where θ is the scattering angle.

The samples were measured in borosilicate capillaries with an inner diameter of $1.5\,\mathrm{mm}$. For the temperature-dependent measurements, a "Linkam HFX350" temperature cell was used (Linkam Scientific Instruments LTD., Redhill, United Kingdom). Before each temperature scan, the samples were equilibrated for 1 h in the capillaries, at a temperature well above T_{agglo} for the respective sample. During the temperature scans, the samples were cooled in steps of $10\,^{\circ}\mathrm{C}$ to $-90\,^{\circ}\mathrm{C}$ or $-130\,^{\circ}\mathrm{C}$. After each change in temperature, the samples were equilibrated for 5 minutes, followed by a SAXS measurement with an acquisition time of 15 minutes (3 times 5 minutes). The data were analyzed as described in the Supporting Information.

Table 3.2.2: Ligand shell densities ρ_{LS} of the nonlinear ligand systems and the linear reference systems

Core diameter	4 nm	8 nm
Ligand	ρ_{LS} (nm^{-2})	ρ_{LS} (nm^{-2})
OAm	4.6	3.8
N_{18}	5.0	3.6
SC_{18}	6.7	6.9
SC_{12}^{br}	5.1	4.9
SC_{12}	5.6	6.5
$S(C_{16})_2$	2.6	2.0
SC_{16}	6.3	7.5

Transmission Electron Microscopy

For the imaging of the gold nanoparticles, a "JEOL JEM2100 LaB_6" electron microscope (JEOL ltd. Tokyo, Japan) with 200 kV acceleration voltage, 0.1 Å line resolution, and a Gatan Orius SC1000 camera (Gatan Inc. Pleasanton, CA, USA) in brightfield mode was used. AuNP samples were prepared by drop-casting of $10-20\,\mu L$ of the particle dispersion in *n*-hexane (2.5 mg/mL) on a TEM copper grid. The analysis of the spacing between particles from TEM images is described in the Supporting Information.

Thermogravimetric Analysis

For the thermogravimetric analysis the samples were prepared by drop-casting of the nanoparticle dispersion into Al_2O_3 crucibles. All nanoparticle systems that were previously measured using SAXS were analyzed. The nanoparticle systems were transferred to *n*-hexane after the second washing step after the ligand exchange. The volume of pentane was smaller than the initial sample volume. Dispersions with concentrations of 20-30 mg/ml were produced.
The dispersions were transferred to the crucibles. The solvent *n*-pentane was evaporated at room temperature. After the evaporation at room temperature, the samples were dried in a vacuum oven (p = 10 mbar) overnight. For the TGA measurement a "STA 449F3" setup from NETZSCH was used. The samples were heated to 1000 °C over 90 minutes. During the heating, an argon atmosphere was used.
The densities of 8 nm SC_{16} and SC_{18} are at the upper possible limit given the binding group's footprint and suggests that a certain amount of free ligand was present.

Molecular Dynamics Simulations

Our model, based on our previous work [58], consisted of a 3.8 nm Au nanoparticle core coated with various ligands, namely hexadecanethiol, undecanethiol, 6-pentylundecanethiol, 6-propylundecanethiol, 6-methylundecanethiol, 10-methylundecanethiol and *cis*-8-hexadecenethiol.

The LigParGen web server [229] was used to generate the initial topology for all ligands. Next, ligand molecules were positioned on the outside of a spherical shell with PACKMOL [230], resulting in our final nanoparticle systems. The NP core was modeled implicitly, with sulfur atoms of the ligands constrained to a shell 0.15 nm above the core surface using the RATTLE algorithm [231]. Sulfur positions were optimized on this shell using a repulsive Coulombic potential (ϵ = 10 kcalmol^{-1}, truncated at 24 Å) to ensure approximately equidistant binding sites. While 4 nm gold particles do have small facets, this spherical approximation has previously been used successfully to study ligand ordering on such particles, with good correspondence between the ligand ordering temperature and experimental agglomeration temperature for a wide range of ligand lengths and solvent types [43, 58, 59, 109]. The surface coverage was set to 4.5 ligands.nm^{-2}, based on values measured experimentally by thermogravimetric analysis. In view of lower values reported by previous work [125], we also investigated a lower coverage of 3 ligands.nm^{-2} for 6-pentylundecane ligands.

Ligands and hexane solvent were modeled using the united-atom TraPPE force-field [107], with each CH_x group treated as a single particle. Interactions between these groups were modeled using a 12-6 Lennard-Jones (LJ) potential, while CH_x-core interactions used a 9-3 LJ potential ($\epsilon/k_{\mathrm{B}} = 88$ K, $\sigma = 3.54$ Å, truncated at 30 Å), as previously employed and described for similar particles [43, 102, 232]. Bond stretching, bending, and torsion terms were included within each molecule.

Simulations were performed using the LAMMPS package [208], with periodic boundary conditions in all directions. Temperature and pressure were controlled using the Nosé-Hoover thermostat [233] and Parrinello-Rahman barostat [234], respectively. While systems with linear ligands were simulated using a time step of 1 fs, branched and bent ligands required a reduced time step of 0.5 fs due to high densities within the ligand shell. To remove any high-energy configurations, we initially relaxed the solvated systems at constant energy for $10\,000$ ts. This was followed by a 1 ns constant volume (NVT) simulation at 300 K to stabilize the temperature. Subsequently, systems were equilibrated at high temperature (400 K) in the NPT ensemble to ensure disordered ligand states, followed by compression of the simulation box to match experimental solvent densities. The systems were then cooled to the desired temperature and equilibrated for at least 12 ns before production runs of 1 ns to 2 ns were performed. Molecular graphics were produced using Visual Molecular Dynamics (VMD)[235].

Potential of Mean Force

To quantify inter-particle interactions, we calculated the potential of mean force (PMF) for pairs of identical particles in explicit hexane using constrained MD simulations. This included 3.8 nm Au NPs coated with bent *cis*-8-hexadecenethiol or branched 6-pentylundecanethiol ligands at

$-53\,^{\circ}\mathrm{C}$. This temperature was chosen to investigate inter-particle interactions where linear ligands typically exhibit ordered shells and strongly attractive interactions. We also repeated the procedure for NPs coated with the bent ligands at a lower temperature of $-95\,^{\circ}\mathrm{C}$, close to the freezing point of hexane ($T_m = -95\,^{\circ}\mathrm{C}$) and, therefore, to the lowest temperatures we could reach in our experiments.

The PMF was computed by gradually decreasing the inter-particle separation from a non-interacting distance at a rate of $1\,\text{Å ns}^{-1}$. At each separation r, we allowed at least $10\,\text{ns}$ for equilibration and sampling, with longer runs employed at lower temperatures due to reduced ligand lability. To improve configurational sampling, we reduced the nanoparticles' moment of rotational inertia by 5% compared to the calculated value for solid gold spheres of their size. This modification allowed for faster rotational motion of the particles while maintaining physically reasonable behavior and energy conservation.

The interactions between the spherical Au cores were modeled using the Hamaker potential [49], with a Hamaker constant of $2\,\text{eV}$ [211]. This approach approximates the solvent and ligand environment as a continuous medium, with the interaction constant adjusted to account for the hydrocarbon environment.

The PMF was evaluated through numerical integration of the mean force between two particles in the direction of the line connecting them, calculated as:

$$F_{mean}(r) = \frac{1}{2} < (\vec{F_2} - \vec{F_1}) \cdot \vec{r} >_{NVT} \tag{3.2.1}$$

where $\vec{F_1}$ and $\vec{F_2}$ are the total forces acting on each NP, and $\vec{r}$ is the unit vector connecting their centers.

Conformational Entropy

We estimated the conformational entropy of ligand shells at various temperatures using the correlation corrected multi-body local approximation (CC-MLA) method, as implemented in CENCALC [224]. This approach captures the entropy contributions from different ligand conformations while accounting for correlations between dihedral angles within each molecule.

We represent the conformational space of each ligand by its dihedral angles, discretizing them into three locally stable states: *trans*, *gauche(-)*, and *gauche(+)*. This process transforms the continuous dihedral angle measurements into discrete random variables, allowing us to apply Shannon information entropy to quantify the conformational entropy of the ligands molecules:

$$S_{conform} = -k_{\mathrm{B}} \sum^{N} P(X) \ln P(X) \tag{3.2.2}$$

where k_{B} is the Boltzmann's constant, $P(X)$ is the probability mass function of the discretized conformational states, and N is the total number of possible configurations.

For our systems, direct application of this expression is impractical due to the large number of possible conformers (3^M, where M is the number of dihedral angles) and would result in negatively-biased entropies due to correlations between dihedral angles. To address these challenges, we employed the CC-MLA method [224], which provides an efficient way to estimate conformational entropy while accounting for genuine correlations between neighboring dihedral angles. The CC-MLA method improves upon traditional mutual information expansion (MIE) approaches by selecting an optimum distance-based cutoff that captures the maximum amount of genuine correlation while avoiding spurious correlations that can arise from limited sampling. Converged estimates of the entropy were obtained by collecting data every 0.5 ps over 2.75 ns for branched and bent ligands and every 1 ps over 5.5 ns for linear ligands. To manage computational complexity due to the large number of molecules in our system, we treated each ligand independently and summed their individual entropies to approximate the entire nanoparticle's ligand shell entropy. We note that, while this method captures intra-molecular correlations, it neglects inter-molecular ones, potentially underestimating entropy changes upon ligand ordering.

3.2.6 Acknowledgement

Dominik Perius (INM) is acknowledged for performing image analyses of the transmission electron microscopy measurements. T.V.K. thanks the DFG for financial support (Geschäftszeichen: KR 3729/18-1). This research was supported in part by the ARC Centre of Excellence in Exciton Science (CE170100026) and by Grant NSF PHY-1748958 to the Kavli Institute for Theoretical Physics (KITP). Additional support was provided by the Australian Government's National Collaborative Research Infrastructure Strategy (NCRIS), with access to computational resources provided by NCI and Pawsey through the National Computational Merit Allocation Scheme and the NCI Flagship program.

3.3 Stabilization of Apolar Gold Nanoparticles by Mixed Ligand Shells

3.3.1 Introduction

In the preceding chapters, various modifications to the shell were presented that improved colloidal stability. The best results were achieved with non-linear ligands (see Chapter 3.2). A moderate improvement was achieved by replacing the original ligand using the additive tetrahydrothiophene (see Chapter 3.1). Due to the structural differences between the ligand and the additive, the shell structure became less and less stabilizing as the exchange increased. For this reason, alkylthiol ligands that differ only in size are combined in this chapter. The aim is to achieve higher exchange rates and to suppress the disorder-order transition of the shell by using suitable ligand combinations.

It has already been shown in the literature that mixed shells can influence colloidal stability. The work by Pang et al. chemically similar carboxylic acids (6-hexanoate and 14-myristate) with different chain lengths were combined [133]. Depending on the ratio of the ligands used, the solubility of the CdSe particles at room temperature increased by a factor of up to 10,000. The authors suggest that the improved solubility is the result of the increased freedom of movement of the ligand molecules. The increased mobility is the result of the modified shell structure. Using ^{13}C-CODEX NMR measurements, the authors were able to show that no random homogeneous distribution occurs in mixed shells. Instead, a heterogeneous distribution is formed depending on the ligand ratio, which makes the shell structure more stable against temperature changes. However, it is unclear whether a transition from disorder to order can occur within the segregated islands.

Elimelech and coworkers investigated the thermodynamic properties of mixed ligand shells using ITC and compared them with calculations on the mixing behavior [134]. They measured the changes in enthalpy and entropy due to ligand exchange with two thiol ligands and found that in mixed shells, a compensation mechanism always leads to only minor changes in the free Gibbs enthalpy when the ligand ratio is changed. For example, in the case of a small fraction of larger ligands in a hexanethiol shell, the overall ligand-ligand interaction is increased. The increase in ligand-ligand interaction leads to denser ligand packing, which reduces entropy. Consequently, a gain in enthalpy is always compensated by a loss in entropy. Additionally, they found that the mixing behavior of the used ligands controls the patterning of the shell.

Ligand distribution was consistently named as a key factor in the properties of mixed shells

[132–134]. In principle, an unlimited number of shell patterns is possible [132]. However, it is possible to influence the formation of the ligand pattern. The greater the difference in ligand size or polarity, the stronger the preference for demixing of the ligands [132, 134]. In our previous work, the demixing of hexadecanethiol and tetrahydrothiophene led to a reduction of the stabilizing effect [113]. It remains unclear how other ligand combinations and their shell patterns affect the temperature-dependent disorder-order transition of the shell.

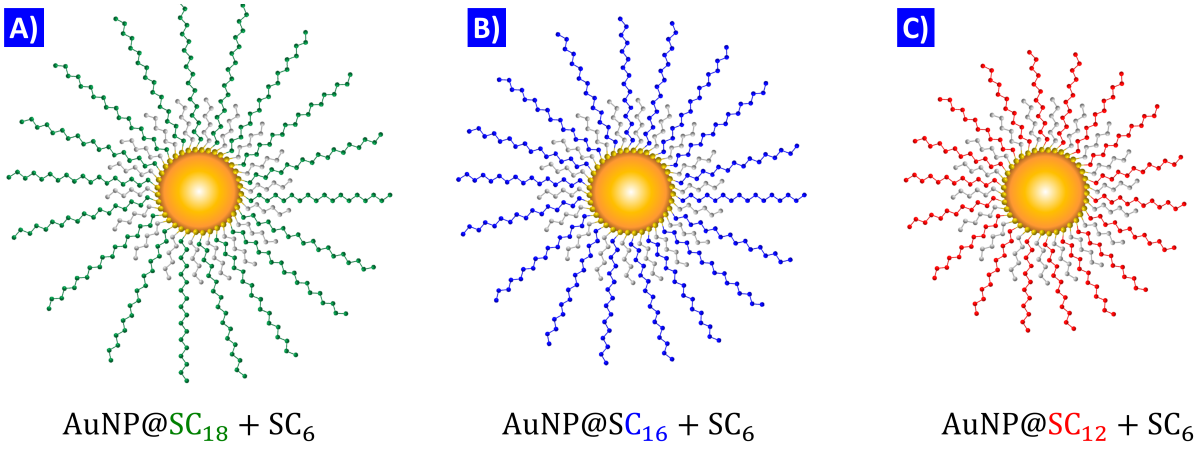


Figure 3.3.1: Principle of nanoparticles with a mixed ligand shell consisting of two linear alkyl thiols with different chain lengths: A) AuNP@SC_{18}+SC_6, B) AuNP@SC_{18}+SC_6, and C) AuNP@SC_{12}+SC_6.

In this chapter, the temperature-dependent colloidal stability of mixed ligand shells is examined. I used 4 nm gold nanoparticles coated with linear alkyl thiols with different chain lengths as shown in Figure 3.3.1. Unlike in the literature, the mixed shells were not prepared in a single step [133, 134], but using a two-stage exchange. The synthesized gold core with oleylamine shell was first coated with the larger thiol. In a second step, a part of the original thiol was then replaced by a shorter thiol. In this work, we used 1-octadecanethiol (SC_{18}), 1-hexadecanethiol (SC_{16}), 1-dodecanethiol (SC_{12}), and 1-hexanethiol (SC_6) for the synthesis of mixed ligand shells. The colloidal stability was analyzed using temperature-dependent small-angle X-ray scattering (SAXS). We found a strong connection between the composition of the shell and the colloidal stability of the dispersion. Additionally, we observed that the size difference of the ligands, Δl, plays a key role in the colloidal stability. The results indicate that mixed-ligand shells can suppress the agglomeration, similar to the non-linear ligands.

3.3.2 Results and Discussions

We compared the colloidal stability of gold nanoparticles (AuNP) with a core diameter of 4.0 nm and uniform ligand shells to those with mixed ligand shells in *n*-hexane and toluene. Mixed ligand shells were formed by partial ligand exchange of the pure ligand shells and analyzed using thermogravimetric analysis (TGA). All dispersions contained particles at concentrations of 10 mg/mL. Temperature-dependent small-angle X-ray scattering (SAXS) was used to quantify particle agglomeration upon cooling down to -90 °C, the lowest temperature that our setup can reach. Lower agglomeration temperatures were interpreted as higher colloidal stabilities.

Pure shells of 1-octadecanethiol (SC_{18} or ODT), 1-hexadecanethiol (SC_{16} or HDT), and 1-dodecanethiol (SC_{12} or DDT) on AuNP with a diameter of approx. 4 nm have been studied previously. They are "shell-dominated", and the disorder-order transition of the shell structure causes agglomeration [58]. Cores coated with 1-hexanethiol (SC_6 or HT) are colloidally unstable at room temperature, and we were not able to perform SAXS measurements of the AuNP@SC_6 system.

Figure 3.3.2a shows the temperature-dependent SAXS patterns of AuNPs with 4 nm diameter cores coated with dodecanethiol (AuNP@SC_{12}). Scattering at 10 °C was dominated by an intensity plateau at q <0.1 Å^{-1} and decreased in intensities at higher q, followed by an intensity maximum at $q = 0.2$ Å^{-1} to 0.3 Å^{-1} from the form factor of spherical particles [200]. The absence of further peaks shows that there is no significant particle-particle interaction, and the particles are fully dispersed.

Cooling the AuNP@SC_{12} dispersion to -90 °C led to the formation of a peak at q_0 ≈0.1 Å^{-1} in n-hexane (Figure 3.3.2C-D). This structure factor peak indicates spatial correlation of AuNPs by agglomeration. Particles with a mixed shell AuNP@SC_{12}+SC_6 that had formed at an SC_6 concentration of 26 mM did not agglomerate until -90 °C. The setup limited the temperature range used for the measurements. In toluene, the same particles (pure and mixed shells) agglomerated earlier and yielded sharper structure factor peaks at 0.13 Å^{-1} (Figure 3.3.2D-F), indicating a more regular packing. For the particles modified with 26 mM SC_6, additional peaks 0.11 Å^{-1}, 0.16 Å^{-1} and 0.26 Å^{-1} indicate a partially crystalline arrangement of the particles in the agglomerates.

The structure factor peak correlates with the agglomeration of the nanoparticles. We used it to quantify the temperature-dependent stability of the dispersion following a previously published approach [109, 113]. A model-based analysis of the temperature-dependent scattering curves (details are shown in the Appendix) yielded the fraction of AuNPs within agglomerates, χ_{agglo}. The temperature-dependent change of the agglomeration fraction χ_{agglo} is shown in Figure 3.3.3 for gold particles coated with SC_{12} that were subsequently modified with different concentrations of SC_6.

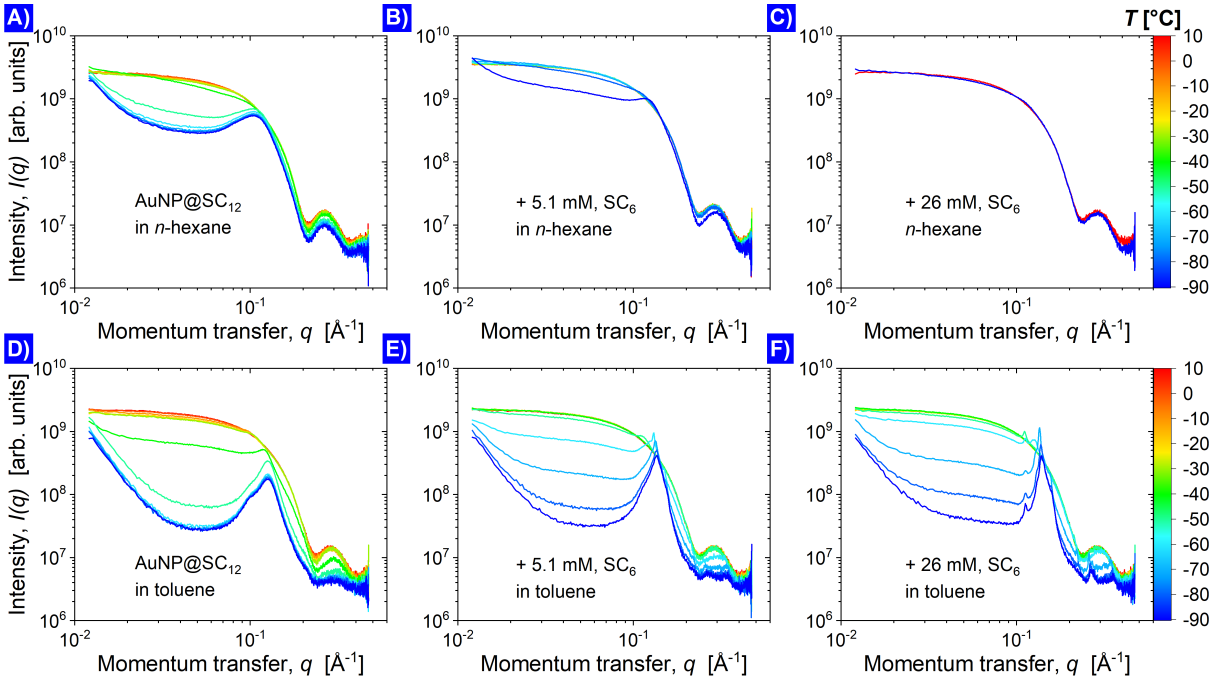


Figure 3.3.2: Temperature dependent small-angle X-ray scattering curves of 4 nm gold nanoparticles with a mixed ligand shell based SC_{12} and different concentrations of SC_6: 0 mM (A,D), 5.1 mM (B, E), and 26 mM (C, F). The samples measured in A)-C) were measured in *n*-hexane. The samples measured in D)-F) were measured in toluene.

The number fraction of particles in agglomerates, χ_{agglo}, increased non-linearly when cooling. We fitted it using eq. 7.3.10 in the Appendix as previously [58, 113] and defined the agglomeration temperature, T_{agglo}, as the temperature at which the sigmoidal fit reached $\chi_{\text{agglo}} = 0.2$.

The agglomeration temperature of non-modified AuNP@SC_{12} was approximately $-40\,°C$ in *n*-hexane and $-30\,°C$ in toluene. Modification with SC_6 reduced T_{agglo} in both solvents. In *n*-hexane, T_{agglo} was reduced so much that we were only able to observe full agglomeration until $-90\,°C$ for AuNP@SC_{12}. In toluene (see Figure 3.3.3C and D), all particles reached at least $\chi_{\text{agglo}} > 0.95$. We calculated changes in agglomeration temperature due to the mixed ligand shell, ΔT_{agglo}, as:

$$\Delta T_{\text{agglo}}(c_{\text{MLS}}) = T_{\text{agglo}}(c_{\text{MLS}}) - T_{\text{agglo}}(c_{\text{ref. ligand}}), \tag{3.3.1}$$

where $T_{\text{agglo}}(c_{\text{MLS}})$ is the agglomeration temperature of the mixed ligand system and $T_{\text{agglo}}(c_{\text{ref. ligand}})$ the agglomeration temperature of the reference system with a shell consisting only of the longer alkyl thiol, following previous work [113]. The results are shown in Figure 3.3.4 for AuNP@SC_{12} and AuNP@SC_{16} modified with SC_6 in toluene (A and C) and *n*-hexane (B and D). Two batches were measured for each combination to extend the concentration range of SC_6; slight batch-to-batch variations are expected. Figure 3.3.4 thus indicates the batches that are separated by a black line.

The overall stabilizing effect of the mixed shells was lower in toluene. In case of the

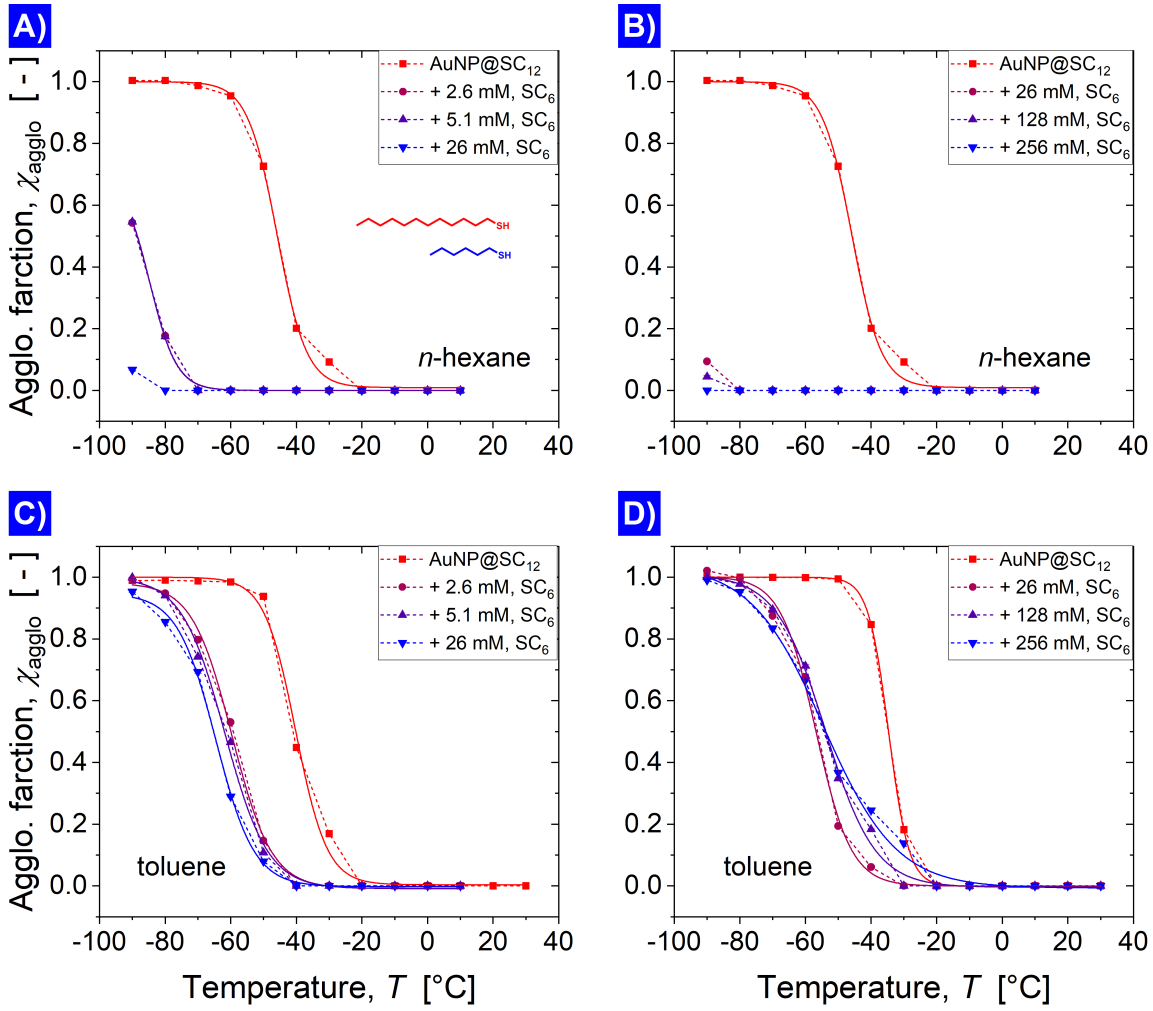


Figure 3.3.3: Temperature-dependent agglomeration fraction χ_{agglo} of 4 nm gold nanoparticles coated with 1-dodecanethiol (SC_{12}) and modified with different concentrations of 1-hexanethiol (SC_6) in *n*-hexane (A + B) and toluene (C + D). The SC_6 concentrations in A) and C) are ranging from 2.6 mM to 26 mM. The SC_6 concentrations in B) and D) are ranging from 26 mM to 256 mM.

AuNP@SC_{12}+SC_6 systems the largest shift was -23.3 K ($c(SC_6)$=26 mM). In hexane the largest shift was -60.3 K ($c(SC_6)$=256 mM). The origin of this solvent-dependent behavior is based on differences in the interactions between ligand and solvent molecules. Doblas and co-workers studied the effect of different solvents on the colloidal solubility of 3.4 nm gold nanoparticles coated with 1-octanethiol [95]. As in the work of Monego et al., they found that cyclohexane and short alkanes are "good" solvents and long alkanes and toluene are "bad" solvents. Interestingly, using the classical model for ideal solubility, toluene should have an almost ideal solubility for the ligand hexadecanethiol. The authors suggested that supramolecular interactions must be considered to understand the solvent-dependent differences. In the case of toluene, the solubility could be affected by the $\pi - \pi$-stacking of the solvent molecules. Consequently, the solvent-solvent and ligand-ligand interactions would increase due to the reduction of the ligand-

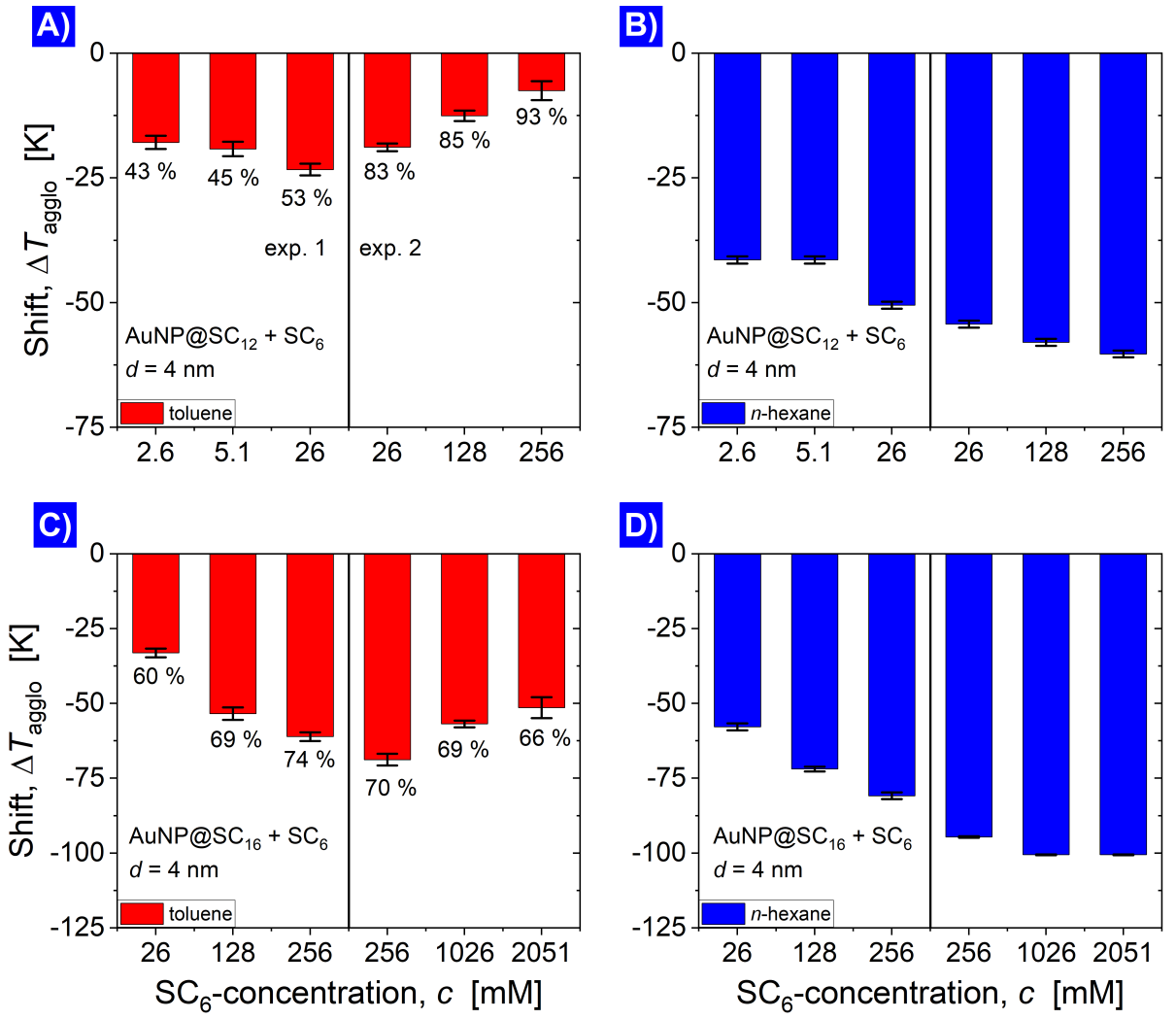


Figure 3.3.4: Stabilizing effect of mixed ligand shells of 4 nm AuNP coated with SC_{12} and modified with different concentrations of SC_6 dispersed in toluene (A) and *n*-hexane (B). Stabilizing effect of mixed ligand shells of 4 nm AuNP coated with SC_{16} and modified with different concentrations of SC_6 dispersed in toluene (C) and *n*-hexane (D). Two concentration series (exp.1 and exp.2) were performed for each combination (as indicated by the black line). Changes in the agglomeration temperature T_{agglo} are compared to the initial ligand system. The changes are shown as the shift of the agglomeration process ΔT_{agglo}. ($\Delta T_{agglo}(c_{MLS}) = T_{agglo}(c_{MLS}) - T_{agglo}(c_{ref.\ ligand})$)

solvent interactions. We concluded that in the case of toluene, it does not matter whether the shell consists of one or more alkylthiol ligands. The destabilizing effect of toluene affects all ligand systems.

The changes in agglomeration temperatures in toluene and *n*-hexane ΔT_{agglo} were a function of SC_6 concentration in the shell. Details on the TGA analysis of the shell composition are shown in Chapter 7.3 of the Appendix. The fractions of SC_6 in the AuNP@SC_{12}+SC_6 and the AuNP@SC_{16}+SC_6 systems are shown in Figure 3.3.4. In the AuNP@SC_{12}+SC_6 systems, the fraction of the short thiol increased continuously with increasing SC_6 concentration during lig-

and exchange. An exchange of 93 % was achieved at a $c(SC_6)$ of 256 mM. In AuNP@SC_{16}+SC_6, the SC_6 fraction increased up to a $c(SC_6)$ of 256 mM, reaching an exchange rate of 74 %, and decreased at higher c. We assume that the thinner shell of the AuNP@SC_{12}+SC_6 system is more easily penetrated by SC_6, increasing the replacement rate. The maximum in the AuNP@SC_{16}+SC_6 system is surprising and may indicate the existence of a low-energy shell structure. Unfortunately, there is no literature on such a shell structure.

Pang and coworkers studied colloidal stability as a function of shell composition, too. They quantified stability by colloidal solubility and found a maximum for 3 nm CdSe NP with a mixed shell of 32 % myristate and 68 % hexanoate. Increasing the hexanoate fraction reduced solubility. The authors do not discuss the origin of this maximum [133], but they report that increasing the fraction of the shorter hexanoate decreased the ligand-ligand interactions between neighboring cores, while the core-core interactions increased. In this work, the increasing effect of core-core interactions could explain the decrease in colloidal stability when the fraction of SC_6 increases in toluene-based dispersions.

Interestingly, we observed different colloidal stabilities for similar SC_6 fractions in the AuNP@SC_{16}+SC_6 systems. In addition to the composition of the shell, the distribution of ligands is an essential property in mixed ligand systems. It is known from the literature that a variety of patterns are possible. The type of pattern depends primarily on the properties of the ligand molecules. Different chain sizes or polarities result in variations in mixing behavior [132, 134]. In our work, the concentration of the shorter ligand was varied for each ligand combination. It is therefore possible that the pattern of the mixed shell is influenced by the different number of SC_6 molecules in the environment. Cluster distributions have been discussed in the literature for ligand systems with different chain lengths [133]. This involves a rather heterogeneous distribution of the two ligands. Depending on the composition, this can result in stripe-like or island-like patterns in the shell. We suspect that the type of pattern influences the disorder-order transition of the shell. Depending on the pattern, e.g., the larger thiol forms bundles, but the size of the bundles is not sufficient to influence colloidal stability. Consequently, only the transition of both ligands can induce agglomeration. A comparable effect was observed in the case of 4 nm gold particles with pure dihexadecylsulfide in Chapter 3.2. The hexadecyl chains were able to arrange themselves, but the resulting bundles were so small that the effect on colloidal stability was negligible. We hypothesize that the differences in the colloidal stability of mixed ligand shells with similar compositions are based on differences in the patterning of the shell.

In the following, I discuss longer alkylthiols in mixed ligand shells and their effect on agglomeration temperatures. Longer ligands in uniform shells lead to an increase in the agglomeration temperature [43]. Mixing long and short ligands led to agglomeration temperatures between $-49\,^{\circ}C$ (AuNP@SC_{18}+SC_6) and $-59\,^{\circ}C$ (AuNP@SC_{16}+SC_6). The shifts ΔT_{agglo} increased with

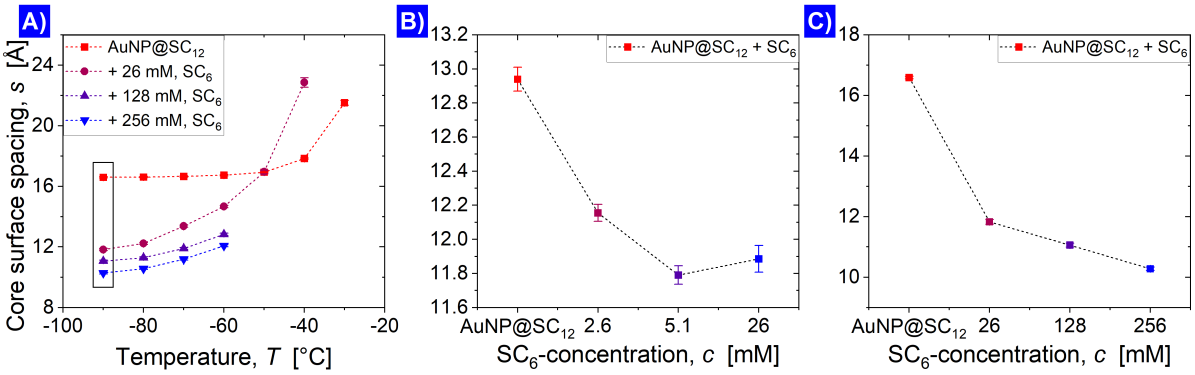


Figure 3.3.5: A) Temperature-dependent core surface spacing s of 4 nm gold nanoparticles coated with 1-dodecanethiol (SC_{12}) and modified with different concentrations of 1-hexanethiol (SC_6) in toluene. B) Final spacing s at $-90\,°C$ for dispersions with SC_6 concentrations ranging from 2.6 mM to 26 mM. C) Final spacing s at $-90\,°C$ for dispersions with SC_6 concentrations ranging from 26 mM to 256 mM.

increasing size difference between the ligands Δl. The AuNP@SC_{12}+SC_6 systems led to ΔT_{agglo} below -23 K (in toluene). For the AuNP@SC_{16}+SC_6 system, the largest shift (in toluene) was -69 K, and ΔT_{agglo} for AuNP@SC_{18}+SC_6 was around -85 K (see Figure 7.3.5 in the Chapter 7.3 in the Appendix). Elimelech and co-workers investigated the effect of the size difference Δl of thiol ligands on 3 nm CdSe NP. They found that the increase of Δl leads to a reduction of end-chain interaction at the interface of both ligands and a gain in entropy due to increased degrees of freedom for the long ligands at the interface [134]. We assume that the increase in the rotational freedom and the reduction of the interaction of the longer ligands hinder the ordering of the shell structure. It is not yet known whether the change in overall ligand distribution or local interactions between neighboring ligands dominate the observed changes in colloidal stability.

I studied the core surface spacing s between the particles with different shell compositions based on a method discussed in previous work [210] (see Chapter 7.3 in the Appendix for experimental details). The temperature-dependent spacing is shown in Figure 3.3.5 for AuNP@SC_{12}+SC_6, those for the mixed SC_{16} and SC_{18} systems in Figure 7.3.6 and 7.3.7 in the Appendix. The spacings were generally dominated by the ligand, with the larger fraction in the shell. In most cases, as the fraction of the second ligand increases, the spacing approaches that of a pure shell of the second ligand. This was consistent with our expectations that the spacing depends primarily on the size of the mixed ligand shell. However, in the case of the AuNP@SC_{16}+SC_6 system, despite the similar SC_6 fraction in the shell, significant differences in the spacing were found. Identical to the colloidal stability, we hypothesize that, in addition to the composition of the shell, the patterning of the two ligands affects the spacing. We hypothesize that, depending on the shell patterning, closer packing of the particles is possible.

Finally, in connection with the ambiguous effect of the shell composition of the AuNP@SC_{16}+SC_6 system, the accuracy of the TGA measurements must also be dis-

cussed. Since the amount of ligand was relatively small (2 mg to 3 mg), the resulting accuracy is limited. For this reason, the composition of the shell should be determined by another method, such as GC, in future experiments.

3.3.3 Conclusion

Combining linear ligands of different sizes is a promising approach to improve the colloidal stability of polar nanoparticle systems. I used small-angle X-ray scattering to show that the agglomeration temperature of alkylthiol-coated gold nanoparticles can be shifted by up to -100 K, depending on ligand combination and solvent.

The largest shifts were found when combining 1-hexanethiol (SC_6) with longer ligands. Generally, the stabilizing effect increases with increasing size difference of the combined alkyl thiols. The detailed analysis of the AuNP@SC_{12}+SC_6 and AuNP@SC_{16}+SC_6 revealed that two shell properties control the colloidal stability of mixed ligand systems. The first property is the shell composition. In toluene, a maximum in the stabilizing effect exists for both systems. The progressive exchange of the initial ligand with SC_6 reduced the overall shell size. The change of the core-shell size ratio leads to an increasing effect of the core-core interaction, resulting in a decrease in the colloidal stability.

The second property was the shell patterning. In the AuNP@SC_{16}+SC_6 system, particles with similar SC_6 fraction have different colloidal stability. Based on the literature, we hypothesized that, depending on the pattern, bundle formation is affected. Consequently, locally small bundles (e.g., of the large ligand) can be formed that have no significant effect on the colloidal stability. Additionally, the patterning-hypothesis was used to explain the differences in the spacings of the AuNP@SC_{16}+SC_6 systems.

Similar to the literature, we found that the solvent has a strong effect on colloidal stability. Using n-hexane as a solvent can significantly improve the colloidal stability of particles with a mixed ligand shell.

The performance of additional experiments and simulations is necessary to understand the observed effects. Nevertheless, as a proof of concept, the produced data demonstrated that some mixed ligand systems can reproduce the stabilizing effect of non-linear ligands. An outlook of further work is demonstrated in Chapter 5.

3.3.4 Materials and Methods

Nanoparticle synthesis:

Gold nanoparticles with a core diameter of 4 nm were synthesized following a method described previously [58]: A mixture of 9 mL of n-pentane (Carl Roth, 99 %) and 9 mL oleylamine (Sigma Alrich, technical grade, $80-90$ %) was added to 100 mg of tetrachloroauric(III) acid trihydrate $HAuCl_4 \cdot 3\,H_2O$. The mixture was stirred (with a magnetic stirrer bar) for 21 min at $22\,^{\circ}C$ under an argon atmosphere. Then, a mixture of 1 mL n-pentane, 1 mL of oleylamine and 40 mg tert-butylamine borane complex (FLUKA, 97 %) was added to the gold precursor solution. The mixture was stirred for 60 min. The dispersion was purified by precipitation with 50 mL of a mixture of ethanol and methanol (ratio 3:2) and centrifugation at 2000 rpm (689 rcf) for 1 min. The supernatant was removed, and the nanoparticles were redispersed in 2.5 mL toluene (gold concentration of $10\,mg/mL$).

First ligand exchange:

A volume of 2.5 mL nanoparticle dispersion was heated to $80\,^{\circ}C$, followed by the addition of the linear alkyl thiol solutions as listed in table 3.3.1. The mixture was stirred for 15 min at 300 rpm and purified by precipitation with 3 times the sample volume (3 mL for 1 mL dispersion) of a mixture of ethanol and methanol (ratio 2:1) and centrifugation at 2000 rpm (689 rcf) for 5 min. The supernatant was removed, and the nanoparticles were redispersed in 2.5 mL toluene. The washing step was repeated once. After the last washing step, the particles were redispersed into toluene and diluted to a gold concentration of $10\,mg/mL$.

Table 3.3.1: Details of the first ligand exchange

Ligand	Volume [mL]	Manufacturer
1-hexanethiol	0.5	Sigma Aldrich (95 %)
1-dodecanethiol	0.78	Sigma Aldrich (≥ 98 %)
1-hexadecanethiol	1.0	Sigma Aldrich (>95 %, GC)
1-octadecanethiol	1.2	Sigma Aldrich (98 %, GC)

Second ligand exchange:

The second ligand was introduced by adding the (shorter) thiol to 2.5 mL of a dispersion of thiol-coated nanoparticles. The ratio of the ligands in the shell was changed by varying the concentration of the shorter ligand in the second exchange reaction. AuNP@SC_{18}, AuNP@SC_{16} and AuNP@SC_{12} were modified with SC_{16}, SC_{12} and SC_6. Table 3.3.2 lists the ligand combinations and the concentrations of the second ligand used.

After adding the second ligand, the sample was shaken for 30 sec and stored for 24 hours without stirring. The dispersion was purified by precipitation with 3 times the sample volume of a mix-

ture of ethanol and methanol (ratio 2:1) and centrifugation at 2000 rpm (689 rcf) for 5 min. The supernatant was removed, and the nanoparticles were redispersed in 2.5 mL toluene or *n*-hexane.

Table 3.3.2: Overview of the ligand combinations and the concentrations used.

concentration	SC_{18}/SC_{16}	SC_{18}/SC_{12}	SC_{18}/SC_{6}	SC_{16}/SC_{12}	SC_{16}/SC_{6}	SC_{12}/SC_{6}
2.6 mM						x
5.1 mM						x
26 mM	x	x	x	x	x	x x
128 mM	x	x	x	x	x	x
256 mM	x	x	x	x	x x	x
1026 mM					x	
2051 mM					x	

Small-angle X-ray scattering:

SAXS measurements were performed on a Xeuss 2.0 instrument (Xenocs SA, Grenoble, France), as in our previous works [113, 210]. The X-ray beam was produced by a copper K_α source (wavelength 1.54 Å) and focused on the sample with a spot size of 0.25 mm^2. The measurements were performed with a sample-detector distance (SDD) of 1200 mm. The measurable momentum transfer q ranges from 0.01 $Å^{-1}$ to 0.5 $Å^{-1}$, with q being defined as $q = 4\pi \sin(\theta/2)/\lambda$, where θ is the scattering angle.

The samples were measured in borosilicate capillaries with an inner diameter of 1.5 mm. For the temperature-dependent measurements, a "Linkam HFX350" temperature cell was used (Linkam Scientific Instruments LTD., Redhill, United Kingdom). Before each temperature scan, the samples were equilibrated for 1 h in the capillaries, at a temperature well above T_{agglo} for the respective sample. During the temperature scans, the samples were cooled in steps of 10 °C to −90 °C. When the samples were measured, the wide-angle X-ray scattering (WAXS) detector was not working, so the aggregate state of *n*-hexane and toluene (at temperatures below −90 °C) could not be determined. For this reason, the sample was only measured down to −90 °C, at which the solvents were still liquid. After each temperature change, the samples were equilibrated for 5 min, followed by a SAXS measurement with an acquisition time of 15 min (3 times 5 min). The data were analyzed as described in the Supporting Information.

Thermogravimetric analysis:

For the thermogravimetric analysis, the samples were prepared by drop-casting of the nanoparticle dispersion into Al_2O_3 crucibles, as in our previous work [210]. All nanoparticle systems that were previously measured using SAXS were analyzed. The nanoparticle systems were transferred to *n*-hexane after the second washing step, after the ligand exchange. The volume of pentane was smaller than the initial sample volume. Dispersions with concentrations of 20-

30 mg/mL were produced.

The dispersions were transferred to the crucibles. The solvent *n*-hexane was evaporated at room temperature. After the evaporation at room temperature, the samples were dried in a vacuum oven (p = 10 mbar) overnight. An STA 449F3 setup from NETZSCH was used for the TGA measurement. The samples were heated to 1000 °C over 90 minutes. During the heating, an argon atmosphere was used.

3.4 Publication 3: Reactive Additive-Induced Joining of Apolar Thiol-Coated Gold Nanoparticle Cores at Low Temperatures

Knapp, T. V.; Niebuur, B.-J.; Matsarskaia, O.; Kraus, T. Reactive Additive-Induced Joining of Apolar Thiol-Coated Gold Nanoparticle Cores at Low Temperatures. *in preparation*

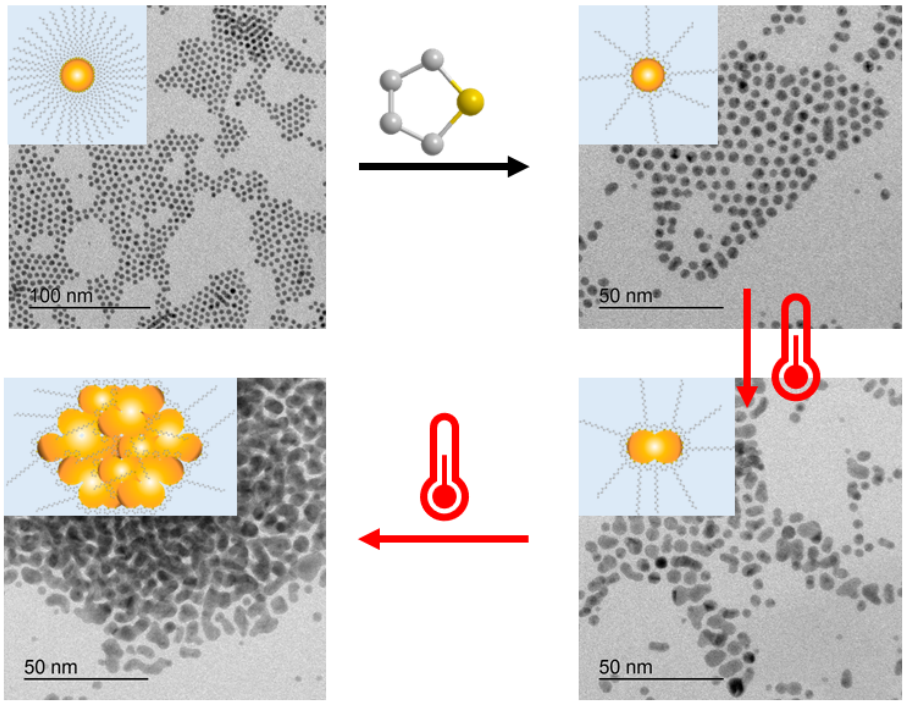


Figure 3.4.1: Table of contents figure of Publication 3.

3.4.1 Abstract

The agglomeration of apolar metallic nanoparticles (NPs) brings them within nanometer distances, enabling non-radiative coupling through electron conduction tunneling and plasmonic interactions. Even stronger coupling can be achieved with metallic connections between the particles. Thermally induced coarsening is often used to join particles in this way, but typically requires high temperatures. For example, the thermal coarsening of thiol-coated NPs in apolar dispersions requires heating above $120\,^{\circ}\mathrm{C}$ to induce ligand desorption. This leads to side reactions, notably Ostwald Ripening and the formation of small particles. Here, we demonstrate that reactive chemical additives can enable NP coarsening at near-ambient conditions. Transmission electron microscopy and small-angle X-ray scattering reveal that adding the cyclic sulfide additive molecule tetrahydrothiophene (R5S) to a dispersion of hexadecanethiol (HDT)-coated gold nanoparticles (AuNPs) induces aggregation at temperatures as low as $40\,^{\circ}\mathrm{C}$ to $60\,^{\circ}\mathrm{C}$. The cores form metallic joints, forming larger continuous gold bodies. An Arrhenius analysis of the temperature-dependent aggregation kinetics identifies the exchange of HDT to R5S on the gold surfaces as the rate-limiting step. Small-angle neutron scattering and thermogravimetry confirm the mechanism and indicate that $\sim 80\,\%$ of HDT is replaced by R5S after $5\,\mathrm{h}$ at $50\,^{\circ}\mathrm{C}$. Progressive ligand exchange reduces the steric repulsion by the shells until aggregation sets in. A comparison with the larger cyclic sulfide thionane and the cyclic amine pyrrolidine, which do not induce coarsening, shows that the prerequisite for ligand desorption at moderate temperatures to enable AuNP coarsening is a small size and strong affinity of the additives to the gold surfaces.

3.4.2 Introduction

The assembly of apolar metallic nanoparticles in dispersions reduces interparticle distances to the nanometer scale, enabling strong coupling through non-radiative mechanisms such as electron conduction and tunneling [236], and strong plasmon resonance coupling [237]. This has been exploited to create functional layers from gold nanoparticles (AuNPs) that are stable, easy to modify chemically, and have attractive optical and electronic properties [238, 239]. Such layers are suitable for sensing [198, 240], catalysis [241, 242], and printable electronics [20, 25, 185].

Apolar AuNPs are typically stabilized by an organic ligand shell [57] with amine [201], phosphine [243], or thiol functionalities [202] that bind the nanoparticle surfaces. Previous studies have shown that apolar AuNP agglomeration upon cooling is affected by a disorder-to-order transition of the ligand shell and the attraction of cores [102, 103]. The ligand shell structure depends on the molecular structure of the ligands, which in turn affects their colloidal stability [59, 95, 109, 210]. The balance between core attraction, ligand shell structure, and ligand-

solvent interactions limits interparticle coupling. Very small spacings would require very thin ligand shells that are unable to stabilize the dispersion [42, 45, 102, 152, 157].

It is often useful to establish metallic connections between the particle cores. This can, for example, be exploited to remove electrical contact resistance between printed particles in electronics [25] or to alter plasmonic absorption bands strongly [244]. Metallic connections can also enhance the mechanical stability of nanoparticle assemblies, enabling the formation of porous gold-based structures from dispersions [245] as well as complex ceramic–metallic bulk architectures [169]. The most common route to metallic connections is the thermally induced coarsening of metal nanoparticles.

In dispersions, elevated temperatures — typically above $120\,^{\circ}\mathrm{C}$ — have been used for the coarsening of apolar, thiol-coated AuNPs [147, 155]. Coarsening has been primarily attributed to the thermal desorption of ligands from the nanoparticle surface that reduces the stabilizing and repulsive effect of the ligand shell [146, 155, 159]. As a result, reactions between different cores are possible. Surface diffusion of gold atoms allows Ostwald ripening after desorption of ligands. If the collision energy between AuNPs is sufficiently high, cores can coarsen by coalescence [146, 155].

The temperature required for ligand desorption depends strongly on the chemical nature of the binding group. For example, linear alkyl thiols typically desorb between $120\,^{\circ}\mathrm{C}$ and $180\,^{\circ}\mathrm{C}$ [41]. Smaller [41] or sterically demanding thiols (that are branched in the α-position) [157] have lower desorption temperatures around $20\,\mathrm{K}$ to $30\,\mathrm{K}$ (depending on the molecular structure) [167]. Linear alkyl amines desorb at even lower temperatures, typically between $50\,^{\circ}\mathrm{C}$ and $120\,^{\circ}\mathrm{C}$ [246]. Coarsening in dry nanoparticle superlattices has been reported for significantly lower temperatures. For example, coalescence of oleylamine-coated gold nanoparticles with a diameter of $8.1\,\mathrm{nm}$ has been observed at $70\,^{\circ}\mathrm{C}$, facilitated by reduced ligand density at the (111) facets and strong interparticle attractions in the dry film that displace ligands from the interface [158].

Coarsening has been reported for nanocomposites, too. Meli et al. demonstrated that self-assembled dodecanethiol-coated AuNPs embedded in a poly(methyl methacrylate) matrix coarsened in two stages at $150\,^{\circ}\mathrm{C}$ [146]. During the first $480\,\mathrm{min}$, coarsening proceeded via simultaneous Ostwald ripening and coalescence. This was initiated by ligand desorption, which reduced surface passivation and allowed the diffusion of atoms or small clusters, thereby enabling ripening. As particle sizes increased within the assembly, the interparticle spacing decreased. Once the gap between particle cores fell below approximately $0.5\,\mathrm{nm}$, a second stage dominated by coalescence set in.

We are interested in reactive coarsening processes that join metal nanoparticle cores without side reactions at low temperatures. Such routes are interesting for the “chemical sintering” of printed nanoparticle films into electrically conductive leads [58], the transformation of plasmonic parti-

cles in sensing to elicit a strong optical response [244, 247], and the formation of metal nanoparticle aerogels [248], for example. Few studies have explored the use of reactive additives that modify nanoparticle surfaces and lower the temperatures required for nanoparticle coarsening. In polar dispersions of AuNPs, Kim et al. reported coalescence induced in citrate-coated AuNPs by the addition of benzyl mercaptan at room temperature [249, 250]. Lee et al. studied the coarsening of citrate-covered AuNPs in aqueous solutions using thiolated poly(ethylene glycol) as a destabilizing agent, also at room temperature [245]. Both found that a partial ligand exchange of citrate on the gold surface reduced the zeta potential and the protective effect of the shell sufficiently to induce aggregation of the AuNPs. In dry films or nanoparticle assemblies, coarsening temperatures are usually above $150\,°C$ [60, 159]. Halide-containing surfactants have been used to reduce this temperature from $190\,°C$ to $205\,°C$ to $165\,°C$ to $175\,°C$ [165]. The oxidation of thiol ligands upon air exposure was found to decrease their binding affinity to the gold surface, reducing the shell stability and thereby increasing the reactivity of AuNPs in dry films [168, 251]. To our knowledge, no reports have addressed the reduction of coarsening temperatures for dispersed apolar gold nanoparticles.

Here, we show that small surface-reactive molecules can be used to join gold nanoparticle cores at low temperature. Our previous work showed that the cyclic sulfide tetrahydrothiophene (R5S) partially replaces the initial hexadecanethiol (HDT) ligands on the AuNP surfaces [113]. This ligand exchange lowered the order-disorder transition temperature of the shell, while the larger cyclic sulfide thionane (R9S) and cyclic amine pyrrolidine (R5N) did not significantly alter the ligand shell structure. Here, we report on the reduction of the AuNP coarsening temperatures in apolar dispersions using small molecular additives.

We used transmission electron microscopy (TEM) and small-angle X-ray scattering (SAXS) to analyze the coarsening of the initially spherical gold cores in the presence of R5S, R5N and R9S at temperatures up to $60\,°C$. The combination of thermogravimetric analysis (TGA) and small-angle neutron scattering (SANS) was used to detect changes in the ligand shell structure, induced by the exchange of the initial HDT ligand by the additives. We found that R5S enables the coarsening of initially HDT-stabilized AuNPs in n-decane by aggregation, while pyrrolidine (R5N) and thionane (R9S) did not show such an effect.

3.4.3 Results and Discussion

Spherical nanoparticles (AuNPs) with core diameters of approx. $4\,nm$ and hexadecanethiol (HDT) ligand shells ("AuNP" in the following) were synthesized using well-established methods [43, 58] and dispersed in n-decane at a gold concentration of $2.5\,mg/mL$. Tetrahydrothiophene (R5S), pyrrolidine (R5N), and thionane (R9S) were added as additives at various concentrations. The dispersions were stored for $24\,h$ at room temperature after the addition

of the additives. We followed the subsequent coarsening of the gold cores with transmission electron microscopy (TEM) and in-situ time-dependent small-angle X-ray scattering (SAXS) at elevated temperatures of 40 °C, 50 °C, and 60 °C, and characterized the shell structure using small-angle neutron scattering (SANS), thermogravimetric analysis (TGA) and SAXS, as discussed in the following.

Stages of AuNP coarsening in the presence of R5S

A AuNP dispersion containing an R5S concentration of 128 mM was heated to 50 °C in a vial (1.5 mL). At selected times, aliquots were taken from the dispersion, cooled to room temperature, and analyzed using TEM. The obtained micrographs were analyzed using label analysis to determine the particle sizes and size distributions (see Materials and Methods for details).

Figure 3.4.2 shows TEM images after 0, 150 and 300 min, illustrating a continuous change in core geometry.The original, additive-free particle dispersion was fully dispersed (see Figure 7.4.1a in the Supporting Information). At t = 0 min, primary AuNPs with an average diameter of d = 3.8 nm and a variance of $\sigma = 0.25$ (Figure 3.4.2d) dominated the dispersion (89 %). Only 7 % of the particles had $d < 3.0$ nm and 4 % of the particles had $d < 4.5$ nm. The small fraction of large particles is composed of aggregates consisting of a few primary particles (Figure 3.4.2a), that formed during the 24 h storage time after the addition of R5S.

After 150 min, aggregates formed (Figure 3.4.2b) that are clearly visible in the diameter distributions shown in Figure 3.4.2e. Analysis of their circularity with TEM (see the TEM section of the Supporting Information for a detailed description) suggests that 70 % of the particles with a diameter between 1.5-4.5 nm were spherical, primary particles. Less than 5 % of particles larger than 4.5 nm were spherical, suggesting that most were aggregates. The size distribution of primary particles was practically unchanged after 150 min, excluding Ostwald ripening as the main coarsening mechanism. Instead, we propose that particles aggregate and begin to fuse. This is consistent with reports indicating that temperatures >120 °C are required for diffusion processes between dispersed particles [146, 155].

After 300 min, large aggregates with diameters between $200-2000$ nm were present (Figure 3.4.2c and Figure 7.4.1b in the Supporting Information). These aggregates are the result of the continuous aggregation process during which both primary particles smaller aggregates join together and form larger structures in the μm-range. Figure 3.4.2c indicates that the smaller aggregates within these large assemblies were partly fused, but primary particles remained discernible. Densification due to complete coalescence was not observed during this stage.

Mechanisms of AuNP coarsening in the presence of R5S

We used SAXS to determine the kinetics of aggregation as a function of temperature. Time-dependent scattering patterns were recorded at 50 °C in intervals of 10 min with an integration

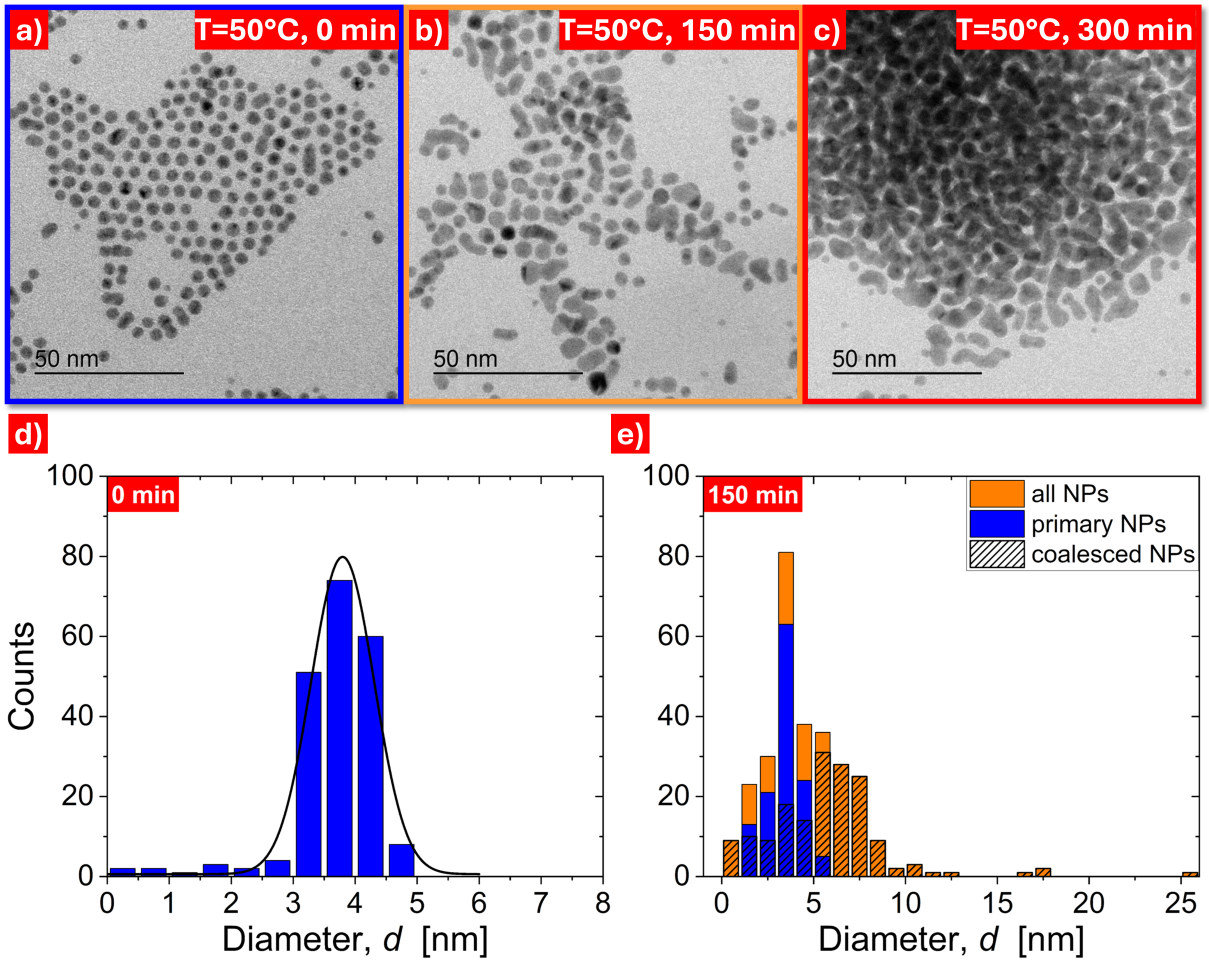


Figure 3.4.2: Coarsening of AuNPs coated with HDT and dispersed in *n*-decane at 50 °C in the presence of R5S at 128 mg/mL. Transmission electron micrographs show the original dispersion (a) before heating, (b) after 150 min at 50 °C and (c) 300 min at 50 °C. The particle size distribution determined from (a) is shown in (d). The particle size distribution after 150 min at 50 °C was determined using three TEM images (see Figure 7.4.3 in the Supporting Information) and is shown in (e). Blue bars in (d) and (e) represent spherical particles (circularity above 0.6), while black dashed bars represent non-spherical particles (circularity below 0.6). Orange bars show the combined size distribution.

time of 5 min (Figure 3.4.3a-b).

The initial scattering from samples 24 h after mixing the AuNPs with R5S prior to heating (Figure 3.4.3a, blue curve) was characterized by an intensity plateau at 0.01 Å to 0.06 $Å^{-1}$, followed by a decay in intensity at $q > 0.06\,Å^{-1}$ and a small peak at 0.27 $Å^{-1}$. It was dominated by the form factor of spherical particles, indicating that no strong coarsening occurred at room temperature. During heating, the slope at low q-values ($q < 0.04\,Å^{-1}$) decreased during the first 150 min and then remained constant. The final slope of $q^{-1.5}$ indicates that the formed particles are mass fractals consisting of networks with a fractal dimension of 1.5 at length scales of ∼10 nm to 100 nm [252], pointing to aggregation by direct collisions and fusion of primary particles, in agreement with the TEM observations above.

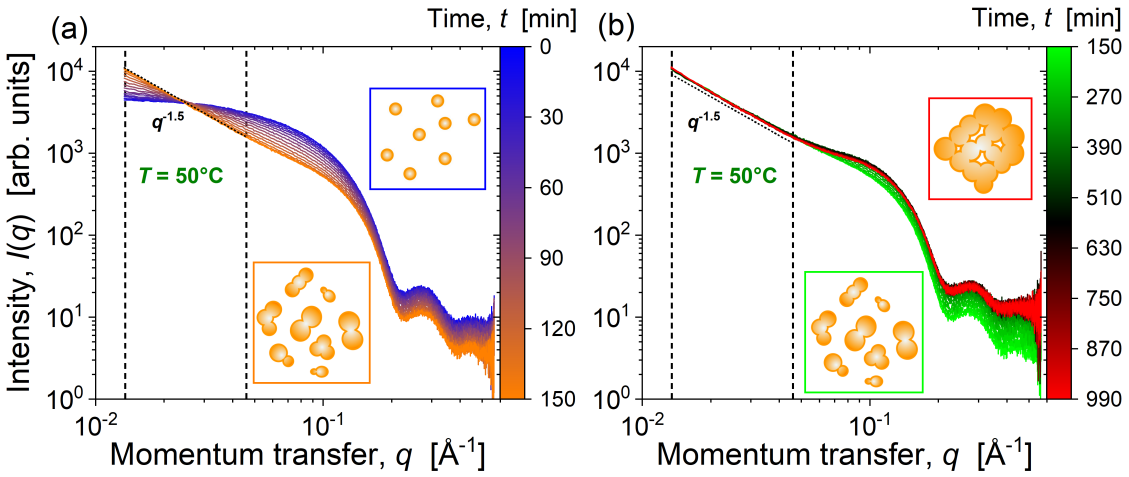


Figure 3.4.3: Time-dependent small-angle X-ray scattering patterns of AuNPs coated with HDT and dispersed in *n*-decane at 50 °C in the presence of R5S at 128 mg/mL. The data was divided into two graphs for clarity, with scattering patterns (a) between 0 and 150 min and (b) between 150 and 990 min.

Further insights into the early stage of coarsening were gained from a quantitative analysis of the obtained SAXS patterns. TEM suggested that spherical, primary nanoparticles and small aggregates consisting of 2 primary nanoparticles were present at early times (0 min to 70 min). Their scattering patterns were modeled using the equation

$$I_{\text{tot}}(q) = I_{\text{Porod}}(q) + I_{\text{pS}}(q) + I_{\text{pDum}}(q) + I_{\text{bkg}} \tag{3.4.1}$$

with $I_{\text{pS}}(q)$ a form factor of polydisperse spheres with a Gaussian size distribution and $I_{\text{pDum}}(q)$ a form factor of dumbbell-shaped particles, i.e., two primary particles with a Gaussian size distribution partly fused together. To account for scattering from larger structures, i.e., aggregates containing more than 2 primary nanoparticles, a Porod term, $I_{\text{Porod}}(q)$, was added. Lastly, I_{bkg} accounts for background scattering. Full equations and details regarding the analysis are given in the Supporting Information.

The initial scattering pattern (Figure 3.4.4a) could satisfactorily be modeled using contributions from spherical nanoparticles and dumbbell-shaped aggregates, while a model considering only polydisperse spheres did not match the data well. This indicates that some aggregation takes place already during the 24 h storage at room temperature after the addition of R5S. Approximately 40 vol% of all particles in the dispersion were dumbbell-shaped, while 60 vol% were spherical primary particles. A Porod term to describe larger structures was not required, suggesting that the fraction of larger aggregates was small. Note that the aggregate fraction from SAXS is above that from TEM analysis. This is likely due to the similarity between the form factors of polydisperse spheres and dumbbells and the statistical limitations of TEM analyis.

After heating for 70 min (Figure 3.4.4b), the scattering pattern displayed a shallow slope at

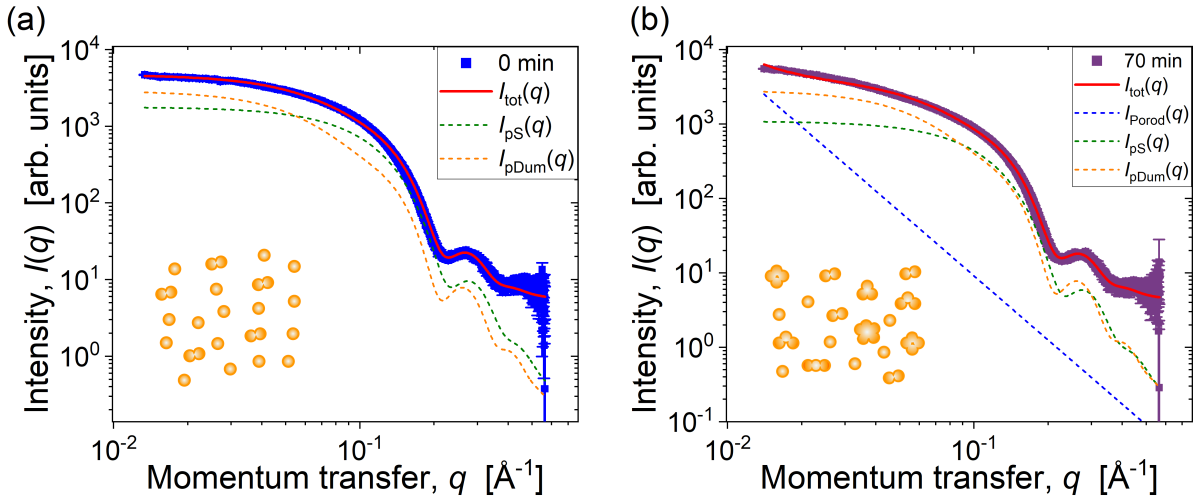


Figure 3.4.4: Model-based analysis of SAXS from coarsening AuNPs dispersions coated with HDT and dispersed in *n*-decane at 50 °C in the presence of R5S at 128 mg/mL after *t*=0 min (a) and after 70 min at 50 °C (b). Solid lines: fits according to eq. 7.4.12 in the Supporting Information. Dashed lines: deconvoluted contributions to the model, as indicated in the graphs.

intermediate q-values (up to 0.1 Å^{-1}), marking the presence of elongated structures. Again, a combination of a form factor of spherical particles and of dumbbell-shaped particles satisfactorily modeled the data. A Porod term was now required to model excess scattering at small q-values, indicating that larger aggregates were present at this stage. 49 % of the particle core volume occupied by spherical primary and dumbbell-shaped particles combined were primary nanoparticles that did not undergo aggregation. However, as aggregates containing more than 2 nanoparticles are not accounted for in this estimation, the overall fraction of primary nanoparticles is lower at this stage, meaning that significantly more primary particles underwent aggregation than after 0 min.

The scattering patterns obtained after 150 min of heating (Figure 3.4.3b) were marked by strong forward scattering, indicating that aggregates containing many primary nanoparticles dominated the dispersion. A shoulder that emerged at approximately 0.1 Å^{-1} is likely due to a structure factor peak that indicates superstructures consisting of primary particles with regular spacings that may be partially fused, in agreement with results from TEM. The dispersion contained large particles with a wide range of geometries. Eq. 3.4.1 became unsuitable and the data were not amenable to model-based fitting.

Effect of the temperature on AuNP coarsening in the presence of R5S

The time-dependent scattering from AuNP dispersions with R5S at 128 mM at 40 °C and 60 °C are shown in Figure 7.4.6 in the Supporting Information. The evolution of scattering at all temperatures was qualitatively similar, but changes occurred at different times. We determined time-dependent power law exponents m of scattering slopes at q-values between 0.013 Å^{-1} and

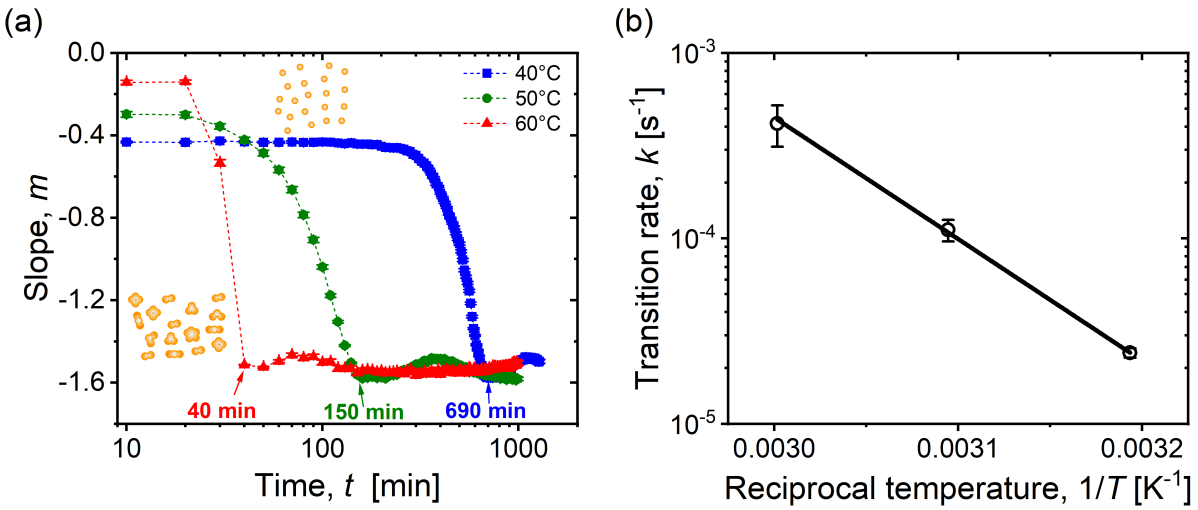


Figure 3.4.5: (a) Slope m of the time-dependent SAXS scattering in the q-range 0.013 Å and 0.045 Å for 40 (blue), 50 (green), and 60 °C (red symbols). (b) Times at which m reached -1.5. Solid line: Arrhenius fit (eq. 7.4.17 in the Supporting Information).

0.045 Å^{-1}, corresponding to length scales of approximately 10 nm to 50 nm. They are shown in log-log representation in Figure 3.4.5 for all investigated temperatures. At all temperatures, the exponent m was constant and slightly below 0 at early times, originating from the intensity-plateau of the form factor of primary particles and dumbbells at small q-values (Figure 3.4.4a). m started to decrease after 20 min at 60 °C and 50 °C and after 280 min at 40 °C. It reached -1.5 after 690, 150, and 40 min for 40 °C, 50 °C, and 60 °C, respectively. This corresponds to mass fractals with fractal dimensions of 1.5 over the probed length scales [252], indicating the formation of branched aggregates.

The continuous decrease in slope reflects the progressive aggregation of primary particles into larger structures. Once the slope stabilized around -1.5, the structure at the probed length scales (approximately 10 nm to 50 nm) remained unchanged. At this point, the majority of primary particles were within aggregates that did not change their structure at length scales of approximately 10 nm to 50 nm. Further growth occurred predominantly through continuous aggregation of existing aggregates rather than primary particles. We define t_f as the time at which the final slope was reached and the majority of the primary particles had coarsened significantly by aggregation.

We used the time-dependent scattering results to assess the kinetics of nanoparticle aggregation and identify rate-limiting steps. First, let us assume that aggregation is limited by diffusion, such that the aggregation rate depends solely on the diffusivity of the primary particles. In this case, the time t_x required to decrease the number of primary particles to a given fraction, $x = N(t_\mathrm{x})/N_0$, can be approximated by

$$t_\mathrm{x} \propto \frac{\eta}{k_\mathrm{B}T} \tag{3.4.2}$$

with η the dynamic viscosity of the solvent, k_B the Boltzmann constant, T the temperature and N_0 the initial number concentration of primary particles (see the Supporting Information for more details).

Increasing temperature increases the diffusion coefficient of primary particles directly and by decreasing solvent viscosity [253, 254], effectively shortening the time between collisions. The expected rate change from $40\,°C$ to $50\,°C$ would imply a decrease of t_x by a factor of 1.13, while increasing the temperature from $40\,°C$ to $60\,°C$ would decrease it by 1.28. Experimentally, we found that t_f decreased much faster, by a factor of 4.6 from $40\,°C$ to $50\,°C$ and by a factor of 17.3 from $40\,°C$ to $60\,°C$. We conclude that the aggregation of nanoparticles in the early stages is not limited by diffusion. A different energy barrier hindering fusion of particles limits the rate of the overall process.

An Arrhenius fit (see equation 7.4.17 in the Supporting Information) of t_f is shown in Figure 3.4.5b. The exponential change of t_f suggests that aggregation is controlled by a single process with an activation energy of 126 ± 4 kJ mol^{-1}. This value is slightly below that of the binding energy of thiol on gold surfaces (130 to 210 kJ/mol [89, 220]) and presumably in the same range as the HDT-R5S exchange energy on the AuNP surfaces. Therefore, it seems reasonable to assume that the exchange reaction of HDT to R5S on the gold surfaces determines the rate of nanoparticle aggregation: An increase in temperature speeds up the process because it reduces the adsorption affinity of both the sulfur and thiol species to the gold surface [41], enabling stronger exchange of HDT by R5S, which is present in excess. In the following, results from SANS, TGA, and SAXS are presented to investigate different additive concentrations to characterize how the ligand exchange rate affects the structural integrity of the shell.

Influence of additive type on AuNP coarsening

We tested the effect of other additives and added the cyclic sulfide thionane (R9S) and the cyclic main pyrrolidine (R5N) to the same dispersions. The goal was to investigate the influence of molecular size and functional group, respectively, on temperature-induced coarsening of AuNPs. For this, temperature-dependent SAXS measurements were performed during heating from $36\,°C$ to $100\,°C$, shown in Figure 7.4.8 in the Supporting Information.

Scattering from dispersions with a gold concentration of $10\,mg/mL$ containing R5S at a concentration of $512\,mM$ continuously changed during heating in a way that was similar to that at constant temperature (Figure 3.4.3 and 7.4.8 in the Supporting Information). Forward scattering increased at $\sim50\,°C$, and a weak structure factor peak at $0.1\,Å^{-1}$ appeared at $\sim70\,°C$, both indicating that aggregation sets in. At temperatures above $80\,°C$, scattering at q-values above $0.03\,Å^{-1}$ clearly decreased, pointing to sedimentation of aggregates. Furthermore, the form factor peak at $0.3\,Å^{-1}$ and the structure factor peak at $0.1\,Å^{-1}$ disappeared, indicating that the

primary nanoparticles within aggregates fused together.

Adding R5N or R9S as additives at equal concentration ($512\,\mathrm{mM}$), the scattering curves did not indicate coarsening of the AuNPs at temperatures up to $100\,^{\circ}\mathrm{C}$. At low temperatures, weak deviations from a form factor of polydisperse spheres at small q-values point to agglomeration of a small fraction of AuNPs, which was not observed for additive-free dispersions (also shown in Figure 7.4.8 in the Supporting Information). With increasing temperature, however, the deviations diminished and only dispersed AuNPs were observed. It can be concluded that R5N and R9S are unable to induce aggregation of AuNPs at temperatures below $100\,^{\circ}\mathrm{C}$.

Ligand shell composition and structure

Earlier MD simulations have shown that R5S replaces HDT on the AuNP surfaces [113], possibly deteriorating the protective function of the ligand shell. R9S molecules, in contrast, are too large to reach the gold surface through a dense ligand shell. R5N is able to reach the surface, but its binding energy is insufficient for exchanging HDT on the gold surface. Consequently, ligand exchange of HDT by R9S and R5N is presumably less pronounced than ligand exchange by R5S, retaining the protective function of the shell, also at elevated temperatures.

To investigate this, SANS was carried out to quantify the structure and composition of the ligand shell in the presence of additive molecules. HDT-coated AuNPs were dispersed in deuterated n-decane (decane-d_{22}) at a gold concentration of $10\,\mathrm{mg/mL}$ to obtain sufficient scattering intensities. R5S, R9S or R5N were added at room temperature at concentrations of 0, 64, 256, and $512\,\mathrm{mM}$ to expose the shells to various amounts of additive molecules. The samples were stored for two days prior to the measurements to allow for an absorption/desorption balance on the gold surface to set in. A measuring temperature of $35\,^{\circ}\mathrm{C}$ was chosen to initiate additive-induced changes in the ligand without the occurrence of strong AuNP coarsening that disrupts the ligand shells entirely.

Figure 3.4.6a shows SANS patterns of AuNP dispersions at different R5S concentrations. All scattering patterns featured a shoulder above $0.02\,\mathrm{Å}^{-1}$ and a faint peak at $0.15\,\mathrm{Å}^{-1}$, in accordance with the scattering pattern expected for spherical core-shell particles. Additionally, weak forward scattering was present in all cases, indicating weak agglomeration of the AuNPs, in agreement with temperature-dependent SAXS measurements (Figure 7.4.8 in the Supporting Information). The overall appearance of the SANS patterns of AuNPs in the presence of R5N and R9N was similar (Figure 7.4.10 in the Supporting Information); most notable are additive-dependent differences in the absolute intensities of the shoulder.

The absolute scattering intensities depend on the contrast between different components in the system: While the scattering length densities of the gold core and the solvent are set, that of the ligand shell depends on its composition and, therefore, on the specific interactions of the additive molecules with the ligand shell. To deduce the composition of the ligand shell, the

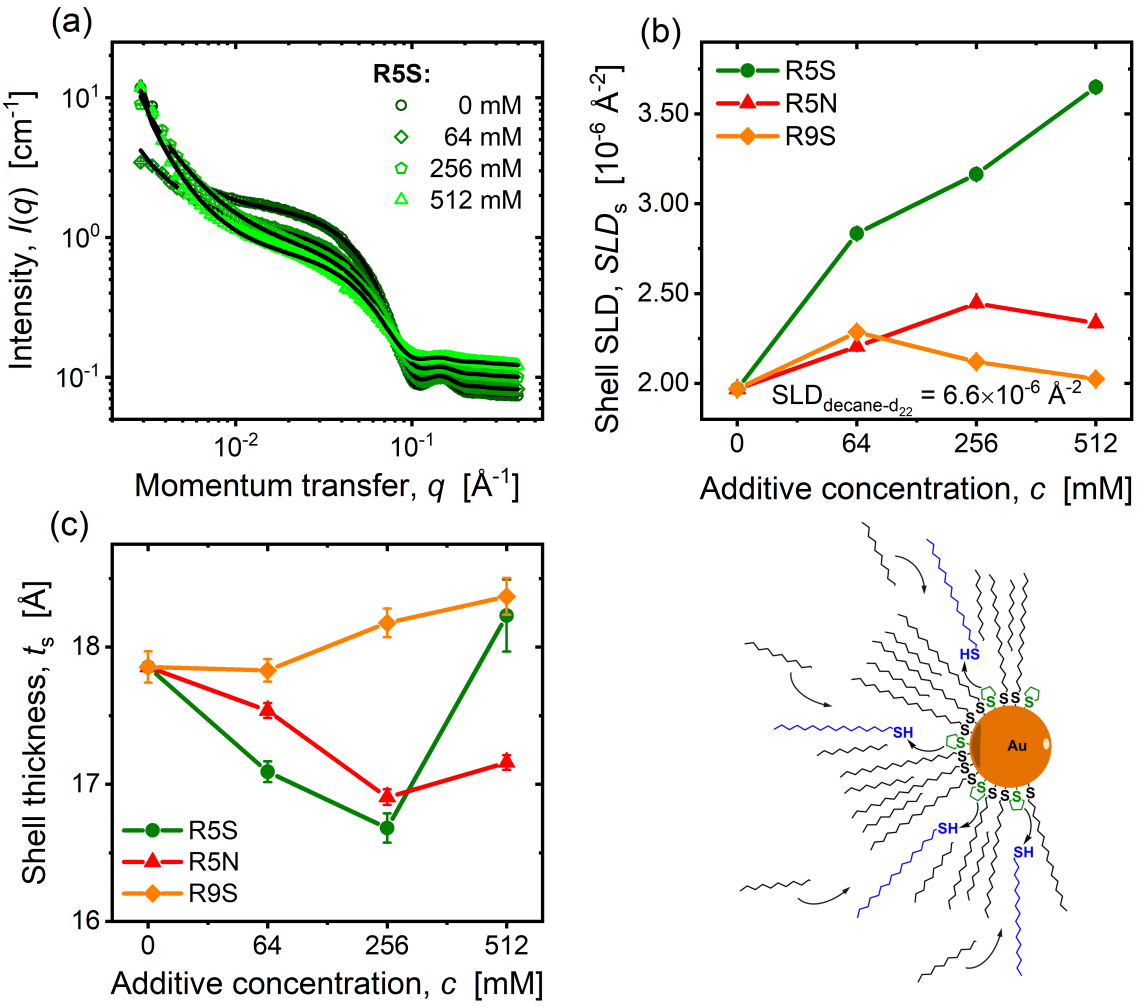


Figure 3.4.6: (a) SANS patterns of AuNP dispersions at a gold concentration of 10 mg/mL in the presence of R5S at concentrations as indicated in the graph. The black lines are model fits according to eq. 3.4.3. (b) Scattering length density, SLD_s, and (c) thickness of the shell, t_s, in dependence on additive concentration for R5S (green data), R5N (red data) and R9S (orange data). (d) Sketch of the ligand exchange mechanism: HDT is replaced by R5S on the surface, opening up space for decane to enter the shell. As a result, SLD_s increases.

SANS patterns were modeled using the equation

$$I_{tot}(q) = I_{Porod}(q) + I_{pCS}(q) + I_{OZ}(q) + I_{bkg} \tag{3.4.3}$$

with $I_{pCS}(q)$ a form factor for polydisperse spherical core-shell particles to describe the core and shell of the AuNPs, which includes the shell thickness t_s and the scattering length density SLD_S of the shell as free variables. $I_{OZ}(q)$ is an Ornstein-Zernike structure factor to describe scattering from composition fluctuations in the solvent and $I_{Porod}(q)$ a Porod term to account for weak agglomeration of the AuNPs. Lastly, I_{bkg} accounts for incoherent background scatter-

ing. Full equations are given in eqs. 7.4.26-7.4.29) and illustrated in Figure 7.4.9, both in the Supporting Information. For R5N and R9S, excellent comparisons between the model and data were obtained. In the case of R5S, slight deviations were observed, most probably caused by the onset of AuNP aggregation.

SLD_s is a measure of the shell composition. It is particularly sensitive to the presence of deuterated n-decane within the shell, as its scattering length density ($6.6 \times 10^{-6}\,\text{Å}^{-2}$) differs significantly from that of the non-deuterated HDT ligands or additive molecules (all in the range of $-0.3 \times 10^{-7}\,\text{Å}^{-2}$ to $-3 \times 10^{-7}\,\text{Å}^{-2}$). In the absence of additive molecules, SLD_s was $1.97 \times 10^{-6}\,\text{Å}^{-2}$ (Figure 3.4.6b). This corresponds to a shell composition of 56:44 n/n HDT to n-decane, assuming bulk molecular volumes for both species. Upon addition of additive molecules, SLD_s increased for all additive types. R5S led to the largest measured SLD_s of $6.65 \times 10^{-6}\,\text{Å}^{-2}$ at $512\,\text{mM}$. In contrast, the presence of R5N and R9S increased SLD_s only weakly. At $256\,\text{mM}$ R5N it was $2.45 \times 10^{-6}\,\text{Å}^{-2}$ before decreasing again at higher concentrations. The larger additive R9S only led to an increase up to $2.29 \times 10^{-6}\,\text{Å}^{-2}$ at $64\,\text{mM}$, followed by a weak decrease at higher concentrations.

Figure 3.4.6c shows t_s in dependence on additive concentration for each investigated additive type. In the absence of additive molecules, the shell thickness was $17.9\,\text{Å} \pm 0.2\,\text{Å}$, slightly below the length of fully stretched HDT ligands [109]. This indicates that the ligands have an extended conformation and that they are homogeneously distributed in the shell. With increasing additive concentration, marginal differences in t_s below ~ 1 Åwere observed. This points to weak structural changes of HDT ligands within the shell during the presence of additive molecules of any type, while remaining in a stretched conformation.

The strong increase in SLD_s in combination with a marginally changing t_s upon the addition of R5S is consistent with a partial exchange of HDT by the smaller additive molecule on the gold surface. This exchange frees up space, allowing more n-decane molecules to solvate the ligand shell. Consequently, the fraction of n-decane in the shell increases, leading to a larger SLD_s. For R5N and R9S, the minimal increase in SLD_s at low concentrations is likely due to a limited ligand exchange. At higher concentrations, the observed reduction of SLD_s points to physisorption of R5N or R9S that may crowd the shell, displacing n-decane and reducing SLD_s. These results were confirmed by TGA. Assuming that all unbound molecules were removed during sample preparation, where we found that $128\,\text{mM}$ of R5S replaced $21\,\%$ of the HDT (in a dispersion with a gold concentration of $2.5\,\text{mg/mL}$) after one day at room temperature and $82\,\%$ after $5\,\text{h}$ at $50\,°\text{C}$ (see Figure 7.4.7a in the Supporting Information). In the case of R5N and R9S, no indication for ligand exchange was found (see Figure 7.4.7b in the Supporting Information).

The desorption of HDT on the gold surface likely weakens the protective function of the ligand shell. This allows gold surfaces of different particles to come closer to each other, initiating aggregation. To confirm this, temperature-resolved small-angle X-ray scattering results were

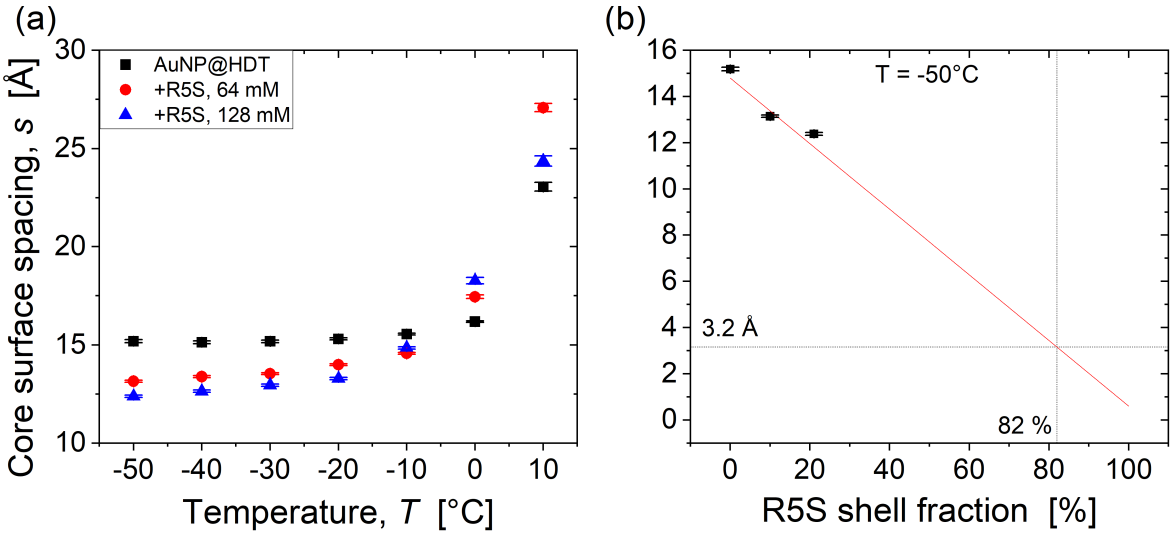


Figure 3.4.7: Temperature-dependent core surface spacings, s, from SAXS for additive-free reference AuNP@HDT (black symbols) and particles treated with R5S of 64 mM (red symbols) and 128 mM (blue symbols) in toluene (a). Linear approximation of the spacing as a function of the R5S fraction in the shell using the spacings of (a) at $-50\,°C$ (b).

performed as discussed in the following.

Additive-dependent core surface spacing

Alkylthiols form dense ligand shells with thicknesses that depend on the ligand length [43, 87, 88]. Partial exchange of HDT by R5S in the AuNP ligand shell may reduce the spacing between gold surfaces in agglomerates. We used controlled partial ligand exchange to replace HDT ligands by R5S without inducing nanoparticle coarsening. To this end, we treated AuNPs with R5S at concentrations of 64 mM or 128 mM for 24 h and purified them to obtain AuNP where either 10 % to 12 % [113] or 21 % of HDT had been replaced by R5S (see Figure 7.4.7 in the Supporting Information). The dispersions were cooled in toluene using well-established protocols to induce AuNP agglomeration [43, 58] while X-ray scattering patterns were obtained at different temperatures. The core surface spacings s were calculated using equation 7.4.11 in the Supporting Information; they are shown in Figure 3.4.7 as a function of temperature in the agglomerated state [210].

s decreased with temperature for all shell compositions, probably due to the increasing bundling of the ligands that allows particles to pack more densely [43, 58]. The AuNP@HDT reference reached a spacing of 15.2 Å at $-50\,°C$. Modification with 64 mM R5S (10 % to 12 % of R5S in the shell) led to a spacing of 13.2 Å at $-50\,°C$, while 128 mM (21 % of R5S in the shell) led to a spacing of 12.4 Å at $-50\,°C$.

We propose that the replacement of the larger HDT in the particles' shells by smaller R5S causes the reduced spacing, which in turn enables joining of the metal surfaces. This is consistent with

literature: For example, Bae and colleagues investigated the approach of gold nanoparticle cores with pure hexadecyltrimethylammonium bromide (CTAB) shells and mixed shells of CTAB and the smaller octylamine during their aggregation. The core-surface spacing for particles coated with pure CTAB decreased continuously from 4 nm to 1 nm before joining, while cores with mixed shells approached abruptly. For both systems, at a critical distance of approximately 1 nm, a jump-to-contact occurs, after which both cores join. It was concluded that the enhanced mobility of mixed shells promotes the rearrangement and detachment of ligands in the gap region, leading to the more rapid aggregation of the nanoparticles [255].

Note that we could not measure the core surface spacings s of our particles for high R5S fractions. Their distribution became too wide for analysis via SAXS when aggregation set in. Figure 3.4.7b shows the three measured spacings at R5S shell fractions below 25%. We can linearly extrapolate and estimate that spacings would drop to below 1 nm at R5S shell fractions above 40%. We can use the same approach to roughly estimate the spacing at the R5S fraction of 82 % that was reached after 5 h at 50 °C (Figure 7.4.7a in the Supporting Information); this would be approximately 3 Å.

Literature suggests that cores of gold nanoparticles with surface spacings in the range of 0.5 nm to 2 nm can form metal connections, depending on the system [255–258]. Two mechanisms are discussed. In one, ligand molecules are displaced from the contact by desorption of rearrangement, allowing direct contact and adhesion of the cores [256–259]. A second mechanism involves the diffusion of gold atoms that form a bridge between cores [161, 260, 261] even if the ligands are not (entirely) displaced. We propose that, in our case, R5S reduces the spacing between gold surfaces and is more easily displaced than HDT, as the sulfide is less strongly bound to the gold. Thus, R5S initiates its own removal by reducing s to below its critical value.

3.4.4 Conclusion

Coarsening of apolar gold nanoparticles is hindered by the steric repulsion of ligand shells that prevents the cores from coming close. Consequently, thermally-induced coarsening typically takes place at temperatures above 120 °C, where the ligand desorption leads to a structural defect in the ligand shell. Here, we showed that chemical additives can be used to provoke structural defects by ligand exchange reactions, leading to coarsening at near-ambient conditions.

Transmission electron microscopy and small-angle X-ray scattering revealed that adding the cyclic sulfide additive molecule tetrahydrothiophene (R5S) to a dispersion of hexadecanethiol (HDT)-coated gold nanoparticles (AuNPs) induces aggregation and joining of cores at temperatures of 40 °C to 60 °C. Initially, AuNPs form small aggregates consisting of only a few AuNPs. These grow over time and form micron-scale aggregates after several hours. Concurrently, metal cores form metallic connections.

An Arrhenius analysis of AuNP aggregation identified the exchange of HDT on the gold surfaces by R5S as the rate-limiting step of the overall process. Small-angle neutron scattering indicated that increasing R5S concentration leads to larger fractions of R5S in the forming mixed monolayer on the nanoparticle surface; thermogravimetric analysis confirmed that the fraction at a given time is temperature-dependent. Particle cores join when a certain fraction of R5S in the shell is reached. In contrast, cyclic sulfide thionane (R9S) or cyclic main pyrrolidine (R5N) did not induce aggregation or joining of AuNP. None of them was able to replace sufficiently large fractions of HDT in the ligand shell.

We identified the core surface spacing as the main factor in the joining of metal particle cores. Temperature-induced agglomeration of AuNP with mixed HDT-R5S monolayers at defined ratios in SAXS indicated that larger R5S fractions reduce the spacing between the gold cores in aggregates. There exist a certain critical spacing (likely below 1 nm) below which the metal cores form metallic joints.

Our work provides a pathway for controlled coarsening of apolar gold nanoparticles under mild conditions. As opposed to their reversible agglomeration, this allows for large changes in interparticle coupling, e.g., electron transfer or plasmonic interactions, that lead to dramatic changes in the system's properties. It paves the way for improved or new materials in fields such as printed electronics and sensing.

3.4.5 Materials and Methods

Nanoparticle synthesis

Gold nanoparticles (AuNPs) with a core diameter of 4 nm were synthesized following a method described previously [58]. In short, a mixture of 9 mL of n-pentane (Carl Roth, 99 %) and 9 mL oleylamine (Sigma Alrich, technical grade, 80 – 90 %) was added to 100 mg of tetrachloroauric(III) acid trihydrate $HAuCl_4 \cdot 3\,H_2O$. The mixture was stirred (with a magnetic stirrer bar) for 21 min at 22 °C under an argon atmosphere. Then, a mixture of 1 mL n-pentane, 1 mL of oleylamine and 40 mg tert-butylamine borane complex (FLUKA, 97 %) was added to the gold precursor solution. The mixture was stirred for 60 min. The dispersion was purified by precipitation with 50 mL of a mixture of ethanol and methanol (ratio 3:2) and centrifugation at 2000 rpm (689 rcf) for 1 min. The supernatant was removed, and the nanoparticles were redispersed in 2.5 mL toluene (gold concentration of 10 mg/mL).

Ligand exchange

For the ligand exchange the dispersion was heated to 80 °C, followed by the addition of 1 mL of hexadecanethiol (Sigma Aldrich, GC, 95 %) (0.4 mL per 1 mL of a dispersion with a gold concentration of 10 mg/mL) [58]. The mixture was stirred for 15 min at 300 rpm.

The dispersion was purified by precipitation with 3 times the sample volume (3 mL for 1 mL dispersion) of a mixture of ethanol and methanol (ratio 2:1) and centrifugation at 2000 rpm (689 rcf) for 5 min. The supernatant was removed, and the nanoparticles were redispersed in 2.5 mL toluene. The washing step was repeated once with a cooled mixture of ethanol and methanol (2:1). After the last washing step, the sample was redispersed in n-decane and diluted to a gold concentration of 2.5 mg/mL.

Synthesis of thionane (R9S)

The synthesis of the additive thionane was based on the protocol described by Singh et al. [204] and described in detail in our earlier work [113].

Addition of additives

Tetrahydrothiophene (R5S, Sigma Aldrich, GC, 99 %), thionane (R9S, own synthesis) and pyrrolidine (R5N, Sigma Aldrich, GC, 99 %) were used as additive. Before their addition to the AuNP dispersions, the AuNP dispersions at a gold concentration of 2.5 mg/mL in n-decane were heated to 50 °C for 10 − 15 min to ensure that all AuNPs were dispersed. Subsequently, the dispersions were cooled to 30 °C and the additives were added. The mixtures were shaken for 1 − 2 min minutes and stored without stirring for 24 h at room temperature.

Small-Angle X-ray Scattering

A laboratory-scale Xeuss 2.0 instrument (Xenocs SA, France) was used for all SAXS measurements. The X-ray beam was produced by a copper K_α source (wavelength 1.54 Å) and focused on the sample with a spot size of 0.25 mm^2. The measurements were performed with a sample-detector distance (SDD) of 1020 mm. The measurable momentum transfer q ranged from 0.01 Å^{-1} to 0.6 Å^{-1}, with q being defined as $q = 4\pi\sin(\theta/2)/\lambda$, were θ is the scattering angle. The samples were measured in borosilicate capillaries with a diameter of 1.5 mm.

Time-dependent aggregation measurements using AuNP dispersions with a gold concentration of 2.5 mg/mL and an additive concentration of 128 mM were performed at 40 °C, 50 °C and 60 °C. Prior to each, a SAXS pattern was acquired at room temperature. After heating to the desired temperature, subsequent measurements with an acquisition time of 5 min per performed with a waiting time of 5 min after each measurement. Measurements were performed until no further changes were visible in the scatter curves.

Temperature-dependent aggregation measurements were performed using AuNP dispersions with a gold concentration of 10 mg/mL and an additive concentration of 512 mM. For these measurements, R5S, R5N, and R9S were used as additives. As a reference, an additive-free dispersion was measured. All samples were heated from 36 °C to 100 °C in steps of 2 K, with a waiting time of 5 min after each step that was followed by the acquisition of a SAXS pattern

with an integration time of 5 min.

Temperature-dependent agglomeration measurements were performed similarly to our previous work [210]. AuNP dispersions with a gold concentration of 2.5 mg/mL and R5S concentrations of 0 mM, 64 mM, and 128 mM were cooled from 20 °C to −50 °C in steps of 10 K. At each temperature, three SAXS patterns were measured with acquisition times of 5 min, following a 5 min waiting time.

The analysis of the time- and temperature-dependent scattering curves is described in the Supporting Information.

Small-Angle Neutron Scattering

SANS measurements were performed at the Institute Laue-Langevin in Grenoble (France) at the instrument D22. Using a neutron wavelength of λ=6 Å with a spread of $\Delta\lambda/\lambda = 0.10$ and sample-detector distances (SDD) of 17.6 m (detector 1) and 1.4 m (detector 2), an accessible q-range from $0.003 - 0.4$ Å^{-1} was covered. The samples were measured in cylindrical quartz glass cells (type QS-120, Hellma, Germany) with a layer thickness of 2 mm. The obtained data were corrected for scattering by the empty cell and for parasitic scattering using a measurement of boron carbide. H_2O was measured to calibrate the detector sensitivity. The measured data were converted to an absolute scale using a direct beam measurement, and the scattered intensity $I(q)$ was obtained by azimuthally averaging the 2D scattering patterns.

AuNP dispersions with a gold concentration of 10 mg/ml dispersed in decane-d_{22} were measured in the presence of R5S, R5N, and R9N at concentrations of 128 mM, 256 mM, and 512 mM. Prior to the measurements, the samples were heated for 10 min at 36 °C, followed by a SANS data acquisition for 30 min. Scattering from the additive solutions (in the absence of AuNPs) was measured as a reference.

Transmission Electron Microscopy

For the imaging of the gold nanoparticles a JEOL JEM2100 LaB6 electron microscope (JEOL ltd. Tokyo, Japan) with 200 kV acceleration voltage, 0.14 nm line resolution, and a Gatan Orius SC1000 camera (Gatan Inc. Pleasanton, CA, USA) in brightfield mode was used. AuNP samples were prepared by drop-casting of $10 - 20$ µL of the particle dispersion in n-decane (2.5 mg/mL) on a TEM copper grid.

For the characterization of the AuNP coarsening kinetics, a dispersion with a R5S concentration of 128 mM was heated to 50 °C. After 70 min, 150 min, and 300 min, samples were taken. These were drop-casted on a copper grid and analyzed using TEM. The analysis of the TEM images is described in the TEM section in the Supporting Information.

Thermogravimetric Analysis

For the thermogravimetric analysis (TGA), additive-free and additive-containing nanoparticle dispersions with gold concentrations of 20-30 mg/mL were prepared. The additive-free dispersion was transferred to n-hexane after the second washing step following the ligand exchange. The additive-containing dispersions were washed twice after the addition of the additive to remove all unbound HDT and R5S molecules and redispersed in n-hexane at a gold concentration of 20-30 mg/mL. Due to the washing, the additive concentration is unknown.

The samples for TGA measurements were prepared by drop-casting the dispersions onto Al_2O_3 crucibles. n-hexane was evaporated at ambient conditions. Subsequently, the samples were dried in a vacuum oven (p = 10 mbar, T = 30 celsius) for 1-2 hours. For the TGA measurement, an STA 449F3 setup from NETZSCH was used. The samples were heated with 10 °C/min to 1000 °C. During the heating, an argon atmosphere was used.

3.4.6 Acknowledgment

The authors acknowledge ILL for allocation of beamtime at instrument D22 (doi: 10.5291/ILL-DATA.9-12-709) and Thomas Kister (INM) for support with the small-angle neutron scattering experiments. Dominik Perius (INM) is acknowledged for performing image analyses of the transmission electron microscopy measurements. T.V.K. thanks the DFG for financial support (Geschäftszeichen: KR 3729/18-1).

3.5 Publication 4: Gold Sponge Formation by Temperature-induced Aggregation of a Stable Nanoparticle Dispersion

Knapp, T. V.; Perius, D.; Niebuur, B.-J.; Nothdurft, B.; Kraus, T. Gold Sponge Formation by Temperature-induced Aggregation of a Stable Nanoparticle Dispersion. *in preparation*

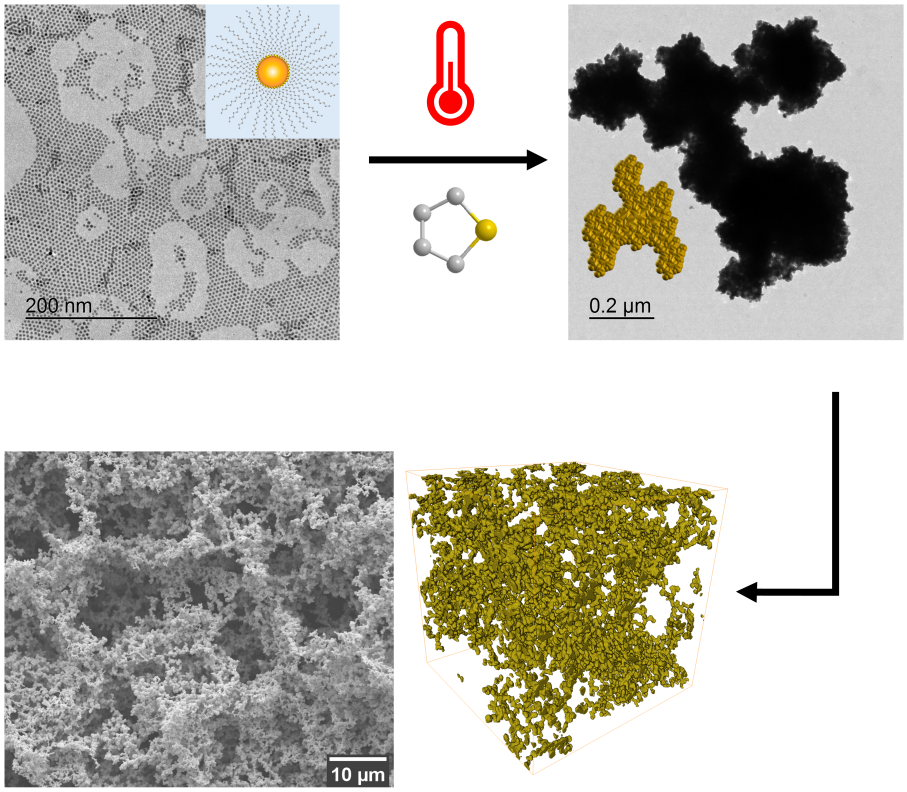


Figure 3.5.1: Table of contents figure of Publication 4.

3.5.1 Abstract

Porosity increases the specific surface area of materials and can reduce the metal mass required in applications. Gold sponges are 3D-porous materials that have been used in catalysis, energy storage, and as electrodes. Here, we introduce a fast and controlled method to synthesize gold sponges from non-polar nanoparticles. Gold spheres with diameters below $10\,\mathrm{nm}$ with hexadecanethiol (HDT) shells reacted with tetrahydrothiophene (R5S). Aggregation and sponge formation were induced by heating the dispersion at $90\,^{\circ}\mathrm{C}$, which induced partial ligand exchange. We used dynamic light scattering and transmission electron microscopy to demonstrate that sponge formation initiated with the coarsening of particles, resulting in colloidal instability and the formation of dense aggregates. Sponges were then formed by sedimentation and fast contact aggregation. They consisted of particle networks with properties that depended on core size and ligand type. Network structures of freeze-dried sponges were reconstructed by FIB-SEM tomography, revealing a porosity of up to $96.1\,\%$ and connected pores with a specific surface area of up to $7.9\,\mathrm{m^2 g^{-1}}$ depending on the used particle system. Our findings demonstrate that modifying the shell structure can be used to induce aggregation and sponge formation.

3.5.2 Introduction

Precious metals such as gold are irreplaceable in many areas due to their chemical and physical properties [262–266]. Their high prices make it attractive to increase the specific surface area of metal-based materials and reduce the required metal mass [267]. Porous nanostructured metals [268–270] are used in catalysis [271–274], as porous electrodes [275–277], in fuel cells [278–281], and in chemical and bio-sensors [282–285].

Metal sponges are non-ordered porous materials with an interlinked structure [286]. They are frequently made by de-alloying [278, 281], usually by removing one alloy phase (e.g., Ag from Au-Ag) by an acid [276, 277]. Template-controlled reduction [287, 288] is an alternative that involves the deposition on a substrate that is then removed [289, 290]. Other methods include the thermal decomposition of suitable metal precursors or electrodeposition [275, 286]. None of them is compatible to printing, and many require templates, strong acids, or drastic reaction conditions [245, 291]. We are interested in routes that require only moderate conditions and yield sponges by printing a precursor layer from an ink that is then converted into a sponge.

Sponge-like structures can be formed from dispersed nanoparticles without the need for a template. Nanoparticle self-assembly yields porous structures that can be converted to metal solids hydrothermally, for example [292]. Upon heating an aqueous dispersion, thiol shells desorb, gold particles aggregate, and coalesce. Ions or molecules can induce aggregation in aqueous particle dispersions, too, forming sponge-like structures at lower temperatures. For example, Liu et al. [293] and Zhang et al. [291] induced the aggregation of citrate-coated gold nanopar-

ticles with core diameters between 15 nm to 65 nm by replacing the citrate ligand with halogen ions, which reduced the electrostatic repulsion such that van der Waals attraction became dominant. Lee et al. replaced citrates with thiolated poly(ethylene glycol), reducing surface charge. The multi-dentate adsorption of the polymer did not provide sufficient steric or electrostatic stabilization, and the particles aggregated [245]. Both the ion-induced reaction in the work of Liu et al. [293] and Zhang et al. [291], as well as the polymer-induced reaction of Lee et al. [245], started briefly after adding the ions or molecules, which limits their use in ink-based applications.

There are far fewer reports on the formation of sponge-like metal structures from apolar dispersions. Zhang and colleagues decomposed dodecanethiol-coated gold nanoparticles (diameter of 2.3 nm) in toluene or toluene-alcohol in an autoclave at 180 °C for 3 h to 9 h to form sponges [292]. Such harsh conditions are often necessary because dense ligand shells, as they are common in apolar dispersions, protect cores against diffusion [42, 152, 154]. To induce ripening or aggregation processes, the shell often has to be desorbed or decomposed [147, 155, 164, 165, 168]. Standard methods for destabilization and ligand desorption, such as the addition of ions, are not suitable for apolar dispersions.

We have shown that the colloidal [113] and shape stabilities of thiol-coated, non-polar gold nanoparticles can be altered using small reactive additives (see Chapter 3.4). Partial replacement of the initial ligand by tetrahydrothiophene (R5S) leads to the formation of gaps in hexadecane shells, for example, and the protective or steric effect of the shell decreases. The exchange kinetics depend on R5S concentration, temperature, and core size. This enables the aggregation of gold cores and the formation of gold sponges by moderate heating, as we will show in the following.

In this work, we demonstrate the formation of gold sponges from a colloidally stable, R5S-containing dispersion ($\leq$ 2.5 vol% of R5S) of hexadecanethiol-coated gold nanoparticles by heating to 90 °C. In less than 20 min, sponges with sizes in the mm-cm range formed. We used dynamic light scattering (DLS) and transmission electron microscopy (TEM) to analyze the formation process of the gold sponges. The results were used to establish a model of the stepwise coarsening, sedimentation, and contact aggregation of ligand-coated gold nanoparticles. Reduction of the gold-surface and desorption of the additive and ligand molecules lead to self-cleaning of the surface, resulting in organic residues $\leq$ 0.5 m%. The properties of the sponges were characterized using thermogravimetric analysis (TGA), gas adsorption with Brunauer-Emmett-Teller analysis (BET), and focused ion beam scanning electron microscopy (FIB-SEM) for 3D reconstruction. Changing core sizes or ligands resulted in sponges with different network structures.

3.5.3 Results and Discussion

Spherical nanoparticles (AuNPs) with core diameters of 4 nm or 9.1 nm were functionalized with hexadecanethiol (HDT) ligands and dispersed in toluene at a gold concentration of 5 mg/mL. The initial core sizes were analyzed using Small-Angle X-ray Scattering (SAXS, see Figure 7.5.18 in the Supporting Information). Tetrahydrothiophene (R5S) was used as an additive in a concentration of 256 mM. This mixture remains stable at room temperature for at least one week, as shown previously (see Chapter 3.4).

The additive-containing dispersion was heated in 5 min to 90 °C and kept at 90 °C (cf. details in the Methods section). During the reaction, the dispersion became turbid and particles sedimented. After 15 min, the sedimented particles formed a flat gel at the bottom of the vial that could be densified by gentle shaking. The densified gel consisted of pieces in the mm to cm range and was transferred to a flask for purification and freeze-drying (see Figure 7.5.17 in the Supporting Information).

Scanning electron microscopy (SEM) was used to analyze the structure of the dried gels. Figure 3.5.2 shows samples prepared from 4 nm gold particles coated with HDT. The analysis reveals that a porous metal formed from the gold nanoparticles (Figure 3.5.2). Its structure was reminiscent of "sponges" reported previously [245, 286, 289, 290, 292, 294]. It is clearly visible that the porous material consists of particles with diameters above 100 nm that formed from the initial nanoparticles. We will refer to this material as "sponge" in the following.

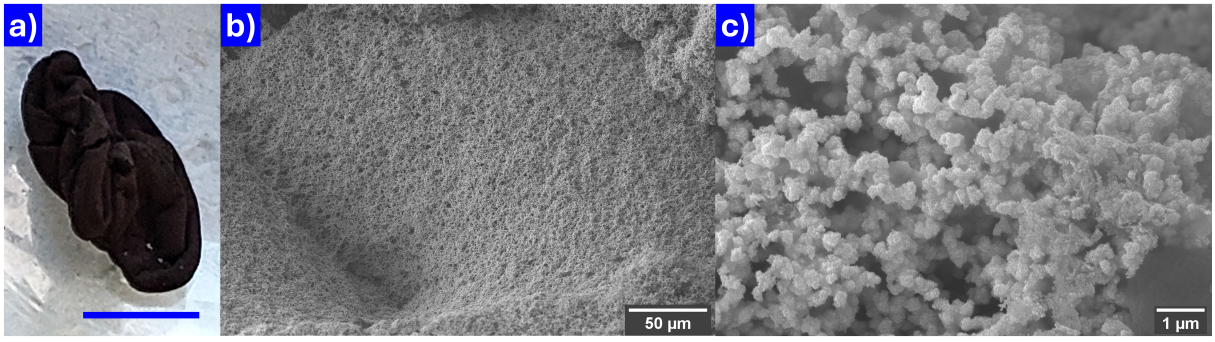


Figure 3.5.2: Image of a gold sponge made from 4 nm AuNP coated with hexadecanethiol. The blue bar corresponds to 0.5 cm (a). Scanning electron micrographs of sponges formed from hexadecanethiol-coated gold nanoparticles reacting with R5S after 15 min at 90 °C (b, c).

Gas adsorption measurements with BET analysis indicated a specific surface area (SSA) of 5 m^2g^{-1}, comparable to the values of 2 m^2g^{-1} to 15 m^2g^{-1} reported for porous gold materials made from self-assembled gold particles in literature [245, 295]. Thermogravimetric analysis showed an organic fraction of below 0.2 %, far below that of the original dispersion. It is known that R5S replaces hexadecanethiol on particles and forms mixed layers (e.g., with an R5S fraction of 82 % after 5 h at 50 °C, see Chapter 3.4).

We calculated the shell density of the sponge system and compared it to the value of the initial nanoparticle system. Details of the calculation are shown in the Supporting Information. Depending on the shell composition, we found densities between $0.17\,\mathrm{nm}$ to $0.23\,\mathrm{nm}^{-2}$. The initial particle system has densities around $6.7\,\mathrm{nm}^{-2}$ (see Chapter 3.4).

The markedly smaller shell density indicates that additional ligand was removed during sponge formation. We suggest that the formation of new, lower-energy facets on the gold surface reduced the average binding energy of the ligands, leading to desorption [296]. Bo et al. reported that $8\,\mathrm{nm}$ AuNPs with (111) facets markedly reduced OAm coverage, reducing spacing and supporting coalescence [158, 226].

To quantify sponge structure, the gold network was reconstructed using focused ion beam tomography. The results of the reconstruction are shown in Figure 3.5.3. Image analysis of the reconstructed network indicated a porosity of $96.1\,\%$ (see Figure 3.5.3a), consistent with the surface appearance in SEM.

Network analysis of the sponge structure indicated a centroid path tortuosity of 4.68 and a fractal dimension of 2.2. This fractal dimension indicates a large degree of bifurcation [297], consistent with the richly nanostructured sponge surfaces shown in Figure 3.5.2c. This suggests that the network forms through irreversible connections upon first particle contact during sedimentation. It is advantageous for applications where large specific surfaces and accessibility are essential.

The tortuosity of porous materials can be used to estimate transport properties [298], for example, the electrical conductivity of gold sponges or their accessibility as a catalyst. For example, a tortuosity of 4 indicates that the shortest path that an electron can take between two points is four times that of the shortest distance. Consequently, large tortuosities of the metal suggest larger electrical resistance; large tortuosities of the pores result in longer diffusion times. A value above 4 indicates that the network's paths are extremely convoluted.

We segmented the sponge structure using image analysis (cf. 3D reconstruction in the Methods section). The removal of narrow connections between gold volumes showed that the sponges consist of spherical building blocks (see Figure 3.5.3d) that resemble the particles observed in the SEM images of the sponges (see Figure 3.5.2). Interestingly, these building blocks show a high degree of uniformity. They have an average diameter of $391\,\mathrm{nm}$ (standard deviation σ=0.30) and a mean sphericity of 0.83 (see Figure 3.5.3c-d). We prepared FIB lift-outs and analyzed them with SEM and TEM to examine the building blocks of the network in more detail. Figures 7.5.15 and 7.5.16 in the Supporting Information show spheres with diameters of several hundred nanometers that are connected. It seems likely that the spherical building blocks formed in the dispersion during aggregation.

Sedimentation of the aggregating particles appears to be critical for gel formation: when we stirred the dispersion during heating, no sponges formed, and we found a sediment consisting of fractal microparticles instead (see Figure 7.5.19 in the Supporting Information). In the

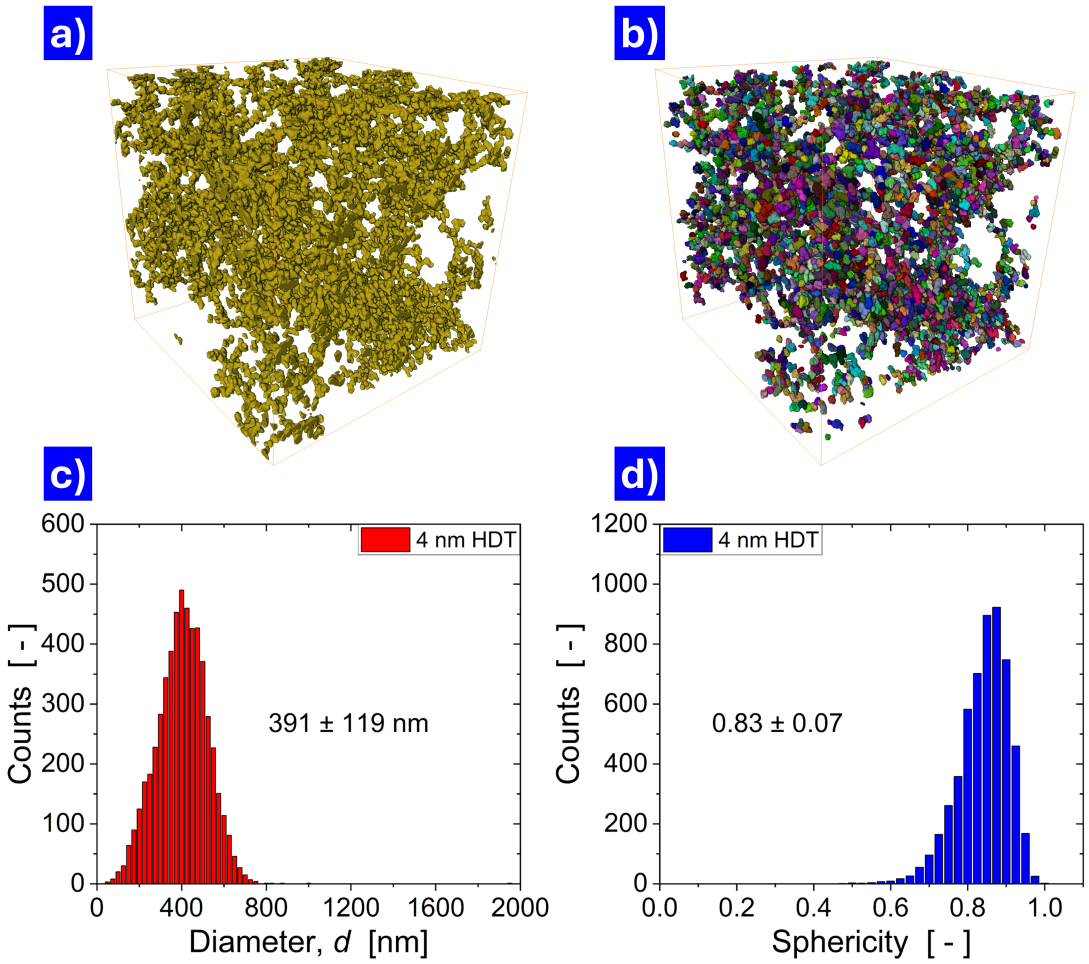


Figure 3.5.3: Metal network structure in gold sponges synthesized from 4 nm diameter AuNP coated with HDT. a) 3D gray-scaled image of the reconstructed sample volume with a size of 18.9 µm×18.9 µm×18.9 µm. b) Reconstructed gold network inside the analyzed sample volume. c) Illustration of the largest connected structures inside the analyzed volume. Structures in the same color are connected. d) Segmented and labeled particles inside the sponge structure. e) The size distribution of the segmented particles. f) Sphericity distribution of the segmented particles.

following, we analyze the gel-formation mechanism with a special focus on the formation of spherical building blocks and their superstructures.

Sponge formation mechanism

We followed particle assembly by removing samples from the reacting colloid in intervals of 2.5 min and quenching them by cooling and diluting by a factor of 100. The samples were characterized using transmission electron microscopy (TEM) and dynamic light scattering (DLS). The evolution of particle size is shown in Figure 3.5.4a. Transmission electron micrographs of all removed samples are presented in Figure 7.5.1 of the Supporting Information.

The average hydrodynamic diameter d_h from DLS of the particles dispersed in the reacting dispersion remained between 6 nm to 10 nm during the first 5 min. The TEM measurements showed

that after 2.5 min and 5 min the primary particles had formed dumbbell-and rod-like particles with a diameter of approximately 10 nm (see Figure 7.5.1 in the Supporting Information). After 7.5 min, d_h had drastically increased to 1361 nm, suggesting a transition to a different mechanism. TEM showed the formation of large aggregates (see Figure 7.5.1d). The images indicate that these aggregates consist of assembled non-spherical nanoparticles that are connected by metallic links.

The large aggregates were similar to those reported before after R5S-induced aggregation at 40 °C to 60 °C with sizes ranging from 200 to 2000 nm (see Chapter 3.4). At 40 °C, it required 12 hours until the majority of particles had aggregated; at 60 °C, the process took only 40 min. In this work, particle aggregation at 90 °C occurred in only 7.5 min. The higher apparently fostered nanoparticle fusion within the aggregates, as shown by structures formed after 10 min and further discussed below.

The aggregates that formed after 7.5 min were similar to those in the TEM lift-outs of the sponges discussed above (see Figure 7.5.16 in the Supporting Information). We could not find the spherical "building blocks" with diameters 400 nm identified after segmentation of FIB-SEM reconstructions, however. It seems likely that these spherical aggregates form rapidly, in less than 2.5 min, and further aggregate into the next hierarchical level immediately after. Concurrent replacement of HDT by R5S and the increasing attraction of the growing gold volumes cause fusion. Similarly, hierarchical aggregation processes have been reported for other gold nanoparticles previously [111, 299].

Born and coworkers studied the temperature-dependent agglomeration of hexadecanethiol-coated 3 nm-diameter gold cores. They found that the agglomeration mechanism was diffusion- or reaction-limited depending on temperature, which changed the structure of the agglomerates [111]. In diffusion-limited agglomeration (DLA), particles attach few collisions [300], while reaction-limited agglomeration (RLA) lets particles rearrange into denser structures [301]. Born et al. reported that globular structures formed in RLA that became the building blocks of the next hierarchical level [111]. Theoretical models for such mechanisms that lead to uniform aggregates have been formulated, for example, by Privman [302]. The same principle seems to be active here.

The size of the aggregates increased until minute 12.5 (2473 nm) through the mechanism discussed above. After 15 min, the average aggregate size from DLS dropped to 1363 nm. This is likely due to sedimentation of the aggregates that quickly depleted large particles from the liquid volume. The experiments were performed in vessels with a liquid height of 1 cm. A compact gold sphere with a diameter of 1.7 µm to 2.5 µm will sediment in 2 min to 3 min in such a geometry. The particles formed after 7.5 min had a size of 1.3 µm, implying a sedimentation time on the order of 6 min (see equation 7.5.7 in the Supporting Information).

A sediment layer had formed at the bottom of the vessel after 12.5 min that was readily visible to

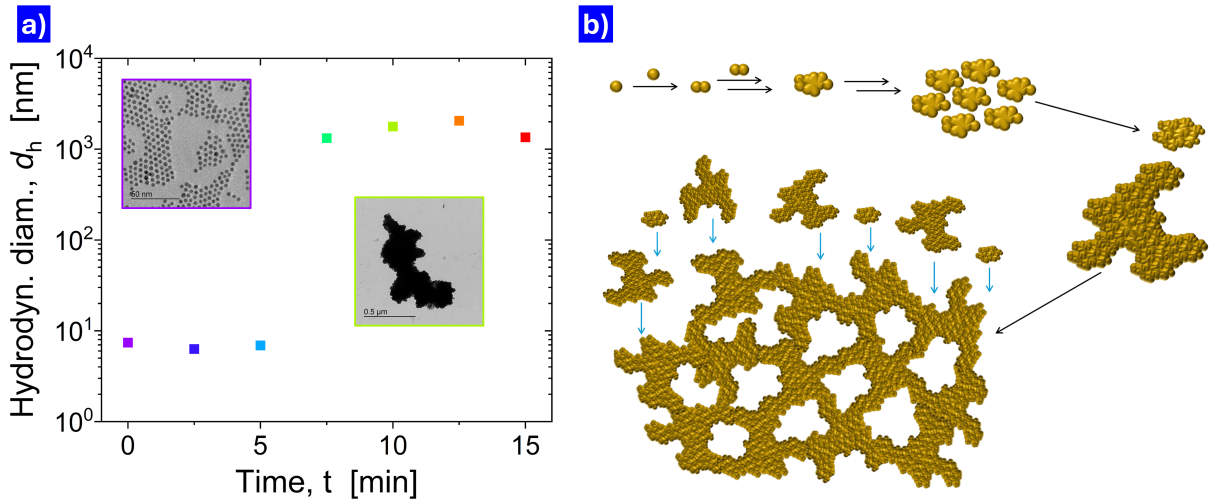


Figure 3.5.4: a) Overview of the evolution of the hydrodynamic diameter of the gold particles formed during the formation reaction of the gold sponge based on 4 nm AuNP@HDT. Detailed DLS data are shown in Figure 7.5.3 in the Supporting Information. TEM micrographs for the primary particles (0 min) and the dense aggregates are shown in a). Additional TEM micrographs are shown in Figure 7.5.1 and 7.5.2 in the Supporting Information. b) Schematic representation of the particle growth and aggregation mechanism from the primary nanoparticles to the final gold sponge.

the naked eye (see Figure 7.5.17 in the Supporting Information). The clear supernatant and the fully connected flat gel body at the bottom support the mechanism discussed above. Shaking the vessel caused the whole gel body to move, indicating an elastic body. We exploited this elasticity during purification and folded the flat gel into a compact volume to simplify repeated solvent exchange (see Figure 7.5.17 in the Supporting Information). We assume that the gel forms by the merging of the aggregates that continuously sediment and come into contact at the vessel's bottom. The gel thickness is limited by the number of aggregates formed (10 mg gold available). The high porosity of 96 % (see Figure 3.5.3a) indicates that the sedimenting aggregates fused rapidly and did not rearrange into a denser assembly.

The spontaneous formation of a large gold gel body (in the *cm*-range, limited only by the vessel) has not yet been reported to our knowledge. Zhang and co-workers reported sponge formation by sedimentation in a solvothermal transformation of dodecanethiol-coated gold nanoparticles with a diameter of 2.3 nm; they separated the sponge pieces from the liquid phase by centrifugation [292]. Literature reports do exist on the formation of sponges from polar particles with intermediate aggregates that can be compared to the reaction observed in this work. Such aggregates reportedly occur when halides are used to induce stepwise agglomeration and aggregation of citrate-capped gold nanoparticles with diameters between 18 nm to 65 nm [291, 293]. The aggregates had pearl-chain-like geometries with chain diameters below 100 nm. Zhang et al. concluded that they formed through the diffusion-limited aggregation of primary particles [291]. Zhang et al. and Liu et al. found aggregates with sizes in the μm range

during sedimentation. These particles had a filamentous or pearl-necklace-like structure of connected globular substructures [292, 293]. The hydrothermal sponge formation from apolar dodecanethiol-coated gold nanoparticles involved intermediate aggregates, too [292]: first, aggregates of two to five nanoparticles formed. They grew into chain-like structures and then into a network. In our work, no chain-like aggregates formed. The aggregates we found were denser and had complex shapes, based on their reaction-limited formation.

The TEM analysis of large aggregates taken from the heated dispersion after 10 min showed that the aggregation at 90 °C led to pronounced fusion of the nanoparticles. The individual primary nanoparticles had disappeared into continuous gold volumes (see Figure 7.5.1 and 7.5.2 in the Supporting Information). Similar fusion processes have been reported in the literature. Ingham and coworkers studied the aggregation of oleylamine-coated 10 nm gold nanoparticles when heating to temperatures between 165 °C to 250 °C in steps. In a first step (T >165 °C), the ligand molecules desorbed or melted, leading to reduced spacings between the assembled cores. In the second step (15 min to 100 min at 250 °C), metal necks formed due to the reduced spacings and increased gold mobility. The grain boundaries of the connected cores remained visible. In the last step (200 min to 500 min at 250 °C), grains grew until a continuous gold volume had formed. Ingham et al. concluded that the removal of the ligand shell drove the reaction [159]. In our dispersions, heating our dispersions to 40 °C to 60 °C only led to initial metal connections within the aggregates (see Chapter 3.4). Higher temperatures are required to connect the metal more thoroughly; even at 90 °C, we still find structures in the *nm*-range on the aggregate surfaces.

Effect of the core size and ligand system on the sponge properties

So far, we used small (4 nm diameter) particles with a strongly bound thiol shell. In the following, we expand our analysis and consider the effects of core size and ligand type on sponge formation.

Particles with core diameters of 4 nm or 9.1 nm were coated with HDT or oleylamine (OAm) and treated with the process described before. All colloids formed sponges as shown in Figure 3.5.5. Their properties are summarized in Table 7.5.2, Figure 7.5.11, and 7.5.12 of the Supporting Information.

Sponges formed from 9.1 nm AuNP with HDT had a porosity of 96 % and contained a network of spherical aggregates with an average diameter of 434 nm and the highest sphericity of all analyzed systems (0.85). The specific surface area of this system was too low to be detected (detection limit of 2 m^2g^{-1}).

Sponges formed from 4.0 nm AuNP with OAm contained a network of spherical aggregates with an average diameter of 529 nm, the lowest sphericity of all (0.79), and a porosity of 89 %.

The connectivity of the gold network was the highest of all analyzed systems $99.4\,\%$. Sponges made from $9.1\,\text{nm}$ AuNP with OAm had intermediate properties at a porosity of $93\,\%$, average spherical aggregate diameter of $498\,\text{nm}$, and a sphericity 0.82. The specific surface area of this system was the highest of all systems ($7.9\,\text{m}^2\text{g}^{-1}$).

Most network properties, such as tortuosity, fractal dimension, pore volume, particle size, and sphericity, were similar across all sponges. Larger particles yielded sponges with smaller surface areas; oleylamine yielded sponges with larger surface areas.

The use of OAm as a ligand of small particles ($4\,\text{nm}$) resulted in a highly cross-linked gold network, with the reconstructed particles exhibiting lower sphericity and a broader size distribution. Apparently, OAm caused a more diffusion-limited aggregation process. The replacement of OAm by R5S is more rapid than that of HDT due to the lower binding energy of the amine [201]. This probably increases the aggregation rate, such that particles cause a more diffusion-limited aggregation. Consequently, the formed aggregates and assemblies are less spherical and less dense.

The use of larger cores increased the vdW attraction between the particles [58]. We assume that the particles agglomerated already at lower R5S fractions than for smaller cores. The short-range attractive potential between the particles with their larger HDT fraction was weaker — the overall potential was "softer" — allowing particles to rearrange before they aggregated. We conclude that using larger cores enhances the reaction-limited behavior of the aggregation process, leading to more spherical substructures.

The use of large particles coated with OAm resulted in sponges composed of interconnected raspberry-like structures. We conclude that these structures result from the combination of cores that favor rearrangement and a shell that enables rapid aggregation. As a result, the properties of this system, such as sphericity, size, and size distribution of the reconstructed particles, specific surface area, and tortuosity, are between those of the $4\,\text{nm}$ OAm sponge system and the $9\,\text{nm}$ HDT system. The results show that the formation of the gold sponges depends strongly on the used particle size and ligand system.

3.5.4 Conclusion

We introduced a new route for the synthesis of gold sponges from apolar gold nanoparticles that is induced by the replacement of HDT by the reactive additive R5S at low temperature. Macroscopic sponges were synthesized at $90\,^\circ\text{C}$ within $15\,\text{min}$.

The sponge structures were characterized using 3D reconstruction based on FIB-SEM tomography. A porosity of $96.1\,\%$ and a specific surface of $5\,\text{m}^2\text{g}^{-1}$ for sponges made from $4\,\text{nm}$ diameter AuNP coated with HDT demonstrates the applicability of the method. The reconstructed sponge structure was segmented, and we identified spherical substructures with diameters of

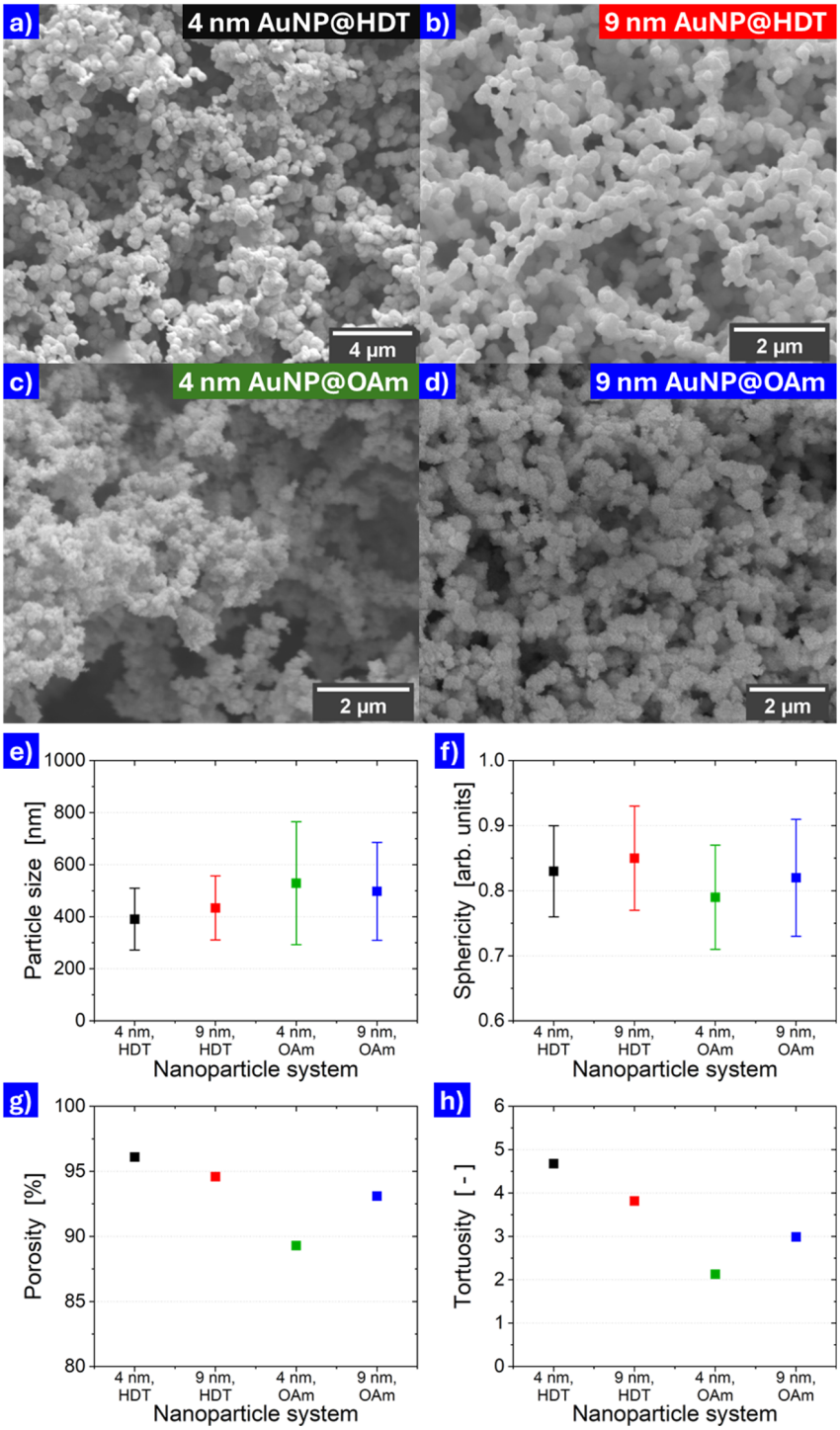


Figure 3.5.5: Scanning electron micrographs of gold sponges obtained from a) 4 nm AuNP coated with HDT, b) 9 nm AuNP coated with HDT, c) 4 nm AuNP coated with OAm, and d) 9 nm coated with OAm. The size of the segmented particles (e), the sphericity(f), the porosity (g) and the connectivity (h) of the different sponge systems are summarized in e) to h).

0.4 µm and a sphericity of 0.83. These particles were formed by rapid, reaction-limited aggregation in the first stage of sponge formation.

We followed the overall formation process using transmission electron microscopy and dynamic light scattering. Initially, aggregates consisting of only a few particles formed that rapidly aggregated to diameters in the μm-range due to increasing core-core attraction. We find that the temperature of $90\,°C$ was sufficient to induce pronounced fusion of the particles. Gaps between the nanoparticles disappear, and compact gold structures form inside the aggregates. They sediment within 5 min to 7.5 min and fuse into a continuous network at the bottom of the vessel.

The properties of the sponge network depended strongly on the initial nanoparticle dispersion. Oleylamine shell formed sponges with a larger specific surface area but less spherical substructures. The amine ligand was more rapidly replaced by R5S, leading to a more diffusion-limited aggregation process. Large cores, on the other hand, started aggregating already when small fractions of HDT were replaced by R5S. This led to a more reaction-limited process where particles rearranged, formed compact spherical building blocks, and, eventually, sponges with a lower surface area and substructures with a higher sphericity.

3.5.5 Materials and Methods

All chemicals were obtained from the named vendors and used without further purification.

Nanoparticle synthesis

Gold nanoparticle with a core diameter of 4 nm were synthesized following a method described previously [58]: A mixture of 9 mL of n-pentane (Carl Roth, $99\,\%$) and 9 mL oleylamine (Sigma Aldrich, technical grade, $80-90\,\%$) was added to 100 mg of tetrachloroauric(III) acid trihydrate $HAuCl_4 \cdot 3\,H_2O$. The mixture was stirred (with a magnetic stirrer bar) for 21 min at $22\,°C$ under an argon atmosphere. Then, a mixture of 1 mL n-pentane, 1 mL of oleylamine and 40 mg tert-butylamine borane complex (FLUKA, $97\,\%$) was added to the gold precursor solution. The mixture was stirred for 60 min. The dispersion was purified by precipitation with 50 mL of a mixture of ethanol and methanol (ratio 3:2) and centrifugation at 2000 rpm (689 rcf) for 1 min. The supernatant was removed, and the nanoparticles were redispersed in 2.5 mL toluene (gold concentration of 10 mg/mL).

Ligand exchange

Ligands were exchanged by heating the dispersion to $80\,°C$, followed by the addition of 1 mL of hexadecanethiol (Sigma Aldrich, GC grade, $95\,\%$) (0.4 mL per 1 mL of the concentrated dispersion) [58]. The mixture was stirred for 15 min at 300 rpm. The dispersion was purified by precipitation with 3 times the sample volume (3 mL for 1 mL dispersion) of a mixture of ethanol and methanol (ratio 2:1) and centrifugation at 2000 rpm (689 rcf) for 5 min. The supernatant was removed, and the nanoparticles were redispersed in 2.5 mL toluene. The washing step was

repeated once with a cooled mixture of ethanol and methanol (2:1). After the last washing step, the sample was redispersed in toluene and diluted to a gold concentration of $5\,\mathrm{mg/mL}$.

Synthesis of 3D porous gold structures

In a $50\,\mathrm{mL}$ vial, $12.5\,\mathrm{mL}$ of a nanoparticle dispersion with a gold concentration of $5\,\mathrm{mg/mL}$ was mixed with $283\,\mu\mathrm{L}$ of the additive tetrahydrothiophene. The mixture was then vortexed for $30\,\mathrm{sec}$. The dispersion was then heated from room temperature to $60\,^{\circ}\mathrm{C}$ within $15\,\mathrm{min}$. The dispersion is then heated at $90\,^{\circ}\mathrm{C}$ for $90\,\mathrm{min}$ to $120\,\mathrm{min}$ without stirring. The reaction vessel remained stationary during the reaction. Once the reaction was complete, the container was allowed to cool to room temperature. The sponge structure was present as a flat film. To facilitate cleaning, the vial was briefly shaken by hand. This created a more compact 3D structure that is easier to transfer to other vials. To remove unbound additive and ligand molecules, the supernatant was removed. The sample was then washed three to four times by solvent exchange. After the last wash, approx. $5\,\mathrm{mL}$ cyclohexane was added to the sponge. The sample was freeze-dried for storage and further analysis.

Scanning electron microscopy

Resin and hardener of an epoxy system (EpoFix Kit, Struers, Denmark) were mixed at a weight ratio of $8:1$ by hand using a wooden spatula for approx. 2 minutes. The mixed solution was evacuated multiple times to remove air bubbles and subsequently poured over the porous gold sponges in a cylindrical mold. The resin infiltrated the porous gold sponges and hardened within 12 hours. The samples were then mechanically grinded on SiC papers until a grain of "P2500". The samples were gold-coated (Autofine Coater, Jeol, USA) prior to transferring to a dual-beam scanning electron microscope (Versa3D, FEI, USA). The additional gold coating was done at $30\,mA$ for $2 \times 60\,s$ and ensured surface conductivity of the samples that prevents image drift and charging during electron imaging.

FIB-SEM tomography

The sample was tilted to $52°$ at the region of interest (ROI) and a $20 \times 20 \times 3\,\mu m$ large platinum pad was deposited using the gas injection system of the gallium ion (Ga^{+}) beam at an acceleration voltage U of $16\,kV$ and a beam current I of $7.5\,nA$. A U-shaped trench around the ROI was removed afterward using regular cross-sections with the Ga^{+} beam at $U = 30\,kV$ and $I = 65\,nA$.

The software "Autoslice & View" (ASV G3, Thermofisher Scientific, USA) was used to intermittently mill approx. 900 rectangular slices with the ion beam ($U = 30\,kV$ and $I = 7\,nA$) of the ROI with $27\,nm$ slice thicknesses. After every milled slice, a tilt-corrected secondary electron (SE) image was recorded ($U = 5\,kV$, $I = 0.19\,nA$, $1\,\mu s$ dwell-time) at a size of

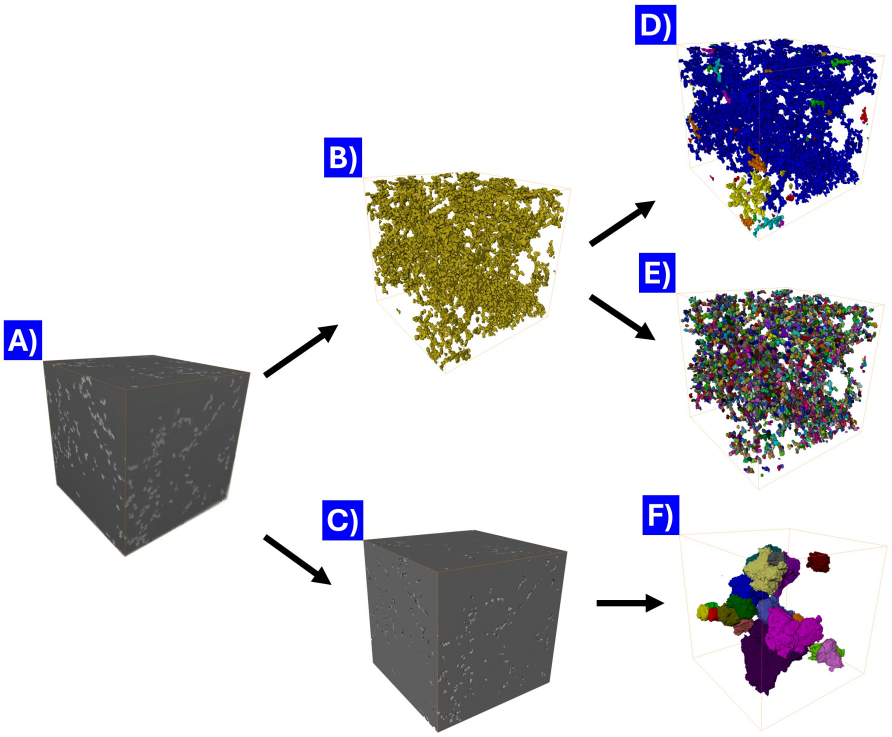


Figure 3.5.6: The A) grayscale SE image was segmented into binary B) Au and C) pore images. From the binary Au image, the D) connected components and E) individual aggregates were determined and individually labelled (in different colors). From the binary pore image, the F) individual pores were determined.

3072×2048 pixels with physical pixel size matching the slice thickness of $27\,nm$. The milling of all slices and intermittent SE image acquisition took approximately five hours with the above-described procedure.

3D reconstruction and post-processing

Three-dimensional representations were reconstructed from the 2D micrographs using the commercial software "Avizo (for EM systems)" (Version 2022, Thermo Fisher Scientific, USA). We executed the following Avizo-specific commands:

1. "Align Slices"
2. "Shear"
3. "Extract Subvolume" ($700 \times 700 \times 700$ voxels)

A description of the reconstruction process can be found in published work [303, 304]. The functions in quotation marks are specific to Avizo, with the parameters in brackets (if any).

The 3D-reconstructed, 8-bit grayscale SE image was $(700\,voxel)^3$ large with physical voxel sizes of $(27\,nm)^3$. The following Avizo-specific functions were used for post-processing:

1. "Background Detection Correction" (Type=B-Spline, Filter Size=1/75/1 (x/y/z))

Table 3.5.1: List of extracted metrics based on 3D-reconstructed images shown in figure 3.5.6.

image name	**extracted metrics**
binary Au image (Figure 3.5.6B))	Au/pore volume fractions centroid path tortuosity fractal dimension
label Au image (connected components, Figure 3.5.6D))	volume fraction of largest structure
label Au image (individual aggregates, Figure 3.5.6E))	number, size and sphericity of individual Au aggregates
label pore image (Figure 3.5.6F))	number, size and sphericity of individual pores

2. "Recursive Exponential Filter" (Interpretation=XY planes, Spread=60)

We used filtering to increase the signal-to-noise ratio of the gold versus the epoxy phase and background detection correction to correct brightness gradients in the vertical direction of the individual SE images. From the post-processed image (Figure 3.5.6A)), the gold phase was segmented using manually histogram thresholding. Thresholding artifacts, i.e., small groups of voxels not corresponding to Au aggregates, were removed using the function "Despeckle" (Interpretation=3D, Kernel Size X/Y/Z: 5/5/5, Threshold Factor=1). This procedure yielded the binary Au image (Figure 3.5.6B)). Inverting the image yielded the binary pore image (Figure 3.5.6C)). From the binary Au image (Figure 3.5.6B)), two separate images were obtained: the connected components (Figure 3.5.6D)) and the individual aggregate image (Figure 3.5.6E)). The first was obtained by "Labeling" (Interpretation=3D, Neighborhood=26) the binary Au image. Connected groups of voxels were assigned unique integer values (represented by different colors in Figure 3.5.6D). The individual aggregate (Figure 3.5.6E)) image was obtained by the following steps (in this order):

1. "Separate Objects" (Method=Chamfer - Conservative, Interpretation=3D, Neighborhood=26, Marker Extent=0, Output Type=split, Algorithm Mode=repeatable)

2. "Border Kill" (Interpretation=3D, Neighborhood=26)

3. "Labeling" (Interpretation=3D, Neighborhood=26)

Here, the connection between sphere-like aggregates was removed. Additionally, aggregates were removed when transitioning the border of the 3D reconstruction. The remaining aggregates were individually labeled (as indicated by the different colors). The image with individual pores (Figure 3.5.6F)) was obtained from the binary pore image (Figure 3.5.6C)) using the same procedure, except the Marker Extent was set to four instead of zero.

Metrics calculation

Table 3.5.1 summarizes the individual images that were produced from a single 3D reconstruc-

tion. We extracted metrics as discussed in the following.

Volume fractions: The volume fraction of a single phase was calculated by dividing the number of phase voxels by the number of voxels in the volume

$$\varphi = \frac{\text{\# of phase voxels}}{\text{\# of voxels in volume}}. \tag{3.5.1}$$

The sum of gold volume fraction φ_{Au} and pore volume fraction φ_{pore} must be unity, therefore $\varphi_{\text{pore}} = 1 - \varphi_{\text{Au}}$. Computing the volume fraction on a label image yields a φ for every unique label. The volume fraction of the largest component, $\varphi_{\text{Au, largest component}}$ is the one with the highest number of voxels, e.g. the blue component in Figure 3.5.6D) and strictly $\varphi_{\text{Au, largest component}} < \varphi_{\text{Au}}$.

Centroid-path tortuosity: The centroid-path tortuosity τ calculates the center-of-gravity (COG) for each individual x-y image along the z-direction of the 3D-reconstructed image stack and computes the length L_g of the effective path by [298]

$$L_g = \sum_{i=1}^{N-1} \sqrt{(x_{i+1} - x_i)^2 + (y_{i+1} - y_i)^2 + (z_{i+1} - z_i)^2} \tag{3.5.2}$$

where x_i, y_i and z_i are the COG's coordinates, N is the total number of x-y slices in the 3D-reconstruction and i the current x-y slice. The centroid-path tortuosity τ then follows as [298]

$$\tau = \frac{L_g}{L} \tag{3.5.3}$$

where L is the 3D-reconstructions side length, here $L = 700$ (both L and L_g in voxel units).

Fractal dimension: The fractal dimension d_f indicates how effectively a complex geometric shape fills the space with values between 2 and 3 and for 3D images. A well-recognized algorithm was used to calculate d_f [305]. It is based on the "box counting" (BC) method [297]: a grid with n number of boxes is created in 3D. The box size is a scaling factor ε and for defined box sizes, the number of boxes occupying the 3D-reconstruction are calculated. Then, the slope of the linear regression in the $log(n) - log(1/\varepsilon)$ plot gives the fractal dimension d_f [297].

Label analysis of Au aggregates and pores: The individual aggregates (Figure 3.5.6E)) and pores (Figure 3.5.6F)) were analyzed using the Avizo function "Label Analysis". For every unique label i, i.e., a detected aggregate was characterized by computing its sphere-equivalent diameter d_i as

$$d_i = 2 \cdot \left(\frac{3V_i}{4\pi} \right)^{\frac{1}{3}} \tag{3.5.4}$$

where V_i denotes the number of voxels labeled with i multiplied by the physical voxel size of $(90\,nm)^3 = 729000\,nm^3$. The number of Au aggregates (Figure 3.5.6E)) was above 3000 per 3D-reconstruction, which enabled the calculation of d-distributions (see Figure 3.5.3c)) with means and standard deviations. In contrast, there were only around 10 pores per 3D reconstruction, so the average pore-size values should be used with caution. We analyzed the shape of labeled regions. The "sphericity" ψ is 1 for a perfect sphere or below 1 for non-spherical shapes:

$$\psi_i = \frac{\pi^{\frac{1}{3}}(6V_i)^{\frac{2}{3}}}{A_i} \tag{3.5.5}$$

where A_i is the surface are of the label and V_i its volume. The area A_i of a labelled region i with $x(t)$, $y(t)$ and $z(t)$ being a parametric representation of a boundary curve X is

$$A_i(X) = \int_{\delta X} \sqrt{x'^2 + y'^2 + z'^2} dt \tag{3.5.6}$$

Transmission electron microscopy

A JEOL JEM2100 LaB6 electron microscope (JEOL ltd. Tokyo, Japan) with 200 kV acceleration voltage, 0.14 nm line resolution, and a Gatan Orius SC1000 camera (Gatan Inc. Pleasanton, CA, USA) in brightfield mode was used to image the nanoparticles. AuNP samples were prepared by drop-casting of $10 - 20$ µL of the particle dispersion in toluene (2.5 mg/mL) on a TEM copper grid.

The preparation of the TEM lift-out measurement is described in detail in the Supporting Information.

Thermogravimetric analysis

The samples were transferred into Al_2O_3 crucibles for the thermogravimetric analysis. For the TGA measurement, an STA 449F3 setup from NETZSCH was used. The samples were heated with 10 °C/min to 1000 °C. During the heating, an argon atmosphere was used.

Small-angle X-ray scattering

A laboratory-scale Xeuss 2.0 instrument (Xenocs SA, France) was used for all SAXS measurements. The X-ray beam was produced by a copper K_α source (wavelength 1.54 Å) and focused on the sample with a spot size of 0.25 mm^2. The measurements were performed with

a sample-detector distance (SDD) of 1020 mm. The measurable momentum transfer q ranged from $0.01\,\text{Å}^{-1}$ to $0.6\,\text{Å}^{-1}$, with q being defined as $q = 4\pi\sin(\theta/2)/\lambda$, were θ is the scattering angle. The samples were measured in borosilicate capillaries with a diameter of $1.5\,\text{mm}$. Dispersions with a gold concentration of $10\,\text{mg/mL}$ were used to determine the particle size. Toluene was used as the solvent. The particle size was determined before ligand exchange. A measurement time of $600\,\text{sec}$ was used.

Determination of the BET surface area

The freeze-dried sponges were transferred to a measuring cell and degassed at $60\,°\text{C}$ for $20\,\text{h}$ under application of a vacuum (using the XeriPrep^{TM} Degasser set-up from the company Quantachrome, Boynton, United States). After cooling, the sample weights were determined, the filling rod was inserted into the measuring cell, and these were then attached to the measuring station.

Recording of a partial range of the adsorption isotherm and determination of the specific surface area according to the BET method by means of 6 points in the relevant pressure range P/P_0 from 0.05 to 0.30. The measurement was repeated 3 times for each sample.

3.5.6 Acknowledgment

Sarah Schumacher and Simon Blum (both INM) are acknowledged for performing BET and TGA measurements. T.V.K. thanks the DFG for financial support (Geschäftszeichen: KR 3729/18-1).

Chapter 4: Discussion

In Chapter 2.4, the goals of this dissertation were presented. In the Chapter 3, different modifications of nanoparticle shells were presented that were used to achieve these goals. In this chapter, I will discuss the extent to which the individual modifications contributed to achieving the desired goals.

The first goal was to improve the colloidal stability of apolar nanoparticles by modifying the ligand shell. In the following sections, the hypothesized effects of each modification and the results obtained from the work are discussed. Three approaches were followed: additives, non-linear ligands, and mixed ligand shells.

4.1 Stabilization with molecular additives

The first modification involved adding molecular additives to nanoparticle dispersions. This modification was based on the following hypothesis:

Hypothesis: Additive molecules in or around the ligand shell can prevent the disorder-order transition and prevent agglomeration.

Result 1: Additives must be chemisorbed to stabilize the disordered shell structure.
Cyclic additive molecules with a functional group were used in Chapter 3.1 to modify the shell, which improved colloidal stability. The sulfide additive tetrahydrothiophene (R5S) shifted agglomeration by $30\,\mathrm{K}$ to lower temperatures at an R5S concentration of $64\,\mathrm{mM}$. We hypothesized that the small cyclic additive disrupts the ordering of the longer linear ligands when bound to the gold surface. Using TGA, we showed that the shell mass decreased when the particle system was modified with R5S. Only the replacement of the heavy HDT ligand by the small sulfide can explain the significant reduction in the shell mass. MD simulations confirmed the hypothesis that only surface-bound additive molecules can stabilize the disordered shell state.

Result 2: The stabilizing effect of R5S decreases at high concentration.
Surprisingly, the stabilizing effect of R5S decreases again with increasing fraction in the shell. Based on the literature on mixed shells [132, 134], we hypothesized that a transition in the ligand-additive distribution from homogeneous to heterogeneous is the origin. Experimentally, the hypothesis could not be proven. MD simulations, however, could confirm this hypothesis, as the effect decreased when additive molecules formed a single cluster in the shell.

Result 3: Chemisorption is hindered by the steric repulsion of larger additive molecules. Contrary to expectations, the use of larger sulfide thionane (R9S) did not increase the stabilizing effect. Since R9S and R5S have similar binding energies to gold, the difference in enrichment behavior must be caused by differences in sterics. Our hypothesis was that R9S is unable to penetrate the dense thiol shell and reach the gold surface. Simulations confirmed that the access of larger additives to the gold surface is hindered due to the high density of the shell.

Result 4: The stabilizing effect of amines is limited by accumulation through physisorption. Amines showed a universally smaller stabilizing effect ($<3\,\mathrm{K}$). Theoretically, the small amine pyrrolidine (R5N) should be able to enter the shell similar to R5S. The observed difference must be the result of the functional group. The lower binding energy of amines limits their interactions with the particle to physisorption. MD simulations indicated that physisorption of additives cannot stabilize the disordered state. They are displaced during the bundling process.

4.2 Stabilization with non-linear ligands

The second modification involved the use of shells made from non-linear ligands. This modification was based on the following hypothesis:

Hypothesis: Shells made of non-linear ligands do not undergo a transition from disordered to ordered.

Result 1: Agglomeration can be prevented almost completely using non-linear ligands.
Gold nanoparticles with a core diameter of 4 nm coated with the kinked OAm and double-armed *dbr*-SC_{16} ligands agglomerated at low temperatures just above solvent freezing. Terminally branched *br*-SC_{12} ligands prevented agglomeration entirely. Several factors can be discussed as contributing to this unusual stabilization. Yamashita et al. demonstrated that changes in shell density resulting from the use of non-linear ligands can enhance the dispersibility of the particles [86]. We used TGA to analyze the shell density of non-linear ligands and the linear reference systems. We found similar densities for linear and non-linear ligand systems. Only in the comparison of a linear thiol and a linear amine with the same chain length can the coverage be used to explain the difference in the agglomeration temperatures. We do not entirely exclude the effect of shell density, but it plays only a minor role for the non-linear systems used.
In the literature, non-linear ligands are also referred to as entropic ligands, as they have a strong influence on conformational entropy. However, simulations couldn't confirm an entropic effect. We suspect a different cause. As has already been shown in other studies, agglomeration is induced by the transition of the shell structure. For this reason, our hypothesis was that shells consisting of non-linear ligands do not undergo this transition, or only partially. Various simulations confirmed this hypothesis.

Result 2: Larger cores can be stabilized even more than small ones using large non-linear ligands.
Surprisingly, the agglomeration temperatures of gold nanoparticles with core diameters above 8 nm and coated with the kinked OAm or double-armed *dbr*-SC_{16} were increased by up to 150 K. In the case of linear ligands, the increase in the core size leads to a rise in the core-core interaction. Large ligands are required to compensate for the stronger core-core interaction [58]. A certain size ratio between shell and core is needed to get colloidally stable particles [123]. This ratio explains why the smaller, non-linear ligand *br*-SC_{12} was unable to stabilize larger cores. The exact mechanism could not be proven experimentally. However, we suspect that several factors influence the colloidal stability of large cores.
TGA measurements revealed larger differences in shell density between linear and non-linear

ligands on large cores compared to small cores. As long as the shell is large enough, a lower shell density can cause lower vdW interactions between the shells and, at the same time, stronger interaction with the solvent, which can lead to improved colloidal stability.

Generally, larger particles have a lower surface curvature and a stronger faceting. In the case of linear ligands, the reduction in the curvature can cause larger differences in the shell density. Additionally, the preferential binding of ligands on specific facets (100) can induce a locally higher density or bundling of the shell. We hypothesize that non-linear ligands can compensate for the changes in shell structure caused by the core, resulting in a more repulsive shell.

4.3 Stabilization with mixed ligand shells

The third modification involved the use of mixed ligand shells. This modification was based on the following hypothesis:

Hypothesis: Mixed-linear ligand shells increase the colloidal stability of shell-dominated particles.

Result 1: The size difference Δl of the combined ligands determines the improvement of the colloidal stability for mixed shells.

Generally, the use of mixed shells results in improved colloidal stability. However, the extent to which colloidal stability improves depends heavily on the size difference between the ligands used. If, for example, two large ligands (such as SC_{18} and SC_{16}) are combined, the agglomeration temperatures lie between the values of particles with pure ligand shells. For these combinations, stabilization depends on the composition of the shell. The disorder-order transition of the shell is therefore not suppressed, but shifts closer to the transition within the shorter ligand system as exchange increases.

However, a larger size difference Δl caused larger shifts in T_{agglo}. Combinations of hexanethiol (SC_6) with hexadecanethiol (Δl=10) or octadecanethiol (Δl=12) caused shifts in toluene between 69 K and 85 K. We assume that the gain in flexibility of the protruding chain is the origin of the improved stability [133, 134]. The resulting rotational freedom hinders the formation of bundles. However, since agglomeration of the particles still occurs depending on the solvent, it is questionable whether the transition of the shell structure is completely suppressed.

Result 2: The composition changes in the shell are not linear with the concentration of the modifying ligand.

In general, SAXS measurements showed that, in addition to the size difference between the combined ligands, the concentration of the modifying ligand in the dispersion influences colloidal stability. We hypothesized a connection between the used ligand concentration and the composition of the mixed ligand shell.

Experimentally, the composition of the shell of two combinations (AuNP@SC_{12}+SC_6 and AuNP@SC_{16}+SC_6) was determined using TGA. Interestingly, a direct correlation between the concentration of SC_6 in the dispersion and the proportion of SC_6 in the shell could not be found for every combination.

For the AuNP@SC_{12}+SC_6 system, as expected, a higher SC_6 concentration during the ligand exchange led to a higher fraction of SC_6 in the shell. In the case of the AuNP@SC_{16}+SC_6,

a maximum of the SC_6 fraction was reached using a concentration of $256\,\mathrm{mM}$. Higher SC_6 concentrations didn't increase the SC_6 fraction. Experimentally, it was not possible to identify the origin of this behavior. We hypothesize that a low-energy shell structure may exist that limits the exchange.

Result 3: The composition of the shell and the distribution of the ligands influence the colloidal stability.

For both systems, AuNP@SC_{12}+SC_6 and AuNP@SC_{16}+SC_6, a correlation between the composition of the shell and $\Delta T_{\mathrm{agglo}}$ could be demonstrated. In toluene, a maximum of $\Delta T_{\mathrm{agglo}}$ exists for both systems. In the AuNP@SC_{12}+SC_6 system this maximum was found at a SC_6 fraction of $53\,\%$. We assume that the reduction of $\Delta T_{\mathrm{agglo}}$ at higher SC_6 fraction is based on the reduction of the repulsive effect of the shell. The progressive exchange reduces the size of the shell; consequently, the core-core interaction becomes more significant, resulting in a decrease in $\Delta T_{\mathrm{agglo}}$.

In the case of the AuNP@SC_{16}+SC_6 for similar composition (with SC_6 fractions between $66\,\%$ to $74\,\%$) different $\Delta T_{\mathrm{agglo}}$. A maximum was found for a SC_6 fraction of $70\,\%$. We hypothesize that the difference in $\Delta T_{\mathrm{agglo}}$ at similar composition is caused by the differences in the ligand distributions in the shell. Differences in the patterning could affect how strongly the bundling in segregated ligand islands affects the repulsive effect of the shell. However, further experiments are needed to test this hypothesis.

The second goal was to reduce the shape stability of apolar nanoparticles by modifying the ligand shell. In the following sections, the hypothesized effects of each modification and the results obtained from the work are discussed.

4.4 Additive-induced aggregation of apolar thiol-coated gold nanoparticles

Hypothesis: The exchange of the initial ligand by the additive R5S can lower the shape stability of gold cores.

Result: The continuous replacement of the ligand HDT by the additive is the driving force of the coarsening reaction.

The small cyclic sulfide R5S can replace the initial ligand HDT and change the shell structure. In Chapter 3.1, we used low R5S shell fractions to improve the colloidal stability when cooling the dispersion. However, heating of the R5S-containing dispersions resulted in the coarsening of the gold cores. TEM and SAXS revealed that the coarsening process was primarily driven by aggregation. The aggregation of particles in a dispersion can have various causes, including the diffusion rate (which affects particle collision) and the passivation of the core by the shell.

Generally, heating of dispersed particles leads to an increase in the diffusion rate. However, we could show that for the temperatures we used ($40\,^{\circ}$C to $60\,^{\circ}$C), this increase is not significant enough to explain the acceleration in the aggregation of the cores. On the other hand, the higher temperatures also lower the energy barrier of the ligand exchange reaction. As a result, we hypothesized that the progressive exchange of the large HDT ligand by the small additive R5S reduces the passivating effect enough to induce coarsening. We could prove a progressive ligand exchange during heating using TGA (up to a R5S shell fraction of $82\,\%$ after 5 hat $50\,^{\circ}$C). Using SAXS and SANS, we demonstrated that this increase in the R5S fraction altered the shell structure, enabling smaller spacings between particles when they attach.

Based on the reduced spacing, two mechanisms can possibly explain the aggregation of the cores. The first approach is based on the simplified displacement of R5S from the gold surface due to the lower binding energy. The neck is formed when the cores come into contact with each other. No binding energy for the Au-S bond for the additive R5S could be found in the literature. Generally, sulfides have lower binding energies to gold than thiols. Since R5S can replace HDT, the difference in binding energy cannot be particularly large. Since no aggregation is observed in the case of a pure HDT shell, it is unlikely that the shell will be displaced/desorbed

in a system in which the ligands/additives are similarly firmly bound. Generally, heating leads to a destabilization of the Au-S bond. We conclude that the destabilization at $40\,^{\circ}$C to $60\,^{\circ}$C is not sufficient to induce the desorption of the shell.

The second approach is based on the formation of a bridge between cores due to the small spacing and low passivation of the shell. In this mechanism, the shell does not need to be removed. The formation of the bond between the cores is based on small spacings and the change in the diffusion or migration behavior of the gold atoms on the particle surface. We suspect that the increase in temperature is sufficient to destabilize the R5S-gold bond to such an extent that the mobility of the gold atoms increases without the additive desorbing, leading to the formation of a connection between the particles.

We suspect that in R5S-containing systems, aggregation is based on the formation of bridges between particles without the shell being removed. However, the mechanism cannot be confirmed without further experiments.

4.5 Formation of gold sponges

Hypothesis: The additive-induced aggregation can be used to induce the formation of sponge-like gold structures.

Result 1: Formation mechanism based on the additive-induced aggregation and sedimentation of nanoparticles.

The formation of gold sponges was observed during the heating of R5S modified gold nanoparticles coated with HDT at temperatures above 90 °C within 15 min (without stirring). We hypothesized that the sponges were formed through the merging of aggregates during sedimentation, a process similar to reactions described in the literature [245, 291–293]. Experimentally, the mechanism was analyzed using DLS, SEM, and TEM measurements. It was found that the particles coarsen, mainly by aggregation, resulting in the formation of large aggregates after 7.5 min to 10 min. We conclude that the initial reaction is based on a mechanism similar to that described in Chapter 3.4. The higher temperatures, however, enable significantly more advanced aggregation compared to the aggregates found in Chapter 3.4. We assume that higher temperatures accelerate diffusion processes, causing crystal grains to grow and merge.

Due to their large size (in the μm-range), the aggregates sediment within minutes. In the sediment, the sponge network forms by the layerwise fusion of aggregates. In contrast to the literature, this reaction produces a coherent sponge. We suspect that the formation of a single sponge is caused by the high particle concentration. Enough aggregates can be produced to form sponge structures across the bottom of the reaction vessel.

Result 2: The sponge consists of connected particles.

The SEM images of the gold sponges suggest that the network is composed of interconnected, relatively spherical particles. The properties of these particles were determined by segmenting the reconstructed gold network. Our initial assumption was that these spherical particles act as building blocks of the network. However, this hypothesis could not be fully confirmed. The calculation of the theoretical sedimentation time of these particles (with a diameter of approx. 400 nm) was significantly longer than the observed reaction time of 15 min. Both the DLS and TEM measurements of samples taken during sponge formation showed the presence of significantly larger aggregates. Both the size and shape of the particles differed significantly from the reconstructed particles.

TEM lift-out measurements showed gold structures comparable to the particles found during sponge formation. Nevertheless, we suspect that spherical aggregates are formed. Our hypothesis is that smaller spherical aggregates are formed at the beginning of the reaction due to reaction-limited aggregation. These spherical aggregates then attach to each other and form

larger aggregates in the μm-range. Comparable processes have already been described in the literature. We suspect that the high speed of the process, driven by strong vdW forces between the aggregates, prevented us from distinguishing the initial stages of the aggregation process.

Result 3: Core size and ligand type affect the aggregation behavior during the reaction.
Experimentally, it was possible to synthesize sponges from various nanoparticle systems, like 4 nm and 9 nm cores coated with HDT or OAm. Characterization using FIB-SEM and 3D reconstruction revealed that both the core size and the ligand type affect the sponge properties. These differences are mainly the result of changes in the formation mechanism and the underlying aggregation and self-assembly processes. Generally, particles can aggregate in a reaction-limited or diffusion-limited manner. In reaction-limited processes, particles can rearrange before aggregation, resulting in more compact assemblies. In diffusion-limited processes, particles aggregate immediately upon contact, resulting in more filamentous assemblies.
Independent of the particle system, the reaction starts with the replacement of the ligand by the additive R5S. Consequently, the ligand type can affect the kinetics of the exchange reaction strongly. We assume that in the case of the OAm-coated particles, the exchange is faster due to the lower binding energy of the ligand to the gold surface. We conclude that the quicker exchange favors the aggregation reaction and decreases the ability to rearrange, resulting in a diffusion-limited reaction. Consequently, strongly connected networks with a lower porosity and with less spherical substructures are formed.
In the case of larger particles, properties such as colloidal stability are influenced by stronger core-core interactions. We assume that minor modifications of the shell are sufficient to reduce the colloidal stability and cause agglomeration. As a result, particles can self-assemble and rearrange before they aggregate. We conclude that larger cores favor reaction-limited aggregation. Consequently, substructures in the sponge network have a higher sphericity.

Chapter 5: Conclusion and Outlook

This dissertation investigated the ability to influence the colloidal stability and the shape stability of apolar nanoparticles by modifying the ligand shell. The aim was to identify the underlying mechanisms. The first goal was to improve colloidal stability. The second goal was to reduce the shape stability. Most of the nanoparticles used were so-called "shell-dominated" systems, in which agglomeration is induced by the transition of the shell structure from a disordered to an ordered state. Both goals were to be achieved by changing the shell structure.

The investigated mechanisms to stabilize the colloidal stability are therefore based on the prevention/disruption of the transition of the shell. A delay in the transition of the shell could be achieved by using additives. However, only certain types of molecules led to a significant stabilization of the dispersion. The size of the molecule and the affinity of the functional group to gold played a decisive role. The "best" additive was tetrahydrothiophene. The small cyclic sulfide penetrated the shell and partially replaced the original thiol ligand. This disrupted the transition of the shell structure. However, the stabilizing effect did not increase continuously with the fraction of the additive in the shell. Instead, a decrease in the stabilizing effect was observed above a certain additive fraction in the shell. This trend could be attributed to the transition of the additive distribution in the shell from a random to a heterogeneous/clustered one. In conclusion, it can be stated that additives can be used to stabilize dispersions, but the transition of the shell can only be delayed and not stopped.

Non-linear ligands were used to suppress the transition of the shell completely. Branched and kinked thiols, amines, and sulfides were used as non-linear ligands. Slight agglomeration was observed experimentally in most non-linear systems at temperatures below $-90\,^{\circ}\mathrm{C}$. However, simulations showed that none of the ligand systems used led to a transition of the shell. The agglomeration observed is mainly the result of the change in solubility or interfacial energy at temperatures close to the solvent's freezing point. The stabilization mechanism is based on the altered interactions between the ligand molecules. The non-linear molecules cause the ligands to arrange themselves differently, influencing their orientation and the general shell density. The ligands are arranged in such a way that alignment with their alkyl chains becomes impossible. The main advantage of non-linear ligands is the extreme stabilization that can be achieved by comparatively simple modification of the particle system. However, these ligand systems have a decisive disadvantage: their low commercial availability.

For this reason, an attempt was made to reproduce the effect of non-linear ligands, using so-called "mixed" ligand shells. In this work, linear alkylthiols with different chain lengths were combined by stepwise ligand exchange. Depending on the combination, moderate to strong improvements in colloidal stability were observed. In particular, combining longer alkylthiols with the shorter hexanethiol led to exceptionally stable systems. However, it was observed that the stabilizing effect does not always depend on the fraction of the shorter ligand. As with the additives, the results indicate that the shell structure and properties depend significantly on the

distribution of the two components. Further experiments and molecular dynamics simulations are currently necessary to prove this hypothesis.

The second part of this work addresses the change in shape stability of the gold cores. The used approach is based on observations made during the additive project. Depending on the tetrahydrothiophene concentration, a change in the particle shape could be observed during storage. The process was studied using TEM and SAXS measurements. It could be shown that the particles coarsened due to aggregation. Interestingly, the coarsening of the particles took place at room temperature within one month. By using moderate temperatures ($40\,^{\circ}$C to $60\,^{\circ}$C), the process could be significantly accelerated. The aggregation is induced by the reduction of the stabilizing effect of the shell due to the progressive replacement of the ligand by the additive. The increasing R5S fraction enabled small spacings between the cores. Additionally, the migration/diffusion of gold atoms allowed the formation of necks between the cores. The progressive aggregation leads to the formation of aggregates in the μm-range.

If higher temperatures are used ($>90\,^{\circ}$C), the formation of fractal microparticles and gold sponges can be observed. Gold sponges can be produced if the dispersion is not stirred during the heating—the formation is based on the sedimentation and merging of large aggregates. As a result, the sponge structure is formed layer by layer. The 3D reconstruction showed that the sponges produced in this work had high porosities (around $90\,\%$). Interestingly, the sponge network consists of spherical particles with a narrow size distribution. This sphericity resulted from the separation of the spherical substructures during image analysis. These substructures result from the merging of smaller spherical aggregates formed at the beginning of the aggregation process. The properties of the sponge structure can be influenced by the size of the initial particles and the type of ligands. Larger cores make the aggregation process more reaction-limited, resulting in a higher sphericity of structures within the network. Oleylamine shells make the aggregation more diffusion-limited, leading to a higher connectivity of the network.

In conclusion, it can be stated that each of the modifications made to the ligand shell significantly influenced the properties of the particle system. Based on the results of this work, various effects could be investigated in more detail in future projects. In particular, the destabilizing effect of the solvent toluene on ligand systems that show no transition of the shell structure in *n*-hexane. The effect could be observed with mixed shells (see Figure 3.3.4). However, a comparable effect was also observed with non-linear ligands (see Figure 5.0.1A and B). Little is known in the literature about the exact interaction between toluene and ligand shells. Simulations and further experiments could be used to investigate the influence of temperature-dependent solubility or the change in interfacial energy.

In addition to this fundamental research, certain modifications could also be extended to in-

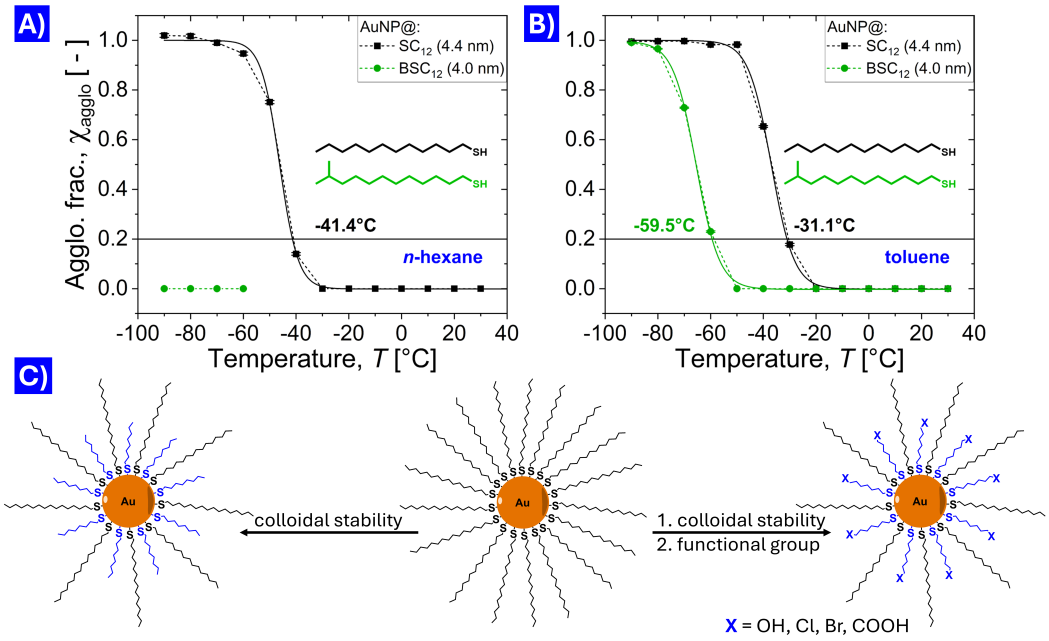


Figure 5.0.1: Temperature-dependent agglomeration fractions of 4 nm gold nanoparticles coated with 1-dodecanethiol (SC_{12}) and 11-methyldodecanethiol (BSC_{12}) dispersed in *n*-hexane (A) and toluene (B). The molecular structures and agglomeration temperatures are shown in the corresponding diagram. C) Overview of the modification possibilities of particles with a monomolecular thiol shell to form a mixed shell. Left: Combination of alkyl thiols with different lengths to improve colloidal stability. Right: Combination of unfunctionalized and functionalized alkylthiols to improve colloidal stability and/or introduce an additional shell function.

crease the functionality of the particle systems. This idea could be implemented, especially for the mixed ligand shells. In this work, only chemically similar alkylthiols were combined to influence the colloidal stability. Combinations of non-functionalized and functionalized alkylthiols have been previously reported in the literature [132, 135]. Functionalized alkylthiols are molecules with an additional functional group in the terminal position, such as a hydroxyl, carbonyl, carboxyl group, or a halogen atom. Such combinations enable the extension of the shell's properties. For example, polar or halogenated solvents or solvent mixtures could be used. Additionally, the terminal functional group can be utilized to incorporate new components into the particle system in subsequent steps (e.g., through substitution reactions). In this way, nanoparticles could be coupled with dyes or fluorescent components.

This work could be further developed by transferring sponge formation to other materials. Our findings could also be used to produce silver or platinum nanoparticles for the formation of porous structures. Alternatively, R5S-induced aggregation of gold nanoparticles could be used to produce porous layers using a printing process.

Bibliography

[1] L. Allen *et al.*, "Publishing: Credit where credit is due," *Nature*, vol. 508, no. 7496, pp. 312–313, 2014. DOI: 10.1038/508312a.

[2] A. Brand *et al.*, "Beyond authorship: attribution, contribution, collaboration, and credit," *Learned Publishing*, vol. 28, no. 2, pp. 151–155, 2015. DOI: 10.1087/20150211.

[3] L. Allen, A. O'Connell, and V. Kiermer, "How can we ensure visibility and diversity in research contributions? How the Contributor Role Taxonomy (CRediT) is helping the shift from authorship to contributorship," *Learned Publishing*, vol. 32, no. 1, pp. 71–74, 2019. DOI: 10.1002/leap.1210.

[4] H. Goesmann and C. Feldmann, "Nanoparticulate Functional Materials," *Angew. Chem. Int. Ed.*, vol. 49, no. 8, pp. 1362–1395, 2010. DOI: 10.1002/anie.200903053.

[5] J. S. Kim *et al.*, "Antimicrobial effects of silver nanoparticles," *Nanomedicine Nanotechnology, Biol. Med.*, vol. 3, no. 1, pp. 95–101, 2007. DOI: 10.1016/j.nano.2006.12.001.

[6] A. M. Mebert, C. J. Baglole, M. F. Desimone, and D. Maysinger, "Nanoengineered silica: Properties, applications and toxicity," *Food Chem. Toxicol.*, vol. 109, pp. 753–770, 2017. DOI: 10.1016/j.fct.2017.05.054.

[7] T. G. Smijs and S. Pavel, "Titanium dioxide and zinc oxide nanoparticles in sunscreens: focus on their safety and effectiveness," *Nanotechnol. Sci. Appl.*, vol. 4, no. 1, pp. 95–112, 2011. DOI: 10.2147/NSA.S19419.

[8] A. Kumar, P. K. Vemula, P. M. Ajayan, and G. John, "Silver-nanoparticle-embedded antimicrobial paints based on vegetable oil," *Nat. Mater.*, vol. 7, no. 3, pp. 236–241, 2008. DOI: 10.1038/nmat2099.

[9] T. C. Teng, T. P. Teng, and S. I. Pan, "Effects of Titania and Silica Nanoparticle on Paint Film," *Adv. Mater. Res.*, vol. 287-290, pp. 1437–1442, 2011. DOI: 10.4028/www.scientific.net/AMR.287-290.1437.

[10] Z.-S. Wu *et al.*, "Graphene Anchored with Co 3 O 4 Nanoparticles as Anode of Lithium Ion Batteries with Enhanced Reversible Capacity and Cyclic Performance," *ACS Nano*, vol. 4, no. 6, pp. 3187–3194, 2010. DOI: 10.1021/nn100740x.

[11] N. Liu *et al.*, "A pomegranate-inspired nanoscale design for large-volume-change lithium battery anodes," *Nat. Nanotechnol.*, vol. 9, no. 3, pp. 187–192, 2014. DOI: 10.1038/nnano.2014.6.

[12] C. He *et al.*, "Carbon-Encapsulated Fe 3 O 4 Nanoparticles as a High-Rate Lithium Ion Battery Anode Material," *ACS Nano*, vol. 7, no. 5, pp. 4459–4469, 2013. DOI: 10.1021/nn401059h.

[13] F. Li *et al.*, "Dynamic Nanoparticle Assemblies for Biomedical Applications," *Adv. Mat.*, vol. 29, no. 14, 2017. DOI: 10.1002/adma.201605897.

[14] P. T. Yin, S. Shah, M. Chhowalla, and K.-B. Lee, "Design, Synthesis, and Characterization of Graphene–Nanoparticle Hybrid Materials for Bioapplications," *Chem. Rev.*, vol. 115, no. 7, pp. 2483–2531, 2015. DOI: 10.1021/cr500537t.

[15] H. Chang *et al.*, "Highly Fluorescent Gold Cluster Assembly," *J. Am. Chem. Soc.*, vol. 143, no. 1, pp. 326–334, 2021. DOI: 10.1021/jacs.0c10907.

[16] Y. Tao, M. Li, J. Ren, and X. Qu, "Metal nanoclusters: novel probes for diagnostic and therapeutic applications," *Chem. Soc. Rev.*, vol. 44, no. 23, pp. 8636–8663, 2015. DOI: 10.1039/C5CS00607D.

[17] Y. Chen *et al.*, "Shortwave Infrared in Vivo Imaging with Gold Nanoclusters," *Nano Lett.*, vol. 17, no. 10, pp. 6330–6334, 2017. DOI: 10.1021/acs.nanolett.7b03070.

[18] L. S. Ardekani and P. W. Thulstrup, "Gold Nanoparticle-Mediated Lateral Flow Assays for Detection of Host Antibodies and COVID-19 Proteins," *Nanomater.*, vol. 12, no. 9, p. 1456, 2022. DOI: 10.3390/nano12091456.

[19] M. A. Dheyab *et al.*, "Focused role of nanoparticles against COVID-19: Diagnosis and treatment," *Photodiagnosis Photodyn. Ther.*, vol. 34, p. 102 287, 2021. DOI: 10.1016/j.pdpdt.2021.102287.

[20] D. J. Kang *et al.*, "Reversible Conductive Inkjet Printing of Healable and Recyclable Electrodes on Cardboard and Paper," *Small*, vol. 16, no. 25, pp. 1–7, 2020. DOI: 10.1002/smll.202000928.

[21] H. W. Tan, J. An, C. K. Chua, and T. Tran, "Metallic Nanoparticle Inks for 3D Printing of Electronics," *Adv. Electron. Mater.*, vol. 5, no. 5, 2019. DOI: 10.1002/aelm.201800831.

[22] R. Buchheit, B. Kuttich, L. González-García, and T. Kraus, "Hybrid Dielectric Films of Inkjet-Printable Core–Shell Nanoparticles," *Adv. Mater.*, vol. 33, no. 41, p. 2 103 087, 2021. DOI: 10.1002/adma.202103087.

[23] K. Yan, J. Li, L. Pan, and Y. Shi, "Inkjet printing for flexible and wearable electronics," *APL Mater.*, vol. 8, no. 12, p. 120 705, 2020. DOI: 10.1063/5.0031669.

[24] M. Deng *et al.*, "A gold nanoparticle ink suitable for the fabrication of electrochemical electrode by inkjet printing," *J. Nanosci. Nanotechnol.*, vol. 14, no. 7, pp. 5114–5119, 2014. DOI: 10.1166/jnn.2014.7208.

[25] Y. Wu *et al.*, "Studies of Gold Nanoparticles as Precursors to Printed Conductive Features for Thin-Film Transistors," *Chem. Mater.*, vol. 18, no. 19, pp. 4627–4632, 2006. DOI: 10.1021/cm0611643.

[26] D. J. Barber and I. C. Freestone, "AN INVESTIGATION OF THE ORIGIN OF THE COLOUR OF THE LYCURGUS CUP BY ANALYTICAL TRANSMISSION ELECTRON MICROSCOPY," *Archaeometry*, vol. 32, no. 1, pp. 33–45, 1990. DOI: 10.1111/j.1475-4754.1990.tb01079.x.

[27] M. Faraday, "X. The Bakerian Lecture. —Experimental relations of gold (and other metals) to light," *Philos. trans. R. Soc. Lond.*, vol. 147, pp. 145–181, 1857. DOI: 10.1098/rstl.1857.0011.

[28] J. Turkevich, P. C. Stevenson, and J. Hillier, "A study of the nucleation and growth processes in the synthesis of colloidal gold," *Discussions of the Faraday Society*, vol. 11, p. 55, 1951. DOI: 10.1039/df9511100055.

[29] G. Frens, "Controlled Nucleation for the Regulation of the Particle Size in Monodisperse Gold Suspensions," *Nature Physical Science*, vol. 241, no. 105, pp. 20–22, 1973. DOI: 10.1038/physci241020a0.

[30] M. Teimouri *et al.*, "Gold nanoparticles fabrication by plant extracts: synthesis, characterization, degradation of 4-nitrophenol from industrial wastewater, and insecticidal activity – A review," *J. Clean. Prod.*, vol. 184, pp. 740–753, 2018. DOI: 10.1016/j.jclepro.2018.02.268.

[31] M. Brust *et al.*, "Synthesis of thiol-derivatised gold nanoparticles in a two-phase Liquid–Liquid system," *J. Chem. Soc., Chem. Commun.*, vol. 0, no. 7, pp. 801–802, 1994. DOI: 10.1039/C39940000801.

[32] B.-H. Wu *et al.*, "Solvent effect on the synthesis of monodisperse amine-capped Au nanoparticles," *Chinese Chem. Lett.*, vol. 24, no. 6, pp. 457–462, 2013. DOI: 10.1016/j.cclet.2013.03.054.

[33] K. Vinodgopal *et al.*, "Sonolytic Design of Graphene−Au Nanocomposites. Simultaneous and Sequential Reduction of Graphene Oxide and Au(III)," *J. Phys. Chem. Lett.*, vol. 1, no. 13, pp. 1987–1993, 2010. DOI: 10.1021/jz1006093.

[34] A. V. Kabashin *et al.*, "Nanofabrication with Pulsed Lasers," *Nanoscale Res. Lett.*, vol. 5, no. 3, pp. 454–463, 2010. DOI: 10.1007/s11671-010-9543-z.

[35] V. Amendola, G. A. Rizzi, S. Polizzi, and M. Meneghetti, "Synthesis of Gold Nanoparticles by Laser Ablation in Toluene: Quenching and Recovery of the Surface Plasmon Absorption," *J. Phys. Chem. B*, vol. 109, no. 49, pp. 23 125–23 128, 2005. DOI: 10.1021/jp055783v.

[36] I. Ijaz, E. Gilani, A. Nazir, and A. Bukhari, "Detail review on chemical, physical and green synthesis, classification, characterizations and applications of nanoparticles," *Green Chem. Lett. Rev.*, vol. 13, no. 3, pp. 223–245, 2020. DOI: 10.1080/17518253.2020.1802517.

[37] X. Liu *et al.*, "A Study on Gold Nanoparticle Synthesis Using Oleylamine as Both Reducing Agent and Protecting Ligand," *J. Nanosci. Nanotechnol.*, vol. 7, no. 9, pp. 3126–3133, 2007. DOI: 10.1166/jnn.2007.805.

[38] M. V. Kirichkov *et al.*, "In situ analysis of the formation steps of gold nanoparticles by oleylamine reduction," *J. Struct. Chem.*, vol. 58, no. 7, pp. 1403–1410, 2017. DOI: 10.1134/S0022476617070186.

[39] A. Cirri, A. Silakov, and B. J. Lear, "Ligand Control over the Electronic Properties within the Metallic Core of Gold Nanoparticles," *Angew. Chemie Int. Ed.*, vol. 54, no. 40, pp. 11 750–11 753, 2015. DOI: 10.1002/anie.201505933.

[40] A. Heuer-Jungemann *et al.*, "The Role of Ligands in the Chemical Synthesis and Applications of Inorganic Nanoparticles," *Chem. Rev.*, vol. 119, no. 8, pp. 4819–4880, 2019. DOI: 10.1021/acs.chemrev.8b00733.

[41] M. Büttner, T. Belser, and P. Oelhafen, "Stability of Thiol-Passivated Gold Particles at Elevated Temperatures Studied by X-ray Photoelectron Spectroscopy," *J. Phys. Chem. B*, vol. 109, no. 12, pp. 5464–5467, 2005. DOI: 10.1021/jp0462355.

[42] J. G. Smith and P. K. Jain, "The Ligand Shell as an Energy Barrier in Surface Reactions on Transition Metal Nanoparticles," *J. Am. Chem. Soc.*, vol. 138, no. 21, pp. 6765–6773, 2016. DOI: 10.1021/jacs.6b00179.

[43] D. Monego *et al.*, "Colloidal Stability of Apolar Nanoparticles: Role of Ligand Length," *Langmuir*, vol. 34, no. 43, pp. 12 982–12 989, 2018. DOI: 10.1021/acs.langmuir.8b02883.

[44] I. Kanelidis and T. Kraus, "The role of ligands in coinage-metal nanoparticles for electronics," *Beilstein J. Nanotechnol.*, vol. 8, no. 1, pp. 2625–2639, 2017. DOI: 10.3762/bjnano.8.263.

[45] D. Napper, "Steric stabilization," *J. Colloid Interface Sci.*, vol. 58, no. 2, pp. 390–407, 1977. DOI: 10.1016/0021-9797(77)90150-3.

[46] B. Derjaguin, "Untersuchungen über die Reibung und Adhäsion, IV," *Kolloid-Zeitschrift*, vol. 69, no. 2, pp. 155–164, 1934. DOI: 10.1007/BF01433225.

[47] B. V. Derjaguin, "Theory of the stability of strongly charged lyophobic sol and of the adhesion of strongly charged particles in solutions of electrolytes," *Acta phys. chim. URSS*, vol. 14, p. 633, 1941.

[48] E. J. W. Verwey, N. Laboratorium, and D. Waals, "Theory of the stability of lyophobic colloids," *J. Phys. Chem.*, vol. 51, no. 3, pp. 631–636, 1947.

[49] H. Hamaker, "The London—van der Waals attraction between spherical particles," *Physica*, vol. 4, no. 10, pp. 1058–1072, 1937. DOI: 10.1016/S0031-8914(37)80203-7.

[50] H. Helmholtz, "Ueber einige Gesetze der Vertheilung elektrischer Ströme in körperlichen Leitern, mit Anwendung auf die thierisch-elektrischen Versuche," *Ann. Phys.*, vol. 165, no. 7, pp. 353–377, 1853. DOI: 10.1002/andp.18531650702.

[51] M. Gouy, "Sur la constitution de la charge électrique à la surface d'un électrolyte," *J. Phys. Théorique Appliquée*, vol. 9, no. 1, pp. 457–468, 1910. DOI: 10.1051/jphystap:019100090045700.

[52] D. L. Chapman, "LI. A contribution to the theory of electrocapillarity," *London, Edinburgh, Dublin Philos. Mag. J. Sci.*, vol. 25, no. 148, pp. 475–481, 1913. DOI: 10.1080/14786440408634187.

[53] O. Stern, "Zur Theorie der elektrolytischen Doppelschicht," *Zeitschrift für Elektrochemie und Angew. Phys. Chemie*, vol. 30, no. 21-22, pp. 508–516, 1924. DOI: 10.1002/bbpc.192400182.

[54] V. P. Debye, "Zur Theorie der Electrolyte," *Phys. Z.*, pp. 185–206, 1923.

[55] S. Asakura and F. Oosawa, "On Interaction between Two Bodies Immersed in a Solution of Macromolecules," *J. Chem. Phys.*, vol. 22, no. 7, pp. 1255–1256, 1954. DOI: 10.1063/1.1740347.

[56] P. G. De Gennes, "Polymer solutions near an interface. Adsorption and depletion layers," *Macromolecules*, vol. 14, no. 6, pp. 1637–1644, 1981. DOI: 10.1021/ma50007a007.

[57] J. J. Calvin, A. S. Brewer, and A. P. Alivisatos, "The role of organic ligand shell structures in colloidal nanocrystal synthesis," *Nat. Synth.*, vol. 1, no. 2, pp. 127–137, 2022. DOI: 10.1038/s44160-022-00025-4.

[58] T. Kister *et al.*, "Colloidal Stability of Apolar Nanoparticles: The Role of Particle Size and Ligand Shell Structure," *ACS Nano*, vol. 12, no. 6, pp. 5969–5977, 2018. DOI: 10.1021/acsnano.8b02202.

[59] D. Monego *et al.*, "When Like Destabilizes Like: Inverted Solvent Effects in Apolar Nanoparticle Dispersions," *ACS Nano*, vol. 14, no. 5, pp. 5278–5287, 2020. DOI: 10.1021/acsnano.9b03552.

[60] M. B. Cortie *et al.*, "On the Coalescence of Nanoparticulate Gold Sinter Ink," *J. Phys. Chem. C*, vol. 117, no. 21, pp. 11 377–11 384, 2013. DOI: 10.1021/jp401815b.

[61] P. G. Jamkhande, N. W. Ghule, A. H. Bamer, and M. G. Kalaskar, "Metal nanoparticles synthesis: An overview on methods of preparation, advantages and disadvantages, and applications," *J. Drug Deliv. Sci. Technol.*, vol. 53, p. 101 174, 2019. DOI: 10.1016/j.jddst.2019.101174.

[62] N. Abid *et al.*, "Synthesis of nanomaterials using various top-down and bottom-up approaches, influencing factors, advantages, and disadvantages: A review," *Adv. Colloid Interface Sci.*, vol. 300, p. 102 597, 2022. DOI: 10.1016/j.cis.2021.102597.

[63] C. Dhand *et al.*, "Methods and strategies for the synthesis of diverse nanoparticles and their applications: a comprehensive overview," *RSC Adv.*, vol. 5, no. 127, pp. 105 003–105 037, 2015. DOI: 10.1039/C5RA19388E.

[64] N. Baig, I. Kammakakam, and W. Falath, "Nanomaterials: a review of synthesis methods, properties, recent progress, and challenges," *Mater. Adv.*, vol. 2, no. 6, pp. 1821–1871, 2021. DOI: 10.1039/D0MA00807A.

[65] H. Agarwal, S. Venkat Kumar, and S. Rajeshkumar, "A review on green synthesis of zinc oxide nanoparticles – An eco-friendly approach," *Resour. Technol.*, vol. 3, no. 4, pp. 406–413, 2017. DOI: 10.1016/j.reffit.2017.03.002.

[66] E. A. Goodilin, P. S. Weiss, and Y. Gogotsi, "Nanotechnology Facets of the Periodic Table of Elements," *ACS Nano*, vol. 13, no. 10, pp. 10 879–10 886, 2019. DOI: 10.1021/acsnano.9b06998.

[67] V. V. Mody, R. Siwale, A. Singh, and H. R. Mody, "Introduction to metallic nanoparticles," *J. Pharm. Bioallied Sci.*, vol. 2, no. 4, p. 282, 2010. DOI: 10.4103/0975-7406.72127.

[68] P. K. Jain, X. Huang, I. H. El-Sayed, and M. A. El-Sayed, "Noble Metals on the Nanoscale: Optical and Photothermal Properties and Some Applications in Imaging, Sensing, Biology, and Medicine," *Acc. Chem. Res.*, vol. 41, no. 12, pp. 1578–1586, 2008. DOI: 10.1021/ar7002804.

[69] E. C. Dreaden *et al.*, "The golden age: gold nanoparticles for biomedicine," *Chem. Soc. Rev.*, vol. 41, no. 7, pp. 2740–2779, 2012. DOI: 10.1039/C1CS15237H.

[70] S. Anu Mary Ealia and M. P. Saravanakumar, "A review on the classification, characterisation, synthesis of nanoparticles and their application," *IOP Conf. Ser. Mater. Sci. Eng.*, vol. 263, no. 3, p. 032 019, 2017. DOI: 10.1088/1757-899X/263/3/032019.

[71] T. Tsuzuki and P. G. McCormick, "Mechanochemical synthesis of nanoparticles," *J. Mater. Sci.*, vol. 39, pp. 5143–5146, 2004. DOI: 10.1023/B:JMSC.0000039199.56155.f9.

[72] T. Prasad Yadav, R. Manohar Yadav, and D. Pratap Singh, "Mechanical Milling: a Top Down Approach for the Synthesis of Nanomaterials and Nanocomposites," *Nanosci. Nanotechnol.*, vol. 2, no. 3, pp. 22–48, 2012. DOI: 10.5923/j.nn.20120203.01.

[73] H. Schreyer *et al.*, "Milling Down to Nanometers: A General Process for the Direct Dry Synthesis of Supported Metal Catalysts," *Angew. Chem., Int. Ed.*, vol. 58, no. 33, pp. 11 262–11 265, 2019. DOI: 10.1002/anie.201903545.

[74] V. Amendola and M. Meneghetti, "Laser ablation synthesis in solution and size manipulation of noble metal nanoparticles," *Phys. Chem. Chem. Phys.*, vol. 11, no. 20, p. 3805, 2009. DOI: 10.1039/b900654k.

[75] P. Asanithi, S. Chaiyakun, and P. Limsuwan, "Growth of Silver Nanoparticles by DC Magnetron Sputtering," *J. Nanomater.*, vol. 2012, no. 1, 2012. DOI: 10.1155/2012/963609.

[76] P. F. M. de Oliveira, R. M. Torresi, F. Emmerling, and P. H. C. Camargo, "Challenges and opportunities in the bottom-up mechanochemical synthesis of noble metal nanoparticles," *J. Mater. Chem. A*, vol. 8, no. 32, pp. 16 114–16 141, 2020. DOI: 10.1039/D0TA05183G.

[77] L. Yang, A. Moores, T. Friščić, and N. Provatas, "Thermodynamics Model for Mechanochemical Synthesis of Gold Nanoparticles: Implications for Solvent-Free Nanoparticle Production," *ACS Appl. Nano Mater.*, vol. 4, no. 2, pp. 1886–1897, 2021. DOI: 10.1021/acsanm.0c03255.

[78] X. Zhang *et al.*, "Hydrothermal synthesis of Ag nanoparticles on the nanocellulose and their antibacterial study," *Inorg. Chem. Commun.*, vol. 100, pp. 44–50, 2019. DOI: 10.1016/j.inoche.2018.12.012.

[79] S. Vinay *et al.*, "Hydrothermal synthesis of gold nanoparticles using spider cobweb as novel biomaterial: Application to photocatalytic," *Chem. Phys. Lett.*, vol. 748, p. 137 402, 2020. DOI: 10.1016/j.cplett.2020.137402.

[80] C. Tan and H. Zhang, "Wet-chemical synthesis and applications of non-layer structured two-dimensional nanomaterials," *Nat. Commun.*, vol. 6, no. 1, p. 7873, 2015. DOI: 10.1038/ncomms8873.

[81] G. A. Vinnacombe-Willson *et al.*, "Direct Bottom-Up In Situ Growth: A Paradigm Shift for Studies in Wet-Chemical Synthesis of Gold Nanoparticles," *Chem. Rev.*, vol. 123, no. 13, pp. 8488–8529, 2023. DOI: 10.1021/acs.chemrev.2c00914.

[82] S. Peng *et al.*, "A facile synthesis of monodisperse Au nanoparticles and their catalysis of CO oxidation," *Nano Res.*, vol. 1, no. 3, pp. 229–234, 2008. DOI: 10.1007/s12274-008-8026-3.

[83] V. K. LaMer and R. H. Dinegar, "Theory, Production and Mechanism of Formation of Monodispersed Hydrosols," *J. Am. Chem. Soc.*, vol. 72, no. 11, pp. 4847–4854, 1950. DOI: 10.1021/ja01167a001.

[84] W. Ostwald, "Studien über die Bildung und Umwandlung fester Körper," *Zeitschrift für Phys. Chemie*, vol. 22U, no. 1, pp. 289–330, 1897. DOI: 10.1515/zpch-1897-2233.

[85] D. B. Sridhar, R. Gupta, and B. Rai, "Effect of surface coverage and chemistry on self-assembly of monolayer protected gold nanoparticles: a molecular dynamics simulation study," *Phys. Chem. Chem. Phys.*, vol. 20, no. 40, pp. 25 883–25 891, 2018. DOI: 10.1039/C8CP04044C.

[86] S. Yamashita, Y. Ito, H. Kamiya, and Y. Okada, "Surface coverage can control the dispersibility of TiO2 and ZrO2 nanoparticles in hydrophobic solvents: Comparison of linear and branched ligands," *Adv. Powder Technol.*, vol. 35, no. 1, p. 104 277, 2024. DOI: 10.1016/j.apt.2023.104277.

[87] R. Dinkel, B. Braunschweig, and W. Peukert, "Fast and Slow Ligand Exchange at the Surface of Colloidal Gold Nanoparticles," *J. Phys. Chem. C*, vol. 120, no. 3, pp. 1673–1682, 2016. DOI: 10.1021/acs.jpcc.5b11055.

[88] M. Kluenker, M. Mondeshki, M. Nawaz Tahir, and W. Tremel, "Monitoring Thiol–Ligand Exchange on Au Nanoparticle Surfaces," *Langmuir*, vol. 34, no. 4, pp. 1700–1710, 2018. DOI: 10.1021/acs.langmuir.7b04015.

[89] D. J. Lavrich, S. M. Wetterer, S. L. Bernasek, and G. Scoles, "Physisorption and Chemisorption of Alkanethiols and Alkyl Sulfides on Au(111)," *J. Phys. Chem. B*, vol. 102, no. 18, pp. 3456–3465, 1998. DOI: 10.1021/jp980047v.

[90] S. J. Khan, F. Pierce, C. M. Sorensen, and A. Chakrabarti, "Self-Assembly of Ligated Gold Nanoparticles: Phenomenological Modeling and Computer Simulations," *Langmuir*, vol. 25, no. 24, pp. 13 861–13 868, 2009. DOI: 10.1021/la9008202.

[91] N. Goubet, J. Richardi, P.-A. Albouy, and M.-P. Pileni, "Which Forces Control Supracrystal Nucleation in Organic Media?" *Adv. Funct. Mater.*, vol. 21, no. 14, pp. 2693–2704, 2011. DOI: 10.1002/adfm.201100382.

[92] M. B. Sigman, A. E. Saunders, and B. A. Korgel, "Metal Nanocrystal Superlattice Nucleation and Growth," *Langmuir*, vol. 20, no. 3, pp. 978–983, 2004. DOI: 10.1021/la035405m.

[93] S. V. Sokolov *et al.*, "Reversible or Not? Distinguishing Agglomeration and Aggregation at the Nanoscale," *Anal. Chem.*, vol. 87, no. 19, pp. 10 033–10 039, 2015. DOI: 10.1021/acs.analchem.5b02639.

[94] G. Nichols *et al.*, "A Review of the Terms Agglomerate and Aggregate with a Recommendation for Nomenclature Used in Powder and Particle Characterization," *J. Pharm. Sci.*, vol. 91, no. 10, pp. 2103–2109, 2002. DOI: 10.1002/jps.10191.

[95] D. Doblas *et al.*, "Colloidal Solubility and Agglomeration of Apolar Nanoparticles in Different Solvents," *Nano Lett.*, vol. 19, no. 8, pp. 5246–5252, 2019. DOI: 10.1021/acs.nanolett.9b01688.

[96] D. H. Napper, *Polymeric stabilization of colloidal dispersions*. Academic Press: London, 1983, ISBN: 9780125139809.

[97] W. D. Luedtke and U. Landman, "Structure and Thermodynamics of Self-Assembled Monolayers on Gold Nanocrystallites," *J. Phys. Chem. B*, vol. 102, no. 34, pp. 6566–6572, 1998. DOI: 10.1021/jp981745i.

[98] P. K. Ghorai and S. C. Glotzer, "Molecular Dynamics Simulation Study of Self-Assembled Monolayers of Alkanethiol Surfactants on Spherical Gold Nanoparticles," *J. Phys. Chem. C*, vol. 111, no. 43, pp. 15 857–15 862, 2007. DOI: 10.1021/jp0746289.

[99] H. Basch and M. A. Ratner, "Molecular binding at gold transport interfaces. IV. Thiol chemisorption," *J. Chem. Phys.*, vol. 120, no. 12, pp. 5771–5780, 2004. DOI: 10.1063/1.1650294.

[100] C. Yi, S. Zhang, K. T. Webb, and Z. Nie, "Anisotropic Self-Assembly of Hairy Inorganic Nanoparticles," *Acc. Chem. Res.*, vol. 50, no. 1, pp. 12–21, 2017. DOI: 10.1021/acs.accounts.6b00343.

[101] D. S. Bolintineanu, J. M. D. Lane, and G. S. Grest, "Effects of Functional Groups and Ionization on the Structure of Alkanethiol-Coated Gold Nanoparticles," *Langmuir*, vol. 30, no. 37, pp. 11 075–11 085, 2014. DOI: 10.1021/la502795z.

[102] A. Widmer-Cooper and P. Geissler, "Orientational ordering of passivating ligands on CdS nanorods in solution generates strong rod-rod interactions," *Nano Lett.*, vol. 14, no. 1, pp. 57–65, 2014. DOI: 10.1021/nl403067p.

[103] J. M. D. Lane and G. S. Grest, "Spontaneous Asymmetry of Coated Spherical Nanoparticles in Solution and at Liquid-Vapor Interfaces," *Phys. Rev. Lett.*, vol. 104, no. 23, p. 235 501, 2010. DOI: 10.1103/PhysRevLett.104.235501.

[104] S. Roke *et al.*, "Surface molecular view of colloidal gelation," *Proc. Natl. Acad. Sci.*, vol. 103, no. 36, pp. 13 310–13 314, 2006. DOI: 10.1073/pnas.0606116103.

[105] A. Widmer-Cooper and P. L. Geissler, "Ligand-Mediated Interactions between Nanoscale Surfaces Depend Sensitively and Nonlinearly on Temperature, Facet Dimensions, and Ligand Coverage," *ACS Nano*, vol. 10, no. 2, pp. 1877–1887, 2016. DOI: 10.1021/acsnano.5b05569.

[106] D. Gerstner and T. Kraus, "Rapid nanoparticle self-assembly at elevated temperatures," *Nanoscale*, vol. 10, no. 17, pp. 8009–8013, 2018. DOI: 10.1039/C8NR00597D.

[107] M. G. Martin and J. I. Siepmann, "Transferable potentials for phase equilibria. 1. United-atom description of n-alkanes," *J. Phys. Chem. B*, vol. 102, no. 14, pp. 2569–2577, 1998. DOI: 10.1021/jp972543+.

[108] A. Badia *et al.*, "Structure and Dynamics in Alkanethiolate Monolayers Self-Assembled on Gold Nanoparticles: A DSC, FT-IR, and Deuterium NMR Study," *J. Am. Chem. Soc.*, vol. 119, no. 11, pp. 2682–2692, 1997. DOI: 10.1021/ja963571t.

[109] M. R. Hasan *et al.*, "The Colloidal Stability of Apolar Nanoparticles in Solvent Mixtures," *ACS Nano*, vol. 17, no. 10, pp. 9302–9312, 2023. DOI: 10.1021/acsnano.3c00812.

[110] A. D. Balan *et al.*, "Unsaturated Ligands Seed an Order to Disorder Transition in Mixed Ligand Shells of CdSe/CdS Quantum Dots," *ACS Nano*, vol. 13, no. 12, pp. 13 784–13 796, 2019. DOI: 10.1021/acsnano.9b03054.

[111] P. Born and T. Kraus, "Ligand-dominated temperature dependence of agglomeration kinetics and morphology in alkyl-thiol-coated gold nanoparticles," *Phys. Rev. E*, vol. 87, no. 6, p. 062 313, 2013. DOI: 10.1103/PhysRevE.87.062313.

[112] A. Pyttlik, B. Kuttich, and T. Kraus, "Microgravity Removes Reaction Limits from Non-polar Nanoparticle Agglomeration," *Small*, vol. 18, no. 46, p. 2 204 621, 2022. DOI: 10.1002/smll.202204621.

[113] T. V. Knapp *et al.*, "Stabilization of Apolar Nanoparticle Dispersions by Molecular Additives," *Langmuir*, vol. 40, no. 26, pp. 13 527–13 537, 2024. DOI: 10.1021/acs.langmuir.4c00996.

[114] P. J. Flory, "Thermodynamics of High Polymer Solutions," *J. Chem. Phys.*, vol. 10, no. 1, pp. 51–61, 1942. DOI: 10.1063/1.1723621.

[115] M. L. Huggins, "Solutions of Long Chain Compounds," *J. Chem. Phys.*, vol. 9, no. 5, pp. 440–440, 1941. DOI: 10.1063/1.1750930.

[116] J.-L. M. Abboud and R. Notari, "Critical compilation of scales of solvent parameters. Part I. Pure, non-hydrogen bond donor solvents," *Pure Appl. Chem.*, vol. 71, no. 4, pp. 645–718, 1999. DOI: 10.1351/pac199971040645.

[117] B. C. Lohman *et al.*, "Solubility of gold nanoparticles as a function of ligand shell and alkane solvent," *Phys. Chem. Chem. Phys.*, vol. 14, no. 18, p. 6509, 2012. DOI: 10.1039/c2cp40645d.

[118] A. P. Sánchez-Camargo *et al.*, "Application of Hansen solubility approach for the sub-critical and supercritical selective extraction of phlorotannins from Cystoseira abies-marina," *RSC Adv.*, vol. 6, no. 97, pp. 94 884–94 895, 2016. DOI: 10.1039/c6ra16862k.

[119] S. Hajiw, J. Schmitt, M. Impéror-Clerc, and B. Pansu, "Solvent-driven interactions between hydrophobically-coated nanoparticles," *Soft Matter*, vol. 11, no. 19, pp. 3920–3926, 2015. DOI: 10.1039/c5sm00176e.

[120] D. F. Sunday and D. L. Green, "Thermal and Rheological Behavior of Polymer Grafted Nanoparticles," *Macromolecules*, vol. 48, no. 23, pp. 8651–8659, 2015. DOI: 10.1021/acs.macromol.5b00987.

[121] J. P. Koski *et al.*, "Phase Behavior of Grafted Polymer Nanocomposites from Field-Based Simulations," *Macromolecules*, vol. 52, no. 14, pp. 5110–5121, 2019. DOI: 10.1021/acs.macromol.9b00720.

[122] B. Faure, G. Salazar-Alvarez, and L. Bergström, "Hamaker constants of iron oxide nanoparticles," *Langmuir*, vol. 27, no. 14, pp. 8659–8664, 2011. DOI: 10.1021/la201387d.

[123] T. Kister, J. H. M. Maurer, L. González-García, and T. Kraus, "Ligand-Dependent Nanoparticle Assembly and Its Impact on the Printing of Transparent Electrodes," *ACS*

Appl. Mater. Interfaces, vol. 10, no. 7, pp. 6079–6083, 2018. DOI: 10.1021/acsami.7b18579.

[124] Y. Yang *et al.*, "Entropic Ligands for Nanocrystals: From Unexpected Solution Properties to Outstanding Processability," *Nano Lett.*, vol. 16, no. 4, pp. 2133–2138, 2016. DOI: 10.1021/acs.nanolett.6b00730.

[125] Y. Yang, H. Qin, and X. Peng, "Intramolecular Entropy and Size-Dependent Solution Properties of Nanocrystal-Ligands Complexes," *Nano Lett.*, vol. 16, no. 4, pp. 2127–2132, 2016. DOI: 10.1021/acs.nanolett.6b00737.

[126] O. Elimelech *et al.*, "Entropy of Branching Out: Linear versus Branched Alkylthiols Ligands on CdSe Nanocrystals," *ACS Nano*, vol. 16, no. 3, pp. 4308–4321, 2022. DOI: 10.1021/acsnano.1c10430.

[127] O. Elimelech, O. Aviv, M. Oded, and U. Banin, "A Tale of Tails: Thermodynamics of CdSe Nanocrystal Surface Ligand Exchange," *Nano Lett.*, vol. 20, no. 9, pp. 6396–6403, 2020. DOI: 10.1021/acs.nanolett.0c01913.

[128] A. Ben-Shaul, I. Szleifer, and W. M. Gelbart, "Statistical thermodynamics of amphiphile chains in micelles," *Proc. Nati. Acad. Sci.*, vol. 81, no. 14, pp. 4601–4605, 1984. DOI: 10.1073/pnas.81.14.4601.

[129] I. Szleifer, "Statistical thermodynamics of polymers near surfaces," *Curr. Opin. Colloid Interface Sci.*, vol. 1, no. 3, pp. 416–423, 1996. DOI: 10.1016/S1359-0294(96)80142-7.

[130] D. Harries and A. Ben-Shaul, "Conformational chain statistics in a model lipid bilayer: Comparison between mean field and Monte Carlo calculations," *J. Chem. Phys.*, vol. 106, no. 4, pp. 1609–1619, 1997. DOI: 10.1063/1.473283.

[131] P. Flory, *Statistical Mechanics of Chain Molecules*. Interscience Publishers, 1969, ISBN: 9780470264959. [Online]. Available: https://books.google.de/books?id=EDZRAAAAMAAJ.

[132] C. Singh *et al.*, "Entropy-Mediated Patterning of Surfactant-Coated Nanoparticles and Surfaces," *Phys. Rev. Lett.*, vol. 99, no. 22, pp. 1–4, 2007. DOI: 10.1103/PhysRevLett.99.226106.

[133] Z. Pang *et al.*, "Partitioning surface ligands on nanocrystals for maximal solubility," *Nat. Commun.*, vol. 10, no. 1, pp. 1–8, 2019. DOI: 10.1038/s41467-019-10389-5.

[134] O. Elimelech, M. Oded, D. Harries, and U. Banin, "Spontaneous Patterning of Binary Ligand Mixtures on CdSe Nanocrystals: From Random to Janus Packing," *ACS Nano*, vol. 17, no. 6, pp. 5852–5860, 2023. DOI: 10.1021/acsnano.2c12676.

[135] J. J. Kuna *et al.*, "The effect of nanometre-scale structure on interfacial energy," *Nat. Mater.*, vol. 8, no. 10, pp. 837–842, 2009. DOI: 10.1038/nmat2534.

[136] Q. Ong, Z. Luo, and F. Stellacci, "Characterization of Ligand Shell for Mixed-Ligand Coated Gold Nanoparticles," *Acc. Chem. Res.*, vol. 50, no. 8, pp. 1911–1919, 2017. DOI: 10.1021/acs.accounts.7b00165.

[137] A. M. Jackson, J. W. Myerson, and F. Stellacci, "Spontaneous assembly of subnanometre-ordered domains in the ligand shell of monolayer-protected nanoparticles," *Nat. Mater.*, vol. 3, no. 5, pp. 330–336, 2004. DOI: 10.1038/nmat1116.

[138] A. M. Jackson, Y. Hu, P. J. Silva, and F. Stellacci, "From Homoligand- to Mixed-Ligand- Monolayer-Protected Metal Nanoparticles: A Scanning Tunneling Microscopy Investigation," *J. Am. Chem. Soc.*, vol. 128, no. 34, pp. 11 135–11 149, 2006. DOI: 10.1021/ja061545h.

[139] K. D. Nolf *et al.*, "Binding and Packing in Two-Component Colloidal Quantum Dot Ligand Shells: Linear versus Branched Carboxylates," *J. Am. Chem. Soc.*, vol. 139, no. 9, pp. 3456–3464, 2017. DOI: 10.1021/jacs.6b11328.

[140] K. M. Harkness, L. S. Fenn, D. E. Cliffel, and J. A. McLean, "Surface Fragmentation of Complexes from Thiolate Protected Gold Nanoparticles by Ion Mobility-Mass Spectrometry," *Anal. Chem.*, vol. 82, no. 7, pp. 3061–3066, 2010. DOI: 10.1021/ac100251d.

[141] Z. Luo *et al.*, "Evolution of the Ligand Shell Morphology during Ligand Exchange Reactions on Gold Nanoparticles," *Angew. Chem. Int. Ed.*, vol. 56, no. 43, pp. 13 521–13 525, 2017. DOI: 10.1002/anie.201708190.

[142] C. E. Mills, E. Ding, and B. D. Olsen, "Cononsolvency of Elastin-like Polypeptides in Water/Alcohol Solutions," *Biomacromolecules*, vol. 20, no. 6, pp. 2167–2173, 2019. DOI: 10.1021/acs.biomac.8b01644.

[143] S. Bharadwaj *et al.*, "Cononsolvency of thermoresponsive polymers: where we are now and where we are going," *Soft Matter*, vol. 18, no. 15, pp. 2884–2909, 2022. DOI: 10.1039/d2sm00146b.

[144] B. Lee, K. Littrell, Y. Sha, and E. V. Shevchenko, "Revealing the Effects of the Nonsolvent on the Ligand Shell of Nanoparticles and Their Crystallization," *J. Am. Chem. Soc.*, vol. 141, no. 42, pp. 16 651–16 662, 2019. DOI: 10.1021/jacs.9b06010.

[145] D. Heymann, "Solubility of C60 in alcohols and alkanes," *Carbon*, vol. 34, no. 5, pp. 627–631, 1996. DOI: 10.1016/0008-6223(95)00213-8.

[146] L. Meli and P. F. Green, "Aggregation and Coarsening of Ligand-Stabilized Gold Nanoparticles in Poly(methyl methacrylate) Thin Films," *ACS Nano*, vol. 2, no. 6, pp. 1305–1312, 2008. DOI: 10.1021/nn800045s.

[147] J. R. Shimpi, D. S. Sidhaye, and B. L. V. Prasad, "Digestive Ripening: A Fine Chemical Machining Process on the Nanoscale," *Langmuir*, vol. 33, no. 38, pp. 9491–9507, 2017. DOI: 10.1021/acs.langmuir.7b00193.

[148] I. Lifshitz and V. Slyozov, "The kinetics of precipitation from supersaturated solid solutions," *J. Phys. Chem. Solids*, vol. 19, no. 1-2, pp. 35–50, 1961. DOI: 10.1016/0022-3697(61)90054-3.

[149] C. Wagner, "Theorie der Alterung von Niederschlägen durch Umlösen (Ostwald-Reifung)," *Zeitschrift für Elektrochemie, Berichte der Bunsengesellschaft für Phys. Chemie*, vol. 65, no. 7-8, pp. 581–591, 1961. DOI: 10.1002/bbpc.19610650704.

[150] M. A. Boles, D. Ling, T. Hyeon, and D. V. Talapin, "The surface science of nanocrystals," *Nat. Mater.*, vol. 15, no. 2, pp. 141–153, 2016. DOI: 10.1038/nmat4526.

[151] J. Owen, "The coordination chemistry of nanocrystal surfaces," *Science*, vol. 347, no. 6222, pp. 615–616, 2015. DOI: 10.1126/science.1259924.

[152] S. Centi *et al.*, "Small Thiols Stabilize the Shape of Gold Nanorods," *J. Phys. Chem. C*, vol. 124, no. 20, pp. 11 132–11 140, 2020. DOI: 10.1021/acs.jpcc.0c00737.

[153] M. Hasan, D. Bethell, and M. Brust, "The Fate of Sulfur-Bound Hydrogen on Formation of Self-Assembled Thiol Monolayers on Gold: 1 H NMR Spectroscopic Evidence from Solutions of Gold Clusters," *J. Am. Chem. Soc.*, vol. 124, no. 7, pp. 1132–1133, 2002. DOI: 10.1021/ja0120577.

[154] H. Häkkinen, "The gold–sulfur interface at the nanoscale," *Nat. Chem.*, vol. 4, no. 6, pp. 443–455, 2012. DOI: 10.1038/nchem.1352.

[155] P. Sahu and B. L. V. Prasad, "Time and Temperature Effects on the Digestive Ripening of Gold Nanoparticles: Is There a Crossover from Digestive Ripening to Ostwald Ripening?" *Langmuir*, vol. 30, no. 34, pp. 10 143–10 150, 2014. DOI: 10.1021/la500914j.

[156] Y. Yang, Y. Yan, W. Wang, and J. Li, "Precise size control of hydrophobic gold nanoparticles using cooperative effect of refluxing ripening and seeding growth," *Nanotechnology*, vol. 19, no. 17, p. 175 603, 2008. DOI: 10.1088/0957-4484/19/17/175603.

[157] E. Ito, J. Noh, and M. Hara, "Steric effects on adsorption and desorption behaviors of alkanethiol self-assembled monolayers on Au(111)," *Chem. Phys. Lett.*, vol. 462, no. 4-6, pp. 209–212, 2008. DOI: 10.1016/j.cplett.2008.07.075.

[158] A. Bo, T. Kraus, and N. de Jonge, "Temperature-Dependent Coalescence of Individual Nonpolar Gold Nanoparticles in Liquid," *ACS Appl. Nano Mater.*, vol. 6, no. 2, pp. 1146–1152, 2023. DOI: 10.1021/acsanm.2c03818.

[159] B. Ingham *et al.*, "How Nanoparticles Coalesce: An in Situ Study of Au Nanoparticle Aggregation and Grain Growth," *Chem. Mater.*, vol. 23, no. 14, pp. 3312–3317, 2011. DOI: 10.1021/cm200354d.

[160] S. Arcidiacono, N. Bieri, D. Poulikakos, and C. Grigoropoulos, "On the coalescence of gold nanoparticles," *Int. J. Multiph. Flow*, vol. 30, no. 7-8, pp. 979–994, 2004. DOI: 10.1016/j.ijmultiphaseflow.2004.03.006.

[161] Y. Wang *et al.*, "In situ TEM observation of neck formation during oriented attachment of PbSe nanocrystals," *Nano Res.*, vol. 12, no. 10, pp. 2549–2553, 2019. DOI: 10.1007/s12274-019-2483-8.

[162] P. Guo and Y. Gao, "Coalescence of Au Nanoparticles without Ligand Detachment," *Phys. Rev. Lett.*, vol. 124, no. 6, p. 066 101, 2020. DOI: 10.1103/PhysRevLett.124.066101.

[163] R. Ristau *et al.*, "Electron microscopy studies of the thermal stability of gold nanoparticle arrays," *Gold Bull.*, vol. 42, no. 2, pp. 133–143, 2009. DOI: 10.1007/BF03214923.

[164] S. Y. Moon, S.-i. Tanaka, and T. Sekino, "Crystal Growth of Thiol-Stabilized Gold Nanoparticles by Heat-Induced Coalescence," *Nanoscale Res. Lett.*, vol. 5, no. 5, pp. 813–817, 2010. DOI: 10.1007/s11671-010-9565-6.

[165] Y. Yu *et al.*, "Role of Halides in the Ordered Structure Transitions of Heated Gold Nanocrystal Superlattices," *Langmuir*, vol. 31, no. 24, pp. 6924–6932, 2015. DOI: 10.1021/acs.langmuir.5b01498.

[166] R. Zou *et al.*, "Thermal stability of gold nanorods in an aqueous solution," *Colloids Surfaces A Physicochem. Eng. Asp.*, vol. 372, no. 1-3, pp. 177–181, 2010. DOI: 10.1016/j.colsurfa.2010.10.012.

[167] T. Hayashi, K. Wakamatsu, E. Ito, and M. Hara, "Effect of Steric Hindrance on Desorption Processes of Alkanethiols on Au(111)," *J. Phys. Chem. C*, vol. 113, no. 43, pp. 18 795–18 799, 2009. DOI: 10.1021/jp906494u.

[168] M. J. Coutts, M. B. Cortie, M. J. Ford, and A. M. McDonagh, "Rapid and Controllable Sintering of Gold Nanoparticle Inks at Room Temperature Using a Chemical Agent," *J. Phys. Chem. C*, vol. 113, no. 4, pp. 1325–1328, 2009. DOI: 10.1021/jp808927t.

[169] Z. Mu, R. Tang, and Z. Liu, "Construction of Inorganic Bulks through Coalescence of Particle Precursors," *Nanomater.*, vol. 11, no. 1, p. 241, 2021. DOI: 10.3390/nano11010241.

[170] Z. Li and X. Peng, "Size/Shape-Controlled Synthesis of Colloidal CdSe Quantum Disks: Ligand and Temperature Effects," *J. Am. Chem. Soc.*, vol. 133, no. 17, pp. 6578–6586, 2011. DOI: 10.1021/ja108145c.

[171] Y. Yin and A. P. Alivisatos, "Colloidal nanocrystal synthesis and the organic–inorganic interface," *Nature*, vol. 437, no. 7059, pp. 664–670, 2005. DOI: 10.1038/nature04165.

[172] C. B. Murray, C. R. Kagan, and M. G. Bawendi, "Synthesis and Characterization of Monodisperse Nanocrystals and Close-Packed Nanocrystal Assemblies," *Annu. Rev. Mater. Sci.*, vol. 30, no. 1, pp. 545–610, 2000. DOI: 10.1146/annurev.matsci.30.1.545.

[173] C. M. Evans *et al.*, "Review of the synthesis and properties of colloidal quantum dots: the evolving role of coordinating surface ligands," *J. Coord. Chem.*, vol. 65, no. 13, pp. 2391–2414, 2012. DOI: 10.1080/00958972.2012.695019.

[174] C. Waltmann, N. Horst, and A. Travesset, "Capping Ligand Vortices as "Atomic Orbitals" in Nanocrystal Self-Assembly," *ACS Nano*, vol. 11, no. 11, pp. 11 273–11 282, 2017. DOI: 10.1021/acsnano.7b05694.

[175] J. Zhou *et al.*, "Ideal CdSe/CdS Core/Shell Nanocrystals Enabled by Entropic Ligands and Their Core Size-, Shell Thickness-, and Ligand-Dependent Photoluminescence Properties," *J. Am. Chem. Soc.*, vol. 139, no. 46, pp. 16 556–16 567, 2017. DOI: 10.1021/jacs.7b07434.

[176] A. J. Houtepen, Z. Hens, J. S. Owen, and I. Infante, "On the Origin of Surface Traps in Colloidal II–VI Semiconductor Nanocrystals," *Chem. Mater.*, vol. 29, no. 2, pp. 752–761, 2017. DOI: 10.1021/acs.chemmater.6b04648.

[177] J. J. Buckley *et al.*, "Chalcogenol Ligand Toolbox for CdSe Nanocrystals and Their Influence on Exciton Relaxation Pathways," *ACS Nano*, vol. 8, no. 3, pp. 2512–2521, 2014. DOI: 10.1021/nn406109v.

[178] F. W. Eagle, N. Park, M. Cash, and B. M. Cossairt, "Surface Chemistry and Quantum Dot Luminescence: Shell Growth, Atomistic Modification, and Beyond," *ACS Energy Lett.*, vol. 6, no. 3, pp. 977–984, 2021. DOI: 10.1021/acsenergylett.0c02697.

[179] S. Ithurria and D. V. Talapin, "Colloidal Atomic Layer Deposition (c-ALD) using Self-Limiting Reactions at Nanocrystal Surface Coupled to Phase Transfer between Polar and Nonpolar Media," *J. Am. Chem. Soc.*, vol. 134, no. 45, pp. 18 585–18 590, 2012. DOI: 10.1021/ja308088d.

[180] V. Sayevich *et al.*, "Hybrid N -Butylamine-Based Ligands for Switching the Colloidal Solubility and Regimentation of Inorganic-Capped Nanocrystals," *ACS Nano*, vol. 11, no. 2, pp. 1559–1571, 2017. DOI: 10.1021/acsnano.6b06996.

[181] T. Kodanek *et al.*, "Phase transfer of 1- and 2-dimensional Cd-based nanocrystals," *Nanoscale*, vol. 7, no. 45, pp. 19 300–19 309, 2015. DOI: 10.1039/C5NR06221G.

[182] L. Jing *et al.*, "Aqueous Based Semiconductor Nanocrystals," *Chem. Rev.*, vol. 116, no. 18, pp. 10 623–10 730, 2016. DOI: 10.1021/acs.chemrev.6b00041.

[183] T. K. Patra *et al.*, "Ligand dynamics control structure, elasticity, and high-pressure behavior of nanoparticle superlattices," *Nanoscale*, vol. 11, no. 22, pp. 10 655–10 666, 2019. DOI: 10.1039/C8NR09699F.

[184] M. A. L. Cordeiro, E. R. Leite, and E. A. Stach, "Controlling the Formation and Structure of Nanoparticle Superlattices through Surface Ligand Behavior," *Langmuir*, vol. 32, no. 44, pp. 11 606–11 614, 2016. DOI: 10.1021/acs.langmuir.6b03026.

[185] J. H. M. Maurer *et al.*, "Direct Nanoimprinting of a Colloidal Self-Organizing Nanowire Ink for Flexible, Transparent Electrodes," *Adv. Mater. Technol.*, vol. 2, no. 6, pp. 1–8, 2017. DOI: 10.1002/admt.201700034.

[186] D. T. Thompson, "Using gold nanoparticles for catalysis," *Nano Today*, vol. 2, no. 4, pp. 40–43, 2007. DOI: 10.1016/S1748-0132(07)70116-0.

[187] M. Haruta, "When Gold Is Not Noble: Catalysis by Nanoparticles," *Chem. Rec.*, vol. 3, no. 2, pp. 75–87, 2003. DOI: 10.1002/tcr.10053.

[188] D. V. Talapin and C. B. Murray, "PbSe Nanocrystal Solids for n- and p-Channel Thin Film Field-Effect Transistors," *Science*, vol. 310, no. 5745, pp. 86–89, 2005. DOI: 10.1126/science.1116703.

[189] Y. Tian *et al.*, "Charge separation in solid-state gold nanoparticles-sensitized photovoltaic cell," *Electrochem. commun.*, vol. 11, no. 8, pp. 1603–1605, 2009. DOI: 10.1016/j.elecom.2009.06.007.

[190] P. Tao *et al.*, "TiO2 nanocomposites with high refractive index and transparency," *J. Mater. Chem.*, vol. 21, no. 46, p. 18 623, 2011. DOI: 10.1039/c1jm13093e.

[191] R. Saidur, K. Leong, and H. Mohammed, "A review on applications and challenges of nanofluids," *Renew. Sustain. Energy Rev.*, vol. 15, no. 3, pp. 1646–1668, 2011. DOI: 10.1016/j.rser.2010.11.035.

[192] S. N. Merz *et al.*, "Computational and Experimental Investigation of Janus-like Monolayers on Ultrasmall Noble Metal Nanoparticles," *ACS Nano*, vol. 12, no. 11, pp. 11 031–11 040, 2018. DOI: 10.1021/acsnano.8b05188.

[193] S. N. Merz *et al.*, "Predicting the effect of chain-length mismatch on phase separation in noble metal nanoparticle monolayers with chemically mismatched ligands.," *Soft Matter*, vol. 15, no. 22, pp. 4498–4507, 2019. DOI: 10.1039/c9sm00264b.

[194] J. Vialetto *et al.*, "Photoswitchable Dissipative Two-Dimensional Colloidal Crystals," *Angew.Chem. Int. Ed.*, vol. 58, no. 27, pp. 9145–9149, 2019. DOI: 10.1002/anie.201904093.

[195] J. Vialetto, S. Rudiuk, M. Morel, and D. Baigl, "From bulk crystallization of inorganic nanoparticles at the air/water interface: tunable organization and intense structural colors," *Nanoscale*, vol. 12, no. 11, pp. 6279–6284, 2020. DOI: 10.1039/C9NR10965J.

[196] J. Vialetto and M. Anyfantakis, "Exploiting Additives for Directing the Adsorption and Organization of Colloid Particles at Fluid Interfaces," *Langmuir*, vol. 37, no. 31, pp. 9302–9335, 2021. DOI: 10.1021/acs.langmuir.1c01029.

[197] V. A. Turek *et al.*, "Plasmonic Ruler at the Liquid–Liquid Interface," *ACS Nano*, vol. 6, no. 9, pp. 7789–7799, 2012. DOI: 10.1021/nn302941k.

[198] M. Retout *et al.*, "Di-Arginine Additives for Dissociation of Gold Nanoparticle Aggregates: A Matrix-Insensitive Approach with Applications in Protease Detection," *ACS Appl. Mater. Interfaces*, vol. 14, no. 46, pp. 52 553–52 565, 2022. DOI: 10.1021/acsami.2c17531.

[199] S. Jendrzej, B. Gökce, and S. Barcikowski, "Colloidal Stability of Metal Nanoparticles in Engine Oil under Thermal and Mechanical Load," *Chem. Eng. Technol.*, vol. 40, no. 9, pp. 1569–1576, 2017. DOI: 10.1002/ceat.201600541.

[200] P. Pusey, "Neutrons, X-rays and Light: Scattering Methods Applied to Soft Condensed Matter," in P. Lindner and T. Zemb, Eds. North-Holland, 2002, ch. Introduction to Scattering Experiments.

[201] R. C. Hoft, M. J. Ford, A. M. McDonagh, and M. B. Cortie, "Adsorption of Amine Compounds on the Au(111) Surface: A Density Functional Study," *J. Phys. Chem. C*, vol. 111, no. 37, pp. 13 886–13 891, 2007. DOI: 10.1021/jp072494t.

[202] M. W. J. Beulen *et al.*, "Evidence for Nondestructive Adsorption of Dialkyl Sulfides on Gold," *Langmuir*, vol. 12, no. 26, pp. 6170–6172, 1996. DOI: 10.1021/la9606660.

[203] P. Angelova *et al.*, "Chemisorbed Monolayers of Corannulene Penta-Thioethers on Gold," *Langmuir*, vol. 29, no. 7, pp. 2217–2223, 2013. DOI: 10.1021/la304600s.

[204] A. Sinqh, A. Mehrotra, and S. L. Regen, "High Yield Medium Ring Synthesis of Thiacycloalkanes," *Synth. Commun.*, vol. 11, no. 5, pp. 409–411, 1981. DOI: 10.1080/00397918108064308.

[205] L. L. Thomas, T. J. Christakis, and W. L. Jorgensen, "Conformation of Alkanes in the Gas Phase and Pure Liquids," *J. Phys. Chem. B*, vol. 110, no. 42, pp. 21 198–21 204, 2006. DOI: 10.1021/jp064811m.

[206] S. W. I. Siu, K. Pluhackova, and R. A. Böckmann, "Optimization of the OPLS-AA Force Field for Long Hydrocarbons," *J. Chem. Theory Comput.*, vol. 8, no. 4, pp. 1459–1470, 2012. DOI: 10.1021/ct200908r.

[207] R. Hockney and J. Eastwood, *Computer Simulation Using Particles*. CRC Press, 2021, ISBN: 9780367806934. DOI: 10.1201/9780367806934.

[208] S. Plimpton, "Fast Parallel Algorithms for Short-Range Molecular Dynamics," *J. Comput. Phys.*, vol. 117, no. 1, pp. 1–19, 1995. DOI: 10.1006/jcph.1995.1039.

[209] A. Grossfield, "WHAM: the weighted histogram analysis method, version 2.0. 9," *Available at membrane. urmc. rochester. edu/content/wham.*,

[210] T. V. Knapp *et al.*, "Maintaining Shell Disorder with Kinked or Branched Ligands Stabilizes Apolar Nanoparticles," *ACS Nano*, vol. 19, no. 39, pp. 35 127–35 140, 2025. DOI: 10.1021/acsnano.5c12697.

[211] T. Ederth, "Computation of Lifshitz−van der Waals Forces between Alkylthiol Monolayers on Gold Films," *Langmuir*, vol. 17, no. 11, pp. 3329–3340, 2001. DOI: 10.1021/la001607w.

[212] N. Geva *et al.*, "Morphology of Passivating Organic Ligands around a Nanocrystal," *J. Phys. Chem. C*, vol. 122, no. 45, pp. 26 267–26 274, 2018. DOI: 10.1021/acs.jpcc.8b08413.

[213] G. Konstantatos *et al.*, "Ultrasensitive solution-cast quantum dot photodetectors," *Nature*, vol. 442, no. 7099, pp. 180–183, 2006. DOI: 10.1038/nature04855.

[214] X. Dai *et al.*, "Solution-processed, high-performance light-emitting diodes based on quantum dots," *Nature*, vol. 515, no. 7525, pp. 96–99, 2014. DOI: 10.1038/nature13829.

[215] X. Michalet *et al.*, "Quantum Dots for Live Cells, in Vivo Imaging, and Diagnostics," *Science*, vol. 307, no. 5709, pp. 538–544, 2005. DOI: 10.1126/science.1104274.

[216] J. J. Calvin *et al.*, "Observation of ordered organic capping ligands on semiconducting quantum dots via powder X-ray diffraction," *Nat. Commun.*, vol. 12, no. 1, p. 2663, 2021. DOI: 10.1038/s41467-021-22947-x.

[217] S. Mourdikoudis and L. M. Liz-Marzán, "Oleylamine in Nanoparticle Synthesis," *Chem. Mater.*, vol. 25, no. 9, pp. 1465–1476, 2013. DOI: 10.1021/cm4000476.

[218] M. Chen *et al.*, "Silver Nanoparticles Capped by Oleylamine: Formation, Growth, and Self-Organization," *Langmuir*, vol. 23, no. 10, pp. 5296–5304, 2007. DOI: 10.1021/la700553d.

[219] C. Wang and S. Sun, "Facile Synthesis of Ultrathin and Single-Crystalline Au Nanowires," *Chem. – An Asian J.*, vol. 4, no. 7, pp. 1028–1034, 2009. DOI: 10.1002/asia.200900002.

[220] A. D. Jewell, S. J. Kyran, D. Rabinovich, and E. C. H. Sykes, "Effect of Head-Group Chemistry on Surface-Mediated Molecular Self-Assembly," *Chem. – A Eur. J.*, vol. 18, no. 23, pp. 7169–7178, 2012. DOI: 10.1002/chem.201102956.

[221] C. Li *et al.*, "Anisotropy in Near-Spherical Colloidal Nanoparticles," *ACS Nano*, vol. 17, no. 18, pp. 17 873–17 883, 2023. DOI: 10.1021/acsnano.3c03466.

[222] L. Motte, F. Billoudet, and M. P. Pileni, "Self-Assembled Monolayer of Nanosized Particles Differing by Their Sizes," *J. Phys. Chem.*, vol. 99, no. 44, pp. 16 425–16 429, 1995. DOI: 10.1021/j100044a033.

[223] C. D. Bain and G. M. Whitesides, "Formation of Monolayers by the Coadsorption of Thiols on Gold: Variation in the Length of the Alkyl Chain," *J. Am. Chem. Soc.*, vol. 111, no. 18, pp. 7164–7175, 1989. DOI: 10.1021/ja00200a040.

[224] E. Suárez, N. Díaz, J. Méndez, and D. Suárez, "CENCALC: A computational tool for conformational entropy calculations from molecular simulations," *J. Comput. Chem.*, vol. 34, no. 23, pp. 2041–2054, 2013. DOI: 10.1002/jcc.23350.

[225] M. Deng *et al.*, "Ligand–Solvent Library Design for Tailoring Interparticle Interactions in Colloidal Nanocrystals," *ACS Nano*, vol. 19, no. 14, pp. 14 299–14 308, 2025. DOI: 10.1021/acsnano.5c01223.

[226] A. Bo *et al.*, "Nanoscale Faceting and Ligand Shell Structure Dominate the Self-Assembly of Nonpolar Nanoparticles into Superlattices," *Adv. Mater.*, vol. 34, no. 20, 2022. DOI: 10.1002/adma.202109093.

[227] A. K. Chew and R. C. V. Lehn, "Effect of Core Morphology on the Structural Asymmetry of Alkanethiol Monolayer-Protected Gold Nanoparticles," *J. Phys. Chem. C*, vol. 122, no. 45, pp. 26 288–26 297, 2018. DOI: 10.1021/acs.jpcc.8b09323.

[228] T. Kister, M. Mravlak, T. Schilling, and T. Kraus, "Pressure-controlled formation of crystalline, Janus, and core–shell supraparticles," *Nanoscale*, vol. 8, no. 27, pp. 13 377–13 384, 2016. DOI: 10.1039/C6NR01940D.

[229] L. S. Dodda, I. C. de Vaca, J. Tirado-Rives, and W. L. Jorgensen, "LigParGen web server: an automatic OPLS-AA parameter generator for organic ligands," *Nucleic Acids Res.*, vol. 45, no. W1, W331–W336, 2017. DOI: 10.1093/nar/gkx312.

[230] L. Martínez, R. Andrade, E. G. Birgin, and J. M. Martínez, "PACKMOL : A package for building initial configurations for molecular dynamics simulations," *J. Comput. Chem.*, vol. 30, no. 13, pp. 2157–2164, 2009. DOI: 10.1002/jcc.21224.

[231] H. C. Andersen, "Rattle: A "velocity" version of the shake algorithm for molecular dynamics calculations," *J. Comput. Chem.*, vol. 52, no. 1, pp. 24–34, 1983. DOI: 10.1016/0021-9991(83)90014-1.

[232] R. Pool, P. Schapotschnikow, and T. J. H. Vlugt, "Solvent Effects in the Adsorption of Alkyl Thiols on Gold Structures: A Molecular Simulation Study," *J. Phys. Chem. C*, vol. 111, no. 28, pp. 10 201–10 212, 2007. DOI: 10.1021/jp071491d.

[233] D. J. Evans and B. L. Holian, "The Nose–Hoover thermostat," *J. Chem. Phys.*, vol. 83, no. 8, pp. 4069–4074, 1985. DOI: 10.1063/1.449071.

[234] G. Bussi, D. Donadio, and M. Parrinello, "Canonical sampling through velocity rescaling," *J. Chem. Phys.*, vol. 126, no. 1, 2007. DOI: 10.1063/1.2408420.

[235] W. Humphrey, A. Dalke, and K. Schulten, "VMD: Visual molecular dynamics," *J. Mol. Graph.*, vol. 14, no. 1, pp. 33–38, 1996. DOI: 10.1016/0263-7855(96)00018-5.

[236] R. H. Terrill *et al.*, "Monolayers in Three Dimensions: NMR, SAXS, Thermal, and Electron Hopping Studies of Alkanethiol Stabilized Gold Clusters," *J. Am. Chem. Soc.*, vol. 117, no. 50, pp. 12 537–12 548, 1995. DOI: 10.1021/ja00155a017.

[237] S. K. Ghosh and T. Pal, "Interparticle Coupling Effect on the Surface Plasmon Resonance of Gold Nanoparticles: From Theory to Applications," *Chem. Rev.*, vol. 107, no. 11, pp. 4797–4862, 2007. DOI: 10.1021/cr0680282.

[238] M. Z. Iqbal *et al.*, "Reversible self-assembly of gold nanoparticles in response to external stimuli," *Mater. Des.*, vol. 205, p. 109 694, 2021. DOI: 10.1016/j.matdes.2021.109694.

[239] S. Yoon, "Controlled assembly of gold nanoparticles: Methods and plasmon coupling properties," *Bull. Korean Chem. Soc.*, vol. 45, no. 8, pp. 689–698, 2024. DOI: 10.1002/bkcs.12886.

[240] K. Saha *et al.*, "Gold Nanoparticles in Chemical and Biological Sensing," *Chem. Rev.*, vol. 112, no. 5, pp. 2739–2779, 2012. DOI: 10.1021/cr2001178.

[241] R. Ciriminna *et al.*, "Industrial Applications of Gold Catalysis," *Angew. Chem., Int. Ed.*, vol. 55, no. 46, pp. 14 210–14 217, 2016. DOI: 10.1002/anie.201604656.

[242] K. Xia *et al.*, "Ultra-stable and highly reactive colloidal gold nanoparticle catalysts protected using multi-dentate metal oxide nanoclusters," *Nat. Commun.*, vol. 15, no. 1, p. 851, 2024. DOI: 10.1038/s41467-024-45066-9.

[243] R. Sharma *et al.*, "NMR Characterization of Ligand Binding and Exchange Dynamics in Triphenylphosphine-Capped Gold Nanoparticles," *J. Phys. Chem. C*, vol. 113, no. 37, pp. 16 387–16 393, 2009. DOI: 10.1021/jp905141h.

[244] H. Pan, S. Ko, and C. Grigoropoulos, "The coalescence of supported gold nanoparticles induced by nanosecond laser irradiation," *Appl. Phys. A*, vol. 90, no. 2, pp. 247–253, 2007. DOI: 10.1007/s00339-007-4320-2.

[245] M.-J. Lee, S.-H. Lim, J.-M. Ha, and S.-M. Choi, "Green Synthesis of High-Purity Mesoporous Gold Sponges Using Self-Assembly of Gold Nanoparticles Induced by Thiolated Poly(ethylene glycol)," *Langmuir*, vol. 32, no. 23, pp. 5937–5945, 2016. DOI: 10.1021/acs.langmuir.6b01197.

[246] D. V. Leff, L. Brandt, and J. R. Heath, "Synthesis and Characterization of Hydrophobic, Organically-Soluble Gold Nanocrystals Functionalized with Primary Amines," *Langmuir*, vol. 12, no. 20, pp. 4723–4730, 1996. DOI: 10.1021/la960445u.

[247] S. R. King, A. R. Gentle, M. B. Cortie, and A. M. McDonagh, "On the Development of Optical Properties during Thermal Coarsening of Gold Nanoparticle Composites," *J. Phys. Chem. C*, vol. 122, no. 22, pp. 12 098–12 105, 2018. DOI: 10.1021/acs.jpcc.8b02744.

[248] D. Wen *et al.*, "Gold Aerogels: Three-Dimensional Assembly of Nanoparticles and Their Use as Electrocatalytic Interfaces," *ACS Nano*, vol. 10, no. 2, pp. 2559–2567, 2016. DOI: 10.1021/acsnano.5b07505.

[249] T. Kim, K. Lee, M.-s. Gong, and S.-W. Joo, "Control of Gold Nanoparticle Aggregates by Manipulation of Interparticle Interaction," *Langmuir*, vol. 21, no. 21, pp. 9524–9528, 2005. DOI: 10.1021/la0504560.

[250] T. Kim, C.-H. Lee, S.-W. Joo, and K. Lee, "Kinetics of gold nanoparticle aggregation: Experiments and modeling," *J. Colloid Interface Sci.*, vol. 318, no. 2, pp. 238–243, 2008. DOI: 10.1016/j.jcis.2007.10.029.

[251] W. Hou, M. Dasog, and R. W. J. Scott, "Probing the Relative Stability of Thiolate- and Dithiolate-Protected Au Monolayer-Protected Clusters," *Langmuir*, vol. 25, no. 22, pp. 12 954–12 961, 2009. DOI: 10.1021/la9018053.

[252] B. Hammouda, "A new Guinier–Porod model," *J. Appl. Cryst.*, vol. 43, no. 4, pp. 716–719, 2010. DOI: 10.1107/S0021889810015773.

[253] D. R. Caudwell, J. P. M. Trusler, V. Vesovic, and W. A. Wakeham, "Viscosity and Density of Five Hydrocarbon Liquids at Pressures up to 200 MPa and Temperatures up to 473 K," *J. Chem. Eng. Data*, vol. 55, no. 11, pp. 5396–5396, 2010. DOI: 10.1021/je1008137.

[254] Z. Fang *et al.*, "Viscosities of p -Xylene, Acetic Acid, and p -Xylene + Acetic Acid at (313.15 to 473.15) K and (0.10 to 3.20) MPa: Determined by the Rolling-Ball Method," *J. Chem. Eng. Data*, vol. 53, no. 12, pp. 2787–2792, 2008. DOI: 10.1021/je800635g.

[255] Y. Bae *et al.*, "Ligand-Dependent Coalescence Behaviors of Gold Nanoparticles Studied by Multichamber Graphene Liquid Cell Transmission Electron Microscopy," *Nano Lett.*, vol. 20, no. 12, pp. 8704–8710, 2020. DOI: 10.1021/acs.nanolett.0c03517.

[256] T. H. Lim *et al.*, "Real-Time TEM and Kinetic Monte Carlo Studies of the Coalescence of Decahedral Gold Nanoparticles," *ACS Nano*, vol. 3, no. 11, pp. 3809–3813, 2009. DOI: 10.1021/nn9012252.

[257] U. Anand *et al.*, "Hydration Layer-Mediated Pairwise Interaction of Nanoparticles," *Nano Lett.*, vol. 16, no. 1, pp. 786–790, 2016. DOI: 10.1021/acs.nanolett.5b04808.

[258] C. Zhu *et al.*, "In-situ liquid cell transmission electron microscopy investigation on oriented attachment of gold nanoparticles," *Nat. Commun.*, vol. 9, no. 1, p. 421, 2018. DOI: 10.1038/s41467-018-02925-6.

[259] M. A. van Huis *et al.*, "Low-Temperature Nanocrystal Unification through Rotations and Relaxations Probed by in Situ Transmission Electron Microscopy," *Nano Lett.*, vol. 8, no. 11, pp. 3959–3963, 2008. DOI: 10.1021/nl8024467.

[260] B. Jin *et al.*, "In Situ Liquid Cell TEM Reveals Bridge-Induced Contact and Fusion of Au Nanocrystals in Aqueous Solution," *Nano Lett.*, vol. 18, no. 10, pp. 6551–6556, 2018. DOI: 10.1021/acs.nanolett.8b03139.

[261] S. Yue *et al.*, "In Situ TEM Observation of the Atomic Transport Process during the Coalescence of Au Nanoparticles," *Nano Lett.*, vol. 22, no. 20, pp. 8115–8121, 2022. DOI: 10.1021/acs.nanolett.2c02491.

[262] T. S. Rodrigues, A. G. M. da Silva, and P. H. C. Camargo, "Nanocatalysis by noble metal nanoparticles: controlled synthesis for the optimization and understanding of activities," *J. Mater. Chem. A*, vol. 7, no. 11, pp. 5857–5874, 2019. DOI: 10.1039/C9TA00074G.

[263] X. Yang *et al.*, "Gold Nanomaterials at Work in Biomedicine," *Chem. Rev.*, vol. 115, no. 19, pp. 10 410–10 488, 2015. DOI: 10.1021/acs.chemrev.5b00193.

[264] T. Pradeep and Anshup, "Noble metal nanoparticles for water purification: A critical review," *Thin Solid Films*, vol. 517, no. 24, pp. 6441–6478, 2009. DOI: 10.1016/j.tsf.2009.03.195.

[265] E. Roduner, "Size matters: why nanomaterials are different," *Chem. Soc. Rev.*, vol. 35, no. 7, p. 583, 2006. DOI: 10.1039/b502142c.

[266] Z. Fan and H. Zhang, "Crystal phase-controlled synthesis, properties and applications of noble metal nanomaterials," *Chem. Soc. Rev.*, vol. 45, no. 1, pp. 63–82, 2016. DOI: 10.1039/C5CS00467E.

[267] C. Zhu, D. Du, A. Eychmüller, and Y. Lin, "Engineering Ordered and Nonordered Porous Noble Metal Nanostructures: Synthesis, Assembly, and Their Applications in Electrochemistry," *Chem. Rev.*, vol. 115, no. 16, pp. 8896–8943, 2015. DOI: 10.1021/acs.chemrev.5b00255.

[268] E. Seker, M. L. Reed, and M. R. Begley, "Nanoporous Gold: Fabrication, Characterization, and Applications," *Materials*, vol. 2, no. 4, pp. 2188–2215, 2009. DOI: 10.3390/ma2042188.

[269] A. Wittstock *et al.*, "Nanoporous Gold Catalysts for Selective Gas-Phase Oxidative Coupling of Methanol at Low Temperature," *Science*, vol. 327, no. 5963, pp. 319–322, 2010. DOI: 10.1126/science.1183591.

[270] A. Wittstock, A. Wichmann, and M. Bäumer, "Nanoporous Gold as a Platform for a Building Block Catalyst," *ACS Catal.*, vol. 2, no. 10, pp. 2199–2215, 2012. DOI: 10.1021/cs300231u.

[271] A. Wittstock, J. Biener, and M. Bäumer, "Nanoporous gold: a new material for catalytic and sensor applications," *Phys. Chem. Chem. Phys.*, vol. 12, no. 40, p. 12 919, 2010. DOI: 10.1039/c0cp00757a.

[272] J. Biener, M. M. Biener, R. J. Madix, and C. M. Friend, "Nanoporous Gold: Understanding the Origin of the Reactivity of a 21st Century Catalyst Made by Pre-Columbian Technology," *ACS Catal.*, vol. 5, no. 11, pp. 6263–6270, 2015. DOI: 10.1021/acscatal.5b01586.

[273] N. Asao *et al.*, "Nanostructured Materials as Catalysts: Nanoporous-Gold-Catalyzed Oxidation of Organosilanes with Water," *Angew. Chem. Int. Ed.*, vol. 49, no. 52, pp. 10 093–10 095, 2010. DOI: 10.1002/anie.201005138.

[274] B. Zugic *et al.*, "Dynamic restructuring drives catalytic activity on nanoporous gold–silver alloy catalysts," *Nat. Mater.*, vol. 16, no. 5, pp. 558–564, 2017. DOI: 10.1038/nmat4824.

[275] A. Othman, H. K. Bilan, E. Katz, and O. Smutok, "Highly Porous Gold Electrodes – Preparation and Characterization," *Chem. Electro. Chem.*, vol. 9, no. 9, 2022. DOI: 10.1002/celc.202200099.

[276] F. Jia, C. Yu, Z. Ai, and L. Zhang, "Fabrication of Nanoporous Gold Film Electrodes with Ultrahigh Surface Area and Electrochemical Activity," *Chem. Mater.*, vol. 19, no. 15, pp. 3648–3653, 2007. DOI: 10.1021/cm070425l.

[277] J. Zhang *et al.*, "Electrocatalytic activity of bimetallic platinum–gold catalysts fabricated based on nanoporous gold," *Phys. Chem. Chem. Phys.*, vol. 10, no. 22, p. 3250, 2008. DOI: 10.1039/b718192b.

[278] J. Wang *et al.*, "One-Pot Synthesis of Dealloyed AuNi Nanodendrite as a Bifunctional Electrocatalyst for Oxygen Reduction and Borohydride Oxidation Reaction," *Adv. Funct. Mater.*, vol. 27, no. 23, 2017. DOI: 10.1002/adfm.201700260.

[279] S. Xiao *et al.*, "Hierarchical Nanoporous Gold-Platinum with Heterogeneous Interfaces for Methanol Electrooxidation," *Sci. Rep.*, vol. 4, no. 1, p. 4370, 2014. DOI: 10.1038/srep04370.

[280] M. U. Christiansen *et al.*, "Chemically controlled interfacial nanoparticle assembly into nanoporous gold films for electrochemical applications," *J. Mater. Chem. A*, vol. 6, no. 2, pp. 556–564, 2018. DOI: 10.1039/C7TA08562A.

[281] Y. Yu *et al.*, "Li Storage in 3D Nanoporous Au-Supported Nanocrystalline Tin," *Adv. Mater.*, vol. 23, no. 21, pp. 2443–2447, 2011. DOI: 10.1002/adma.201004331.

[282] X.-Y. Lang *et al.*, "Nanoporous gold supported cobalt oxide microelectrodes as high-performance electrochemical biosensors," *Nat. Commun.*, vol. 4, no. 1, p. 2169, 2013. DOI: 10.1038/ncomms3169.

[283] N. Minh Vuong, D. Kim, and H. Kim, "Porous Au-embedded WO_3 Nanowire Structure for Efficient Detection of CH_4 and H_2S," *Sci. Rep.*, vol. 5, no. 1, p. 11 040, 2015. DOI: 10.1038/srep11040.

[284] Q. Wei *et al.*, "Nanoporous gold film based immunosensor for label-free detection of cancer biomarker," *Biosens. Bioelectron.*, vol. 26, no. 8, pp. 3714–3718, 2011. DOI: 10.1016/j.bios.2011.02.024.

[285] Y. Li *et al.*, "Molecularly imprinted polymer decorated nanoporous gold for highly selective and sensitive electrochemical sensors," *Sci. Rep.*, vol. 5, no. 1, p. 7699, 2015. DOI: 10.1038/srep07699.

[286] N. R. Hemanth *et al.*, "Metallic nanosponges for energy storage and conversion applications," *J. Mater. Chem. A*, vol. 10, no. 27, pp. 14 221–14 246, 2022. DOI: 10.1039/D2TA02057B.

[287] M. U. D. Sheikh *et al.*, "Surfactant-assisted morphological tuning of porous metallic silver sponges: facile synthesis, characterization and catalytic performance," *J. Sol-Gel Sci. Technol.*, vol. 76, no. 3, pp. 572–581, 2015. DOI: 10.1007/s10971-015-3807-0.

[288] G. Tong *et al.*, "Generalized green synthesis and formation mechanism of sponge-like ferrite micro-polyhedra with tunable structure and composition," *Nanoscale*, vol. 6, no. 2, pp. 778–787, 2014. DOI: 10.1039/C3NR03745B.

[289] F. Khan and S. Mann, "Fabrication of Metal and Metal Oxide Sponges by Self-Bubbled Triton X-45 Hydrogel Templates," *J. Phys. Chem. C*, vol. 113, no. 46, pp. 19 871–19 874, 2009. DOI: 10.1021/jp9076068.

[290] S. Kwak *et al.*, "Synthesis of Au sponges based on agarose template," *Scr. Mater.*, vol. 196, p. 113 769, 2021. DOI: 10.1016/j.scriptamat.2021.113769.

[291] Z. Zhang *et al.*, "Investigation of Halide-Induced Aggregation of Au Nanoparticles into Spongelike Gold," *Langmuir*, vol. 30, no. 10, pp. 2648–2659, 2014. DOI: 10.1021/la4046447.

[292] Y. X. Zhang and H. C. Zeng, "Gold Sponges Prepared via Hydrothermally Activated Self-Assembly of Au Nanoparticles," *J. Phys. Chem. C*, vol. 111, no. 19, pp. 6970–6975, 2007. DOI: 10.1021/jp071481c.

[293] Y. Liu, L. Liu, and R. Guo, "Br^-- Induced Facile Fabrication of Spongelike Gold/Amino Acid Nanocomposites and Their Applications in Surface-Enhanced Raman Scattering," *Langmuir*, vol. 26, no. 16, pp. 13 479–13 485, 2010. DOI: 10.1021/la101219r.

[294] M.-J. Lee, S.-H. Kang, J. Dey, and S.-M. Choi, "Porous Silica-Coated Gold Sponges with High Thermal and Catalytic Stability," *ACS Appl. Mater. Interfaces*, vol. 10, no. 26, pp. 22 562–22 570, 2018. DOI: 10.1021/acsami.8b04811.

[295] Y. H. Tan *et al.*, "Surface area and pore size characteristics of nanoporous gold subjected to thermal, mechanical, or surface modification studied using gas adsorption isotherms, cyclic voltammetry, thermogravimetric analysis, and scanning electron microscopy," *J. Mater. Chem.*, vol. 22, no. 14, pp. 6733–6745, 2012. DOI: 10.1039/c2jm16633j.

[296] B.-K. Pong, J.-Y. Lee, and B. L. Trout, "First Principles Computational Study for Understanding the Interactions between ssDNA and Gold Nanoparticles: Adsorption of Methylamine on Gold Nanoparticulate Surfaces," *Langmuir*, vol. 21, no. 25, pp. 11 599–11 603, 2005. DOI: 10.1021/la052116k.

[297] R. Wang, A. K. Singh, S. R. Kolan, and E. Tsotsas, "Fractal analysis of aggregates: Correlation between the 2D and 3D box-counting fractal dimension and power law fractal dimension," *Chaos, Solit. Fractals*, vol. 160, p. 112 246, 2022. DOI: 10.1016/j.chaos.2022.112246.

[298] J. Fu, H. R. Thomas, and C. Li, "Tortuosity of porous media: Image analysis and physical simulation," *Earth-Sci. Rev.*, vol. 212, p. 103 439, 2021. DOI: 10.1016/j.earscirev.2020.103439.

[299] A. K. Boal *et al.*, "Self-assembly of nanoparticles into structured spherical and network aggregates," *Nature*, vol. 404, no. 6779, pp. 746–748, 2000. DOI: 10.1038/35008037.

[300] T. A. Witten and L. M. Sander, "Diffusion-limited aggregation," *Phys. Rev. B*, vol. 27, no. 9, pp. 5686–5697, 1983. DOI: 10.1103/PhysRevB.27.5686.

[301] P. Meakin and F. Family, "Structure and dynamics of reaction-limited aggregation," *Phys. Rev. A*, vol. 36, no. 11, pp. 5498–5501, 1987. DOI: 10.1103/PhysRevA.36.5498.

[302] V. Privman, "Mechanisms of Diffusional Nucleation of Nanocrystals and Their Self-Assembly into Uniform Colloids," *Ann. N.Y. Acad. Sci.*, vol. 1161, no. 1, pp. 508–525, 2009. DOI: 10.1111/j.1749-6632.2008.04323.x.

[303] L. Holzer *et al.*, "FIB-Nanotomography of Particulate Systems—Part I: Particle Shape and Topology of Interfaces," *J. Am. Ceram. Soc.*, vol. 89, no. 8, pp. 2577–2585, 2006. DOI: 10.1111/j.1551-2916.2006.00974.x.

[304] L. Holzer and M. Cantoni, "Review of FIB Tomography," in *Nanofabrication Using Focused Ion and Electron Beams: Principles and Applications*. Oxford University Press, USA, 2012, pp. 410–435, ISBN: 9780199920990.

[305] K. Falconer, *Fractal Geometry: Mathematical Foundations and Applications*, 3rd ed. John Wiley & Sons, 2013, ISBN: 9781118762868. [Online]. Available: https://books.google.de/books?id=XJN7AgAAQBAJ.

[306] J. K. Percus and G. J. Yevick, "Analysis of Classical Statistical Mechanics by Means of Collective Coordinates," *Physical Review*, vol. 110, no. 1, pp. 1–13, 1958. DOI: 10.1103/PhysRev.110.1.

[307] G. Porod, "Die Röntgenkleinwinkelstreuung von dichtgepackten kolloiden Systemen," *Kolloid-Zeitschrift*, vol. 124, no. 2, pp. 83–114, 1951. DOI: 10.1007/BF01512792.

[308] A. Guinier, *X-ray Diffraction in Crystals, Imperfect Crystals, and Amorphous Bodies* (Dover Books on Physics Series). Dover Publications, 1994, ISBN: 9780486680118. [Online]. Available: https://books.google.de/books?id=H-uFHO8osokC.

[309] E. P. Cox, "A Method of Assigning Numerical and Percentage Values to the Degree of Roundness of Sand Grains," *J. Paleontol.*, vol. 1, no. 3, pp. 179–183, 1927.

[310] C. Gutiérrez-Wing *et al.*, "The role of ad-atoms in the coalescence of alkanethiol-passivated gold nanoparticles," *Electrochim. Acta*, vol. 101, pp. 301–307, 2013. DOI: 10.1016/j.electacta.2012.12.103.

[311] J. C. Azcárate, M. H. Fonticelli, and E. Zelaya, "Radiation Damage Mechanisms of Monolayer-Protected Nanoparticles via TEM Analysis," *J. Phys. Chem. C*, vol. 121, no. 46, pp. 26 108–26 116, 2017. DOI: 10.1021/acs.jpcc.7b08525.

[312] G. Beaucage, "Small-Angle Scattering from Polymeric Mass Fractals of Arbitrary Mass-Fractal Dimension," *J. Appl. Crystallogr.*, vol. 29, no. 2, pp. 134–146, 1996. DOI: 10.1107/S0021889895011605.

[313] H. Kaya, "Scattering from cylinders with globular end-caps," *J. Appl. Crystallogr.*, vol. 37, no. 2, pp. 223–230, 2004. DOI: 10.1107/S0021889804000020.

[314] M. V. V. Smoluchowski, "Mathematical Theory of the Kinetics of the Coagulation of Colloidal Solutions," *Z. Phys. Chem.*, vol. 92, no. 129, 1917.

[315] S. B. Grant, J. H. Kim, and C. Poor, "Kinetic Theories for the Coagulation and Sedimentation of Particles," *J. Colloid Interface Sci.*, vol. 238, no. 2, pp. 238–250, 2001. DOI: 10.1006/jcis.2001.7477.

Appendix

7.1 Supporting Information - Stabilization of Apolar Nanoparticle Dispersions by Molecular Additives

Reprinted with permission from [113]. Copyright © 2025 American Chemical Society.

Small angle X-ray scattering (SAXS) analysis

Nanoparticle characterization

The gold nanoparticles (AuNPs) used in this study were characterized using SAXS. Figure 7.1.1 shows the scattered intensity, $I(q)$ of AuNPs in dependence on momentum transfer, q, in their dispersed state, i.e., the scattering pattern represents the form factor of AuNPs. As the scattering contrast between the organic ligands and solvent molecules is negligible, only the Au cores are visible. Therefore, the size of the cores was determined by modeling the obtained scattering pattern using the expression

$$I(q) = P_{\text{pS}}(q) + I_{\text{bkg}} \tag{7.1.1}$$

with $P_{\text{pS}}(q)$ a form factor of polydisperse spheres [200] and I_{bkg} a constant accounting for background scattering. P_{pS} is given by

$$P_{\text{pS}}(q) = C \int_0^\infty F^2(q,r) r^6 G(r)\, \mathrm{d}r \tag{7.1.2}$$

with $F(q,r)$ the scattering amplitude of a sphere with radius r, $G(r)$ the distribution of radii, and C a scaling constant. $F(q,r)$ is given by

$$F(q,r) = 3 \cdot \frac{\sin qr - qr\cos qr}{(qr)^3} \tag{7.1.3}$$

$G(r)$ is approximated by a Gaussian distribution, given by

$$G(r) = \frac{1}{\sqrt{2\pi\sigma^2}} \exp\left(-\frac{(r - r_{\text{avg}})^2}{2\sigma^2} \right) \tag{7.1.4}$$

with r_{avg} the average core radius and σ its standard deviation.

The AuNPs from all batches used in this study had an r_{avg} in the range of $3.8 - 4.1\,\text{nm}$ and σ in the range of $10 - 11\,\%$. The spherical shape of the AuNPs was confirmed using transmission electron microscopy, shown in Figure 7.1.2 for AuNPs after ligand exchange with hexadecanethiol (HDT).

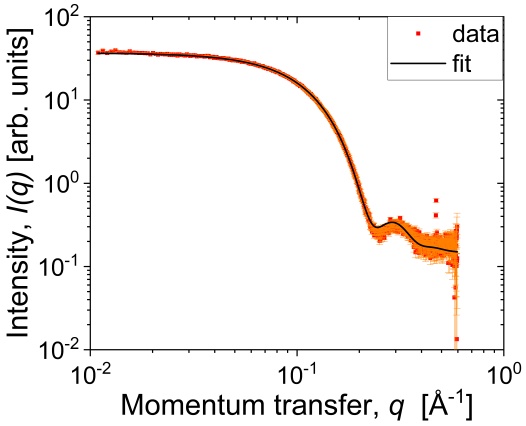


Figure 7.1.1: Scattering pattern of a dispersion of 4 nm AuNPs after the ligand exchange with HDT in decane at 36 °C. The black solid line is a fit according to eq. 7.1.1.

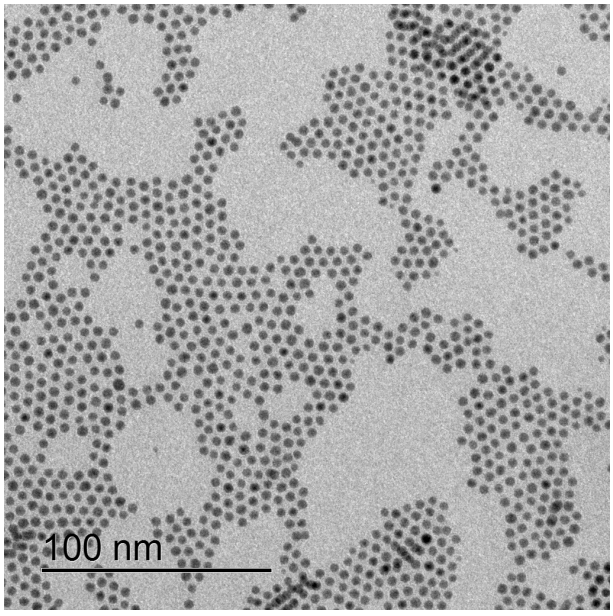


Figure 7.1.2: Transmission electron microscopy image of 4 nm AuNP after the ligand exchange with HDT.

Characterization of the agglomeration behavior

Agglomeration of the dispersion was analyzed using a method similar to that described in the work of Hasan et al. [109], exemplarily shown in Figure 7.1.3. In this method, the agglomeration fraction was determined by fitting the corresponding scattering curve using the expression

$$I(q) = I_{\text{Porod}}(q) + (1-\chi)P_{\text{pS}}(q) + \chi P_{\text{pS}}(q)S_{\text{HS}}(q) + I_{\text{bkg}} \tag{7.1.5}$$

Here, χ represents the agglomeration fraction, i.e., the number fraction of AuNPs located inside agglomerates. $S_{\text{HS}}(q)$ the Percus-Yevick hard-sphere structure factor [306], accounting for spatial correlation between AuNPs inside agglomerates. $I_{\text{Porod}}(q)$ is a generalized Porod law [307], which accounts for scattering by the agglomerates. During fitting, r_{avg} and σ were kept fixed at the values obtained at the highest measured temperature of each run. At the lowest measured temperatures, values of ~0.8 were obtained. These were normalized to 1 to reflect the complete agglomeration expected at these temperatures.

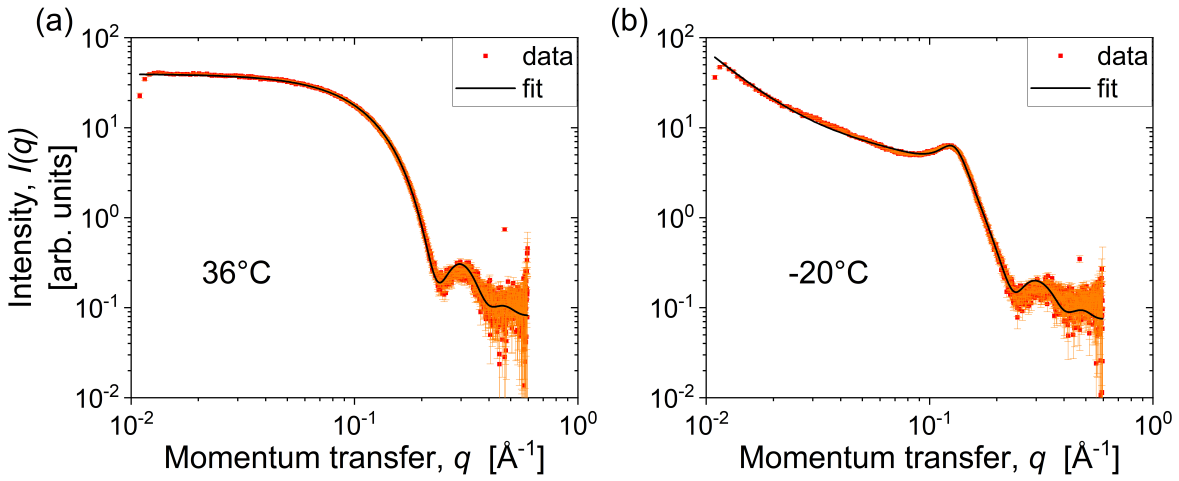


Figure 7.1.3: Scattering patterns of 4 nm AuNP@HDT in decane with a R5S concentration of 64 mM obtained at 36 °C (a) and at −20 °C (b). The black solid lines are fits according to eq.7.1.5.

The agglomeration temperature T_{agglo}, defined as temperature at which χ equals 0.2, determined by fitting the normalized $\chi(T)$ using a Boltzmann sigmoid function, given by

$$\chi_{\text{agglo}} = \frac{A_1 - A_2}{1 + \exp\left(\frac{T-T_0}{dT}\right)} + A_2 \tag{7.1.6}$$

with A_1 a parameter related to plateau at high temperatures, A_2 a parameter related to plateau at low temperatures, T_0 the temperature at $\chi_{\text{agglo}} = \frac{A_1+A_2}{2}$ and dT the range in which the transition occurs, as illustrated in Figure 7.1.4.

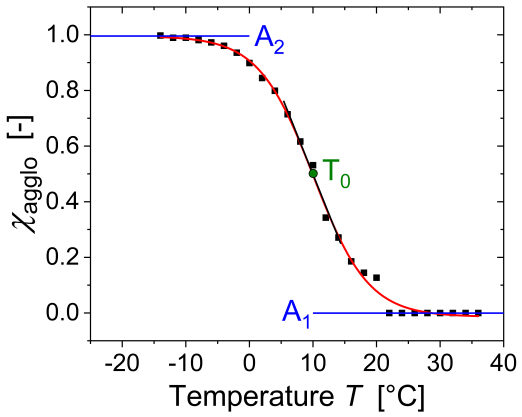


Figure 7.1.4: Analysis of χ_{agglo} with the a Boltzmann fit function (red). The borders A_1 and A_2 are marked blue. The inflection point T_0 is marked green.

Agglomeration behavior of AuNPs in the presence of amine-based additives

The stabilizing effect of the amines was much smaller than the effect of the sulfides. To see the effect more clearly, only the concentration-dependent ΔT_{agglo} values of the amines are shown in Figure 7.1.5.

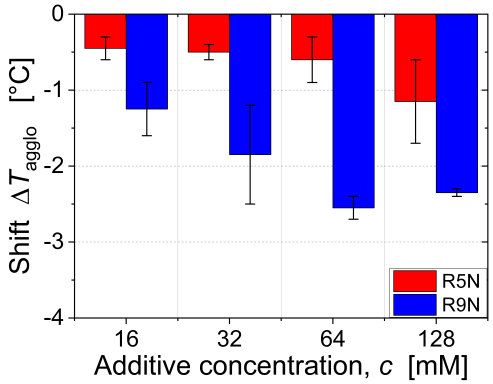


Figure 7.1.5: Stabilizing effects of different cyclic amine-based additives. Changes in the agglomeration temperature T_{agglo} are compared to pure n-decane for R5N and R9N.

Characterization of thionane (R9S)

The additive thionane (R9S) was not commercially available. Consequently, we had to produce the compound ourselves. Thionane was synthesized following Sinqh et al. [204]. The synthesized thionane was characterized with NMR and CHNS. For the NMR measurements a few mg of the thionane were dissolved in toluene-d_8. For the measurements, an Avance III HD 300 spectrometer from Bruker (Billerica, U.S.) was used. The NMR spectra is shown in Figure 7.1.6. The CHNS-analysis showed a composition of:

C: 66.52 % (66.60 %)

H: 10.68 % (11.18 %)

S: 22.63 % (22.22 %)

The theoretical composition of R9S is given by the value in the brackets.

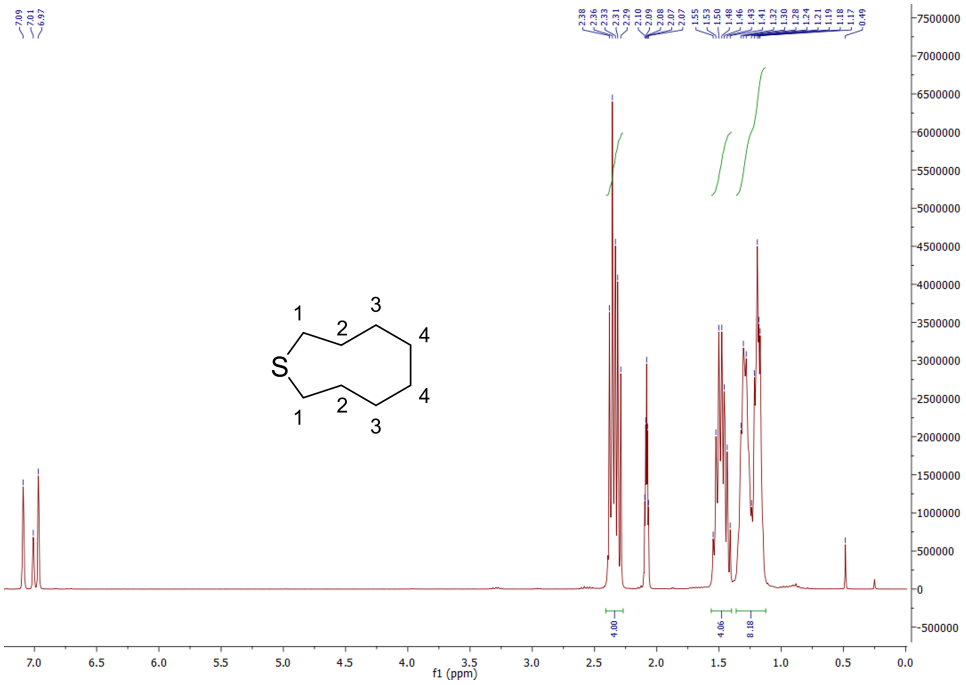


Figure 7.1.6: ^{1}H-NMR spectrum of thionane. Chemical shift δ: 7.09-6.97 = toluene-8, 2.38-2.29 = thionane C_1, 2.10-2.07 = toluene-d_8, 1.55-1.41 thionane C_2, 1.32-1.28 = thionane C_3, 1.24-1.17 = thionane C_4.

Thermogravimetric analysis

TGA of R5S containing dispersions

TGA was used to determine the composition of the ligand shells and the exchange behavior of the additive R5S. Figure 7.1.7 shows the mass loss curves of the R5S containing particle system and the additive-free AuNP@HDT system.

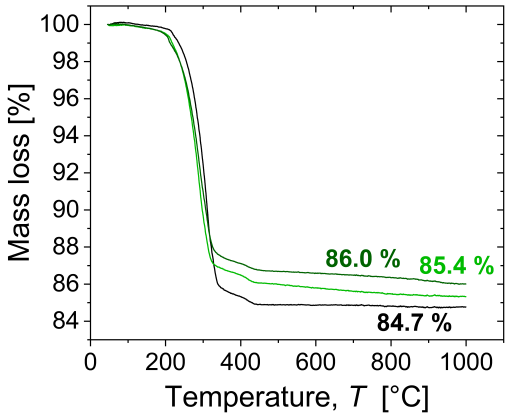


Figure 7.1.7: Thermogravimetric mass loss of pure AuNP@HDT (black) and two AuNP@HDT samples with a R5S additive concentration of 64 mM after one additional washing step (dark and light green).

To characterize ligand exchange, the ligand shell density of the additive-free particle system must be calculated. The surface area A_{core} of one particle cores is

$$A_{\text{core}} = 4\pi r_{\text{core}}^2 \tag{7.1.7}$$

The number of particles N_{AuNP} follows from the gold mass m_{gold} remaining in the crucible after the TGA measurement as

$$N_{\text{AuNP}} = \frac{m_{\text{gold}}}{m_{\text{core}}} = \frac{m_{\text{gold}}}{V_{\text{core}} \cdot \rho_{\text{gold}}} = \frac{m_{\text{gold}}}{4/3\pi r_{\text{core}}^3 \cdot \delta_{\text{gold}}} \tag{7.1.8}$$

and leads to the overall surface of all cores as

$$A_{\text{AuNP}} = A_{\text{core}} \cdot N_{\text{AuNP}}. \tag{7.1.9}$$

The number of surface-bound HDT ligands as a function of their mass m_{loss} lost in TGA their molar mass $258.51\ \text{g/mol}$ is

$$N_{\text{ligand}} = \frac{m_{\text{loss}}}{M_{\text{ligand}}} \cdot N_{\text{A}}, \tag{7.1.10}$$

where N_{A} is the Avogadro constant ($6.022 \cdot 10^{23}\ \text{mol}^{-1}$). The ligand shell density

$$\rho_{\text{LS}} = \frac{N_{\text{ligand}}}{A_{\text{AuNP}}} \tag{7.1.11}$$

that follows is used to find an exchange factor a for the ligand exchange reaction,

$$m_{\text{loss}} = \frac{A_{\text{AuNP}} \cdot \rho_{\text{LS}}(HDT) \cdot [a \cdot M_{\text{additive}} + (1-a) \cdot M_{\text{ligand}}]}{N_{\text{A}}}, \tag{7.1.12}$$

which is equivalent to

$$a = \frac{\frac{m_{\text{loss}} \cdot N_{\text{A}}}{A_{\text{AuNP}} \cdot \rho_{\text{LS}}(HDT)} - M_{\text{ligand}}}{M_{\text{additive}} - M_{\text{ligand}}}. \tag{7.1.13}$$

The number of the surface bound can be calculated with the exchange factor a:

$$N_{\text{additive}} = a \cdot \frac{N_{\text{ligand}}}{N_{\text{AuNP}}} \tag{7.1.14}$$

The number of additive molecules that could be removed by the washing step can be calculated based on the number of surface-bound additives:

$$N_{\text{additive, free}} = N^*_{\text{additive}} - N_{\text{additive}} \cdot N_{\text{AuNP}} \tag{7.1.15}$$

with N^*_{additive} the number of all additive molecules in the sample volume.
We assumed that the ligand shell density ρ_{LS}(HDT) remains constant during the additive-ligand exchange and is identical to the density of the additive-free reference system. The reason for this assumption is explained in a subsequent section. Table 7.1.1 summarizes the results of all TGA experiments with additive containing dispersions and their analyses using equations 7.1.10 to 7.1.16.

TGA of an AuNP@HDT reference system

Figure 7.1.8 shows the result of SAXS and TGA measurements of an AuNP@HDT reference system. The additional washing step has no significant effect on the shell composition and the agglomeration temperature T_{agglo} of the AuNP@HDT dispersion.
The num% of removed HDT molecules can be calculated as followed:

$$N\%^{\text{loss}}_{\text{HDT}} = 100 - \frac{100 \cdot N\%^{\text{washed}}_{\text{HDT}}}{N\%^{0}_{\text{HDT}}} \tag{7.1.16}$$

Table 7.1.2 summarizes the result of the TGA measurement of the AuNP@HDT reference system.

Table 7.1.1: Result of the TGA measurement of the R5S containing system

Parameter	measurement 1	measurement 2
r_{core}	2.16 nm	
m_{gold}	16.97 mg	21.39 mg
m_{loss}	2.90 mg	3.48 mg
M_{additive}	88.17 g/mol	
A_{AuNP}	$1.22 \cdot 10^{18}$ nm^2	$1.54 \cdot 10^{18}$ nm^2
ρ_{LS}(HDT)	5.85 nm^{-2}	
N_{ligand}	$7.14 \cdot 10^{18}$	$7.14 \cdot 10^{18}$
N^*_{additive}	$3.082 \cdot 10^{20}$	
N_{additive}	$1.01 \cdot 10^{18}$	$1.64 \cdot 10^{18}$
$N^{free}_{\text{additive}}$	$3.076 \cdot 10^{20}$	$3.072 \cdot 10^{20}$
a	0.081	0.160
a_{Average}	0.12	

Table 7.1.2: Result of the TGA measurement of the AuNP@HDT system

Parameter	AuNP@HDT	AuNP@HDT washed
r_{core}	2.05 nm	
m_{gold}	19.98 mg	18.99 mg
m_{loss}	3.81 mg	3.51 mg
M_{HDT}	258.5 g/mol	
N_{HDT}	$8.87 \cdot 10^{18}$	$8.18 \cdot 10^{18}$
A_{AuNP}	$1.51 \cdot 10^{18}$ nm^2	$1.44 \cdot 10^{18}$ nm^2
ρ_{LS}(HDT)	5.86 nm^{-2}	5.68 nm^{-2}
$N\%^{loss}_{\text{HDT}}$	3.0 %	

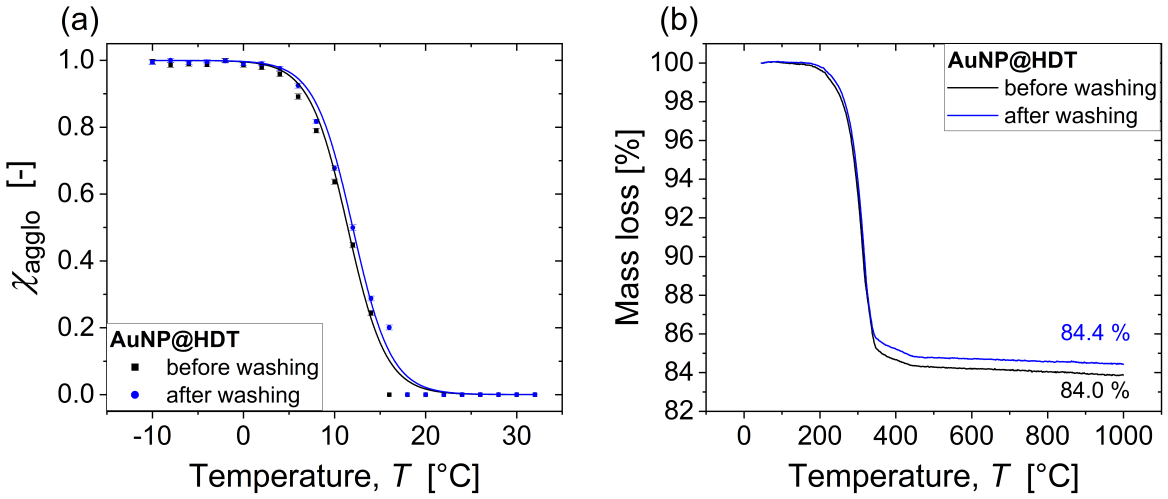


Figure 7.1.8: (a) Temperature-dependent agglomeration fractions χ_{agglo} from SAXS for AuNP@HDT dispersions in pure n-decane before washing (black curve) and after washing (blue curve). (b) TGA curves of AuNP@HDT samples before washing (black curve) and after washing (blue curve).

Limitation of the synthesis of an AuNP@R5S reference system

In order to be able to determine the exchange behavior more precisely, an attempt was made to produce an AuNP@R5S reference system. Figure 7.1.9 shows a dispersion of particles after the ligand exchange with R5S. It was not possible to redisperse the particles. The particles were aggregated. Due to the changed particle geometry no TGA measurement were performed.

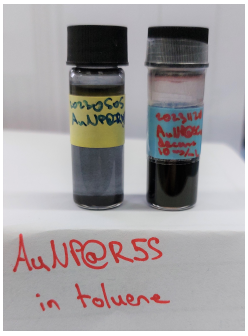


Figure 7.1.9: Image of a disperion of AuNP@R5S and AuNP@HDT after the ligand exchange.

Transmission electron microscopy showed that the particles are partially aggregated due to ligand exchange (see Figure 7.1.10).

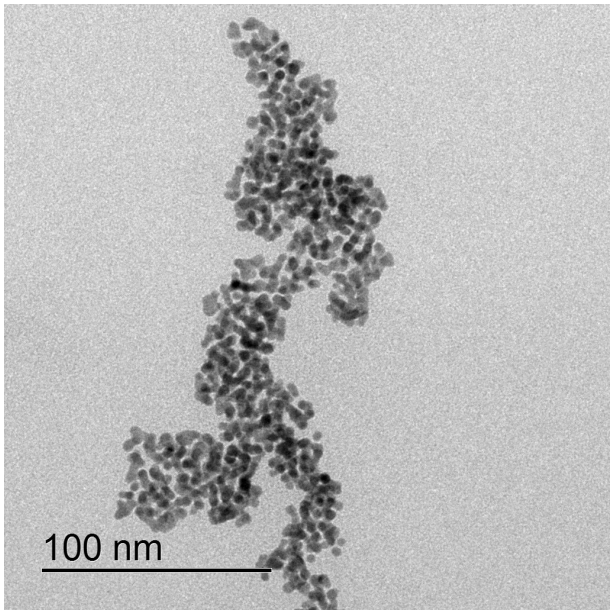


Figure 7.1.10: TEM image of aggregated particles after the ligand exchange with R5S.

Due to the strong deviation of the aggregates from the original particle shape, no TGA measurement was performed. We assume that the AuNP@HDT and the AuNP@R5S system have different ligand densities. Since this could not be determined, an exchange of one additive molecule per ligand molecule was assumed for the calculation of the exchange factor.

Molecular Dynamic (MD) simulations

Simulations of physisorbed R5S were performed using a single AuNP@HDT particle surrounded by 6000 decane molecules and either 100 or 1000 R5S molecules. At 300 K, this is roughly equivalent to R5S concentrations of 76 mM and 718 mM, respectively, as shown in Table 7.1.3.

Table 7.1.3: Concentration of R5S in simulations of physisorbed additives.

Number of R5S	Length of cubic simulation cell at 300 K (Å)	Concentration (mM)
100	130.7	76
1000	133.4	718

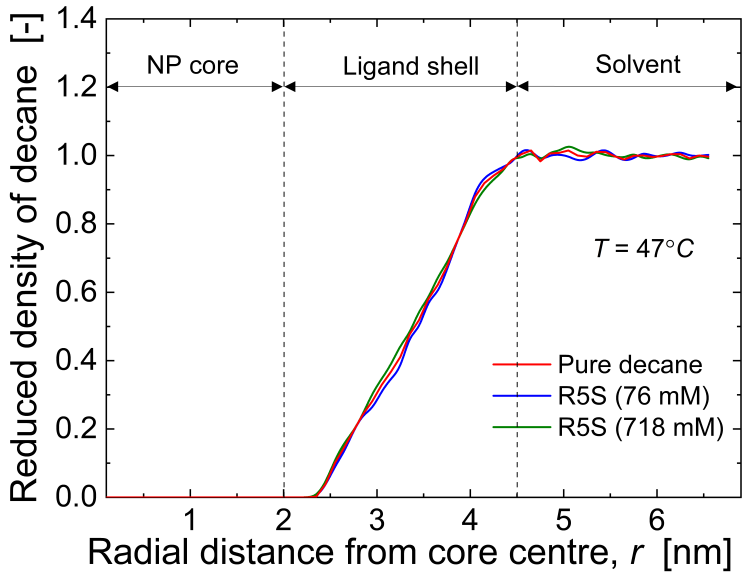


Figure 7.1.11: Reduced radial density distributions of n-decane near an isolated AuNP@HDT particle at T_{order} in pure decane and in the presence of unbound R5S at 76 mM and 718 mM concentrations. The radial distance is measured from the centre of the AuNP, and the density of each solvent component has been divided by its density in the bulk solution.

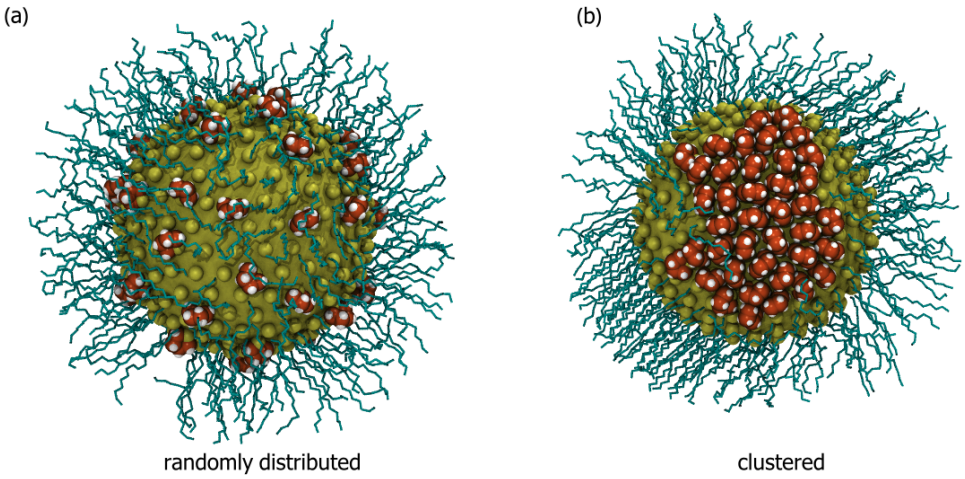


Figure 7.1.12: Snapshots of our simulation set up when the additives are bound to the surface of an isolated 4 nm AuNP (represented by the golden sphere in the centre) covered in hexadecanethiol ligands (represented by C–C bonds which are colored in cyan, C–H are hidden for clarity). The snapshots show 40 R5S molecules (coloured in yellow for S, red for C, and white for H atoms) that are (a) randomly distributed and (b) clustered on the particle surface. Solvent molecules have been hidden for clarity.

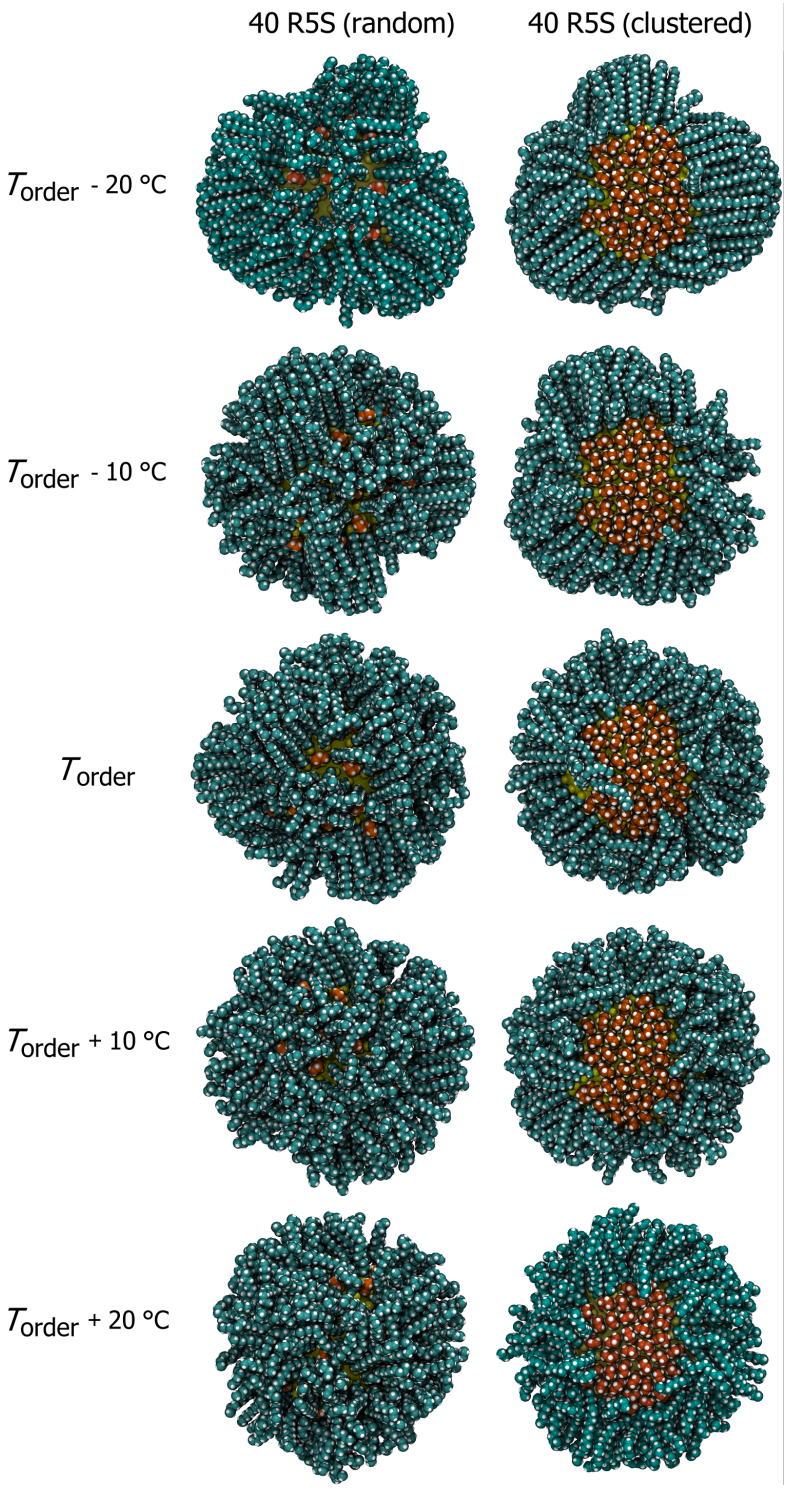


Figure 7.1.13: Simulation snapshots of 4 nm AuNPs at the ligand ordering temperature $T_{\text{order}} \pm 20°\text{C}$ showing the difference between having 40 R5S molecules randomly distributed vs clustered on the particle surface. Solvent molecules have been hidden for clarity.

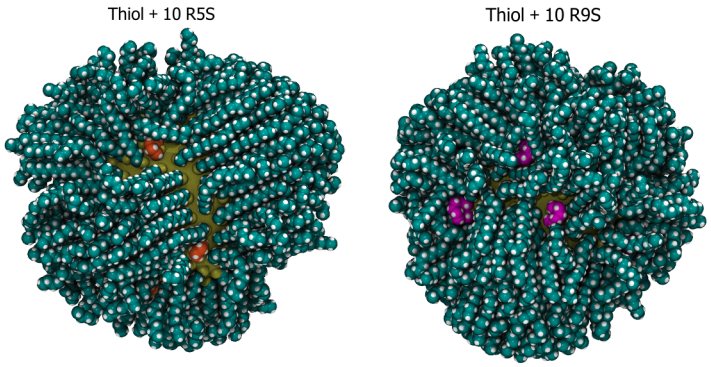


Figure 7.1.14: Simulation snapshots of individual 4 nm AuNPs at the ligand ordering temperature T_{order} showing the similarity between having 10 R5S (left) and 10 R9S (right) randomly distributed on the surface. Solvent molecules have been hidden for clarity.

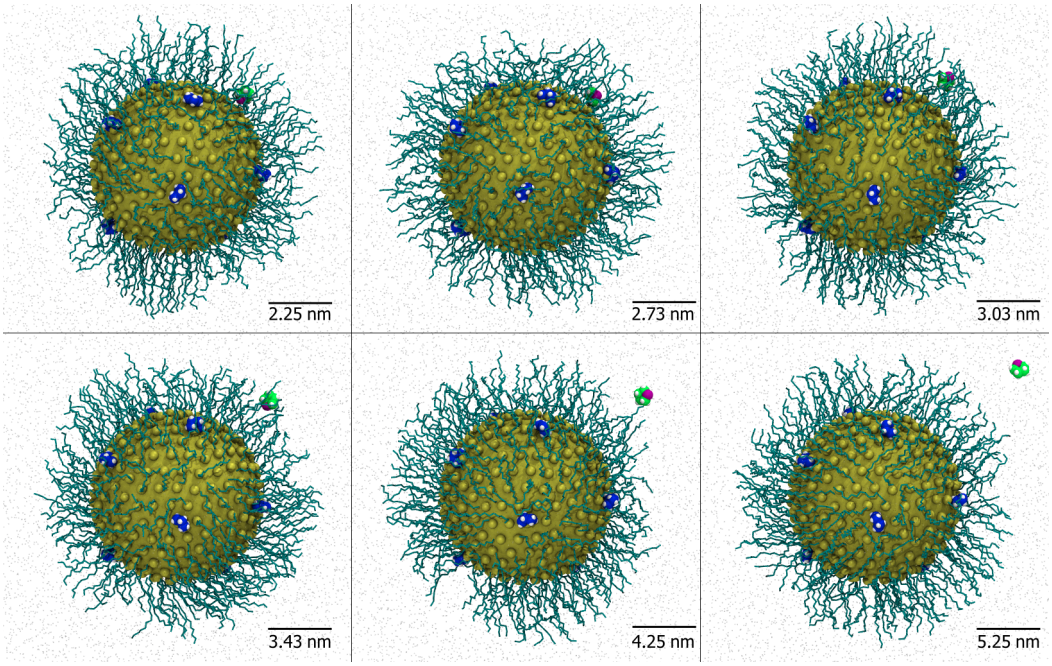


Figure 7.1.15: Simulation snapshots showing the path used to calculate the potential of mean force for the non-covalent interaction between the additives and the AuNP in decane at 67°C. Out of 10 R5S molecules, 9 R5S (depicted in yellow-blue-white) were randomly bound to the particle surface, and 1 unbound R5S (shown in purple-green-white) was placed R5S near the particle surface (top left). This was then gradually moved away from the particle surface while calculating the mean force, allowing for normal dynamics of the rest of the system. The scaling number displayed in the snapshots indicates the separation distance between the unbound R5S and the center of the particle core.

7.2 Supporting Information - Maintaining Shell Disorder with Kinked or Branched Ligands Stabilizes Apolar Nanoparticles

Reprinted with permission from [210]. Copyright © 2025 American Chemical Society.

NMR data to synthesis of 11-methyldodecanthiol

The branched *br*-SC_{12} ligand 11-methyldodecanethiol was prepared in-house. The final product and the intermediates were characterized by NMR. The spectra are shown in Figure 7.2.1, 7.2.2 and 7.2.3.

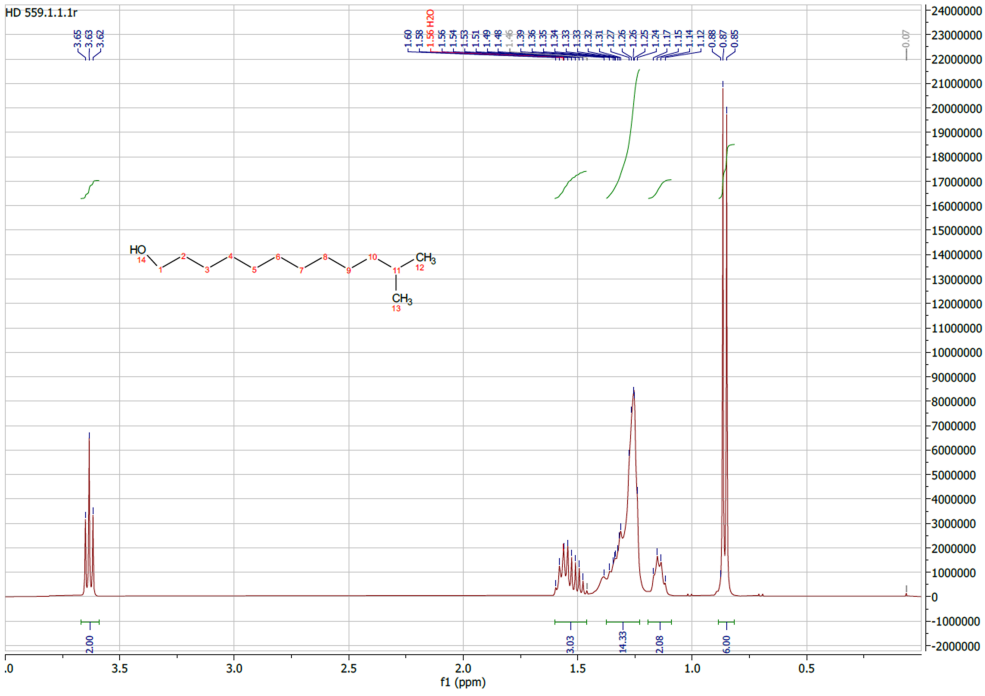


Figure 7.2.1: ^{1}H NMR of 11-methyldodecanol (400 MHz, CDCl3, δ in ppm): 3,63 (t, 2H, H1), 1.62-1.46 (m, 3H, H2+H11), 1.39-1.22 (m, 14H, H3-9), 1,15 (m, 2H, H10), 0.87 (d, 6H, H12+13).

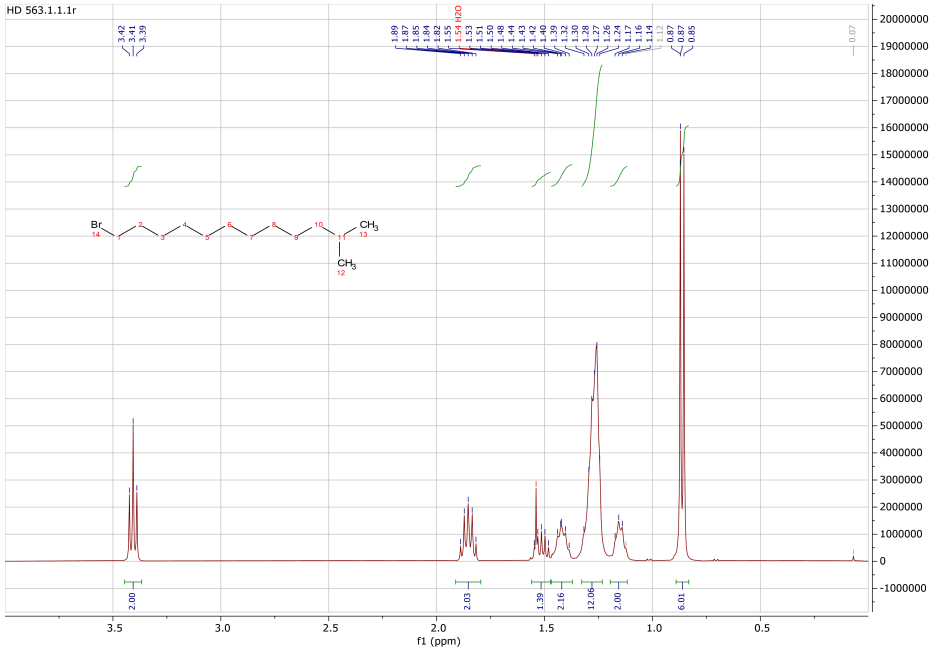


Figure 7.2.2: ^{1}H NMR of 11-methyldodecylbromide (400 MHz, CDCl3, δ in ppm): 2.41 (t, 2H, H1), 1.85 (q, 2H, H2), 1.51 (m, 1H, H11), 1.42 (m, 2H, H3), 1.31-1.22 (m, 12H, H4-9), 2.05 (m, 2H, H10), 0.87 (d, 6H, H12+13).

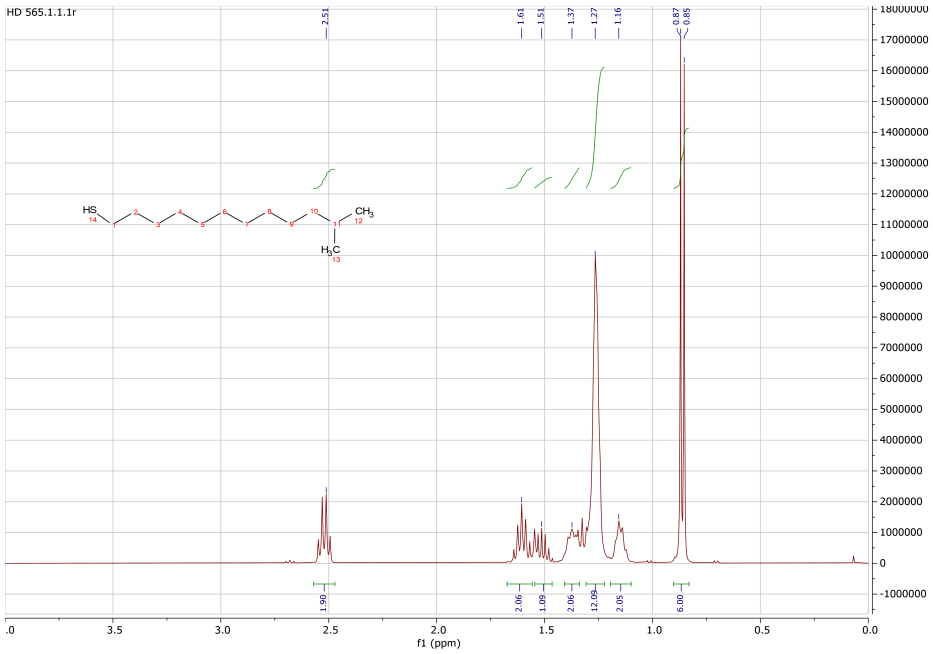


Figure 7.2.3: ^{1}H NMR of 11-methyldodecanthiol (400 MHz, CDCl3, δ in ppm): 2.51 (q, 2H, H1), 1.61 (m, 2H, H2), 1.51 (m, 1H, H11), 1.37 (m, 2H, H3), 1.31-1.22 (m, 12H, H4-9), 2.05 (m, 2H, H10), 0.87 (d, 6H, H12+13).

Small- and wide-angle X-ray scattering

The gold nanoparticles (AuNPs) used in this study were characterized using SAXS. Figure 7.2.4, 7.2.5 and Figure 7.2.6 show the scattered intensity, $I(q)$ of AuNPs in dependence on momentum transfer, q, in their dispersed state, i.e., the scattering pattern represents the form factor of AuNPs. In addition to the SAXS measurements, wide-angle X-ray scattering (WAXS) measurements were performed to detect freezing of the solvent, apparent from the presence of sharp structure factor peaks at q-values of 1-3 Å^{-1} (see Figure 7.2.5). In most samples, the solvent freezes at temperatures of around $-110\,°\text{C}$.

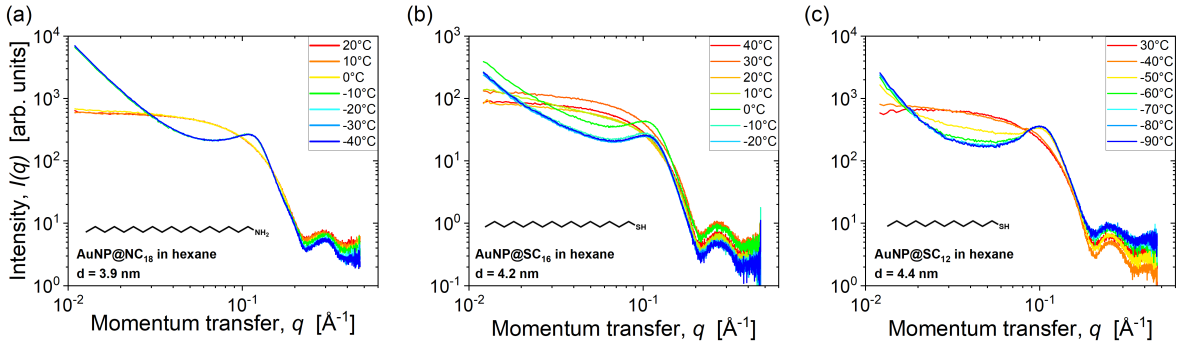


Figure 7.2.4: Temperature-dependent scattering patterns of AuNPs dispersed in hexane with a core diameter of 4.2 nm to 4.4 nm coated with linear amines and thiols: NC_{18} (a), SC_{16} (b) and SC_{12} (c).

As the scattering contrast between the organic ligands and solvent molecules is negligible, only the Au cores are visible. Therefore, the size of the cores was determined by modeling the obtained scattering patterns using the expression (see Figure 7.2.9a):

$$I(q) = P_{\text{pS}}(q) + I_{\text{bkg}} \tag{7.2.1}$$

with $P_{\text{pS}}(q)$ a form factor of polydisperse spheres [200] and I_{bkg} a constant accounting for background scattering. P_{pS} is given by

$$P_{\text{pS}} = \int_0^\infty G(r)F(q,r)\,dr \tag{7.2.2}$$

with r the core radius, $F(q,r)$ the form factor for monodisperse spheres and $G(r)$ the size distribution of the core radius. $F(q,r)$ is given by

$$F(q,r) = 3 \cdot \frac{\sin qr - qr\cos qr}{(qr)^3} \tag{7.2.3}$$

$G(r_{\text{c}})$ is described by a Gaussian distribution, given by

$$G(r) = \frac{1}{\sigma\sqrt{2\pi}} \exp\left[-\frac{1}{\sigma^2}(r - r_{\text{avg}})^2\right] \tag{E4}$$

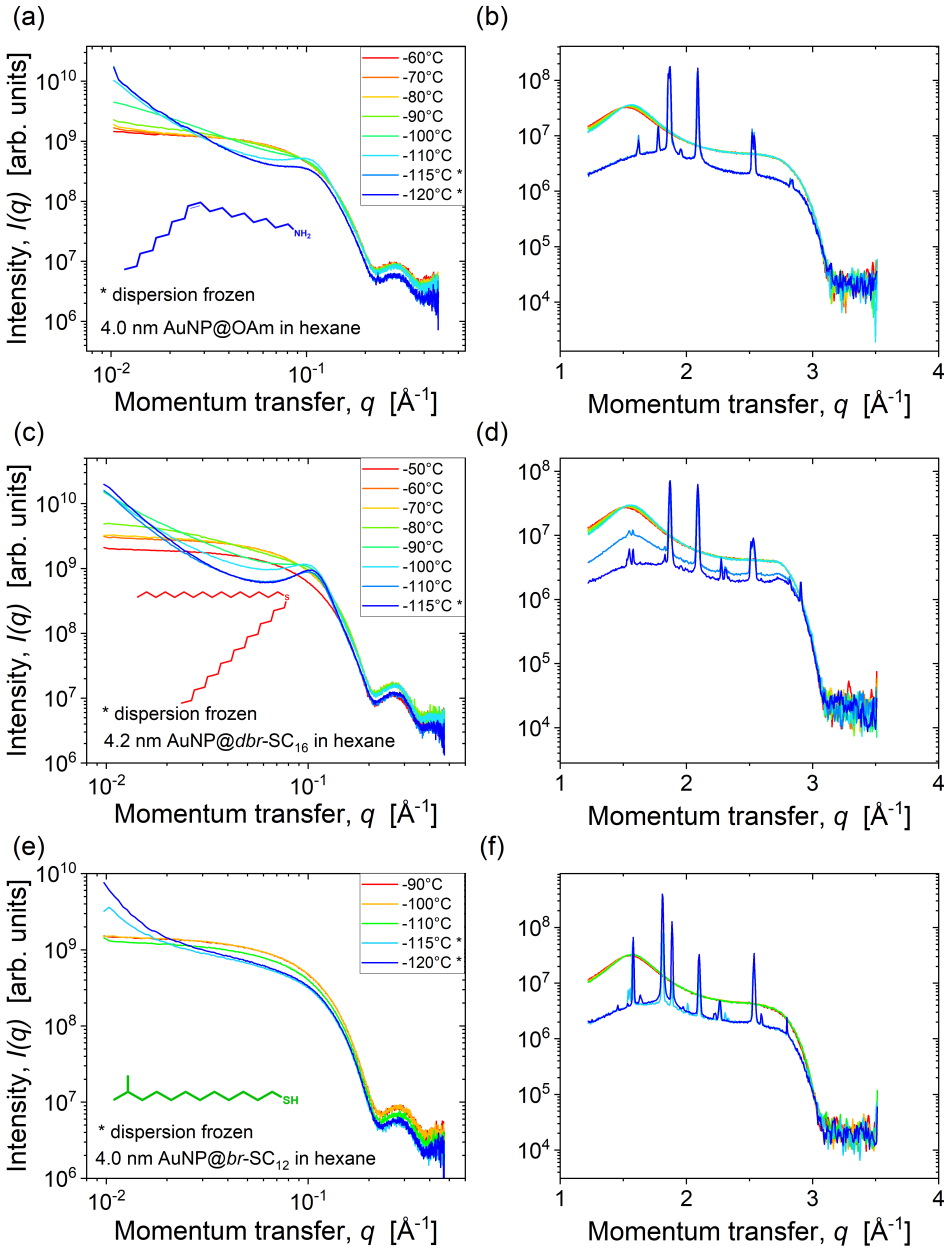


Figure 7.2.5: Temperature-dependent SAXS (a, c, e) and WAXS (b, d, f) patterns of AuNPs dispersed in hexane with a core diameter of of 4.2 nm to 4.4 nm coated with OAm ligands (a, b), *dbr*-SC_{16} ligands (c, d) branched *br*-SC_{12} ligands (e, f).

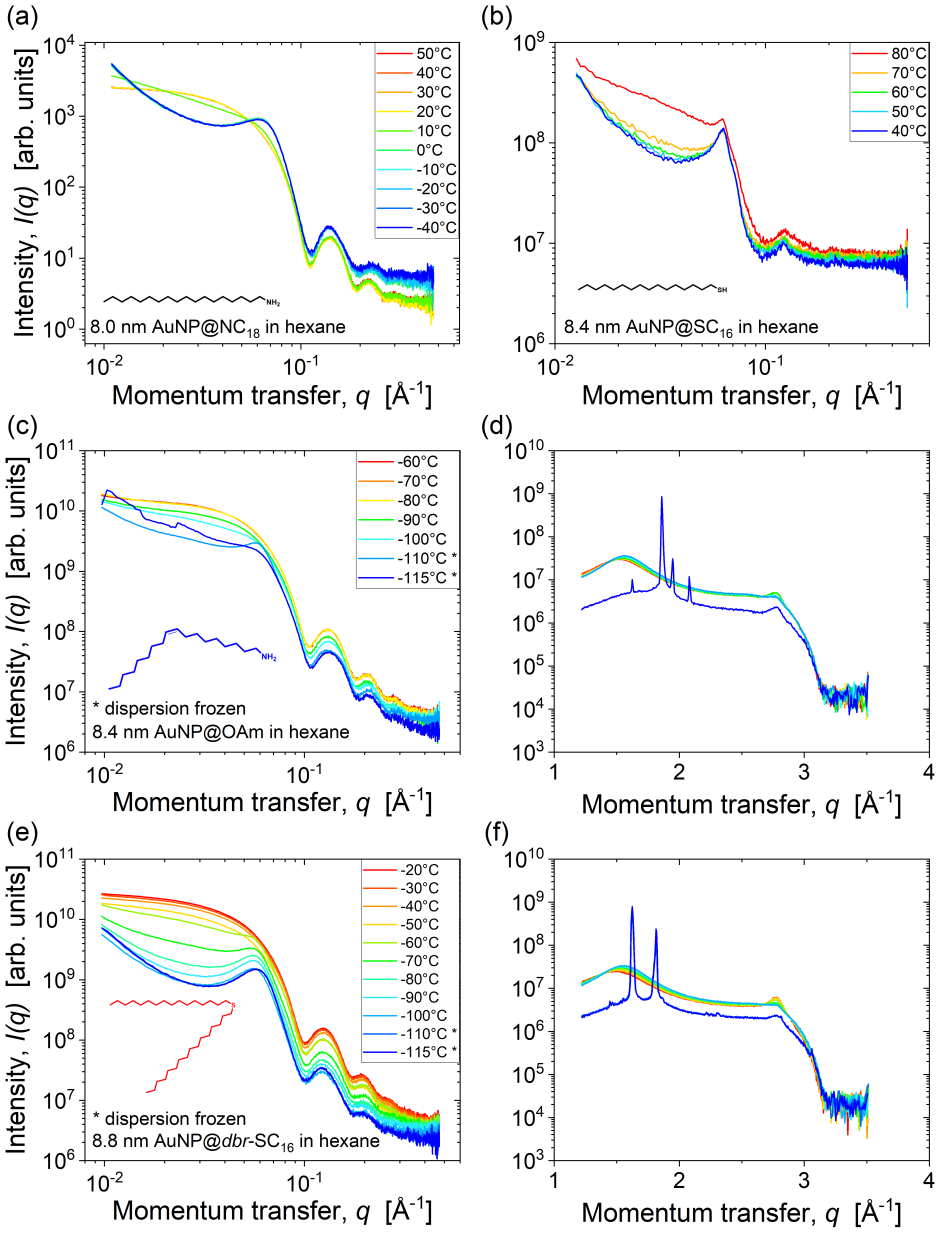


Figure 7.2.6: Temperature-dependent SAXS (a, b, c, e) and WAXS (d, f) patterns of AuNPs dispersed in hexane with a core diameter of 8.0 nm to 8.8 nm coated with NC_{18} ligands (a), SC_{16} ligands (b), OAm ligands (c, d) and *dbr*-SC_{16} ligands (e, f).

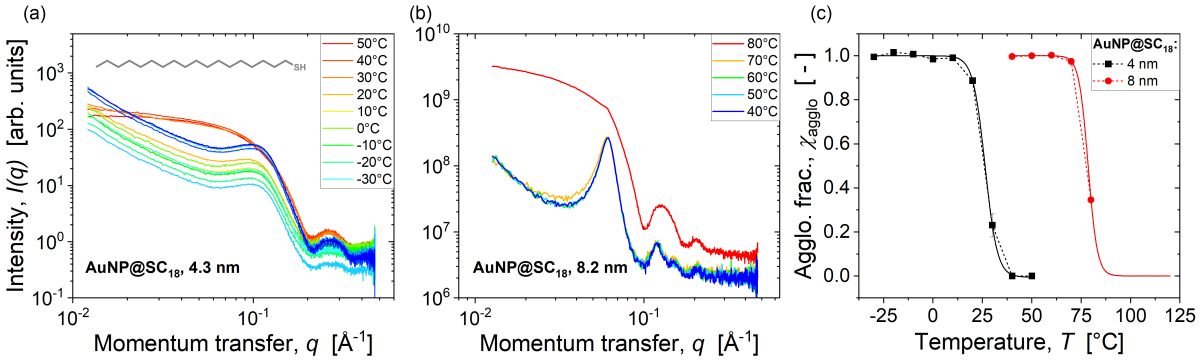


Figure 7.2.7: Temperature-dependent scattering patterns of AuNPs dispersed in hexane with core diameters of (a) 4.3 nm and (b) 8.2 nm coated with SC_{18}. (c) Temperature-dependent number fraction of AuNPs located in agglomerates, χ_{agglo}, of AuNPs coated with linear SC_{18} with core diameters of 4.3 nm (black) and 8.2 nm (red).

with r_{avg} the average core radius. σ is given by:

$$\sigma = \frac{r_{\text{c}}}{r_{\text{avg}}} \tag{7.2.5}$$

The AuNPs from all batches used in this study had an r_{avg} in the range of $4.2-4.4$ nm (σ=10 $-$11 %) and $8.3-8.6$ nm (σ=8 $-$9 %). The spherical shape of the AuNPs was confirmed using transmission electron microscopy, shown in Figure 7.2.8.

The temperature-dependent SAXS patterns were analyzed following a method similar to that described by Hasan et al. [109]. In this method, the SAXS patterns are modeled using the expression

$$I(q) = I_{\text{P}}(q) + P_{\text{pS}}(q)\left[1 - \chi_{\text{agglo}} + \chi_{\text{agglo}} \cdot S_{\text{HS}}(q)\right] + I_{\text{bkg}} \tag{7.2.6}$$

Here, χ_{agglo} is the number fraction of AuNPs located inside agglomerates, $I_{\text{P}}(q)$ is a generalized Porod law [307], accounting for scattering by the agglomerates, and $S_{\text{HS}}(q)$ is the Percus-Yevick hard-sphere structure factor [306] accounting for spatial correlation between AuNPs inside agglomerates. $S_{\text{HS}}(q)$ can be calculated as [200]

$$S_{\text{HS}}(q) = \frac{1}{1 + 24\eta_{\text{HS}} G(2R_{\text{HS}}q)/(2R_{\text{HS}}q)} \tag{7.2.7}$$

with R_{HS} the hard sphere radius and η_{HS} the hard-sphere volume fraction inside agglomerates. The function $G(x)$ is defined as:

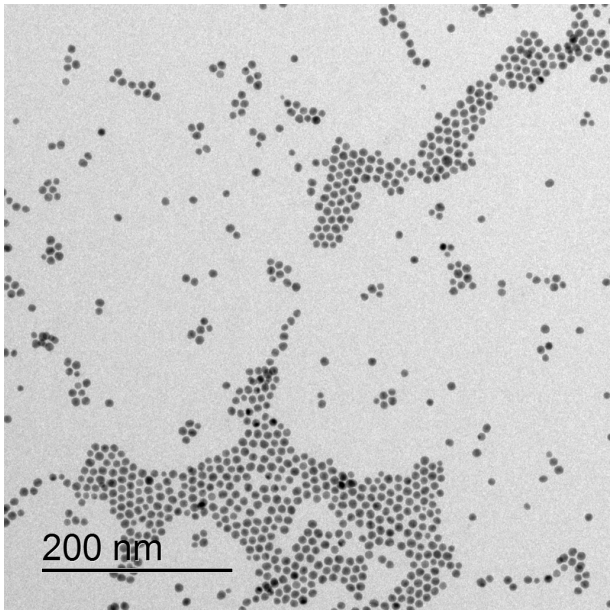


Figure 7.2.8: Transmission electron microscopy image of 8.4 nm AuNPs coated with the kinked oleylamine ligand (OAm).

$$G(x) = \gamma' \frac{\sin x - x\cos x}{x^2} + \delta' \frac{2x\sin x + (2-x^2)\cos x - 2}{x^3} + \epsilon' \frac{-x^4\cos x + 4[(3x^2-6)\cos x + (x^3-6x)\sin x + 6]}{x^5} \tag{7.2.8}$$

Here, γ', δ' and ϵ' are help functions, given by

$$\gamma' = \frac{(1+2\eta)^2}{(1-\eta)^4}, \quad \delta' = \frac{-6\eta(1+\eta/2)^2}{(1-\eta)^4}, \quad \epsilon' = \frac{\eta\gamma'}{2} \tag{7.2.9}$$

During fitting, r_{avg} and σ were kept fixed using the values obtained at the highest measured temperature of each respective run, i.e., where no agglomerates are present. At the lowest measured temperatures, values of χ_{agglo} of ∼0.8 were obtained. These were normalized to 1 to reflect the complete agglomeration expected at these temperatures.

The agglomeration temperature, T_{agglo}, defined as temperature at which χ_{agglo} equals 0.2, determined by fitting the normalized $\chi_{\text{agglo}}(T)$ using a Boltzmann sigmoid function [113], given by

$$\chi_{\text{agglo}} = \frac{A_1 - A_2}{1 + \exp\left(\frac{T-T_0}{dT}\right)} + A_2 \tag{7.2.10}$$

with A_1 a parameter related to plateau at high temperatures, A_2 a parameter related to plateau at low temperatures, T_0 the temperature at $\chi_{\text{agglo}} = \frac{A_1+A_2}{2}$ and dT the range in which the transition occurs.

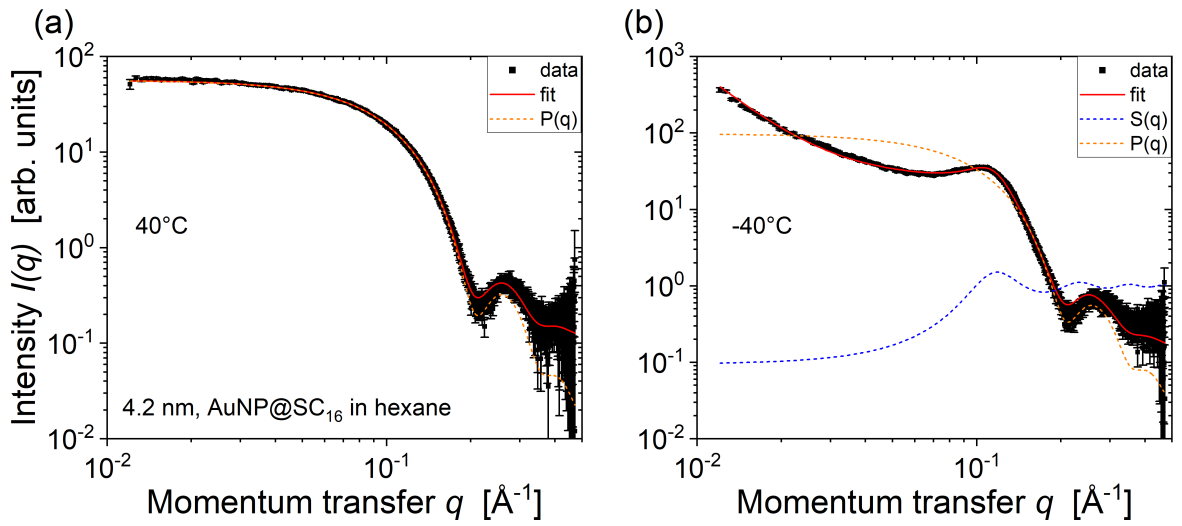


Figure 7.2.9: Scattering patterns of AuNPs with a core diameter of $4.2\,\mathrm{nm}$ coated with SC_{16} and dispersed in hexane at $50\,^{\circ}\mathrm{C}$ (a) and $-30\,^{\circ}\mathrm{C}$ (b). Black dots: measured data. Red lines: fits according to eq. 7.2.1 (a) and eq. 7.2.6 (b). Dashed orange line: contribution of $P(q)$ to the model. Dashed blue line: contribution of $S(q)$ to the model.

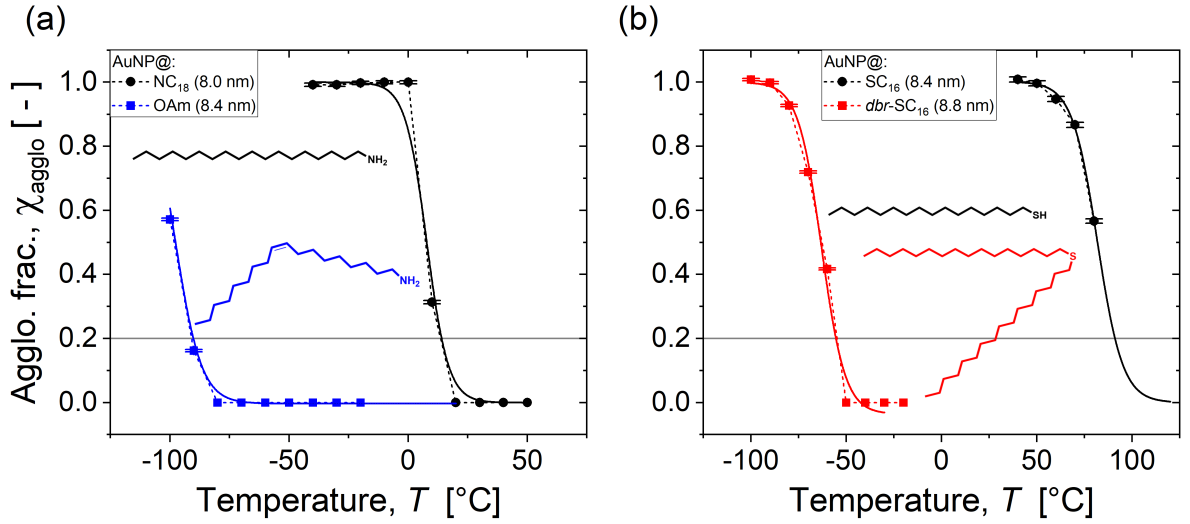


Figure 7.2.10: (a) Temperature-dependent number fraction of AuNPs located in agglomerates, χ_{agglo}, of AuNPs coated with linear NC_{18} (core diameter of $8.0\,\mathrm{nm}$) and branched OAm (core diameter of $8.4\,\mathrm{nm}$) and (b) linear SC_{16} (core diameter of $8.4\,\mathrm{nm}$) and double-armed *dbr*-SC_{16} ligands (core diameter of $8.8\,\mathrm{nm}$). The solid lines represent sigmoidal fits according to eq. 7.2.10.

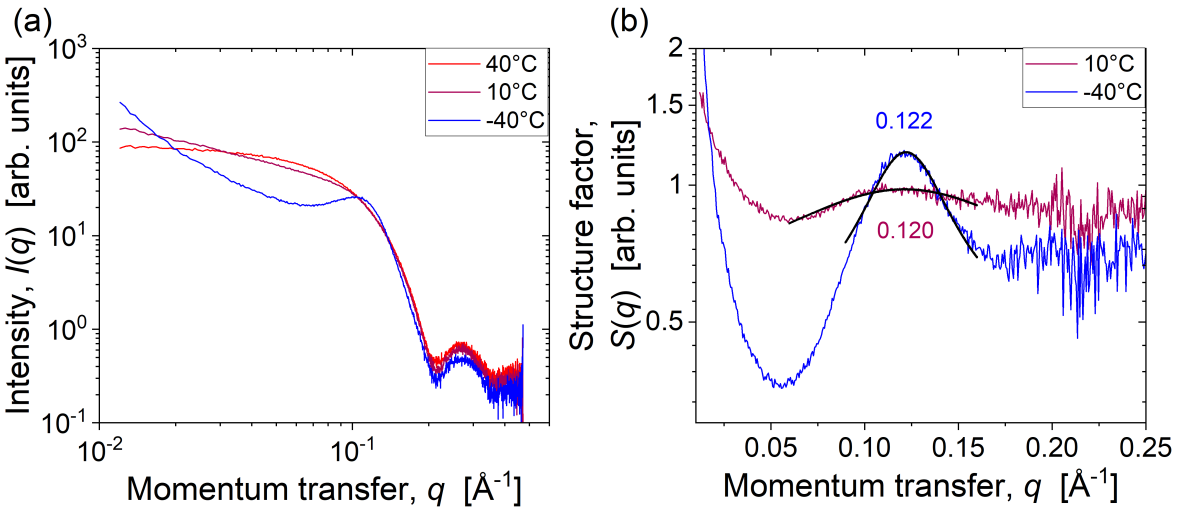


Figure 7.2.11: (a) Scattering patterns of AuNPs with a core diameter of 4 nm and coated with a HDT shell dispersed in *n*-hexane at 40 °C (dispersed particles), around T_{agglo} (10 °C) and at −40 °C (agglomerated particles). (b) $S(q)$ of the AuNPs around T_{agglo} and at −40 °C, calculated according to eq. 7.2.12. Solid black line: fit of the primary structure factor peak using a Lorentz distribution function.

R_{HS} can be used to calculated the core surface spacing s between gold surfaces of neighboring particles in agglomerates as

$$s = 2(R_{\text{HS}} - r_{\text{avg}}) \tag{7.2.11}$$

In previous publications, s was determined using a different method [58, 59], as is depicted in Figure 7.2.11 for 4 nm AuNPs coated with HDT ligands and dispersed in *n*-hexane. In a first step, $S(q)$ was determined as

$$S(q) = \frac{I(q)}{P(q)} \tag{7.2.12}$$

with $P(q)$ the form factor of the particles determined using a measurement of dispersed AuNPs. The q value of the first intensity maximum, determined using a Lorentz distribution as depicted in Figure 7.2.11b, was related to the center-to-center distance of neighboring particles, $D_{\text{C-C}}$, following the expression

$$D_{\text{C-C}} = 1.23\frac{2\pi}{q} \tag{7.2.13}$$

From $D_{\text{C-C}}$, the core surface spacing s was calculated as

$$s = D_{\text{C-C}} - 2r_{\text{avg}} \tag{7.2.14}$$

In equation 7.2.13 a correction factor (1.23) was used that was established by Ehrenfest [308]. Using this method for AuNPs with a core diameter of 4 nm and coated with a HDT shell dispersed

in n-hexane, a spacing (s) of 2.2 nm at T_{agglo} were determined, which is approximately 0.6 nm above that determined according to eq 7.2.6. In the work of Kister et al. a spacing 2.4 nm could be found for AuNPs with a core diameter of 4 nm coated with HDT ligands and dispersed in n-decane around T_{agglo} [58]. Consequently, the differences in between the present and previous work are due to the differences in the analysis method.

Analysis of the spacing of 7.3 nm AuNP@OAm using transmission electron microscopy

The TEM images were recorded at an acceleration voltage of $200\,\mathrm{kV}$ in bright-field imaging mode. The magnification was $200\,kx$ and digital images (1024×1024 pixels) with isotropic physical pixel dimensions of $0.65\,\mathrm{nm}^2$ were recorded (Figure 7.2.12a). The 8-bit greyscale images were analyzed using the software "Avizo" (Avizo 3D 2022.1, ThermoFisher Scientific, Waltham, Massachusetts, USA). Sub-images were cropped from the raw TEM images (Figure 7.2.12b) using the function "Extract Subvolume". The uneven background present in some images were corrected using the function "Background Detection Correction" which uses a B-spline to fit and correct greyscale pixel values that gradually change in the x- or y-direction of the image. To increase the signal-to-noise ratio, the greyscale images were were subsequently denoised using a "Non-Local Means Filter" (Figure 7.2.12c). The filtered greyscale images were segmented to obtain binary images (Figure 7.2.12d) using histogram thresholding. The thresholds were set manually at the minimum between the two peaks of the greyscale histograms (seen insert in Figure 7.2.12c). Artifacts, e.g., apparent holes within the particles or greyscale noise removed using the functions "fill holes" and "remove small spots" (Figure 7.2.12e). Particles partially located outside of the images were masked using the function "Border Kill" (Figure 7.2.12f) and the remaining particles were labeled using the function "Labeling" (Figure 7.2.12g). Pixels that belonged visibly to connected regions were assigned unique particle labels. A standard label analysis for the label images (Figure 7.2.12g) was carried out to obtain the coordinates of the particles' centers of mass. The center-to-center distances, $D_{\text{C-C}}$, between each pair of particles present were determined to obtain their pair distribution function.

This measurement on 2D particle films provides a lower bound for the core surface spacing s, because ligands in monolayers can extend above or below the plane of particle packing in a way that is not possible in 3D agglomerates.

Four TEM images at the given microscope settings and above-described image analysis route were analyzed, which contained a total of 105 particles. The first maximum of the combined pair distribution function, corresponding to the nearest neighbor center-to-center distances in the close-packed hexagonal arrangement of the AuNPs, is plotted in Figure 7.2.13a. A fit using a Gaussian distribution function yielded an average of $D_{\text{C-C}}$ of $9.2\,\mathrm{nm}$ between nearest neighbors. Using a radius of the particles of $7.3\,\mathrm{nm}$, as determined using SAXS (Figure 7.2.13b), an average gold surface-to-surface distance between nearest neighbors, s, of $1.9\,\mathrm{nm}$ was calculated.

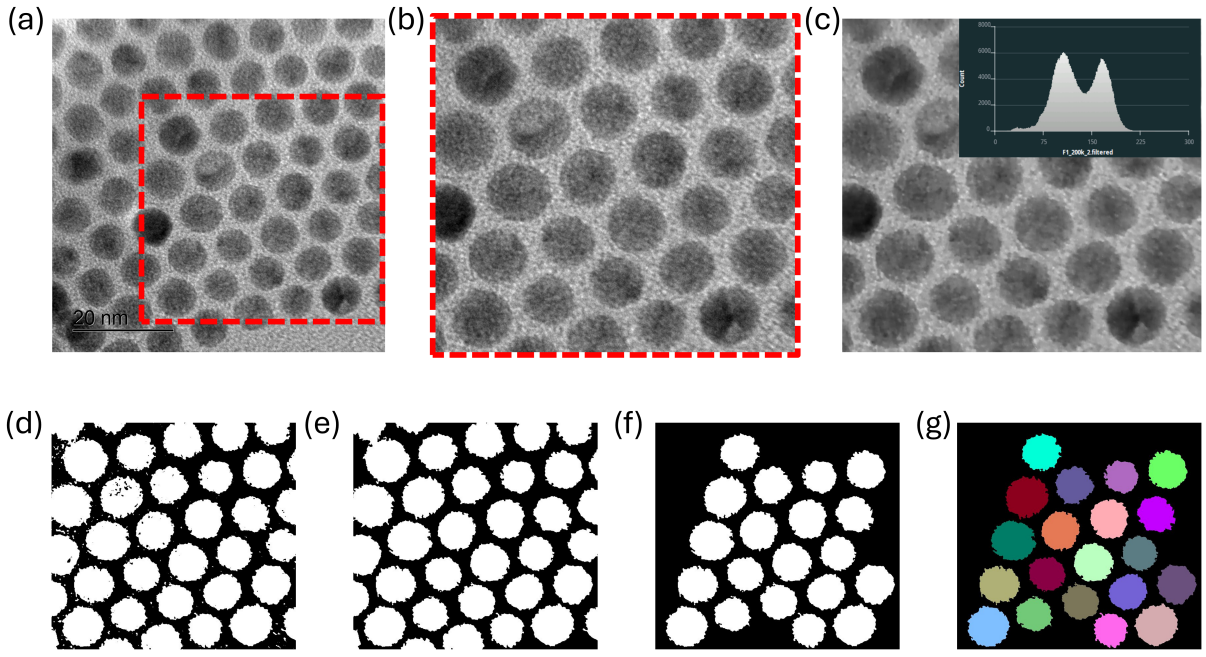


Figure 7.2.12: (a) Raw TEM image. (b) Extracted sub-image. (c) non-local means de-noised sub-image with greyscale histogram insert. (d) Segmented, binary sub-image. (e) Artifact-cleaned binary sub-image. (f) Border-killed, binary sub-image. (g) Labelled sub-image.

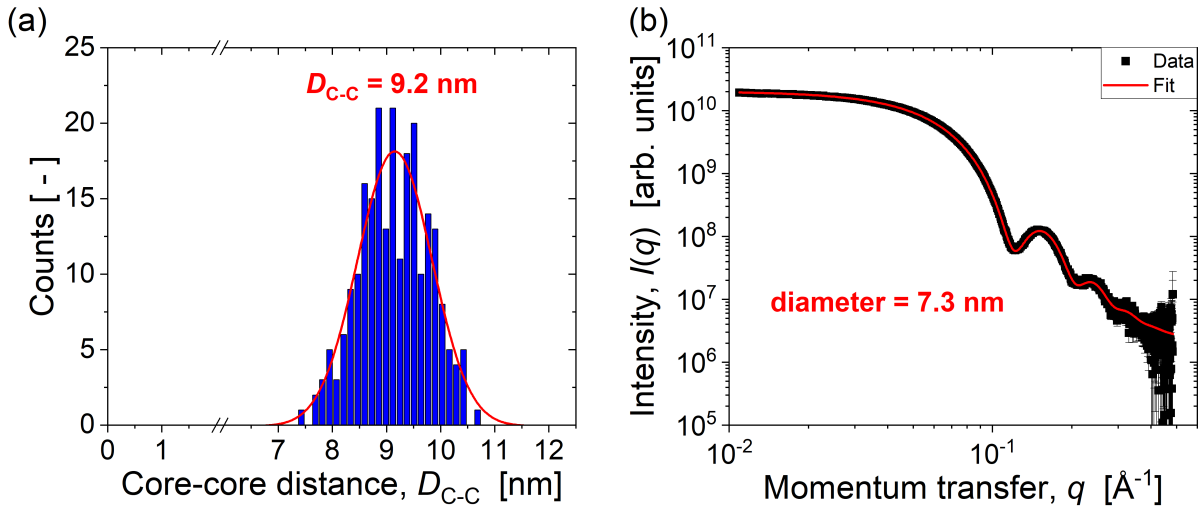


Figure 7.2.13: (a) Distribution of the center-to-center distances, $D_{C\text{-}C}$, between AuNPs with a core diameter of 7.3 nm, coated with oleylamine and arranged in a monolayer, determined using a nearest-neighbor analysis. (b) SAXS pattern of oleylamine coated AuNPs. The red line is a model fit according to eq. 7.2.1.

Thermogravimetric analysis

Thermogravimetric analysis (TGA) was used to analyze the mass of the ligand shell. The temperature-dependent changes of the mass of all particle systems are shown in Figure 7.2.14. The loss of sample mass during heating from room temperature to $1000\,^{\circ}\mathrm{C}$ is related to the number of surface-bound ligands present, N_{ligand}, which can be determined as

$$N_{\mathrm{ligand}} = \frac{m_{\mathrm{loss}}}{M_{\mathrm{ligand}}} \cdot N_{\mathrm{A}}, \tag{7.2.15}$$

with m_{loss} the mass loss of the sample during a TGA measurement, M_{ligand} the molar mass of the ligands, and N_{A} the Avogadro constant ($6.022 \cdot 10^{23}\mathrm{mol}^{-1}$). Using N_{ligand}, the ligand shell density, ρ_{LS}, is calculated as

$$\rho_{\mathrm{LS}} = \frac{N_{\mathrm{ligand}}}{A_{\mathrm{AuNP}}} \tag{7.2.16}$$

where A_{AuNP} is the surface of all nanoparticles, given by

$$A_{\mathrm{AuNP}} = A_{\mathrm{core}} \cdot N_{\mathrm{AuNP}}. \tag{7.2.17}$$

where A_{core} is the surface of one nanoparticle, as calculated from the particle size, and N_{AuNP} the total number of particles present, as determined from the remaining sample mass after the TGA measurement.

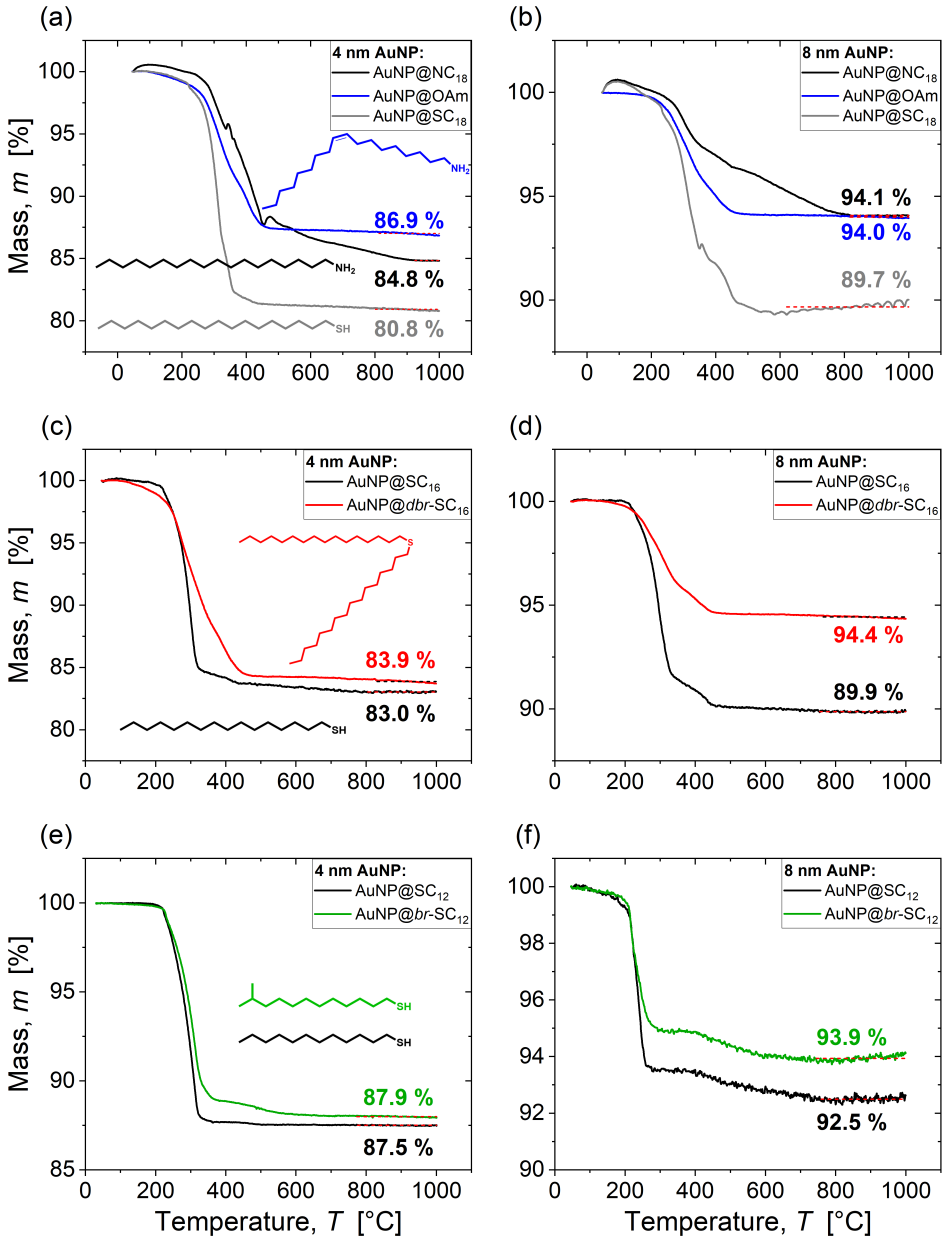


Figure 7.2.14: Thermogravimetric change of the sample mass during heating of AuNPs with a core diameter of 4 nm (a, c, e) and 8 nm (b, d, f) with linear (black curves) and non-linear ligand systems (colored curves).(a, b) AuNPs coated with NC_{18} (black) and OAm (blue) ligands. (c, d) AuNPs coated with SC_{16} (black) and *dbr*-SC_{16} (red) ligands. (e, f) AuNPs coated with SC_{12} (black) and *br*-SC_{12} (red) ligands. The dashed red or black line indicates the x-domain of each curve that was used to determine the mass loss using a linear fit function.

MD simulations

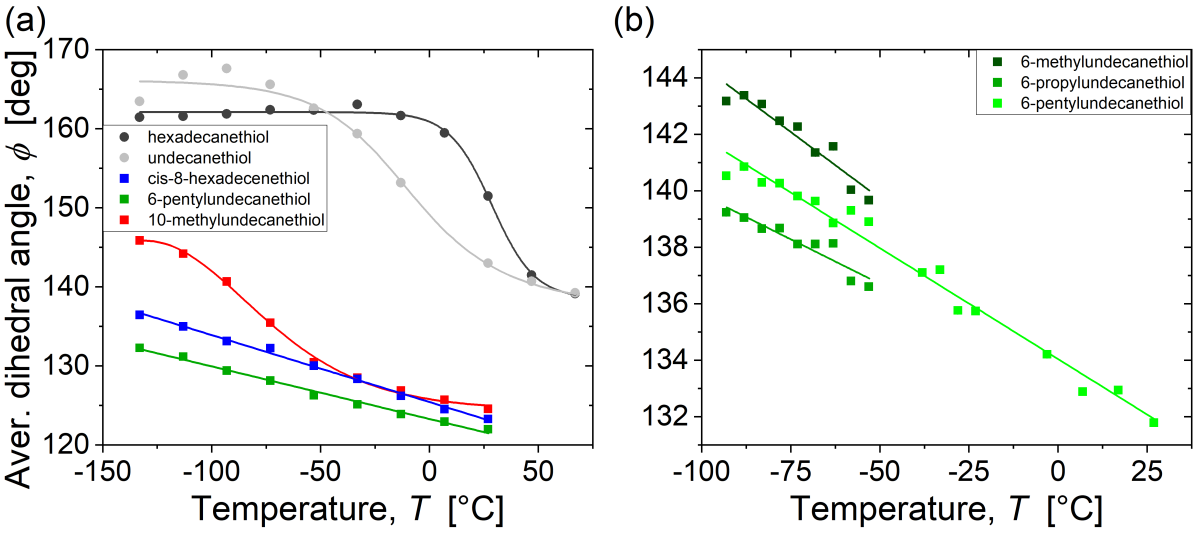


Figure 7.2.15: Average dihedral angle between CHx groups for (a) linear and branched ligands on 3.8 nm Au particles in vacuum and (b) branched ligands of varying branch lengths on 3.8 nm Au particles in hexane. Trends were fit to two-step sigmoid functions for linear and 10-methylundecanethiol ligands, and linear functions for other ligands.

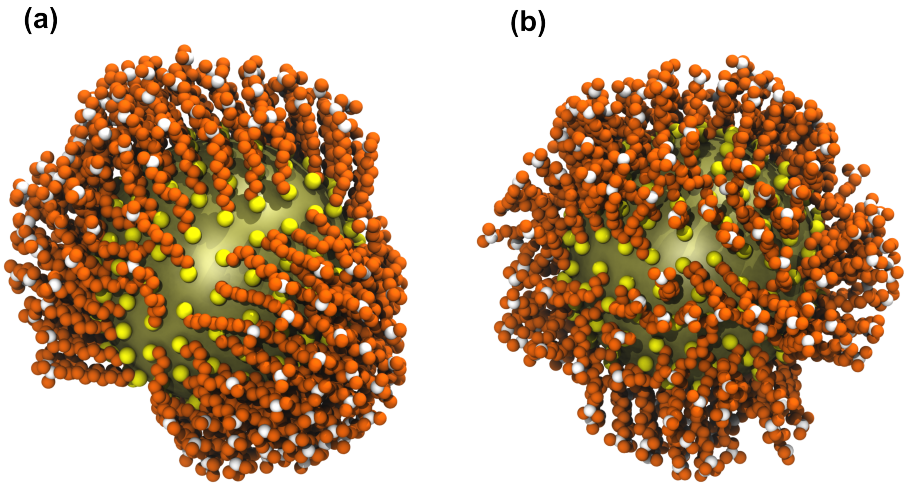


Figure 7.2.16: Simulation snapshots of a 3.8 nm Au particle coated with 10-methylundecane ligands at −93 °C in (a) vacuum and (b) hexane show ordering of ligands in vacuum.

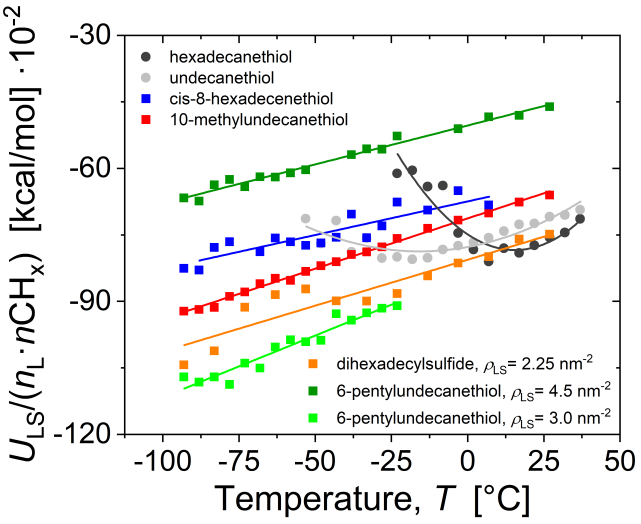


Figure 7.2.17: Ligand-solvent interaction energy for different ligands on the single 3.8 nm Au particle in hexane. The values have been normalized by the number of carbon atoms in all ligands $n_{\mathrm{L}}.n_{\mathrm{CH}}$. In order to display the trends clearly, polynomial and linear functions were fitted to the values.

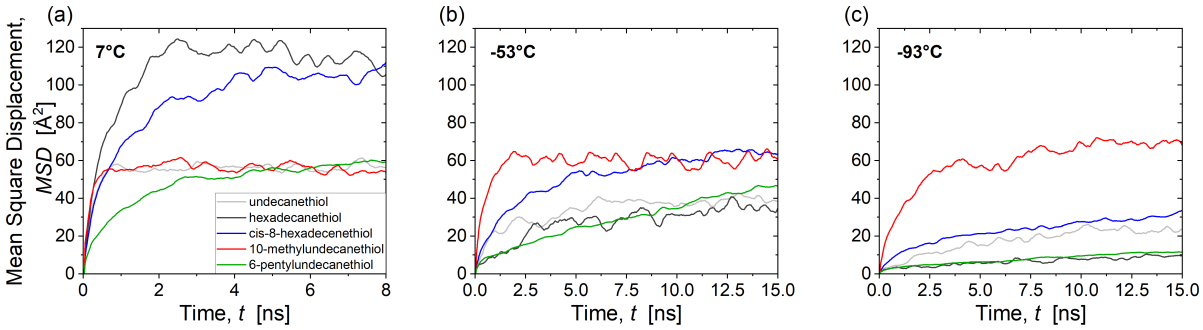


Figure 7.2.18: Comparison of ligand mobilities at (a) 7 °C, (b) −53 °C, and (c) −93 °C. The plots show the mean square displacement of ligand atoms as a function of time. To eliminate noise and enhance visualization, the curves were smoothed using discrete convolution.

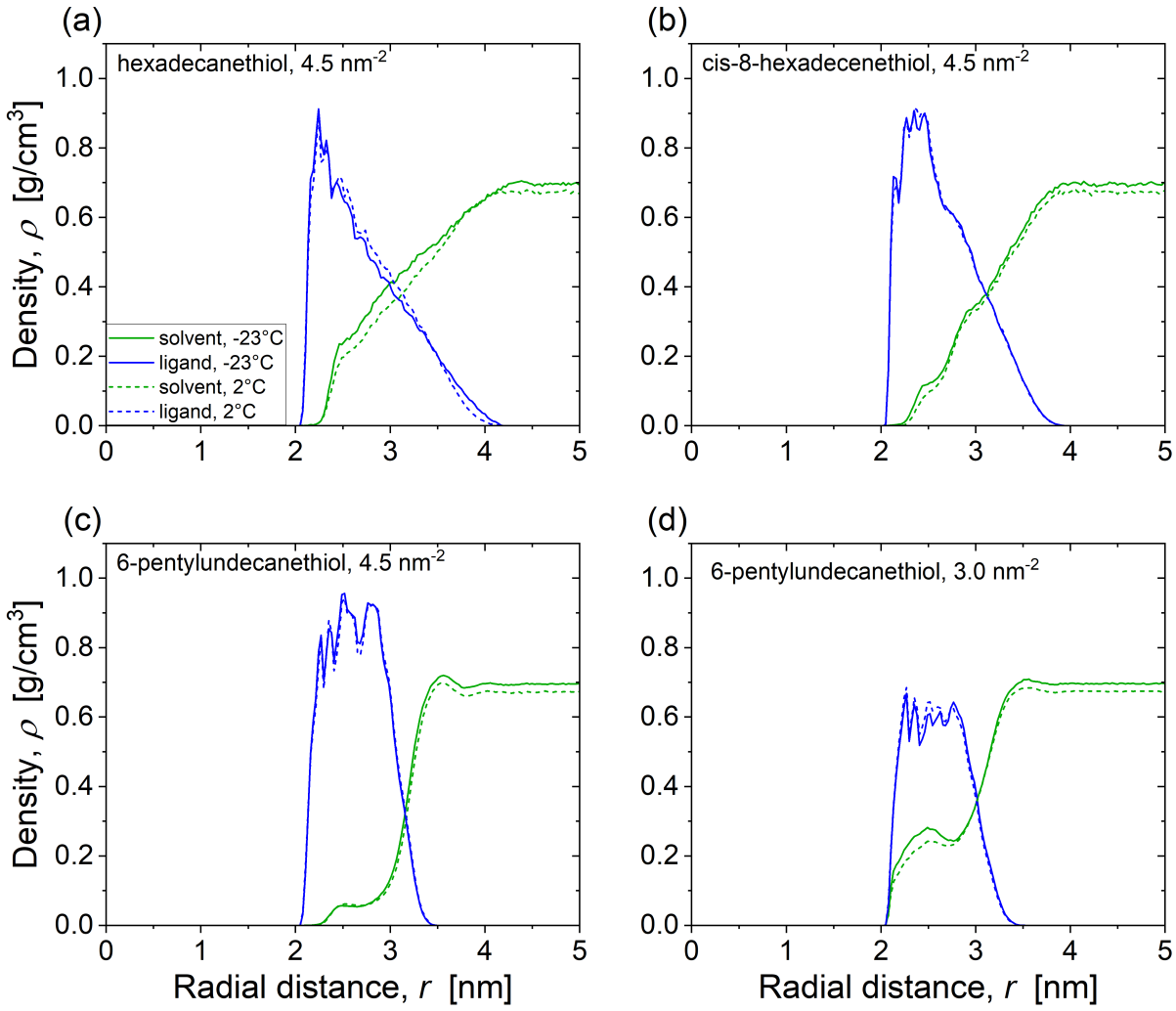


Figure 7.2.19: Radial density distribution as a function of the distance r from the centre of the Au core for ligand and solvent molecules at two different temperatures for (a) hexadecanethiol, (b) cis-8-hexadecenethiol and (c) 6-pentylundecanethiol, with 4.5 nm^{-2} density and (d) 6-pentylundecanethiol with 3 nm^{-2} density.

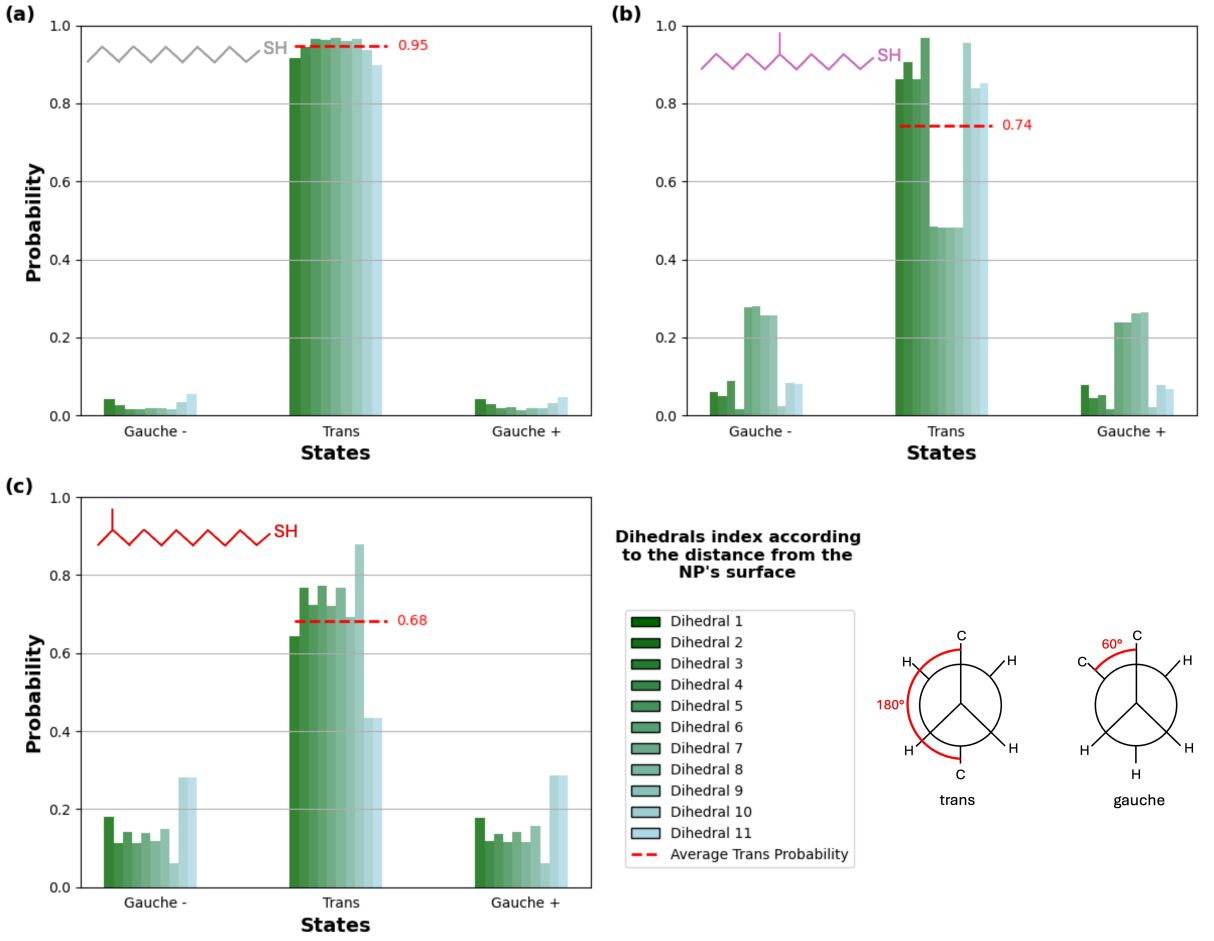


Figure 7.2.20: Probability distribution functions of dihedral states observed for ligand shells composed of (a) undecane, (b) 6-methylundecane, and (c) 10-methylundecane. The dihedrals are indexed based on their distance from the nanoparticle surface, with Dihedral 1 corresponding to the S–C–C–C dihedral in case. The gauche+, trans and gauche- states consist of all angles from 0°–120°, 120°–240°, and 240°–360°, respectively. The red dashed lines indicate the average probability of observing a dihedral angle belonging to the trans state.

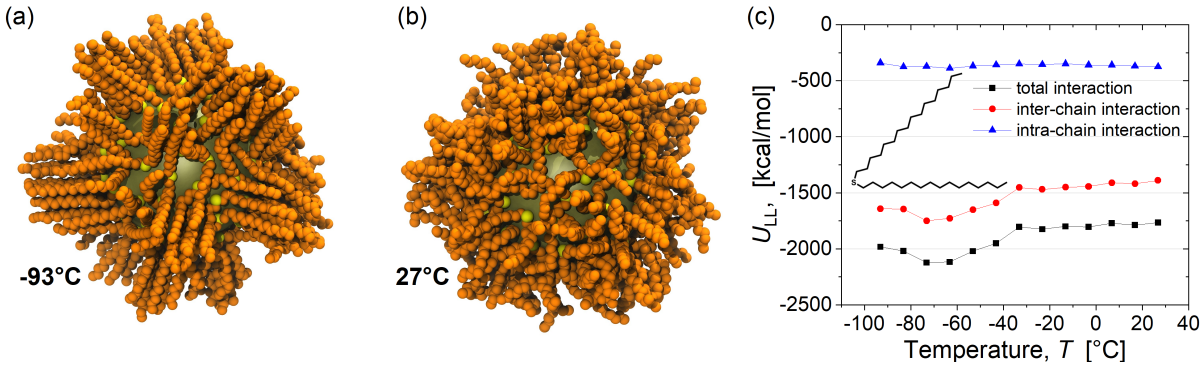


Figure 7.2.21: Simulation snapshots of a 3.8 nm Au particle coated with dihexadecylsulfide ligands at (a) $-93\,^{\circ}\mathrm{C}$ and (b) $27\,^{\circ}\mathrm{C}$, showing ordering of ligands into small bundles at low temperature. (c) The ligand-ligand interaction energy as a function of temperature, decomposed into intra and inter ligand contributions, shows that bundle formation coincides with an increase only in the inter ligand interaction energy. This is consistent with the snapshots showing that the bundles are composed of only one tail from each ligand, which limits their size.

7.3 Supporting Data - Stabilization of Apolar Gold Nanoparticles by Mixed Ligand Shells

Small-angle X-ray scattering

The size of the cores was determined by modeling the scattering patterns of the gold core using the expression (see Figure 7.3.1a):

$$I(q) = P_{\mathrm{pS}}(q) + I_{\mathrm{bkg}} \tag{7.3.1}$$

with $P_{\mathrm{pS}}(q)$ a form factor of polydisperse spheres [200] and I_{bkg} a constant accounting for background scattering. P_{pS} is given by

$$P_{\mathrm{pS}} = \int_0^\infty G(r)F(q,r)\,dr \tag{7.3.2}$$

with r the core radius, $F(q,r)$ the form factor for monodisperse spheres and $G(r)$ the size distribution of the core radius. $F(q,r)$ is given by

$$F(q,r) = 3 \cdot \frac{\sin qr - qr\cos qr}{(qr)^3} \tag{7.3.3}$$

$G(r_{\mathrm{c}})$ is described by a Gaussian distribution, given by

$$G(r) = \frac{1}{\sigma\sqrt{2\pi}} \exp\Big[-\frac{1}{\sigma^2}(r - r_{\mathrm{avg}})^2\Big] \tag{7.3.4}$$

with r_{avg} the average core radius. σ is given by:

$$\sigma = \frac{r_{\mathrm{c}}}{r_{\mathrm{avg}}} \tag{7.3.5}$$

The temperature-dependent SAXS patterns were analyzed following a method similar to that described by Hasan et al. [109]. In this method, the SAXS patterns are modeled using the expression

$$I(q) = I_{\mathrm{P}}(q) + P_{\mathrm{pS}}(q)\,[1 - \chi_{\mathrm{agglo}} + \chi_{\mathrm{agglo}} \cdot S_{\mathrm{HS}}(q)] + I_{\mathrm{bkg}} \tag{7.3.6}$$

Here, χ_{agglo} is the number fraction of AuNPs located inside agglomerates, $I_{\mathrm{P}}(q)$ is a generalized Porod law [307], accounting for scattering by the agglomerates, and $S_{\mathrm{HS}}(q)$ is the Percus-Yevick hard-sphere structure factor [306] accounting for spatial correlation between AuNPs inside agglomerates. $S_{\mathrm{HS}}(q)$ can be calculated as [200]

$$S_{\mathrm{HS}}(q) = \frac{1}{1 + 24\eta_{\mathrm{HS}}G(2R_{\mathrm{HS}}q)/(2R_{\mathrm{HS}}q)} \tag{7.3.7}$$

with R_{HS} the hard sphere radius and η_{HS} the hard-sphere volume fraction inside agglomerates. The function $G(x)$ is defined as:

$$G(x) = \gamma' \frac{\sin x - x\cos x}{x^2} + \delta' \frac{2x\sin x + (2-x^2)\cos x - 2}{x^3} + \epsilon' \frac{-x^4\cos x + 4[(3x^2-6)\cos x + (x^3-6x)\sin x + 6]}{x^5} \tag{7.3.8}$$

Here, γ', δ' and ϵ' are help functions, given by

$$\gamma' = \frac{(1+2\eta)^2}{(1-\eta)^4}, \quad \delta' = \frac{-6\eta(1+\eta/2)^2}{(1-\eta)^4}, \quad \epsilon' = \frac{\eta\gamma'}{2} \tag{7.3.9}$$

During fitting, r_{avg} and σ were kept fixed using the values obtained at the highest measured temperature of each respective run, i.e., where no agglomerates are present. At the lowest measured temperatures, values of χ_{agglo} of ~0.8 were obtained. These were normalized to 1 to reflect the complete agglomeration expected at these temperatures.

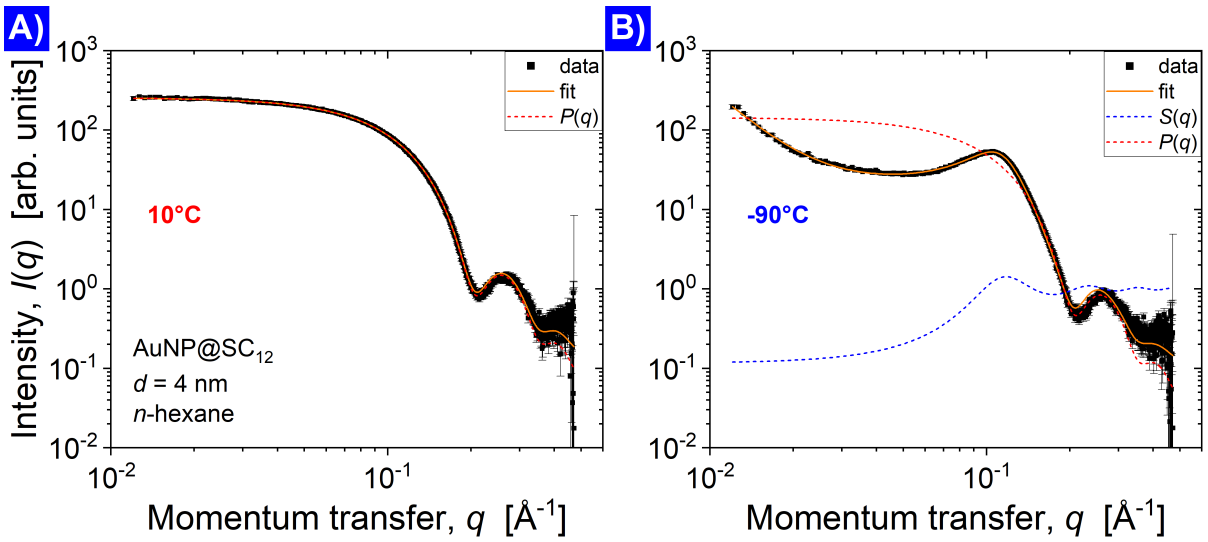


Figure 7.3.1: Scattering curves of 4 nm AuNP caoted with 1-dodecanethiol dispersed in *n*-hexane at a) 30 °C and b) −90 °C. The red dashed curve shows the form factor $P(q)$. The blue dashed curve shows the structure factor $S(q)$. The orange curve shows the resulting fit function used to analyze the scattering curves.

The agglomeration temperature, T_{agglo}, defined as temperature at which χ_{agglo} equals 0.2, determined by fitting the normalized $\chi_{\mathrm{agglo}}(T)$ using a Boltzmann sigmoid function [113], given by

$$\chi_{\mathrm{agglo}} = \frac{A_1 - A_2}{1 + \exp\left(\frac{T-T_0}{dT}\right)} + A_2 \tag{7.3.10}$$

with A_1 a parameter related to plateau at high temperatures, A_2 a parameter related to plateau at low temperatures, T_0 the temperature at $\chi_{\text{agglo}} = \frac{A_1+A_2}{2}$ and dT the range in which the transition occurs. The results are shown Figure 3.3.3, 7.3.2 and 7.3.3.

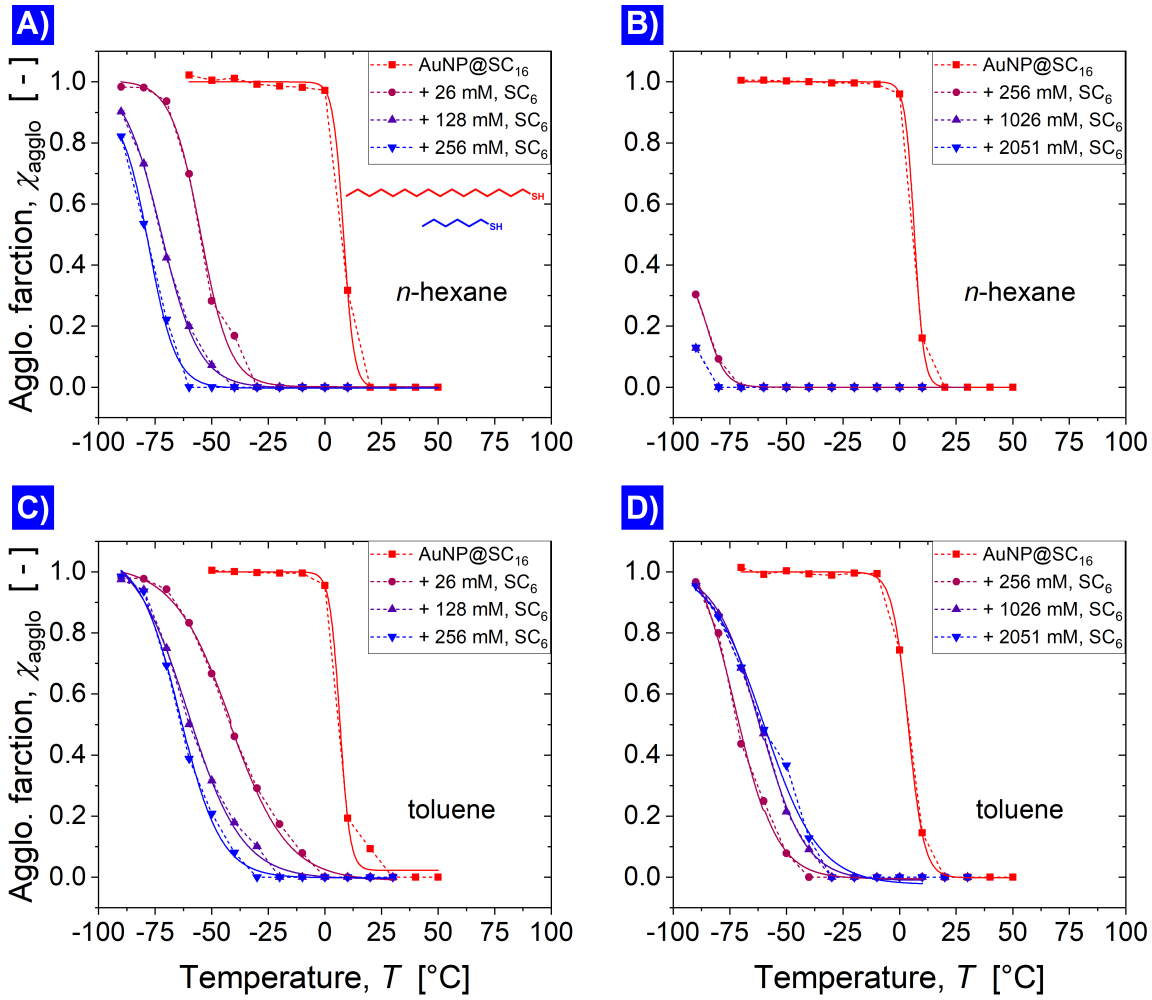


Figure 7.3.2: Temperature-dependent agglomeration fraction χ_{agglo} of 4 nm gold nanoparticles coated with 1-hexadecanethiol (SC_{16}) and modified with different concentrations of 1-hexanethiol (SC_6) in *n*-hexane (a + b) and toluene (c+d). The SC_6 concentrations in a) and c) are ranging from 26 mM to 256 mM. The SC_6 concentrations in a) and c) are ranging from 256 mM to 2056 mM.

The agglomeration temperature can be used to calculate the shift of the agglomeration process ΔT_{agglo} (see eq. 3.3.1 in Chapter 3.3). The results are shown Figure 3.3.4, 7.3.4 and 7.3.5. The core surface spacing s between neighboring particles can be calculated as follows:

$$s = 2(R_{\text{HS}} - r_{\text{avg}}) \tag{7.3.11}$$

The results are shown Figure 3.3.5, 7.3.6 and 7.3.7.

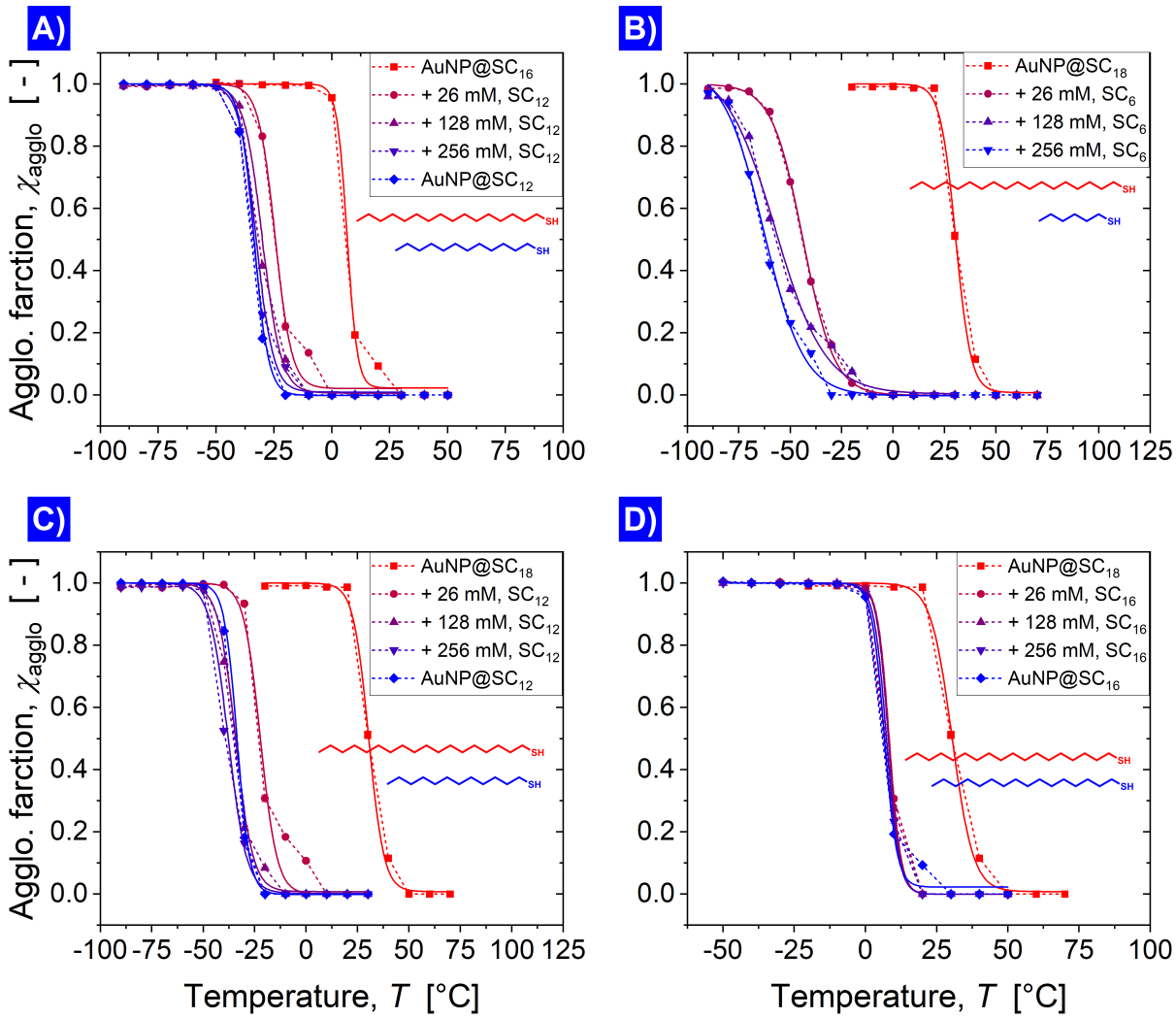


Figure 7.3.3: a) Temperature-dependent agglomeration fraction χ_{agglo} of 4 nm gold nanoparticles coated with 1-hexadecanethiol (SC_{16}) and modified with different concentrations of 1-dodecanethiol (SC_{12}) in toluene. b) Temperature-dependent χ_{agglo} of 4 nm gold nanoparticles coated with 1-octadecanethiol (SC_{18}) and modified with different concentrations of 1-hexadecanethiol (SC_{16}) in toluene. c) Temperature-dependent χ_{agglo} of 4 nm gold nanoparticles coated with 1-octadecanethiol (SC_{18}) and modified with different concentrations of 1-dodecanethiol (SC_{12}) in toluene. d) Temperature-dependent χ_{agglo} of 4 nm gold nanoparticles coated with 1-octadecanethiol (SC_{18}) and modified with different concentrations of 1-hexanethiol (SC_6) in toluene. The concentrations of the second ligand in all systems are ranging from 26 mM to 256 mM.

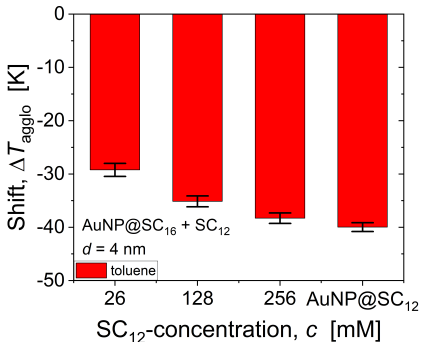


Figure 7.3.4: Stabilizing effect of mixed ligand shells of 4 nm AuNP coated with SC_{16} and modified with different concentrations of SC_{12} dispersed in toluene. The changes are shown as the shift of the agglomeration process ΔT_{agglo}. ($\Delta T_{agglo}(c_{MLS}) = T_{agglo}(c_{MLS}) - T_{agglo}(c_{ref.\ ligand})$)

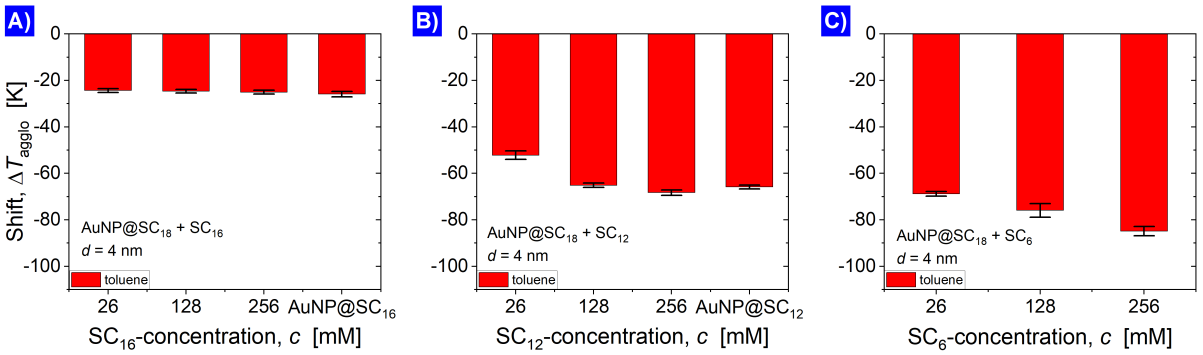


Figure 7.3.5: a) Stabilizing effect of mixed ligand shells of 4 nm AuNP coated with SC_{18} and modified with different concentrations of SC_{16} dispersed in toluene. b) Stabilizing effect of mixed ligand shells of 4 nm AuNP coated with SC_{18} and modified with different concentrations of SC_{12} dispersed in toluene. c) Stabilizing effect of mixed ligand shells of 4 nm AuNP coated with SC_{18} and modified with different concentrations of SC_6 dispersed in toluene. Changes in the agglomeration temperature T_{agglo} are compared to the initial ligand system. The changes are shown as the shift of the agglomeration process ΔT_{agglo}. ($\Delta T_{agglo}(c_{MLS}) = T_{agglo}(c_{MLS}) - T_{agglo}(c_{ref.\ ligand})$)

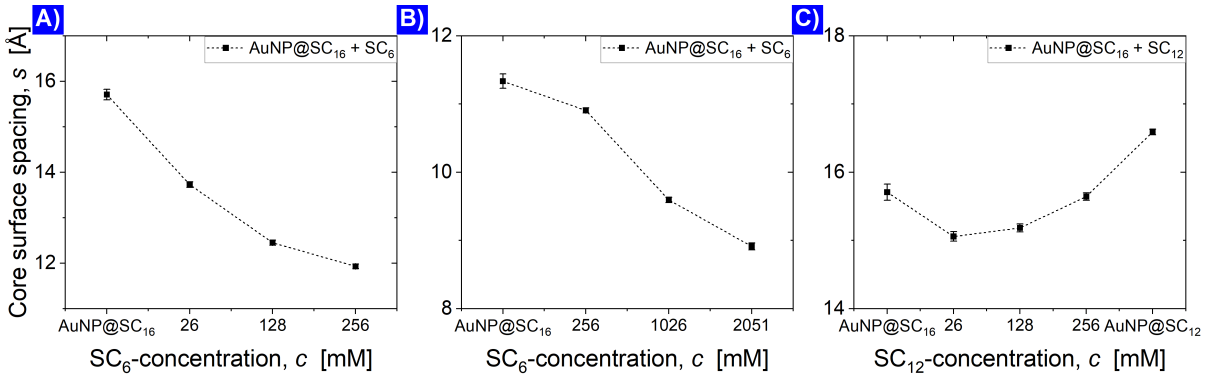


Figure 7.3.6: a) Final core surface spacing *s* of 4 nm AuNPs coated with 1-hexadecanethiol (SC_{16}) and modified with 1-hexanethiol (SC_6) using concentrations ranging from 26 mM to 256 mM) dispersed in toluene. b) Final core surface spacing *s* of 4 nm AuNPss coated with 1-hexadecanethiol (SC_{16}) and modified with 1-hexanethiol (SC_6) using concentrations ranging from 256 mM to 2051 mM) dispersed in toluene. c) Final core surface spacing *s* of 4 nm AuNPs coated with 1-hexadecanethiol (SC_{16}) and modified with 1-dodecanethiol (SC_{12}) using concentrations ranging from 26 mM to 256 mM) dispersed in toluene.

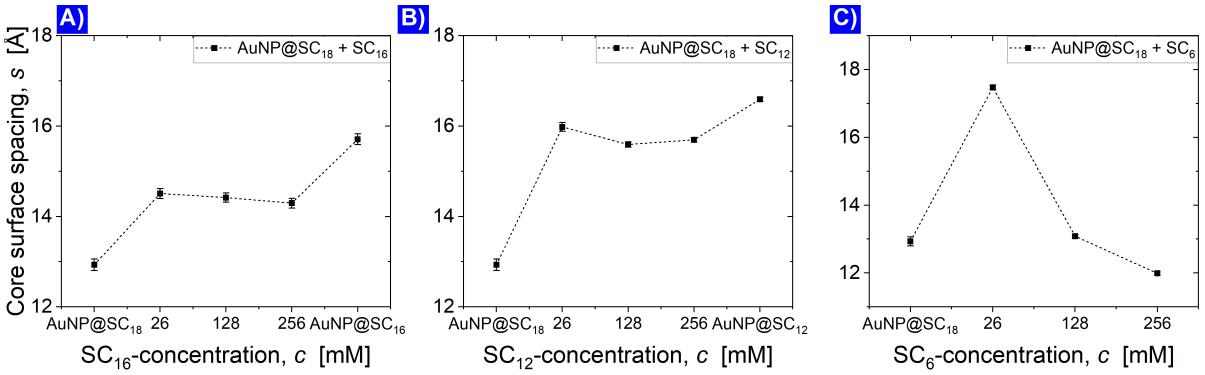


Figure 7.3.7: a) Final core surface spacing *s* of 4 nm AuNPs coated with 1-octadecanethiol (SC_{18}) and modified with 1-hexadecanethiol (SC_{16}) using concentrations ranging from 26 mM to 256 mM) dispersed in toluene. b) Final core surface spacing *s* of 4 nm AuNPs coated with 1-hexadecanethiol (SC_{18}) and modified with 1-dodecanethiol (SC_{12}) using concentrations ranging from 26 mM to 256 mM) dispersed in toluene. c) Final core surface spacing *s* of 4 nm AuNPs coated with 1-octadecanethiol (SC_{18}) and modified with 1-hexanethiol (SC_6) using concentrations ranging from 26 mM to 256 mM) dispersed in toluene.

Thermogravimetric analysis

Figure 7.3.8 and 7.3.9 show the TGA curves used for the calculation of the shell composition shown in Figure 3.3.4.

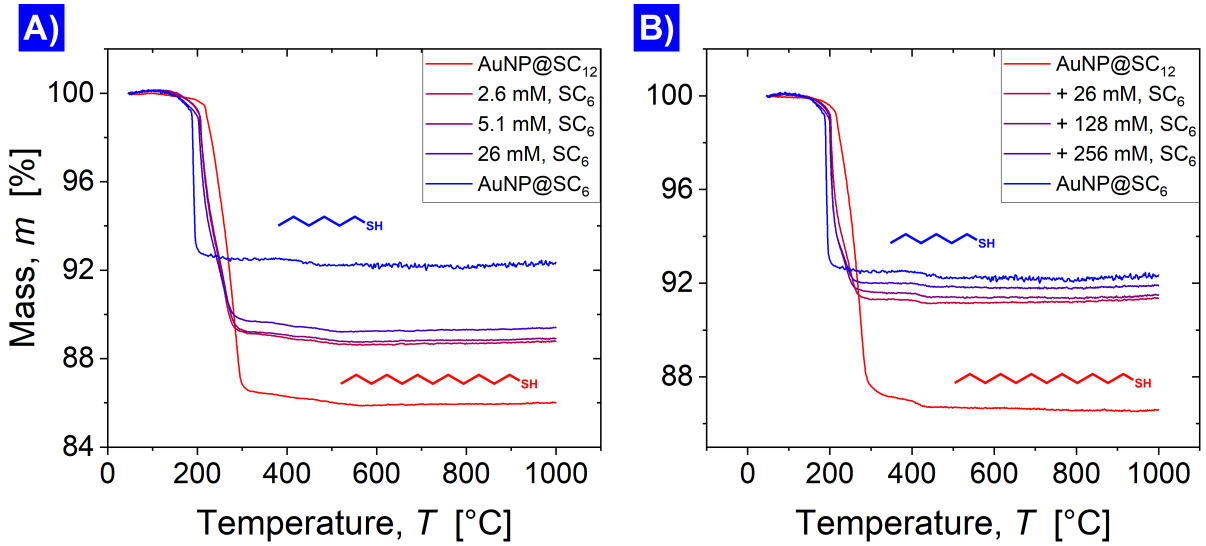


Figure 7.3.8: a) TGA curves of 4 nm gold nanoparticles coated with a mixed ligand shell based on 1-dodecanethiol with 1-hexanthiol concentrations between 2.6 mM and 26 mM. a) TGA curves of 4 nm gold nanoparticles coated with a mixed ligand shell based on 1-dodecanethiol with 1-hexanthiol concentrations between 2.6 mM and 256 mM.

The calculation of the shell composition is based on our previous work with additives [113]. The primary difference lies in the use of two reference systems instead of just one.

To characterize ligand exchange, the ligand shell density of the reference particle system must be calculated. The surface area A_{core} of one particle cores is

$$A_{\text{core}} = 4\pi r_{\text{core}}^2 \tag{7.3.12}$$

The number of particles N_{AuNP} follows from the gold mass m_{gold} remaining in the crucible after the TGA measurement as

$$N_{\text{AuNP}} = \frac{m_{\text{gold}}}{m_{\text{core}}} = \frac{m_{\text{gold}}}{V_{\text{core}} \cdot \rho_{\text{gold}}} = \frac{m_{\text{gold}}}{4/3\pi r_{\text{core}}^3 \cdot \delta_{\text{gold}}} \tag{7.3.13}$$

and leads to the overall surface of all cores as

$$A_{\text{AuNP}} = A_{\text{core}} \cdot N_{\text{AuNP}}. \tag{7.3.14}$$

The number of surface-bound HDT ligands can be calculated using the mass loss m_{loss} (measured using TGA), and the molar mass of the ligand molecule M_{L}:

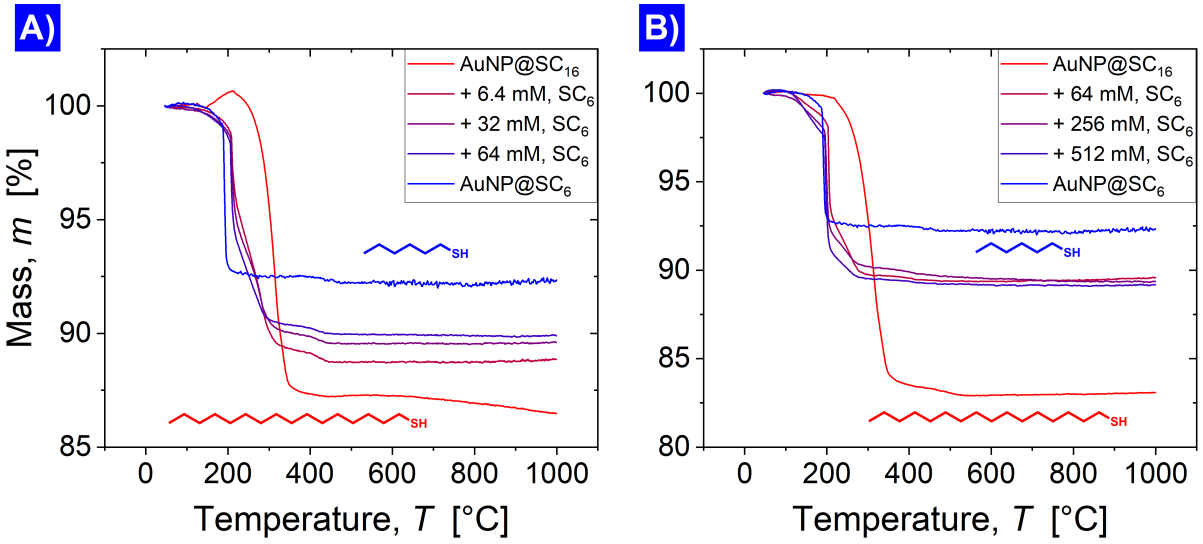


Figure 7.3.9: a) TGA curves of 4 nm gold nanoparticles coated with a mixed ligand shell based on 1-hexadecanethiol with 1-hexanthiol concentrations between 26 mM and 256 mM. a) TGA curves of 4 nm gold nanoparticles coated with a mixed ligand shell based on 1-hexadecanethiol with 1-hexanthiol concentrations between 256 mM and 2051 mM.

$$N_{\text{ligand}} = \frac{m_{\text{loss}}}{M_{\text{L}}} \cdot N_{\text{A}}, \tag{7.3.15}$$

N_{A} is the Avogadro constant ($6.022 \cdot 10^{23}$ mol^{-1}). The ligand shell density of a pure shell can be calculated as follows

$$\rho_{\text{LS}} = \frac{N_{\text{ligand}}}{A_{\text{AuNP}}} \tag{7.3.16}$$

To calculate the composition of a mixed ligand shell based on the use of two reference systems. The following equation is using the mass loss of the missed ligand system to calculate an exchange factor a for the ligand exchange reaction:

$$m_{\text{loss}} = \frac{A_{\text{AuNP}} \cdot [a \cdot \rho_{\text{L}_2} + (1-a)\rho_{\text{L}_1}] \cdot [a \cdot M_{\text{L}_2} + (1-a) \cdot M_{\text{L}_1}]}{N_{\text{A}}}, \tag{7.3.17}$$

To calculate the exchange rate a, the molar mass M_{L} and shell density ρ_{L} of both pure ligand systems need to be considered.

This equation can be converted to calculate a:

$$a = \frac{-A_{\text{AuNP}} \cdot M_{\text{L}_1} \cdot \rho_{\text{L}_2} - A_{\text{AuNP}} \cdot M_{\text{L}_2} \cdot \rho_{\text{L}_1} + 2 \cdot A_{\text{AuNP}} \cdot M_{\text{L}_1} \cdot \rho_{\text{L}_1} - \sqrt{F}}{2 \cdot A_{\text{AuNP}} \cdot M_{\text{L}_2} \cdot \rho_{\text{L}_2} - A_{\text{AuNP}} \cdot M_{\text{L}_1} \cdot \rho_{\text{L}_2} - A_{\text{AuNP}} \cdot M_{\text{L}_2} \cdot \rho_{\text{L}_1} + A_{\text{AuNP}} \cdot M_{\text{L}_1} \cdot \rho_{\text{L}_1}} \tag{7.3.18}$$

here F is defined as:

$$
\begin{aligned}
F = [A_{\text{AuNP}} \cdot M_{\text{L}_2} \cdot \rho_{\text{L}_1}]^2 - 4 \cdot m_{\text{loss}} \cdot N_{\text{A}} \cdot A_{\text{AuNP}} \cdot M_{\text{L}_2} \cdot \rho_{\text{L}_1} \\
+4 \cdot m_{\text{loss}} \cdot N_{\text{A}} \cdot A_{\text{AuNP}} \cdot M_{\text{L}_1} \cdot \rho_{\text{L}_1} \\
-2 \cdot A_{\text{AuNP}}^2 \cdot M_{\text{L}_1} \cdot M_{\text{L}_2} \cdot \rho_{\text{L}_1} \cdot \rho_{\text{L}_2} + [A_{\text{AuNP}} \cdot M_{\text{L}_1} \cdot \rho_{\text{L}_2}]^2 \\
+4 \cdot m_{\text{loss}} \cdot N_{\text{A}} \cdot A_{\text{AuNP}} \cdot M_{\text{L}_2} \cdot \rho_{\text{L}_2} \\
-4 \cdot m_{\text{loss}} \cdot N_{\text{A}} \cdot A_{\text{AuNP}} \cdot M_{\text{L}_1} \cdot \rho_{\text{L}_2}
\end{aligned}
\tag{7.3.19}
$$

7.4 Supporting Data - Reactive Additive-Induced Joining of Apolar Thiol-Coated Gold Nanoparticle Cores at Low Temperatures

Transmission electron analysis

Transmission electron microscopy (TEM) measurements were performed to determine the size and shape of AuNPs. Figure 7.4.1a shows a TEM micrograph of 4 nm AuNPs, directly after their ligand exchange with hexadecanethiol (HDT).

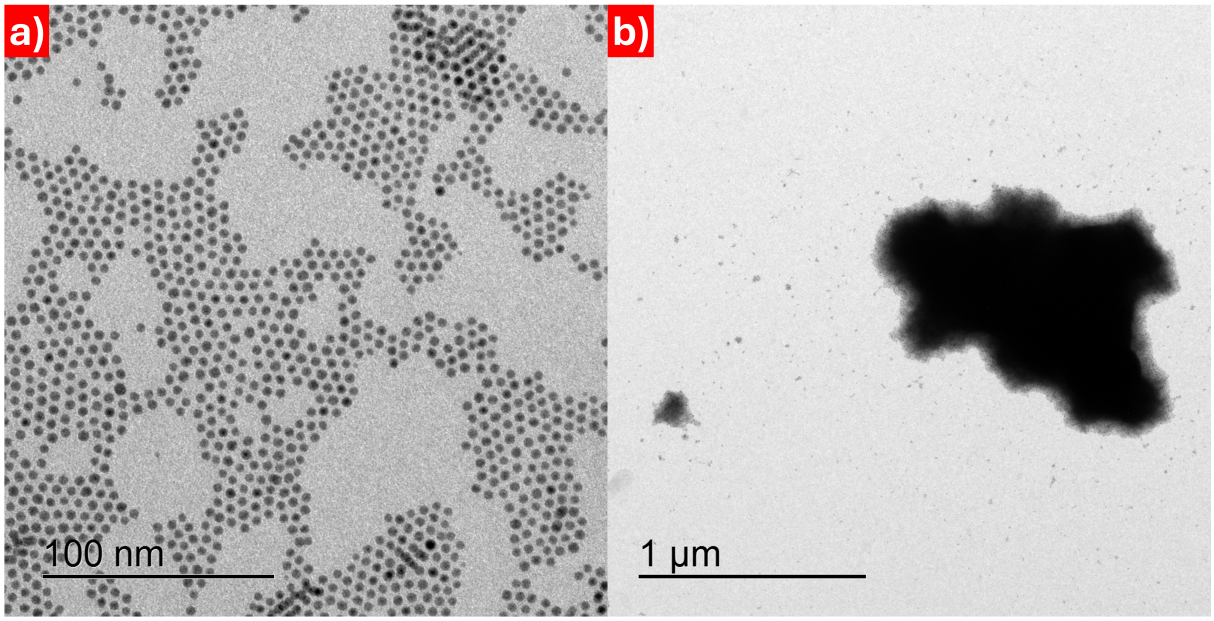


Figure 7.4.1: Transmission electron microscopy image of (a) 4 nm AuNP after the ligand exchange with HDT and (b) after the addition of R5S (128 mM) and heating at 50 °C for more than 300 min.

The particle diameter in the TEM images was determined in a stepwise image analysis using the software "Avizo" (Avizo 3D 2022.1, ThermoFisher Scientific, Waltham, Massachusetts, USA), similar to our previous work [210]. First, various filters ("Background Detection Correction", "greyscale filter", etc.) were applied to increase the contrast of the particles. Incomplete particles at the edge of the images were masked. The remaining particles were labeled using the function "Labeling". Using this method, the center-of-mass and the size of the particles were determined. The particle circularity was analyzed using the function [309]:

$$f_{\text{circ}} = \frac{4\pi A}{P^2} \tag{7.4.1}$$

with A the area (pixel count), and P the perimeter. The circularity describes how closely the 2D particle image approximates a circle. The parameter ranges from 0 to 1, with 1 representing the

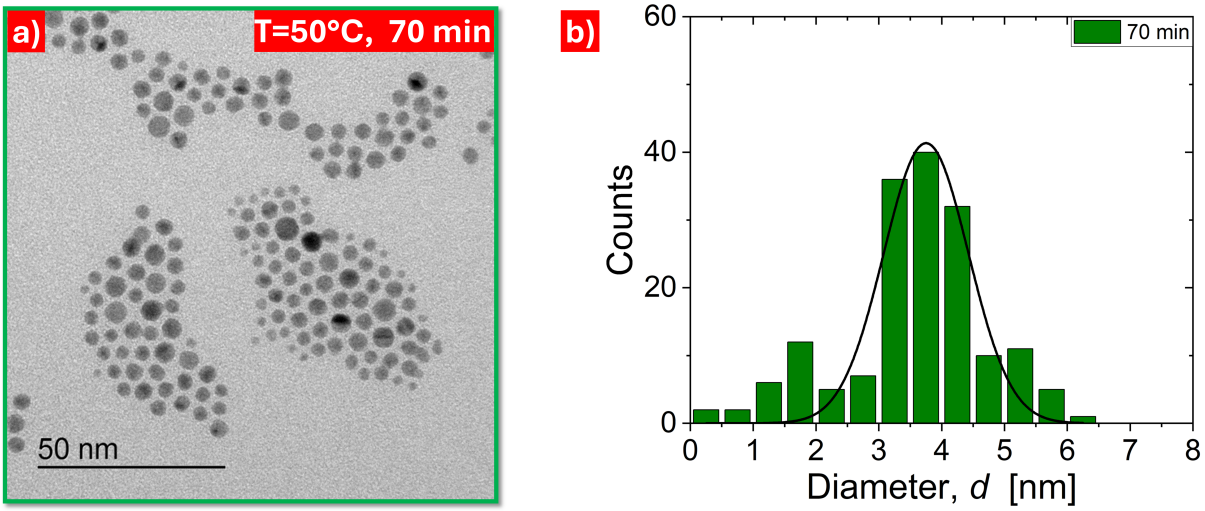


Figure 7.4.2: Coarsening of 3.8 nm gold nanoparticles coated with HDT dispersed in *n*-decane at 50 °C in the presence of R5S in a concentration of 128 mM. (a) Transmission electron micrograph shows the dispersion after 70 min at 50 °C. (b) Results of the size analysis of the micrograph.

case of a perfectly spherical object [309]. The circularity of the particles before heating, shown in Figure 1a and d in the main text, was 0.86. We defined particles with a circularity of more than 0.6 as spheres.

Figure 7.4.2a shows a TEM micrograph of AuNPs modified with 128 mM of R5S and heated for 70 min at 50 °C. Its size distribution (Figure 7.4.2b) is broader than that of the primary particles before modification (Figure 1 in the main text), pointing to coarsening of the AuNPs by Ostwald ripening. As changes in the AuNP size dispersity could not be observed using SAXS, we assume that the coarsening by Ostwald ripening is mainly due to electron irradiation of particles during TEM measurements.

In the work of Gutiérrez-Wing et al. and Azcárate et al., the effect of electron irradiation on the core geometry was analyzed [310, 311]. For both thiol-coated and blank gold nanoparticles on a carbon substrate under electron irradiation, it was found that Ostwald ripening and coalescence occur within 5 min after the start of the electron irradiation.

Gutiérrez-Wing and co-workers found that ripening is energetically favored. They discovered that ripening involves the migration of ad-atoms and/or thiol-ad-atom clusters from smaller particles to larger ones. This process is based on the lower stability of ad-atoms on small cores due to the lower coordination resulting from the larger curvature. Additionally, they could demonstrate that the alkyl chains of the ligand can interact with the substrate through van der Waals forces, leading to the fixation of the particles. This fixation hinders the coalescence of the cores [310].

Azcárate et al. could show that for coalescence, two equal planes (often the 100 planes) need to face each other, and the ligand coverage must be small. They could demonstrate that particles can

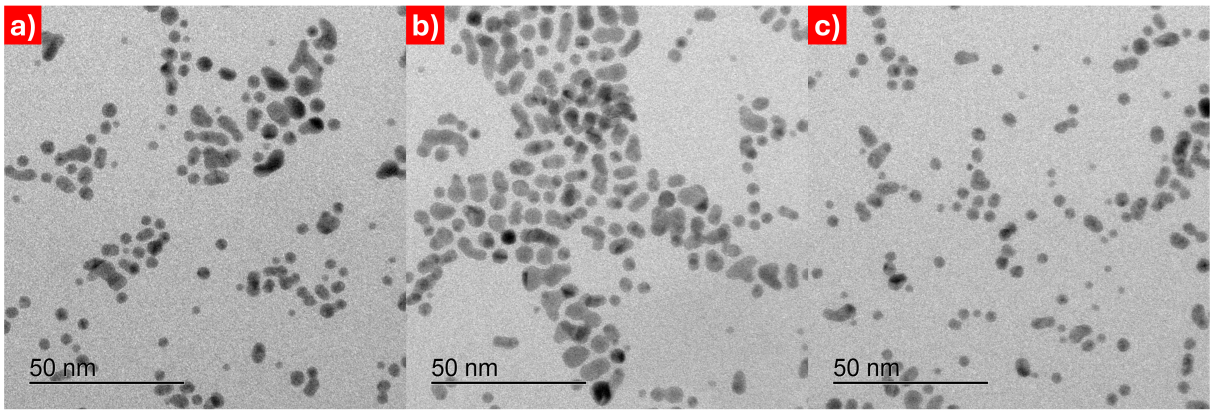


Figure 7.4.3: TEM micrographs of HDT-coated 4 nm AuNP dispersed in *n*-decane with an additive concentration of 128 mM after heating at 50 °C for 150 min. These micrographs were used for the analysis of the sphericity and particle size shown in Figure 1e in the main manuscript.

reorient to align with specific planes. As a result, coalescence is favored for blank cores [311]. Bo et al. studied the heat-induced coalescence of oleylamine-coated gold particles using liquid-phase electron microscopy. They could demonstrate that coalescence was primarily induced by the heat treatment, rather than by the electron irradiation [158]. We conclude that the irradiation of the electron beam is the main cause of the observed Ostwald ripening in this work.

Small-angle X-ray scattering (SAXS)

SAXS model fitting

The gold nanoparticles (AuNPs) used in this study were characterized using SAXS. Figure 7.4.4a shows the scattered intensity, $I(q)$, of AuNPs in dependence on momentum transfer, q, in their dispersed state, i.e., the scattering pattern represents the form factor of AuNPs. As the scattering contrast between the organic ligands and solvent molecules is negligible, only the Au cores are visible. The size of the cores was determined by modeling the obtained scattering pattern using the expression

$$I(q) = I_{\mathrm{pS}}(q) + I_{\mathrm{bkg}} \tag{7.4.2}$$

with $I_{\mathrm{pS}}(q)$ a form factor of polydisperse spheres [200] and I_{bkg} a constant accounting for background scattering. I_{pS} is given by

$$I_{\mathrm{pS}}(q) = C \int_0^\infty F_{\mathrm{S}}^2(q,r) r^6 G(r)\,\mathrm{d}r \tag{7.4.3}$$

with $F_{\mathrm{S}}(q,r)$ the scattering amplitude of a sphere with radius r, $G(r)$ the distribution of radii, and C a scaling constant. $F(q,r)$ is given by

$$F_{\mathrm{S}}(q,r) = 3 \cdot \frac{\sin qr - qr\cos qr}{(qr)^3} \tag{7.4.4}$$

$G(r)$ is approximated by a Gaussian distribution, given by

$$G(r) = \frac{1}{\sqrt{2\pi\sigma^2}} \exp\left(-\frac{(r - r_{\mathrm{avg}})^2}{2\sigma^2} \right) \tag{7.4.5}$$

with r_{avg} the average core radius and σ its standard deviation.

The AuNPs from all batches used in this study had an r_{avg} in the range of $3.8 - 4.1$ nm and σ in the range of $10 - 11$ %. The spherical shape of the AuNPs was confirmed using transmission electron microscopy, shown in Figure 7.4.1 for AuNPs after ligand exchange with HDT.

The temperature-dependent SAXS patterns (see Figure 7.4.5 and 7.4.4b) of the cooling experiments were analyzed following a method similar to that described by Hasan et al. [109]. In this method, the SAXS patterns are modelled using the expression

$$I(q) = I_{\mathrm{Porod}}(q) + I_{\mathrm{pS}}(q)\left[1 - \chi_{\mathrm{agglo}} + \chi_{\mathrm{agglo}} \cdot S_{\mathrm{HS}}(q)\right] + I_{\mathrm{bkg}} \tag{7.4.6}$$

Here, χ_{agglo} is the number fraction of AuNPs located inside agglomerates. $I_{\mathrm{Porod}}(q)$ is a generalized Porod law [307], accounting for scattering by the agglomerates, given by

$$I_{\mathrm{Porod}} = \frac{B}{q^m} \tag{7.4.7}$$

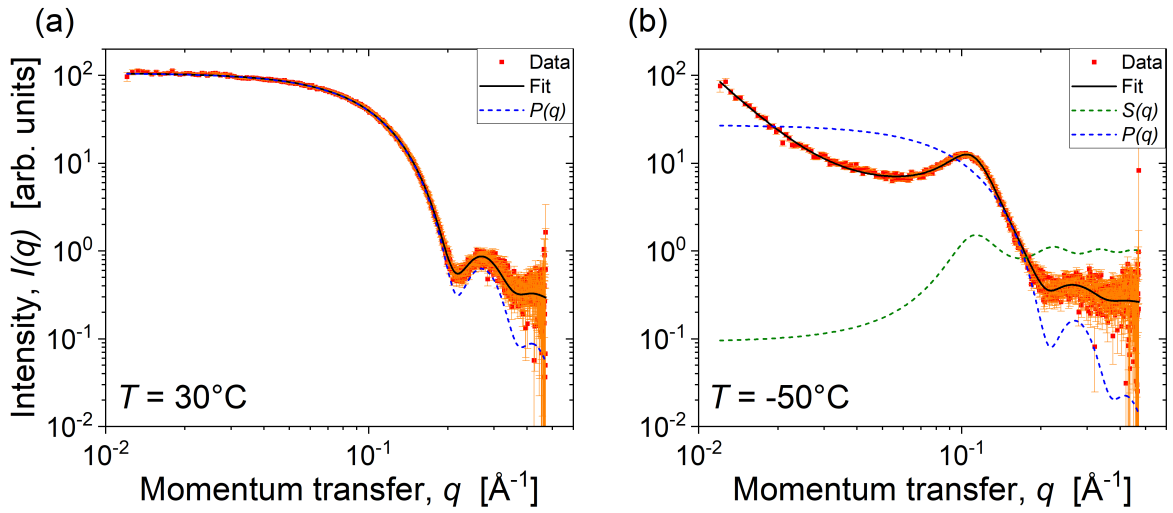


Figure 7.4.4: (a) SAXS pattern of 4 nm AuNPs dispersed in n-decane after the ligand exchange with HDT at 30 °C. Red dots: data. Black line: fit according to eq. 7.4.2. Blue dotted line: sphere form factor $P(q)$. (b) SAXS pattern of agglomerated AuNPs at −50 °C. Black line: fit according to eq. 7.4.6. Blue dotted line: sphere form factor $P(q)$. Green line: structure factor $S(q)$ for amorphous assemblies.

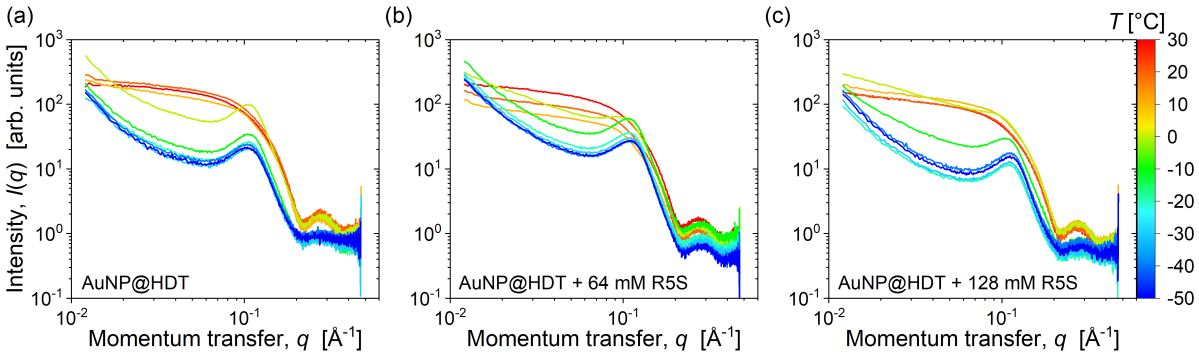


Figure 7.4.5: Temperature-dependent scattering curves of 4 nm coated with HDT (a) and modified with 64 mM (b) and 128 mM (c) of R5S dispersed in toluene during the cooling induced self-assembly.

with B a pre-factor and m the Porod exponent, indicative of the fractal properties of the agglomerates [312]. $S_{\mathrm{HS}}(q)$ is the Percus-Yevick hard-sphere structure factor [306] accounting for spatial correlation between AuNPs inside agglomerates. $S_{\mathrm{HS}}(q)$ can be calculated as [200]

$$S_{\mathrm{HS}}(q) = \frac{1}{1 + 24\eta_{\mathrm{HS}} G_{\mathrm{HS}}(2R_{\mathrm{HS}}q)/(2R_{\mathrm{HS}}q)} \tag{7.4.8}$$

with R_{HS} the hard sphere radius and η_{HS} the hard-sphere volume fraction inside agglomerates. The function $G_{\mathrm{HS}}(x)$ is defined as:

$$\begin{aligned} G_{\mathrm{HS}}(x) = \gamma' \frac{\sin x - x\cos x}{x^2} + \delta' \frac{2x\sin x + (2 - x^2)\cos x - 2}{x^3} \\ + \epsilon' \frac{-x^4 \cos x + 4[(3x^2 - 6)\cos x + (x^3 - 6x)\sin x + 6]}{x^5} \end{aligned} \tag{7.4.9}$$

Here, γ', δ' and ϵ' are help functions, given by

$$\gamma' = \frac{(1 + 2\eta)^2}{(1 - \eta)^4}, \quad \delta' = \frac{-6\eta(1 + \eta/2)^2}{(1 - \eta)^4}, \quad \epsilon' = \frac{\eta\gamma'}{2} \tag{7.4.10}$$

During fitting, r_{avg} and σ were kept fixed using the values obtained at the highest measured temperature of each respective run, i.e., where no agglomerates are present.
R_{HS} can be used to calculated the core surface spacing s between gold surfaces of neighboring particles in agglomerates as

$$s = 2(R_{\mathrm{HS}} - r_{\mathrm{avg}}) \tag{7.4.11}$$

The model employed to analyze SAXS patterns during the coarsening process is based on a combination of a polydisperse sphere form factor, a polydisperse dumbbell form factor, and a Porod term, given by

$$I_{\mathrm{tot}}(q) = I_{\mathrm{Porod}}(q) + I_{\mathrm{pS}}(q) + I_{\mathrm{pDum}}(q) + I_{\mathrm{bkg}} \tag{7.4.12}$$

The polydisperse dumbbell form factor, $I_{\mathrm{pDum}}(q, r)$, describes fused bodies consisting of two equally sized spheres with a Gaussian size distribution $G(r)$, and is given by

$$I_{\mathrm{pDum}}(q) = \frac{C}{V} \int_0^\infty P_{\mathrm{Dum}}(q, r) r^6 G(r) dr \tag{7.4.13}$$

with C a scaling amplitude, V the total volume of the particle. $P_{\mathrm{Dum}}(q, r)$ the form factor of monodisperse dumbbells, given by

$$P_{\mathrm{Dum}}(q) = \int_0^{\pi/2} F^2_{\mathrm{Dum}}(q, r, \theta) \sin(\theta) d\theta \tag{7.4.14}$$

which is the average of the scattering amplitude $F_{\mathrm{D}}(q,r,\theta)$ squared, over all orientations. $F_{\mathrm{D}}(q,r,\theta)$ is written as [313]

$$F_{\mathrm{D}}(q,r,\theta) = 4\pi r^3 \int_{-h/R}^{1} \cos\left[q\cos\theta(rt+h)\right] \times(1-t^2)\frac{J_1[qR\cdot\sin\theta(1-t^2)^{1/2}]}{qR\cdot\sin\theta(1-t^2)^{1/2}}\mathrm{d}t \tag{7.4.15}$$

Here, $J_1(x)$ is the first-order Bessel function and h the distance between the center of the core and the cross-plane between the two spheres, r_{n}, given by

$$h = \sqrt{r^2 - r_{\mathrm{n}}^2} \tag{7.4.16}$$

During the fitting, the sphere radius *r* in $P_{\mathrm{pS}}(q)$ and in $P_{\mathrm{pDum}}(q)$ were kept identical.

AuNP coarsening at $40\,^{\circ}\mathrm{C}$ **and** $60\,^{\circ}\mathrm{C}$

The SAXS patterns obtained during AuNP coarsening at different times at $40\,^{\circ}\mathrm{C}$ and $60\,^{\circ}\mathrm{C}$ are shown in Figure 7.4.6.

Arrhenius analysis of AuNP coarsening

The activation energy, E_{A}, of the coalescence process was calculated using the Arrhenius equation, given by

$$k = A\cdot e^{-\frac{E_{\mathrm{A}}}{RT}} \tag{7.4.17}$$

with k the transition rate, determined as $1/t_{\mathrm{f}}$, R the gas constant and T the absolute temperature.

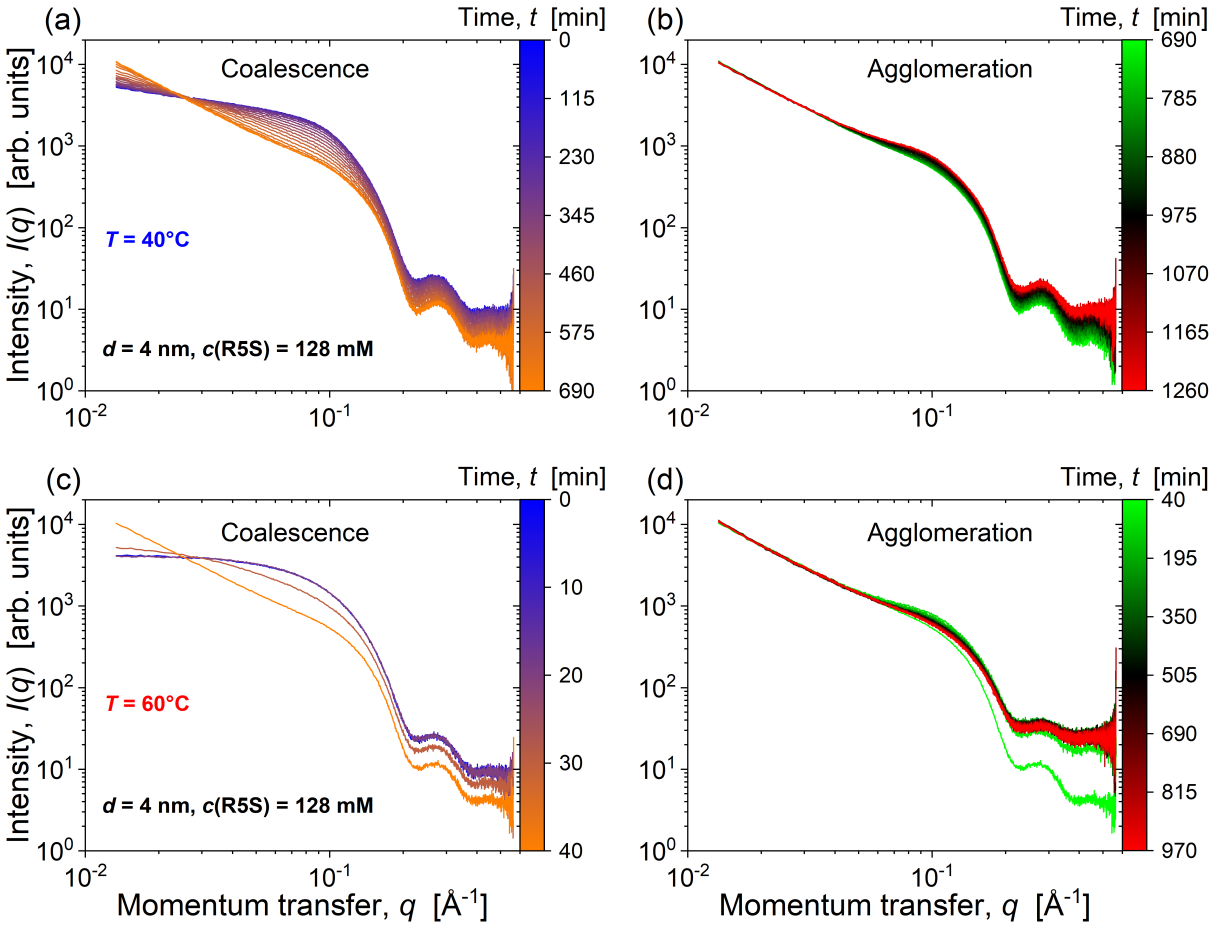


Figure 7.4.6: SAXS patterns of AuNPs, dispersed in n-decane with a R5S concentration of 128 mM during heating at 40 °C (a,b) and at 60 °C (c,d).

Thermogravimetric analysis (TGA)

TGA of R5S containing dispersions

Similar to our previous work, TGA was used to determine the composition of the ligand shells and the exchange behavior of the additive R5S [113]. Figure 7.4.7a shows the mass loss curves of the additive-free AuNP@HDT system and of the R5S containing particle system at a concentration of 128 mM, both stored for one day at room temperature and for 5 h at 50 °C. The overall shell mass decreased in the presence of R5S, which is attributed to the ligand exchange of the large HDT by the small R5S. In the case of R5N and R9S (Figure 7.4.7b), the shell mass increases after the modification with the additive, excluding a ligand exchange.

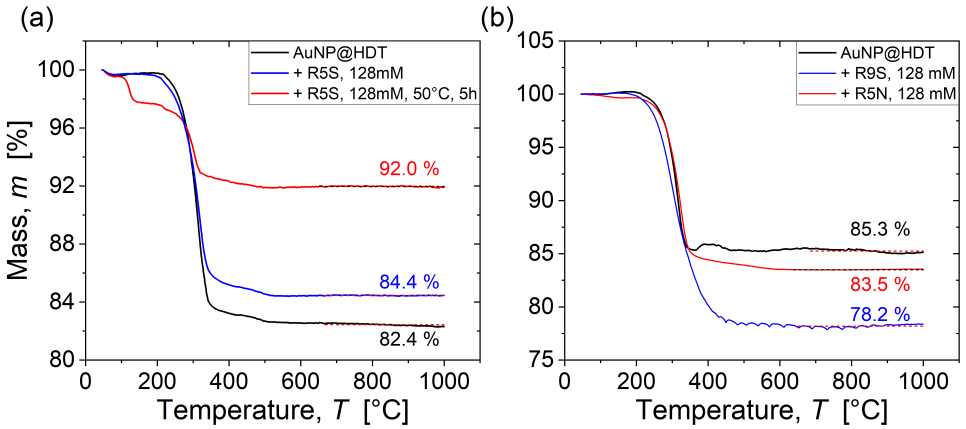


Figure 7.4.7: Results of the thermogravimetric analysis of different nanoparticle systems. (a) Mass loss of pure AuNP@HDT (black) and two AuNP@HDT samples with a R5S additive concentration of 128 mM after one day (blue) and after 5 h at 50 °C (red). (b) mass loss of pure AuNP@HDT (black) and AuNP@HDT modified with R9S at a concentration of 128 mM after one day of storage (blue), and with R5N at a concentration of 128 mM after one day of storage (red). The dotted lines indicate the areas of the curve used to determine the change in mass.

To quantify ligand exchange, the ligand shell density of the additive-free particle system must be calculated. The surface area A_{core} of one particle cores is

$$A_{\text{core}} = 4\pi r_{\text{core}}^2 \tag{7.4.18}$$

The number of particles N_{AuNP} follows from the total gold mass m_{gold} remaining in the crucible after the TGA measurement as

$$N_{\text{AuNP}} = \frac{m_{\text{gold}}}{m_{\text{core}}} = \frac{m_{\text{gold}}}{V_{\text{core}} \cdot \rho_{\text{gold}}} = \frac{m_{\text{gold}}}{\frac{4}{3}\pi r_{\text{core}}^3 \cdot \rho_{\text{gold}}} \tag{7.4.19}$$

With m_{core} the mass of a single AuNP core, V_{core} the volume of a single AuNP core and ρ_{gold} the density of gold. N_{AuNP} relates to the total core surface of all AuNPs in the crucible as

$$A_{\text{total}} = A_{\text{core}} \cdot N_{\text{AuNP}}. \tag{7.4.20}$$

Table 7.4.1: Result of the TGA measurement of the R5S containing system

Parameter	AuNP@HDT	+ R5S 128 mM (1 d, 25 °C)	+ R5S 128 mM (5 h, 50 °C)
r_{core}	2.1 nm		
m_{gold}	14.03	17.47 mg	12.94 mg
m_{loss}	2.99	3.21 mg	1.27 mg
A_{total}	$1.037 \cdot 10^{18}$ nm^2	$1.29 \cdot 10^{18}$ nm^2	$9.57 \cdot 10^{17}$ nm^2
ρ_{LS}	6.71 nm^{-2}		
a	0	0.207	0.819

The total number of surface-bound HDT ligands, N_{total}, is determined from the mass loss, m_{loss}, during the TGA measurement as

$$N_{\text{total}} = \frac{m_{\text{loss}}}{M_{\text{HDT}}} \cdot N_{\text{A}}, \tag{7.4.21}$$

where M_{ligand} is the HDT molar mass ($258.51\,\text{g/mol}$) and N_{A} is the Avogadro constant. Subsequently, the ligand shell density of the additive-free particle system, ρ_{LS}, is calculated as

$$\rho_{\text{LS}} = \frac{N_{\text{ligand}}}{A_{\text{total}}} \tag{7.4.22}$$

In the following, the fraction of HDT that is exchanged during surface modification by R5S, a, is determined. Here, it is assumed that the total number of surface-bound ligands remains constant during the ligand exchange, i.e., no HDT ligand desorbs without being replaced by an R5S molecule and no R5S molecule adsorbs without replacing a HDT ligand, and equals that of unmodified AuNPs. By extending eq. 7.4.21, the mass loss during the TGA experiment is given by

$$m_{\text{loss}} = \frac{N_{\text{total}}[aM_{\text{R5S}} + (1-a)M_{\text{HDT}}]}{N_{\text{A}}}, \tag{7.4.23}$$

with M_{R5S} the molar mass of R5S (88.17 g/mol). Rewriting yields an expression for a, given by

$$a = \frac{m_{\text{loss}}N_{\text{A}} - N_{\text{total}}M_{\text{HDT}}}{N_{\text{total}}\left[M_{\text{R5S}} - M_{\text{HDT}}\right]} \tag{7.4.24}$$

Table 7.4.1 summarizes the results of all TGA experiments with additive-containing dispersions and their analyses using equations 7.4.18 to 7.4.24.

Thermal treatment of additive-free, R9S and R5N reference systems

AuNP coarsening in the presence of additive molecules is investigated by SAXS during heating from 40 °C to 100 °C in steps of 2 K. Figure 7.4.8 shows the obtained SAXS patterns of an additive-free AuNP dispersion (Figure 7.4.8a), and in the presence of R5S, R9S and R5N (Figure 7.4.8b, c, d, respectively).

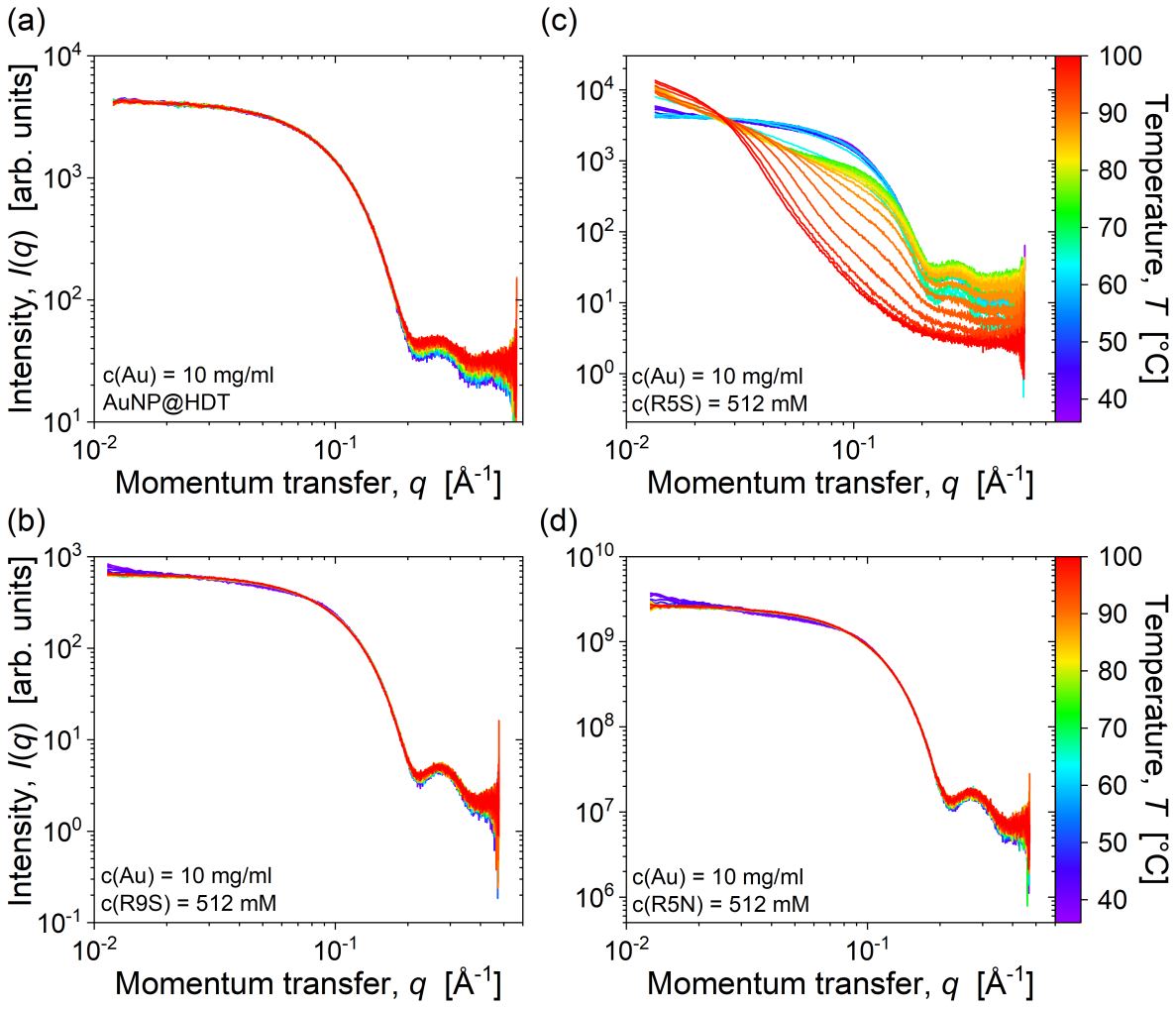


Figure 7.4.8: Temperature-dependent scattering curve of AuNP dispersions with a gold concentration of 10 mg/mL without additives (a), with R5S at a concentration of 512 mM (b), with R9S at a concentration of 512 mM (c), and with R5N at a concentration of 512 mM (d).

Small-angle neutron scattering (SANS)

Following the method described in our previous work [109], the obtained SANS patterns on AuNP dispersions were modeled using the expression

$$I_{\text{tot}}(q) = I_{\text{pCS}}(q) + I_{\text{OZ}}(q) + I_{\text{Por}}(q) + I_{\text{bkg}} \tag{7.4.25}$$

with $I_{\text{pCS}}(q)$ a form factor of polydisperse spherical core-shell particles, $I_{\text{OZ}}(q)$ an Ornstein-Zernike structure factor, $I_{\text{Porod}}(q)$ a Porod term (eq. 7.4.7), and I_{bkg} the incoherent background scattering.

$I_{\text{pCS}}(q)$ is given by

$$I_{\text{pCS}}(q) = \int_0^\infty G(r_{\text{c}}) I_{\text{CS}}(q, r_{\text{c}}) dr_{\text{c}} \tag{7.4.26}$$

with r_{c} the core size, $I_{\text{CS}}(q, r_{\text{c}})$ the form factor of monodisperse core-shell particles and $G(r_{\text{c}})$ the core radius distribution function, approximated by a Schultz-Zimm distribution. $I_{\text{CS}}(q)$ is calculates as

$$I_{\text{CS}}(q, r_{\text{c}}) = N \left[\frac{3V_{\text{c}}(SLD_{\text{c}} - SLD_{\text{s}}) J(qr_{\text{c}})}{qr_{\text{c}}} + \frac{3V_{\text{c+s}}(SLD_{\text{s}} - SLD_{\text{m}}) J(q(r_{\text{c}} + t_{\text{s}}))}{q(r_{\text{c}} + t_{\text{s}})} \right]^2 \tag{7.4.27}$$

Here is N the number density of the particles in the system, V_{c} the volume of the core, $V_{\text{c+s}}$ the total particle volume, r_{c} the radius of the core, t_{s} the thickness of the shell, SLD_{c} the scattering length density of the core, SLD_{s} the scattering length density of the shell, SLD_{m} the scattering length density of the medium. $J(x)$ is given by

$$J(x) = \frac{\sin x - x \cos x}{x^2} \tag{7.4.28}$$

Lastly, $I_{\text{OZ}}(q)$ is given by

$$I_{\text{OZ}}(q) = \frac{I_0}{1 + (q\xi_{\text{OZ}})^2} \tag{7.4.29}$$

with I_0 the scattering amplitude and ξ_{OZ} the correlation length of concentration fluctuations.

Figure 7.4.9 exemplarily shows a model fit according to eq. 7.4.25 including its individual contributions. In Figure 7.4.10, SANS patterns of AuNP dispersions in the presence of R5N and R9S are shown in Figure 7.4.10.

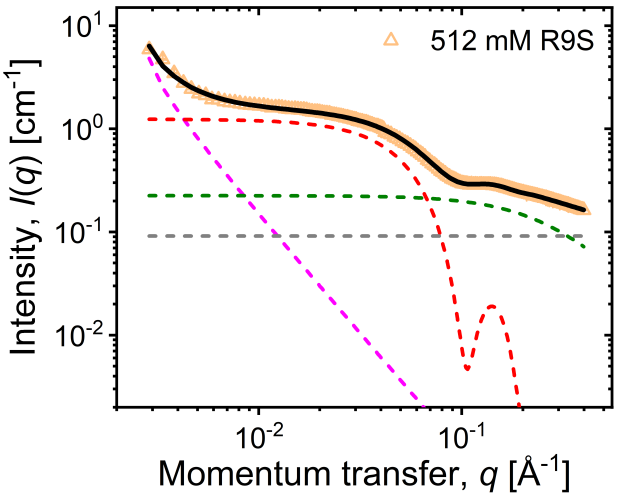


Figure 7.4.9: SANS pattern of 4 nm AuNPs dispersed in n-decane-d_{22} at a concentration of 10 mg ml^{-1} in the presence of R9S at a concentration of 512 mM. Furthermore shown are a model fit according to eq. 7.4.25 (black line) and its individual contributions: $I_{\mathrm{pCS}}(q)$ (red dotted line), $I_{\mathrm{OZ}}(q)$ (green dotted line), $I_{\mathrm{Porod}}(q)$ (purple dotted line) and I_{bkg} (grey dotted line).

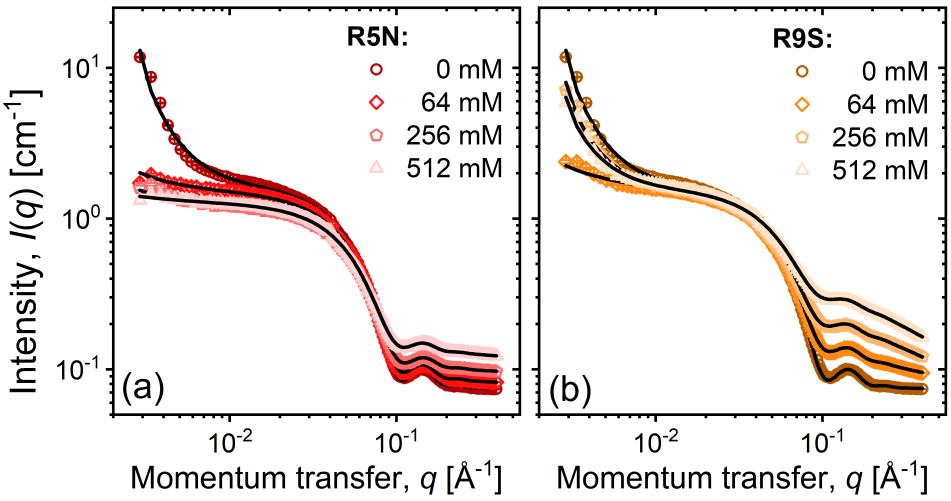


Figure 7.4.10: SANS patterns of 4 nm AuNPs dispersed in n-decane-d_{22} at a concentration of 10 mg ml^{-1} in the presence of R5N (a) and R9S (b) at concentrations as indicated in the graphs. Black lines represent model fits according to eq. 7.4.25.

Diffusion-limited aggregation theory

The Smoluchowski coagulation equation is a differential equation that describes the time-evolution of particle number densities as they coagulate [314], and is given by

$$\frac{dn_j}{dt} = \frac{1}{2}\sum_{i+k=j} K_{ik}\, n_i\, n_k - n_j \sum_{i\geq 1} K_{ij}\, n_j \tag{7.4.30}$$

with n_j the number concentration of particle clusters containing j primary particles, and K_{ij} a coagulation kernel, describing the rate of collisions between clusters containing i and j primary particles. K may assumed to be constant for agglomeration processes of narrowly-dispersed particles in their early stage [315].

Following previous work [315], the Smoluchowski coagulation equation can be solved analytically assuming a constant K, yielding the number concentration of primary particles as a function of time, $N(t)$, and is given by

$$N(t) = N_0 \frac{1}{1 + \frac{1}{2} K N_0 t} \tag{7.4.31}$$

with N_0 the initial number concentration of primary particles.

Rearranging eq. 7.4.31 yields the time required to decrease the number of primary particles to a given fraction, $x = N(t_\mathrm{x})/N_0$, given by

$$t_x = 2\frac{1-x}{xKN_0} \tag{7.4.32}$$

For diffusion-limited aggregation, K may be approximated by [315]

$$K = \frac{8 k_\mathrm{B} T}{3\eta} \tag{7.4.33}$$

with T the temperature, k_B the Boltzmann constant and η the dynamic viscosity of the solvent. Combining eqs. 7.4.32 and 7.4.33 gives

$$t_x \propto \frac{1}{K} \propto \frac{\eta}{k_\mathrm{B} T} \tag{7.4.34}$$

Thus, the time required to decrease the number concentration of primary particles to a given value depends only on T and η.

7.5 Supporting Data - Gold Sponge Formation by Temperature-induced Aggregation of a Stable Nanoparticle Dispersion

Formation mechanism of gold sponges

Note that the first steps of the mechanism are identical to those reported earlier (see Chapter 3.4). The reaction begins with the replacement of HDT ligands by the additive R5S. This replacement changes the structure and properties of the shell, which leads to the formation of links between the cores. The addition of further cores results in the formation of aggregates in the μm-range at the end of the reaction.

Time-dependent TEM measurements

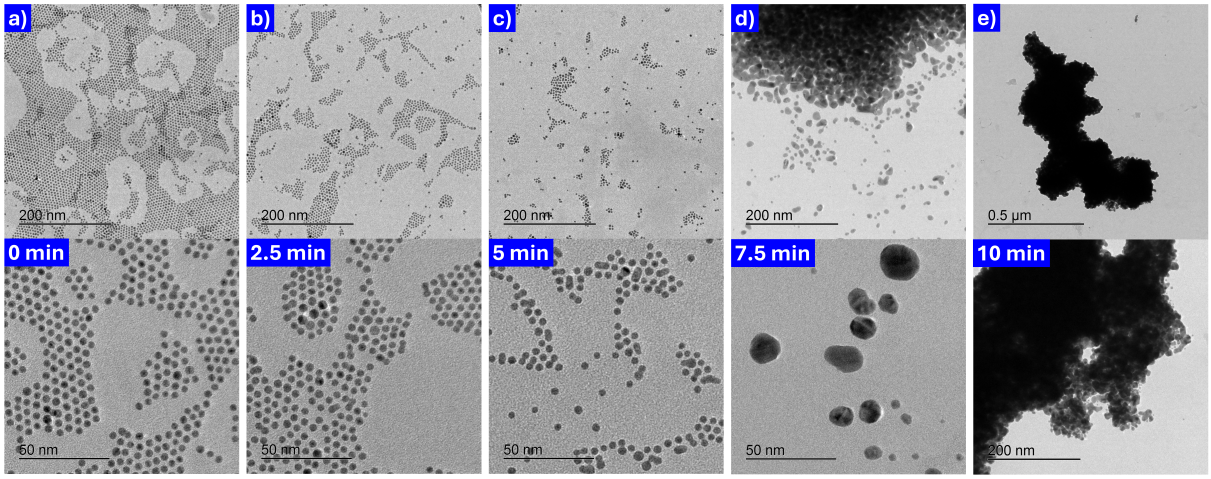


Figure 7.5.1: Scanning electron micrographs at different magnifications of 4 nm core diameter gold nanoparticles coated with hexadecanethiol at different times during heating at 90 °C.

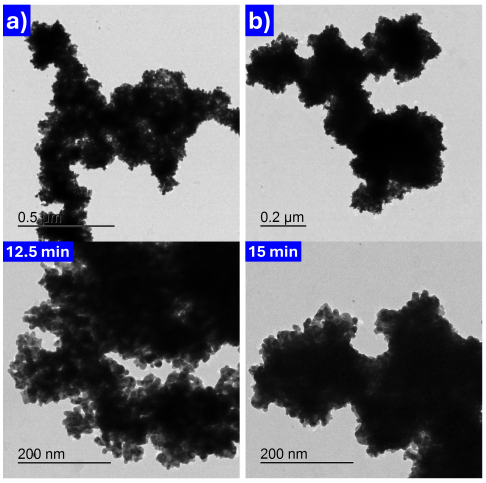


Figure 7.5.2: Scanning electron micrographs at different magnifications of 4 nm core diameter gold nanoparticles coated with hexadecanethiol at different times during heating at 90 °C.

Time-dependent dynamic light scattering measurements

Dynamic light scattering measurements were performed to characterize the change in the average particle size. The intensity autocorrelation functions, $g_2(\tau)$ are shown in Figure 7.5.3. They were modelled using the expression

$$g_2(\tau) - 1 = A_{slow} \left[g_{1,slow}(\tau)\right]^2 + A_{fast}(\tau) \left[g_{1,fast}\right]^2 \tag{7.5.1}$$

with τ the lag time, $g_{1,slow}(\tau)$ and $g_{1,fast}(\tau)$ field correlation functions, and A_{slow} and A_{fast} amplitudes of the slow and fast mode, respectively. A slow mode indicates large particles/aggregates, while a fast mode indicates small particles. The field correlation functions are approximated by stretched exponential functions, given by

$$g_{1,i}(\tau) = e^{-(\frac{\tau}{\tau_i})^{b_i}} \tag{7.5.2}$$

Here, b_i are stretching exponents with i being $slow$ or $fast$, quantifying the width of the distribution of correlation times of the respective mode. The mean decay times were calculated from τ_{slow} and τ_{fast} as

$$\langle\tau_i\rangle = \frac{\tau_i}{b_i}\Gamma(\frac{1}{b_i}) \tag{7.5.3}$$

The diffusion coefficients, D_i, are calculated from $\langle\tau_i\rangle$ as

$$D_i = \frac{1}{\langle\tau_i\rangle q^2} \tag{7.5.4}$$

with *q* the wave vector, calculated as

$$q = \frac{4\pi n_0}{\lambda} \sin\frac{\theta}{2} \tag{7.5.5}$$

Here, n_0 is the refractive index of the solvent, λ, the wavelength of incident photons, and θ the detector angle.

The hydrodynamic diameter of the aggregates can be calculated using the Stokes-Einstein relation:

$$r_h = \frac{k_B T}{6\pi\eta D} \tag{7.5.6}$$

Here is k_B the Boltzmann constant, T the temperature (303.15 K), η the viscosity and *D* the diffusion coefficient.

We estimated the sedimentation rate of gold particles and their aggregates from their D_h using

$$v = \frac{2}{9}\frac{(\rho_c - \rho_s) r^2 g}{\eta_0} \tag{7.5.7}$$

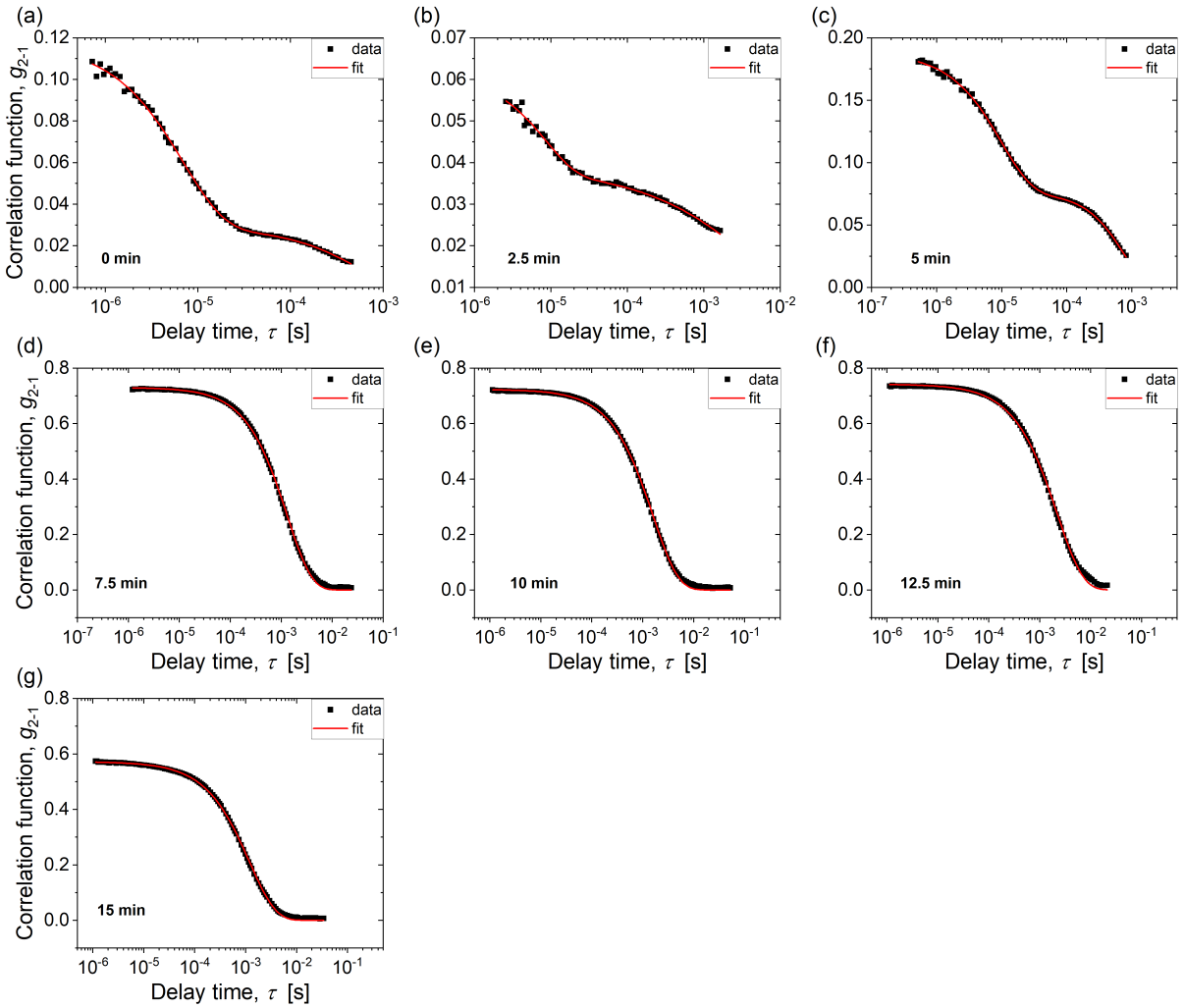


Figure 7.5.3: Correlation curves of the DLS measurement of a sponge reaction based on 4 nm particles coated with HDT after: a) 0 min, b) 2.5 min, c) 5 min, d) 7.5 min, e) 10 min, f) 12.5 min and g) 0 min. The black squares show the measured data. The red line shows the fit curve.

Table 7.5.1: Sedimentation rates of the aggregates formed during the sponge reaction.

Reaction time, [min]	Radius r, [nm]	Sedimentation rate v, [mm/s]	Time for 10 mm, [min]
7.5	680 ± 60	0.031	5.4
10	866 ± 77	0.050	3.3
12.5	1237 ± 145	0.10	1.6
15	682 ± 65	0.031	5.4

with ρ_c the density of the gold core ($19.3\,\mathrm{g/cm^3}$), ρ_s the density of the solvent toluene ($0.87\,\mathrm{g/cm^3}$), r the radius of the particle, g the standard gravity, and η_s the viscosity of the solvent ($0.6\,\mathrm{mPa\,sec}$).

Effect of the core size and ligand system on the sponge properties

Aggregate size and shape

Figures 7.5.4 to 7.5.6 show micrographs of the aggregates formed during sponge formation.

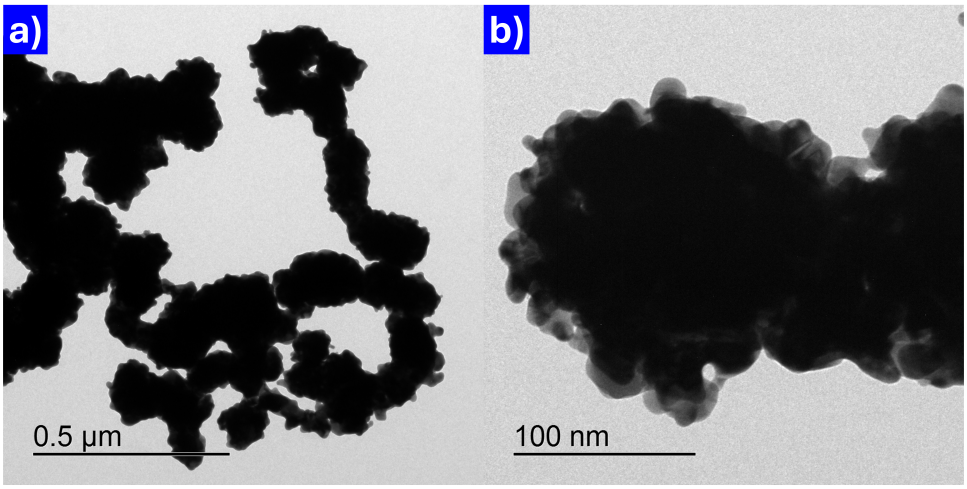


Figure 7.5.4: Scanning electron micrographs at different magnifications of gold aggregates synthesized from 9 nm core diameter gold nanoparticles coated with hexadecanethiol.

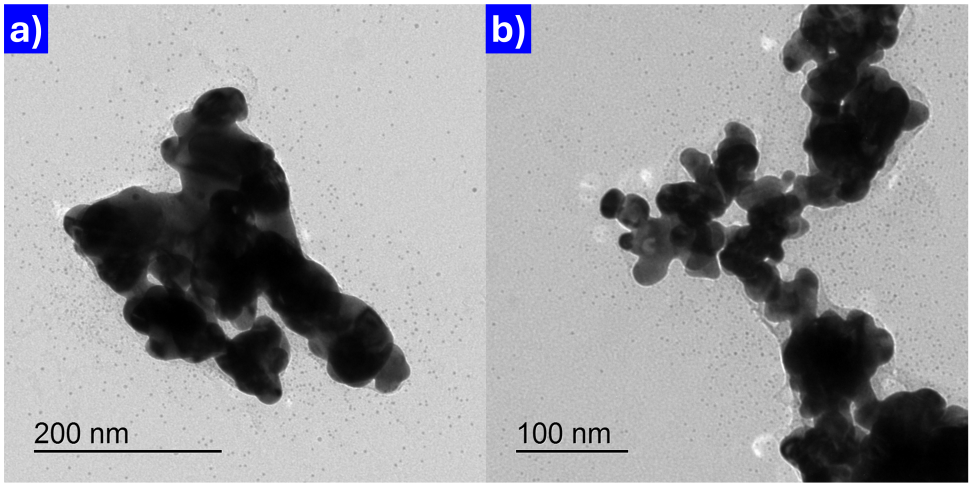


Figure 7.5.5: Scanning electron micrographs at different magnifications of gold aggregates synthesized from 4 nm core diameter gold nanoparticles coated with oleylamine.

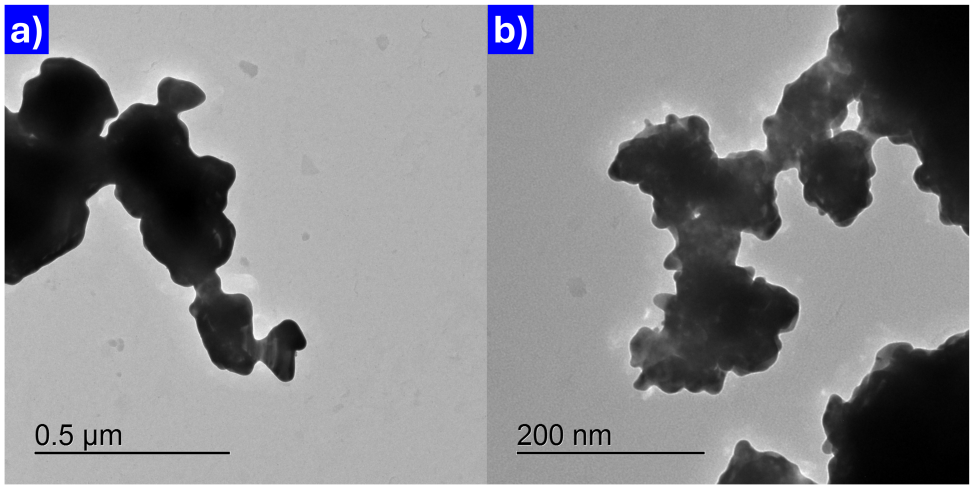


Figure 7.5.6: Scanning electron micrographs at different magnifications of gold aggregates synthesized from 9 nm core diameter gold nanoparticles coated with oleylamine.

SEM measurements of the sponge systems

Scanning electron micrographs of the freeze-dried sponges made from particles with different cores and ligand shells are shown in Figure 7.5.7 to 7.5.10.

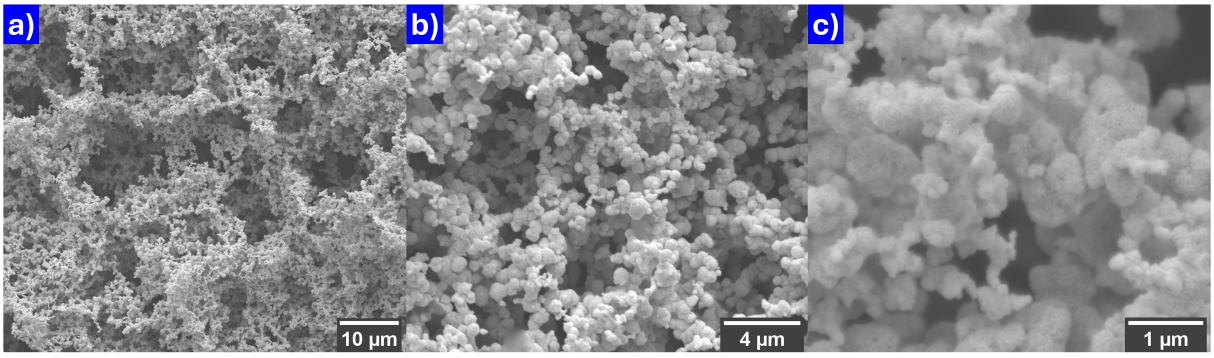


Figure 7.5.7: Scanning electron micrographs of a gold sponge synthesized from 4 nm core diameter particles coated with HDT.

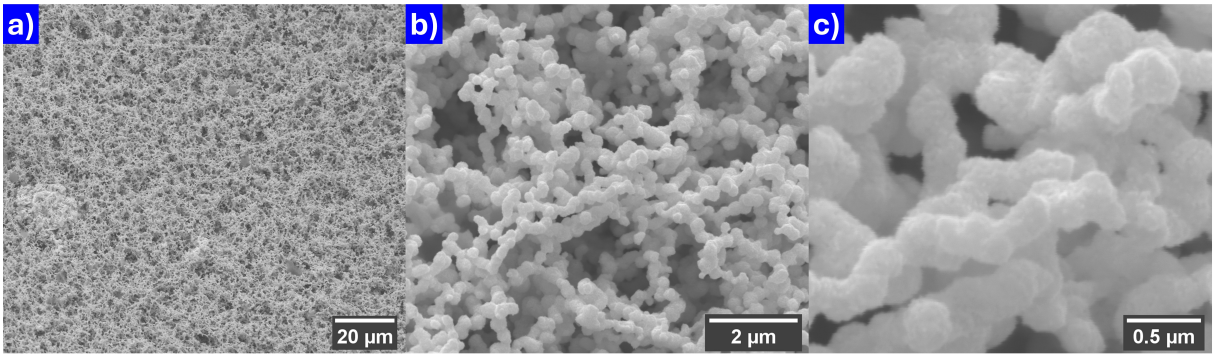


Figure 7.5.8: Scanning electron micrographs of a gold sponge synthesized from 9 nm core diameter particles coated with HDT.

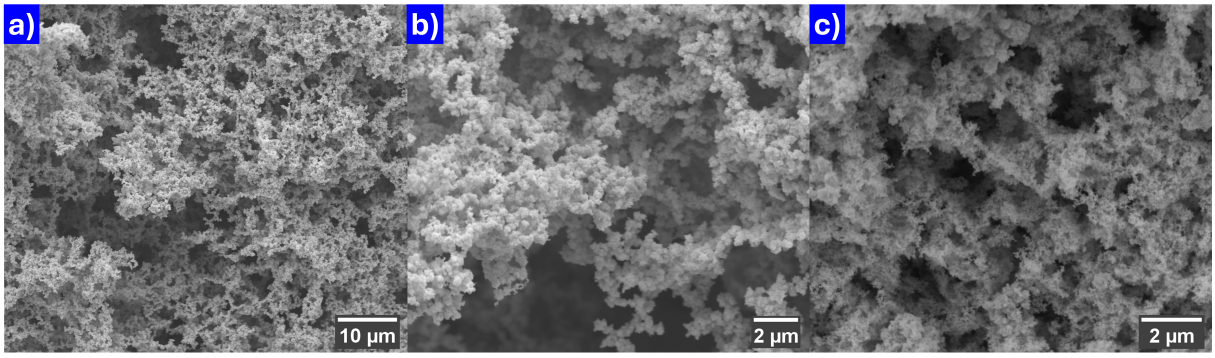


Figure 7.5.9: Scanning electron micrographs of a gold sponge synthesized from 4 nm core diameter particles coated with OAm.

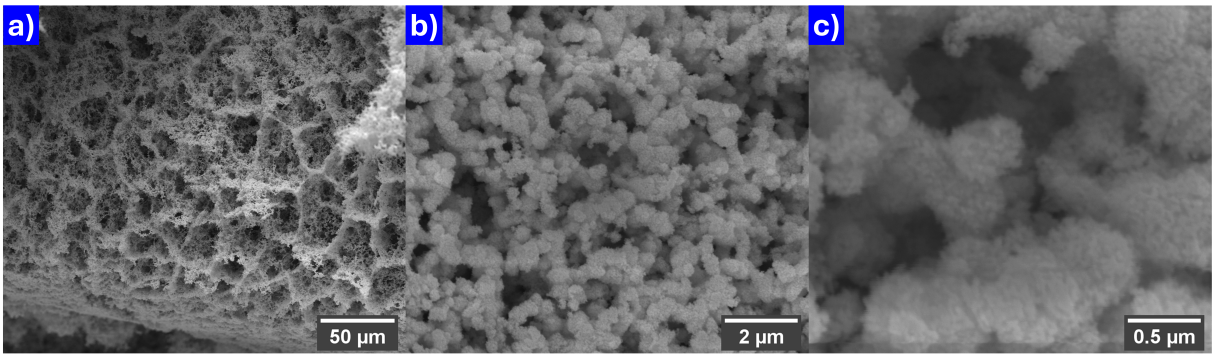


Figure 7.5.10: Scanning electron micrographs of a gold sponge synthesized from 9 nm particles coated with OAm.

Results of the label analysis

Figure 7.5.11 and 7.5.12 and Table 7.5.2 summarize the results of the label analysis of the 3D reconstruction of the different sponge systems (details of the analysis are shown in the methods section in the main manuscript). The values are discussed in the part of the Results and Discussions section in the main manuscript.

Table 7.5.2: Properties of the gold sponges depending on the used particle system.

vol% gold	vol% main structure	tortuosity [1, ∞]	fractal dimension
4 nm HDT			
3.92	3.69	4.68	2.2
9 nm HDT			
5.39	5.11	3.82	2.2
4 nm OAm			
10.69	10.63	2.13	2.3
9 nm OAm			
6.92	5.98	2.99	2.2

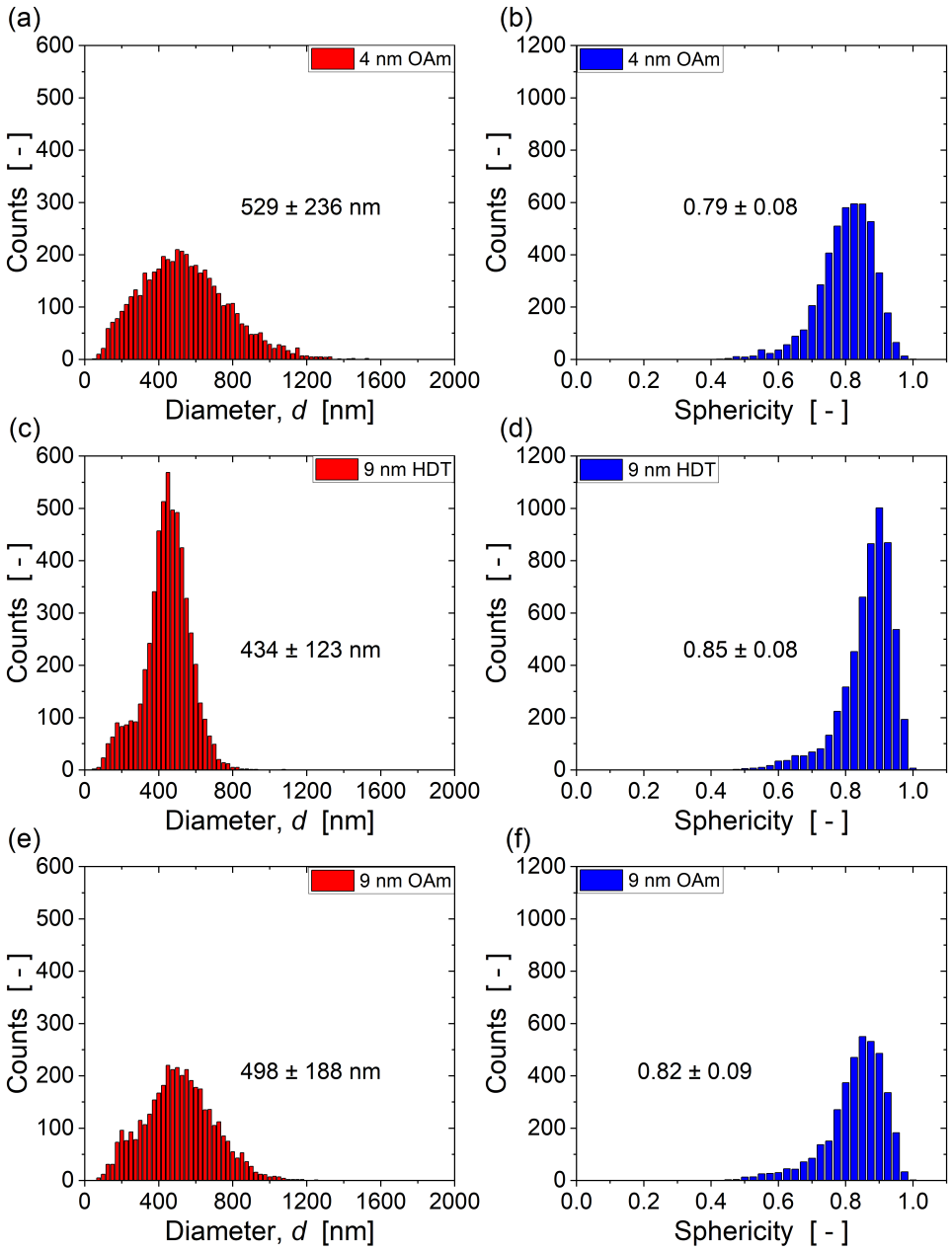


Figure 7.5.11: Histogram of the size and the sphericity of particles inside of the sponge structure for samples made from: 4 nm AuNP coated with oleylamine (a, b), 9 nm core diameter AuNP coated with hexedaceanethiol (c, d) and, 9 nm AuNP coated with oleylamine (e, f).

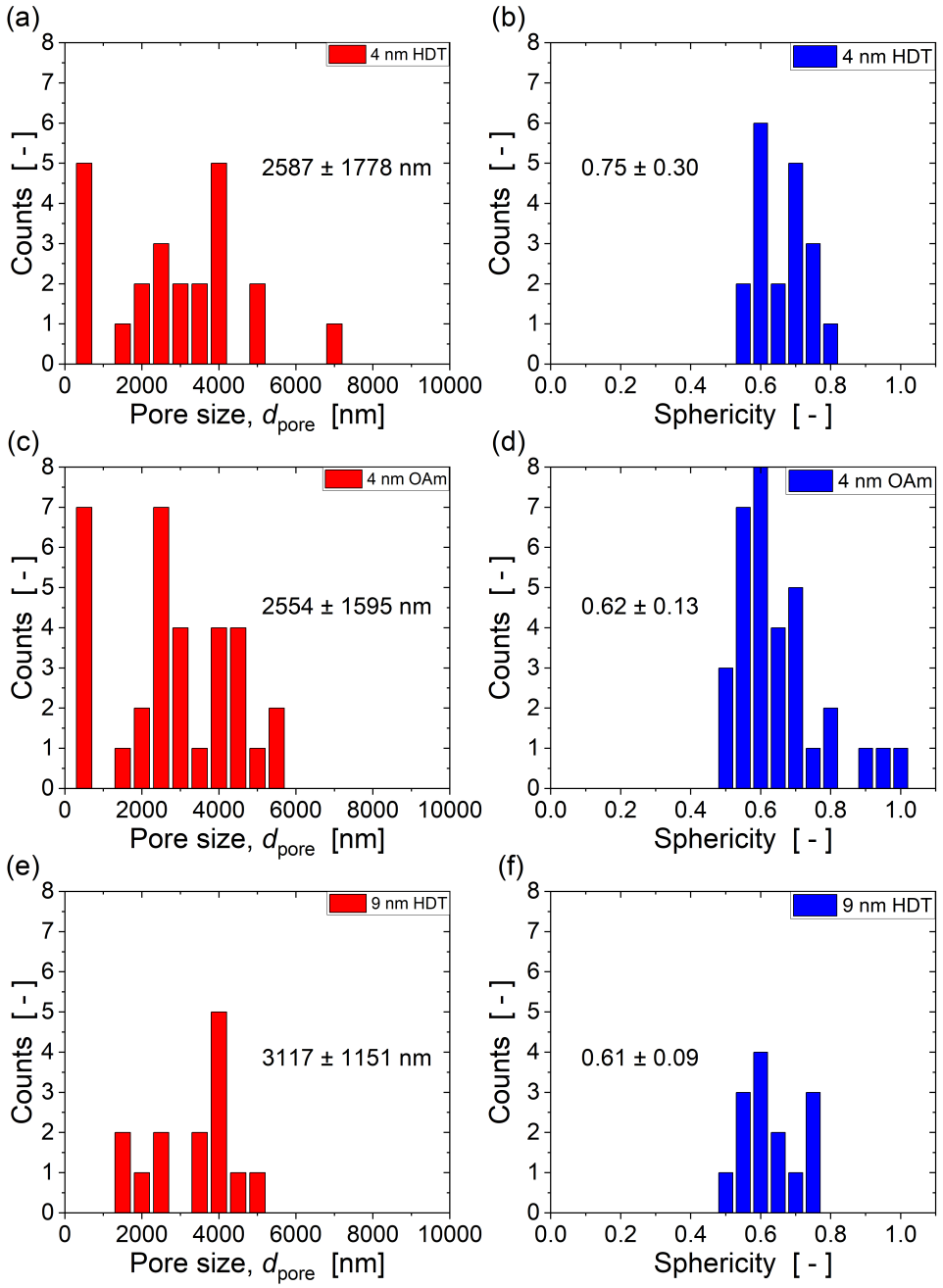


Figure 7.5.12: Histogram of the size and the sphericity of pores inside the sponge structure for samples made from: 4 nm AuNP coated with hexadeacnethiol (a, b), 4 nm core diameter AuNP coated with oleylamine (c, d) and, 9 nm AuNP coated with hexadecanethiol (e, f).

Thermo-gravimetric analysis

Figure 7.5.13 illustrates the change in the sample mass of all four sponge systems during heating from room temperature to 1000 °C.

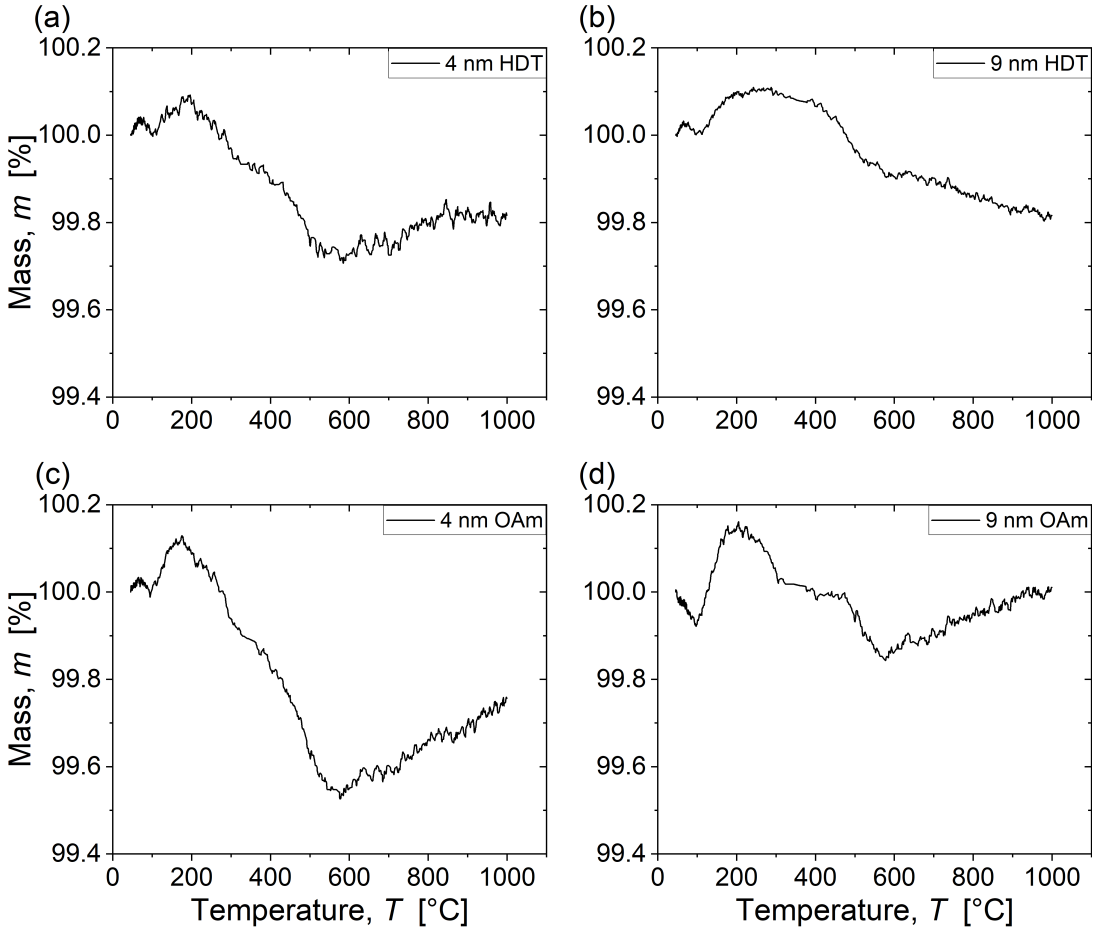


Figure 7.5.13: Results of the thermogravimetric analysis of gold sponges made from a) 4 nm AuNP coated with HDT, b) 9 nm AuNP coated with HDT, c) 4 nm AuNP coated with OAm, and d) 9 nm AuNP coated with OAm.

Gas adsorption

Gas adsorption measurements with BET analysis were performed to analyze the specific surface of the gold sponges. A detailed description of the performed measurements is shown in the method section of the main manuscript. Each sample was measured three times. The measured gas isotherms are shown in Figure 7.5.14.

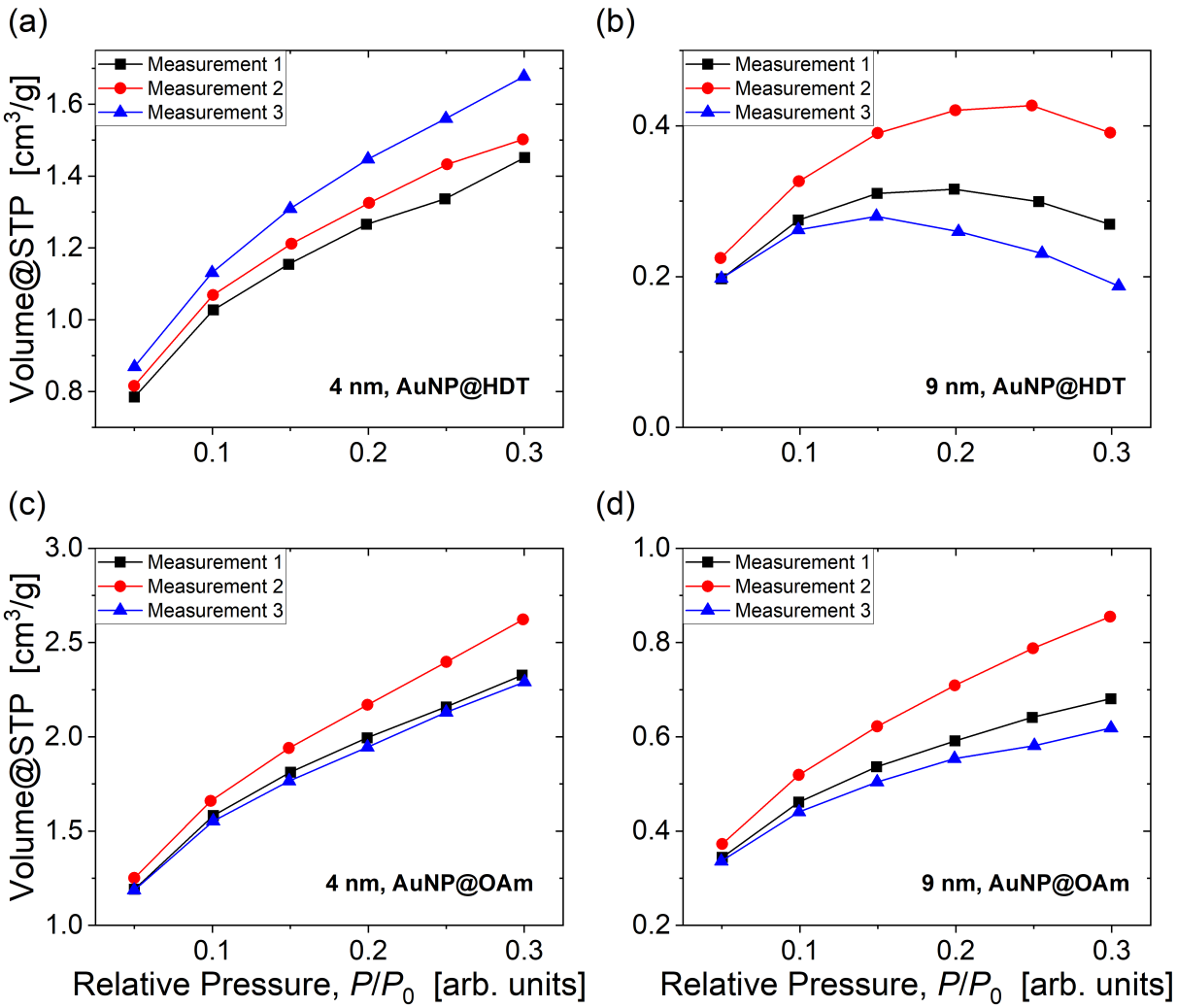


Figure 7.5.14: Gas isotherms of the different sponge systems: a) 4 nm AuNP@HDT, a) 9 nm AuNP@HDT, a) 4 nm AuNP@OAm, a) 9 nm AuNP@OAm.

The specific surfaces shown in the main manuscript are the average values of the three measurements. The individual surface area values are shown in Table 7.5.3.

Calculation of the change of the gold surface and ligand coverage

To estimate the effect of the surface reduction during the sponge formation on the coverage of the HDT/R5S molecules. To determine the shell density, we calculated the sponge's surface

Table 7.5.3: Specific surface of the different sponge systems.

particle system	m1 [m^2g^{-1}]	m2 [m^2g^{-1}]	m3 [m^2g^{-1}]	av. [m^2g^{-1}]
4 nm AuNP@HDT	4.65	4.88	5.47	5.00
9 nm AuNP@HDT	/	/	/	< 2
4 nm AuNP@OAm	7.59	8.67	7.45	7.90
9 nm AuNP@OAm	2.24	2.92	2.00	2.39

area from the BET results (only for the sponge made from particles with a core diameter of 4 nm coated with HDT).

$$A_{\text{sponge}} = m_{\text{sponge, BET}} \cdot A_{\text{specific}} \tag{7.5.8}$$

Here is $m_{\text{sponge, BET}}$, the mass of the sponge used for the BET measurement, and A_{specific} the specific surface area determined by the BET measurement.
The number of surface-bound HDT/R5S molecules $N_{\text{HDT/R5S}}$ was calculated using the results of the TGA measurement.

$$N_{\text{HDT/R5S}} = \frac{m_{\text{shell}}}{M_{\text{HDT/R5S}}} \cdot N_{\text{A}} \tag{7.5.9}$$

Here is m_{shell}, the mass of the shell found in the TGA measurement, $M_{\text{HDT/R5S}}$, the molecular mass of the surface-bound molecules, and N_{A}, the Avogadro constant. The shell density of the sponge ρ_{sponge} was calculated as follows:

$$\rho_{\text{sponge}} = \frac{N_{\text{HDT/R5S}}}{A_{\text{sponge}}} \tag{7.5.10}$$

We compared the sponge's shell density with the density of the initial nanoparticle system. In our previous work, we found a density of 6.71 nm^{-2} for HDT-coated nanoparticles. Considering the increasing R5S fraction during heating we calculated the density for two different shell compositions. The first system was a shell with an R5S fraction of 100 num%. The second system is based on our previous findings, where the shell consists of 82 num% of R5S and 18 num% of HDT (after 5 h at 50 °C, see Chapter 3.4). The results are summarized in Table 7.5.4.
Independent of the shell composition, the shell density of the sponge system is significantly lower than the shell density of the nanoparticle system.

Table 7.5.4: Specific surface of the different sponge systems.

particle /sponge system	4 nm AuNP@HDT
Mass of the sponge, $m_{\text{sponge, BET}}$	0.193 g
Specific surface area, SSA	5.0 m^2g^{-1}
Surface surface of the sponge, A_{sponge}	0.96 m^2
Mass of the TGA sample, m_{TGA}	16 mg
Mass of the shell, m_{shell}	0.032 mg
Molecular mass R5S, M_{R5S}	88.1 g/mol
Molecular mass HDT, M_{HDT}	258.5 g/mol
Shell density 100 num% R5S,	0.23 nm^{-2}
Shell density 82 num% R5S,	0.17 nm^{-2}

Preparation of the TEM lift-out samples

We prepared lamellae for TEM lift-out of the sponge synthesized from 4 nm core diameter AuNP@HDT using the infiltrated sample prepared for the FIB-SEM (cf. Method section in the main manuscript). A combined FIB/SEM - dualbeam scanning microscope (Versa 3D Low Vac) from FEI (USA) was used for cutting and lift-out. The Epofix-infiltrated gold sample was prepared in the following way:

1. Deposition of a local protecting Pt-layer (area: 25×5 µm) using a electron beam (2 kV, 1.1 nA, z=0.3 µm (thickness), tilting 0°) and a ion beam (30 kV, 1.0 nA, z=3 µm (thickness), tilting 52°).

2. A cross-section is prepared using an ion beam directly on the front edge of the Pt protective layer. The process is divided into two steps: the deep cutting of a trench (regular cross-section, application: PMMA, 30 kV, 15 nA, x-y-z: 25 µm-10 µm-4 µm) and the polishing of the vertical cut surface (cleaning cross-section, application: PMMA, 30 kV, 5 nA, z = 1 µm, tilting +1° (total: 53°).

In the next step, the lamella was separated from the prepared cross-section:

1. Deep cutting of a "trench" on the opposite side of the cross-section (= above Pt deposition, mirror-inverted) at 52° (= perpendicular to the ion beam)

2. Stepwise cutting of the remaining ridge using the
cleaning function at a beam current of 3 nA until a thickness of 1 µm.

3. Cut through this bar with the ion beam at a 5° tilt angle with individual "rectangles" at 0.3 nA; cut the lamella to a dimension of approx. 20 x 7 µm. (a small connection should be left).

4. The sample is now precisely aligned so that the micro-manipulator ("omniprobe") can be inserted and its tip welded to the free-cut edge of the lamella using Pt deposition. The attached lamella is then removed and reattached to a special grid (Cu) for the TEM sample holder using Pt deposition.

5. Here, the welded-on lamella is thinned further to a thickness of < 100 nm: Starting from the 52° angle, thin on both sides at $\pm$ 1° tilt angle with gradually lower ion beam current until a thickness of just 80 nm to 100 nm can be measured on the image: to do this, set "cleaning cross section" (= CCS) patterns and thin the ridge alternately with 0.3 nA and 0.1 nA at z=0.3 µm. Control the process with a short snapshot image.

Caution with inhomogeneous, anisotropic, phase-rich or composite samples: Strong stresses can occur within the material, causing the lamella to bend from a certain thickness!

6. Final polishing of the lamella sides with the following setting: 5 kV (ion-beam), 77 pA, with $\pm$ 20° tilt to the ion beam. Each side should be scanned (polished) for approx. 40 sec to 60 sec with the "rectangle" pattern.

The polished sample was transferred to the TEM.

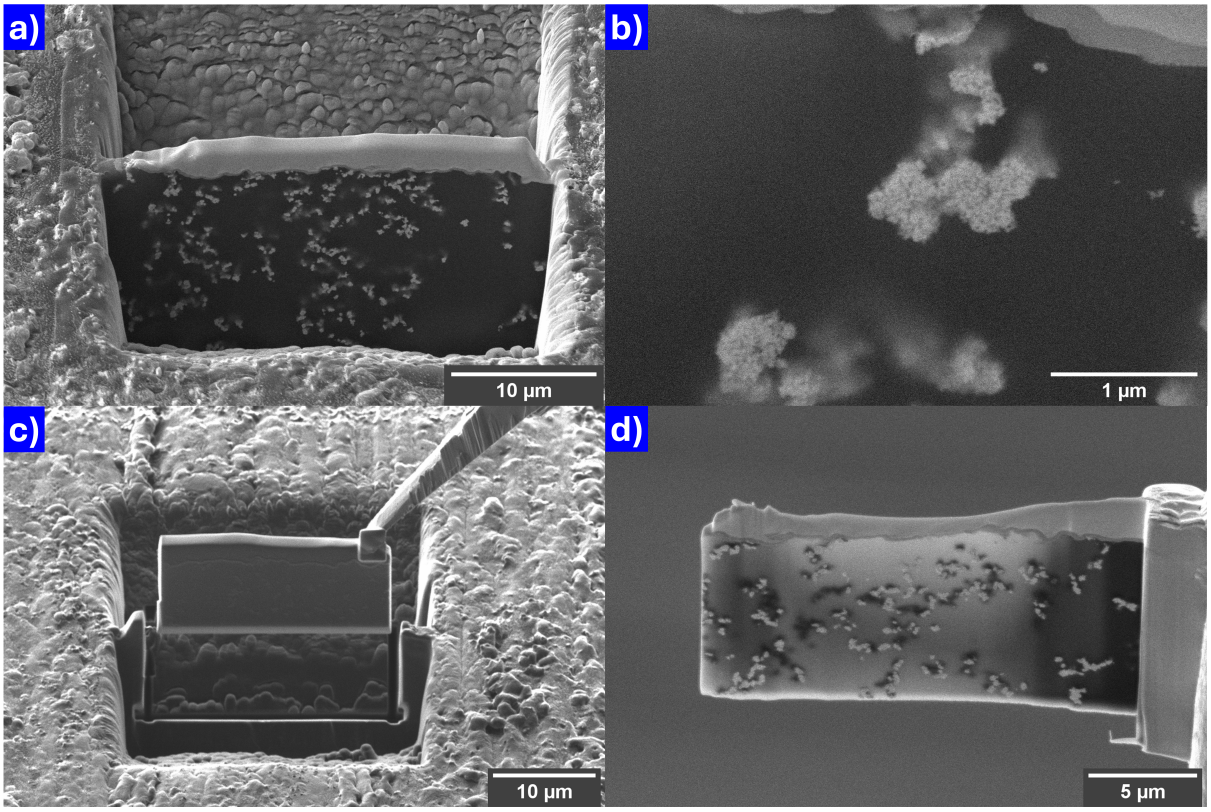


Figure 7.5.15: Scanning electron micrographs taken during the FIB cutting process of the lamella.

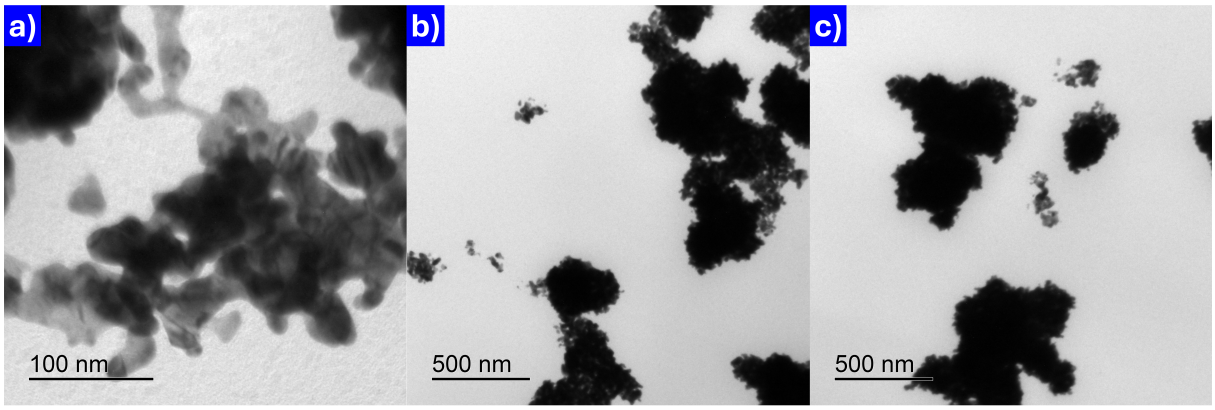


Figure 7.5.16: Transmission electron micrographs of the gold structures inside the sponge lamella.

Purification of gold sponges

The purification of the sponges is described in detail in the methods section of the main manuscript. Figure 7.5.17a shows a gold sponge after synthesis from 4 nm AuNP with an HDT shell. The transparent supernatant shows that most of the particles were converted in the reaction. Figure 7.5.17b shows the folded gold sponge after shaking the container. Figure 7.5.17c shows the sponge after freeze-drying.

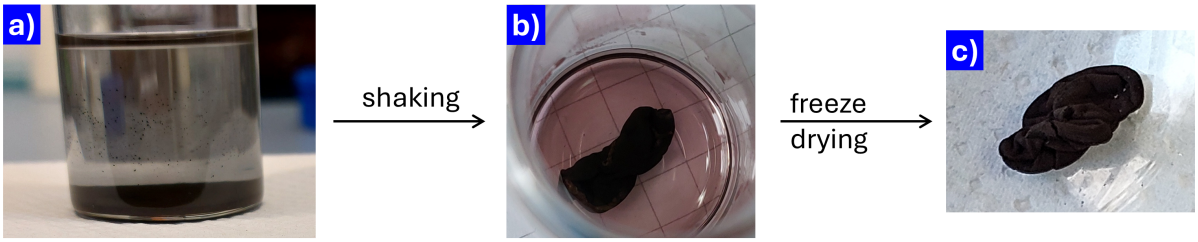


Figure 7.5.17: Stepwise purification and separation of the gold sponges. In the first step, the flat sponges get folded by shaking. In the second step, the solvent is removed by freeze-drying.

Small-angle X-ray scattering

Small-angle X-ray scattering measurements were performed to analyze the size of the particles used for the synthesis of sponge structures. The scattering contrast between the organic ligands and solvent molecules is negligible, and only the Au cores were visible in the scattering patterns. Therefore, the size of the cores was determined by modeling the obtained scattering patterns using the expression (see Figure 7.5.18)

$$I(q) = P_{\mathrm{pS}}(q) + I_{\mathrm{bkg}} \tag{7.5.11}$$

with $P_{\mathrm{pS}}(q)$ a form factor of polydisperse spheres [200] and I_{bkg} a constant accounting for background scattering. P_{pS} is given by

$$P_{\mathrm{pS}} = \int_0^\infty G(r)F(q,r)\,dr \tag{7.5.12}$$

with r the core radius, $F(q,r)$ the form factor for monodisperse spheres and $G(r)$ the size distribution of the core radius. $F(q,r)$ is given by

$$F(q,r) = 3 \cdot \frac{\sin qr - qr\cos qr}{(qr)^3}. \tag{7.5.13}$$

$G(r_{\mathrm{c}})$ is described by a Gaussian distribution, given by

$$G(r) = \frac{1}{\sigma\sqrt{2\pi}} \exp\Big[-\frac{1}{\sigma^2}(r - r_{\mathrm{avg}})^2\Big] \tag{7.5.14}$$

with r_{avg} the average core radius. σ is given by

$$\sigma = \frac{r_{\mathrm{c}}}{r_{\mathrm{avg}}} \tag{7.5.15}$$

The two types of AuNPs from all batches used in this study had cores with r_{avg} of 2 nm (σ=11.5 %) or 4.55 nm (σ=7.7 %).

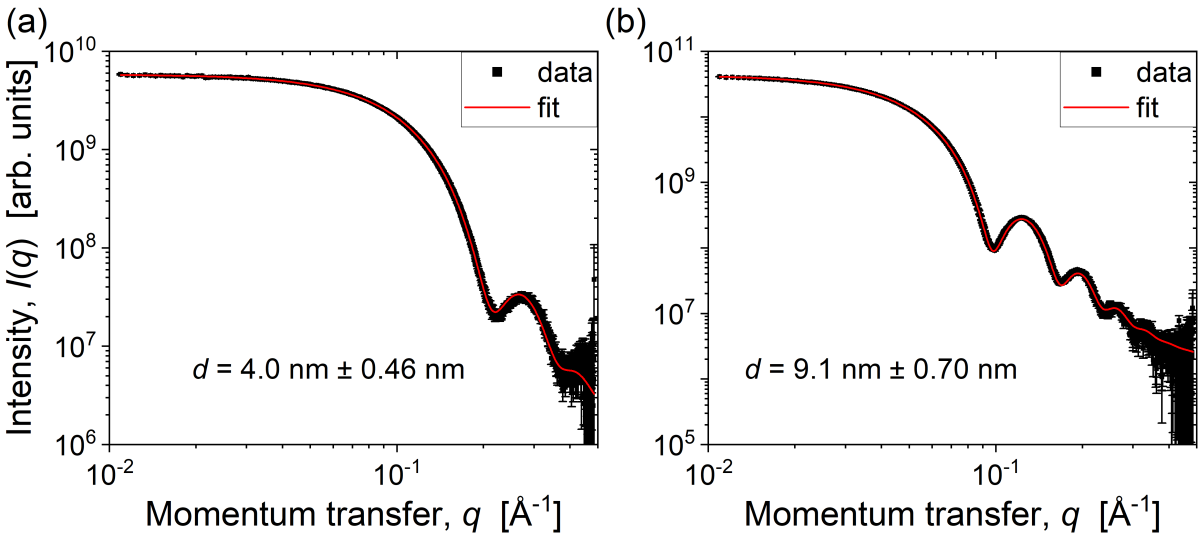


Figure 7.5.18: SAXS curves of oleylamine coated AuNPs after the synthesis with a size diameter of 4.0 nm (a) and 9.1 nm (b). The red line is the model fit according to eq. 7.5.11.

Microparticle formation

If the dispersion is stirred during the heating at 90 °C, microparticles are formed. Such particles are shown in Figure 7.5.19.

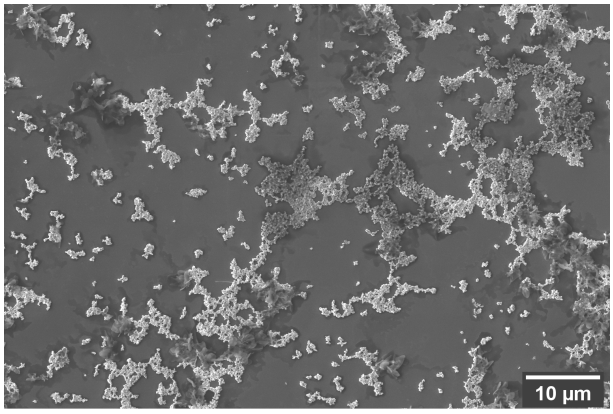


Figure 7.5.19: Scanning electron micrograph of the microparticles formed when the dispersion is stirred during the reaction.